UNIVERSITY OF OKLAHOMA

GRADUATE COLLEGE

ROCK TYPING IN ORGANIC SHALES: EAGLE FORD, WOODFORD, BARNETT AND WOLFCAMP FORMATIONS

A THESIS

SUBMITTED TO THE GRADUATE FACULTY

in partial fulfillment of the requirements for the

Degree of

MASTER OF SCIENCE

By

ISHANK GUPTA
Norman, Oklahoma
2017

ROCK TYPING IN ORGANIC SHALES: EAGLE FORD, WOODFORD, BARNETT AND WOLFCAMP FORMATIONS

A THESIS APPROVED FOR THE
MEWBOURNE SCHOOL OF PETROLEUM AND GEOLOGICAL ENGINEERING

BY

_____
Dr. Chandra Rai, Chair

_____
Dr. Carl Sondergeld

_____
Dr. Deepak Devegowda

Dedicated to

“My Professors, Family and Friends”

Acknowledgements

I would like to thank Devon, Cimarex, Shell, ConocoPhillips, BHP, Pioneer, Apache, and Drilling Info for providing the cores and logs to carry out the study.

I would like to thank Dr. Chandra Rai and Dr. Carl Sondergeld for this lifetime opportunity. Their continuous support and guidance has helped me both professionally and personally. Their courses namely Seismic Reservoir Modelling and Unconventional Reservoirs are some of the best courses I have taken in my life. I look up to them and I promise to work hard, because it does not matter if the oil industry is going up or down, I am here to stay.

I would also like to thank Dr. Deepak Devegowda, as he has been a source of inspiration for many reasons. He helped me in getting assistantship when I initially got accepted to OU. He certainly inspired me to stay fit and work hard in the gym. Finally, his course "Data Mining for Petroleum Engineers" has been instrumental to my thesis completion.

I would also like to thank fellow IC^3 colleagues, especially Mikki and Gary for taking out the time to teach me and troubleshooting the machines in the lab.

I would also like to thank my friends Priyank and Abhishek for making this journey a lot of fun.

Finally, I would like to thank my sister, Swati, and my parents for being patient with me. They always stood by my decisions and me. You all are the world to me.

Table of Contents

List of Tables

List of Figures

Abstract

Shales are the most common sedimentary rocks found on earth. Most US shale plays are spatially extensive with regions of different maturity and varying prospects. With increasing understanding of the heterogeneity, microstructure and anisotropy of shales, efforts are now directed to identifying sweet spots and optimizing completion zones in any shale play. Rock typing is a step in this direction. It is becoming an integral part of the unconventional reservoir characterization workflow.

In this work, an integrated workflow is presented for rock typing using lab petrophysical measurements, logs, and production data. The key petrophysical parameters used for rock typing are porosity, total organic carbon (TOC), mineralogical compositions and mercury injection capillary pressure (MICP). Principal Component Analysis (PCA) is used to reduce dimensionality of the dataset and improve efficiency of the clustering algorithms. Unsupervised clustering algorithms like K-Means and Self Organizing Maps (SOM) are used to define rock types. The integrated workflow is applied separately for four shale plays namely Barnett, Eagle Ford, Woodford and Wolfcamp.

A total of 25 wells with core data are considered for rock typing in the four shale plays. The rock types are upscaled to more than 140 wells representing a 20,000-ft. depth interval. A manual approach would have been prohibitively time-consuming.

Rock Type 1 is generally characterized by high porosity, high TOC, and high brittleness. Not surprisingly, Rock Type 1 has the highest positive impact on well productivity. Rock Type 2 has intermediate values of porosity and TOC and thus,

moderate source potential and storage. Rock Type 3 has the highest carbonate content (except Eagle Ford) and poor storage (except Eagle Ford) and source rock potential.

Classification algorithms like Support Vector Machines (SVM) are used to upscale rock types from core data to logs. The training datasets comprise of depths at which both core and log data are available. Different logs like gamma ray, resistivity, neutron porosity and density are used for upscaling. Finally, a rock type ratio (RTR) is defined based on the fraction of Rock Type 1 over gross thickness. RTR is found to strongly correlate with normalized oil equivalent production rate.

The study is unique as it integrates core, log, and production data to identify different rock types. Multiple algorithms are used and the similarity of results between their outputs further bolstered the confidence in the derived rock types. The rock type logs can aid the reservoir or production engineer in optimizing perforation intervals and number of fracture stages. Rock Type 3 is poor reservoir and may not warrant any perforation or fracturing. On the other hand, Rock Type 1 can be selectively perforated and fractured to save cost and maximize production from a well. Other applications of rock typing are 3D reservoir modeling, identifying sweet spots in combination with seismic attributes, new well locations, improved volumetric estimates and uncertainty and risk analysis.

Chapter 1: Introduction

Advancements in reservoir characterization techniques have significantly improved the success of wildcat drilling from 75% in 1974 to 95% in 2010 (Williams 2008). Rock typing is one of those techniques. It is central to meaningful interpretation of the diverse data types acquired over diverse length scales and with varying resolutions for both conventional and unconventional reservoirs.

In conventional reservoirs, initial rock typing methods used core-derived permeability-porosity cross-plots. If core data is not available, well log-derived porosity and permeability values can also be used. Although well logs do not provide direct estimates of permeability, several correlations have been developed for permeability estimation (Timur 1968, Coates and Dumanoir 1974, Thomeer 1983). Permeability can also be derived from NMR logs (Timur-Coates model, SDR model (Kenyon et al. 1988)). Pittman (1992) proposed the use of r35 measurements from mercury injection experiments using a modified Winland approach. The MICP measurements suffer from experimental artifacts like compressibility effect before intrusion (Bailey 2009), entry pressure not enough to see pores smaller than 3 nm, etc. Amaefule et al. (1993) introduced the concept of Rock Quality Index (RQI) by modifying Kozeny-Carman equation. He proposed Rock Quality Index (RQI) or Flow Zone Indicator (FZI) cut-offs to define different rock types. The application of such rock typing techniques is largely restricted to sandstones and carbonates that are characterized by a large dynamic range of porosity and permeability values. Rebelle & Bruno (2014) gave a critical review of different rock typing methods namely FZI, RQI, Lucia classification, J Leverett function, Thomeer function, etc.

Corbett and Potter (2004) used FZI technique to develop a universal rock typing scale to compare different wells, reservoirs, fields and basins. They created 10 global hydraulic units (GHE) with FZI values varying from 0.0938 to 48. They believed that selecting the same reference frame for different reservoirs will make the rock typing exercise more robust and predictive, especially where core data is limited. One of the biggest developments in rock typing was integration across disciplines. Rock typing was more accurate and predictive when carried out across disciplines like geology, petrophysics, engineering and covering multiple length scales from pore scale to log scale. Knackstedt et al. (2010) combined a range of experimental and computational tools to carry out rock typing across disciples covering diverse length scales. Rebelle et al. (2009) also discussed the importance of integrating geologic facies (based on depositional environment and diagenesis), petro facies (based on porosity, permeability, capillary pressure, etc.), electrofacies (based on logs) and dynamic rock types (based on two phase relative permeability curves).

In tight sands, however, majority of the conventional rock-typing methods were found to be inadequate (Rushing et al. 2008) and it was emphasized to include other quantities such as rock texture and composition, core-based descriptions, clay mineralogy for effective rock typing. Rahmanian et al. (2010) discussed the importance of pore and throat structure (distribution, connectivity, geometry, etc.) on storage and flow capacity of tight porous media. The integrated approach was necessary to generate robust rock types. Spain and Liu (2011) used mainly NMR and mercury injection capillary pressure measurements to characterize Cotton Valley tight sandstones in East Texas. They identified three rock types – Rock Type 1 characterized by large pores

connected by large pore throats, Rock Type 2 having average sized pores connected by small pore throats and finally Rock Type 3 having small pores connected by small pore throats.

Merletti et al. (2014) presented another integrated approach using porosity, mineralogy, photomicrographs and core descriptions. Depositional facies and diagenetic controls on pore geometry were evaluated to identify three rock types. Rock Type 1 was rich in fluvial and coastal plain deposits, had high quartz content and a steep porosity-permeability trend. The higher quartz content prevented mechanical compaction and grain leaching, thereby preserving primary porosity and preventing secondary porosity development. Rock Type 2 and 3 had abundant secondary porosity development but had poor flow capacity due to authigenic clay which occludes pore space and clogs pore throats. The authors further used Multi Detector Pulsed Neutron (MDPN) logs to calculate silica content proxy at the log level, which in combination with other logs were used to determine rock types at log level. There have been several other attempts to characterize tight sand reservoirs (Walls 1982, Randolph et al. 1984, Davies et al. 1993, Xu and Verdin 2013).

Rock typing is relatively new in unconventional shale reservoirs. Several operators have already begun incorporating rock typing in their full field modeling and simulation workflows to help identify sweet spots and optimize fracture placement. Conventional techniques like Pittman (1992) and Amaefule et al. (1993) are not adequate because of the limited dynamic range of porosity and permeability in unconventionals. Secondly, accurate permeability measurements on shale samples are difficult to make and time consuming. Additionally, other key variables such as source

potential and brittleness are absent in conventional rock typing methods. Lieber and Dunn (2013) stressed consideration of three parameters for rock typing. They were hydrocarbons in place (porosity, clay volume, fluid saturations), brittleness (sonic data, mineralogy) and potential deliverability.

Kale et al. (2010) carried out rock typing for Barnett and included several petrophysical parameters such as TOC, mineralogy, helium porosity and mercury injection capillary pressure (MICP). Sondhi (2011) employed a similar approach for the Eagle Ford shale while Gupta (2012) performed rock typing for the Woodford formation. Li et al. (2015) used permeability measurements, NMR porosity, and quantitative mineralogy from 2D Scanning Electron Microscope (SEM) images to classify four facies in Bakken formation.

Amin et al. (2016) attempted a log-based rock typing for the Eagle Ford formation using two wells. Triple-combo and Elemental Capture Spectroscopy (ECS) logs were jointly interpreted to get saturation, porosity and mineralogical compositions. They computed a TOC log by correlating core measurements with bulk density log. Additionally, they determined Young's modulus and Poisson's ratio logs through Self Consistent Algorithms (SCA) in absence of acoustic logs. They determined five rock types and explained higher production in one of the wells due to higher fraction of brittle rock type. Aranibar et al. (2013) discussed another log-based rock typing case study from the Haynesville shale. They used bulk density, neutron porosity, Photoelectric Effect (PE), resistivity, sonic, and ECS logs. These logs were interpreted to give TOC, Poisson's ratio, Young's modulus, total porosity and mineralogical compositions, which were used as inputs to the neural network.

This study focusses on Wolfcamp, Barnett, Woodford, and Eagle Ford. The study is unique as it uses two independent techniques like K-Means and Self Organizing Maps (SOM) to predict rock types. The upscaling of core based rock types to log based rock types using a support vector machine algorithm is also unique to this study. Finally, a large database of production wells was created from Drillinginfo, which had the required logs. The correlation between Rock Type Ratio (RTR) and production from these wells differentiates this work from a purely academic exercise to one having strong implications in the field.

1.1 Organization of Chapters

The thesis is organized in eight chapters. Chapter 2 starts with a brief review of the laboratory procedures that were used to make petrophysical measurements used in the study. The chapter is divided into three sections. The first section deals with procedures for petrophysical measurements like total organic carbon (TOC), mineralogy (Fourier Transform Infrared Spectroscopy), porosity (low pressure helium porosity), V_p and V_s (compressional, P-wave and shear, S-wave velocities), Young's modulus (nano-indentation), mercury injection capillary pressure (MICP), etc. The second section gives details about the log analysis techniques used to calculate porosity and TOC logs. The third section of Chapter 2 gives a general overview of data mining and analytic techniques. Specifically, it deals with different clustering algorithms like K-means (Lloyd 1957, Macqueen 1967) and SOM (Kohonen and Honkela 2007) which help to find meaningful relationships in multi-dimensional data and define rock types. The section also describes classification algorithms like SVM (Cortes and Vapnik 1995) that were used to upscale rock types from core to logs.

Chapters 3, 4, 5, and 6 show the complete workflow applied to four shale plays namely Barnett, Eagle Ford, Woodford, and Wolfcamp, respectively. The chapters begin with a brief geological background, which helps to understand the context of rock typing. The chapters also summarize the core, log, and production data available for each shale play. Then, the results of clustering and rock typing analysis are presented. Thereafter, for each play, the rock types are upscaled and upscaled logs are presented as well section windows. Finally, a Rock Type Ratio (RTR) is created based on the fraction of the best rock type over gross thickness. This RTR is shown to have a strong correlation with normalized production for different wells thus validating the robustness of the rock typing workflow.

Chapter 7 uses SEM images to establish micro-structural controls on different petrophysical properties like porosity, TOC, etc. SEM images are also used to validate the rock typing exercise by showing the stark differences in the microstructure between different rock types.

Chapter 8 summarizes the rock typing results from the preceding chapters and gives some useful insights by comparing results from different shale plays. The methodology described in this work can easily be extended to several other applications such as the optimization of well locations (3-D reservoir modeling), well trajectories (with real-time Logging while drilling) and well completions.

Chapter 2: Experimental Procedure

2.1 Laboratory Measurements

Petrophysical measurements were done in Integrated Core Characterization lab (IC^3). Different measurements used in this study were porosity, mineralogy, TOC, V_p, V_s, Young's modulus, source rock analysis data (S1, S2), mercury injection capillary pressure (MICP), etc.

2.1.1 Porosity Measurements

Helium porosity measurements were made using Karastathis' (2007) method. In his method, samples are dried at 100 ˚C for 24 hours. The samples are then cooled to room temperature in a desiccator. Bulk volume is measured using mercury immersion technique. The samples are crushed to fine particle size (392 ±192 μm, Kale 2009). The mass loss during crushing is kept to a minimum (<0.1 wt. %) and calculated porosity is corrected for the weight loss. The crushed samples are kept at 100 ˚C for 24 hours to remove any moisture. Finally, grain volume is measured using a helium porosimeter and porosity is calculated from grain and bulk volumes. Karastathis (2007) showed that porosities measured using this technique are comparable with porosities from commercial labs.

2.1.2 Mineralogy Measurements

The mineralogy of the samples is determined using Fourier Transform Infrared Spectroscopy (FTIR). Different minerals have different signatures on the absorbance spectrum. The technique is used to identify sixteen minerals by inverting the absorbance spectrum. The inversion package developed in IC^3 lab allows quantification (in wt. %) of the following minerals; quartz, calcite, dolomite, aragonite, siderite, oligoclase,

albite, orthoclase, illite, chlorite, kaolinite, smectite, mixed-layer clays, apatite, anhydrite, and pyrite. The accuracy of FTIR is comparable to X-ray diffraction and point counting. In particularly shales, FTIR gives better quantitative clay volume measurement (Sondergeld and Rai 1993; Ballard 2007).

The key precaution to take while preparing the samples is to remove moisture and any organic carbon as they exhibit strong peaks in the mid-infrared region, which masks the absorption peaks of other minerals. To prevent this, the samples are ashed in low temperature plasma asher where organics are oxidized at low temperatures.

2.1.3 TOC measurement

TOC measurements were done using dry pyrolysis technique (Law 1999). The samples were crushed to fine particles (35 Mesh) and carefully acidized to remove any carbonate. This step is critical as carbonates can artificially inflate the TOC. The acidized samples are dried to remove the acid and then burned inside the TOC apparatus. The organic carbon is combusted to generate carbon dioxide, which is measured and converted to TOC by wt. %.

The measurements do not contain free volatile hydrocarbons as these are removed during the drying process. Thus, dry-pyrolysis measurements can be smaller than pyrolysis flame-ionization detection (PFID) TOC if there are considerable free volatile hydrocarbons present in the sample.

Source rock potential is governed by three factors namely source rock richness, source rock quality and source rock maturity. TOC is a measure of source rock richness. A higher TOC is indicative of higher source rock potential provided kerogen quality and maturity are favorable.

2.1.4 Source Rock Analysis (SRA)

In pyrolysis flame-ionization detection (PFID), the sample is kept in an inert atmosphere and progressively heated to 550°C. First, the volatile hydrocarbons are vaporized and are recorded as S1 peak. S1 peak mostly corresponds to mobile hydrocarbons and is important from rock typing point of view. S1 together with TOC is indicative of source rock potential. As the temperature rises, kerogen in the sample cracks to generate hydrocarbons, hydrocarbon-like compounds, (recorded as S2 peak), CO_2 (recorded as S3 peak), and water. The residual carbon is recorded as S4. All peaks namely S1, S2, S3 and S4 are reported in mg/gm of rock. Welte (1984) and Law (1999) are some excellent references on source rock analysis (SRA).

2.1.5 Young's Modulus (E)

A nanoindenter apparatus can be used for Young's modulus measurement on core samples. The equipment used in this study was Agilent G200 nanoindenter. The Young's modulus is calculated from continuous measurement of load and displacement. A magnet and coil assembly moves the indenter. A capacitance displacement gauge is used for measuring displacement in the vertical direction. An optical microscope is used to select locations for indentation. Figure 1a shows the schematic of nanoindenter. The instrument can apply forces as low as 1nN and measure displacements as small as 0.1 nm.

A single nanoindentation experiment consists of gradually loading the sample at 33 mN/sec for 15 seconds. The peak load at the end of 15 seconds is 50 gf. The peak load is held for 10 seconds before unloading the sample. Figure 1b shows a typical loading-unloading curve during a nanoindentation experiment. Young's modulus

calculation is done at the peak load (P). Stiffness of an elastic body is a measure of resistance to deformation. It is given by the expression

$$\frac{dP}{dh} = 2E^* \sqrt{\frac{A}{P}}$$

a) b)

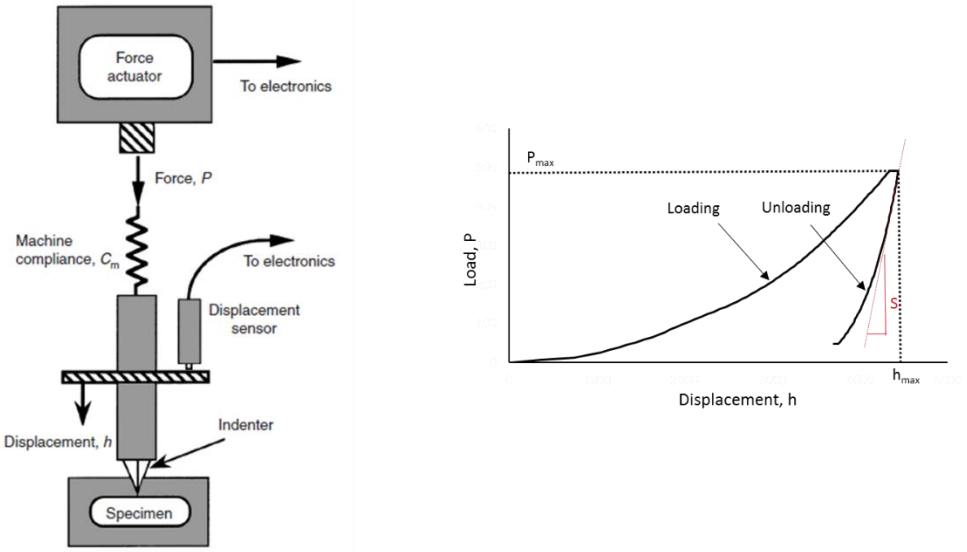

Figure 1 a) Schematic of nanoindenter showing the magnet and coil force actuator assembly and the capacitive displacement measurement assembly b) Typical shape of loading-unloading curve during a nanoindentation experiment (Hay and Pharr 2000).

Where h is the displacement, A is the indentation area and E* is the reduced Young's modulus. In the above equation, dP/dh is calculated from the unloading curve at the peak load. Indentation area is calculated through an area function dependent on the contact height. The above equation is used to calculate the reduced Young's modulus. It is called reduced Young's modulus because displacements occur in both the sample and the indenter. The sample Young's modulus is calculated using the expression

$$\frac{1}{E^*} = \frac{1 - v_i^2}{E_i} + \frac{1 - v'^2}{E'}$$

Where v_i, E_i are the Poisson's ratio and Young's modulus of the sample respectively. v', E' are the corresponding values for the indenter. A diamond Berkovich tip indenter is used for which Poisson's ratio and Young's modulus are known. The Poisson's ratio for the sample is assumed to be 0.25. Hay and Pharr (2000) noted that a ±0.1 uncertainty in Poisson's ratio results in only about 5% uncertainty in Young's modulus.

A key requirement for nano-indentation is the smooth sample preparation. The IC^3 lab procedure involves mechanical polishing using silicon carbide papers from 180 to 1200 grit size. At the end of mechanical polishing, top and bottom surfaces should be parallel and maximum thickness difference should not exceed 0.01 mm. It is followed by broad beam argon ion milling for 3 hours. A total of 100 measurements (four 5*5 arrays) are made and averaged to yield the Young's modulus. The instrument is calibrated using fused silica before making measurements on the shale sample.

The static Young's modulus measurements from nanoindenter compares well with dynamic measurements. Shukla et al. (2013) showed the comparison for several formations namely Wolfcamp, Woodford, Haynesville and Kimmeridge. Figure 2 shows the comparison.

2.1.6 Mercury Injection Capillary Pressure

Mercury injection capillary pressure (MICP) is used to measure pore throat sizes and connected pore space as a function of pressure. The pressure steps are varied from 5 to 60,000 psia. The mercury intruded into the sample is recorded at each pressure step and the collected data is used to generate a capillary pressure curve for the sample. Once pressure reaches 60,000 psia, it is gradually reduced and extrusion volume is measured

as a function of pressure. The intrusion and extrusion curves are used to determine hysteresis which can be useful to determine if actual intrusion of mercury into the sample has taken place.

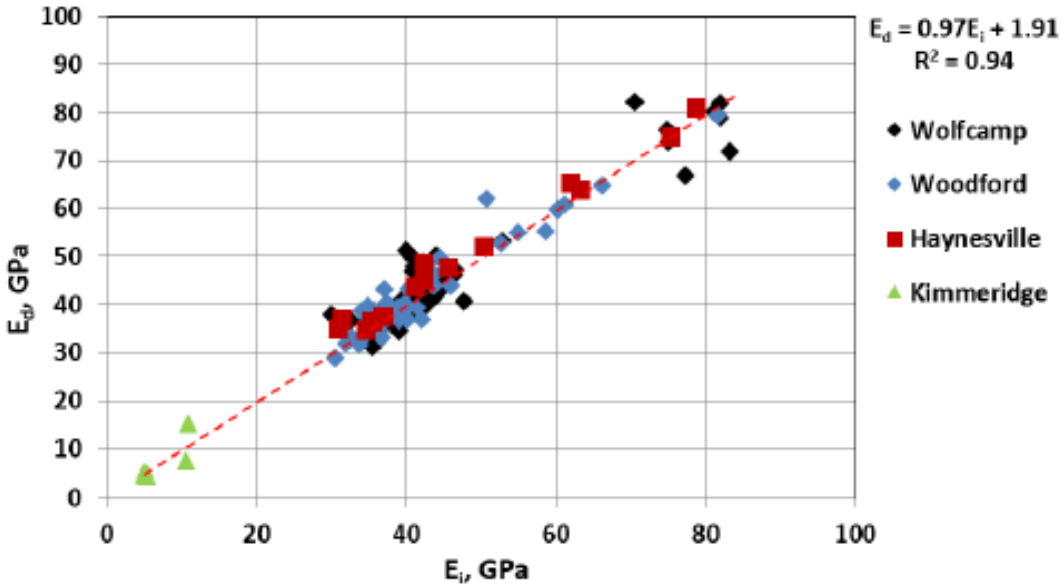

Figure 2: Comparison of dynamic and indentation Young's modulus. There is a very strong correlation given by R^2 of 0.94 (Shukla et al. 2013).

The sample is dried, placed in a special assembly called penetrometer and sealed. The assembly with sample is entered into the low-pressure section of AutoPore IV machine. Pressure is reduced to 200 mm of mercury and maintained at that level for one hour to remove trace moisture and air from the sample and apparatus. Thereafter, mercury is introduced at 5 psia to fill the void volume in the penetrometer and surround the sample. The pressure is increased to 20 psia and time is given to attain pressure equilibrium.

The penetrometer assembly is than taken out of the low-pressure section and transferred to the high-pressure section. The pressure is increased based on pre-identified steps up to 60,000 psia. At each pressure step, pressure is stabilized for over

60 seconds before increasing the pressure to the next pressure step. External pressure is applied using nitrogen in the low-pressure section and with mineral oil in the high-pressure section. As mercury enters the pore space, the mercury filled length of the penetrometer stem decreases. The stem of penetrometer is made of glass and coated with metal film from outside and thus acts as a capacitor. The capacitance of the penetrometer stem changes with decreasing mercury level during the intrusion cycle. This change in capacitance can be converted to intruded mercury volume at each pressure step.

However, if the sample is very tight and mercury intrusion does not happen until higher pressures, the sample compresses which leads to a decrease in the mercury volume in the penetrometer stem. This may be interpreted as intrusion. This false intrusion can be detected by plotting the incremental intrusion as a function of pressure. Bailey (2009) discusses the details about the corrections to the capillary pressure data.

2.1.7 Ultrasonic Measurements

The ultrasonic measurements were made on horizontal plugs one inch in diameter; core lengths varied from one to two inches. The top and bottom faces of the plugs are polished to be parallel to each other and perpendicular to the plug axis.

Pulse transmission technique (Junck and Benson, 1973) is used for ultrasonic velocity measurements. A sample is placed inside an impermeable neoprene jacket. The jacket is larger than the sample to accommodate endcaps at both ends. Each end cap has three piezoelectric transducers (P, S1 and S2). The end caps are fastened to the jacket using hose clamps and the entire assembly is pressure sealed from external fluid.

The three piezoelectric crystals at each endcap generate compressional (P) and two orthogonally polarized shear waves (S1 and S2). The waves travel through the sample and are recorded at the other end. The length of the plug and travel times are used to determine velocities. Measurements are done at several confining pressure steps namely 500, 750, 1000, 1500, 2000, 2500, 3000, 4000, 5000 and 6000 psi.

2.1.8 SEM Images

SEM images were analyzed using FEI Helios Nanolab 600 Dual-Beam Focus Ion Beam (FIB) and Scanning Electron Microscope (SEM). The detailed procedure is explained in Curtis et al. (2011) and Curtis et al. (2012).

2.2 Log Analysis

2.2.1 Porosity Calculation

There are mainly three different types of porosity logs namely density, neutron and sonic; none measures porosity directly. They are indirect nuclear and acoustic measurements from which porosity can be derived. The interpretation of these logs are effected by many variables downhole, thus, a combination of these logs is required for accurate porosity determination.

In density logs, the radioactive sources namely Ce and Co are employed to emit gamma rays. These interact with electrons of the formation and get absorbed. The electrons emit gamma rays which are recorded as a count rate proportional to formation density. Advanced schematic like dual detector scheme helps to compensate for mudcake and minor hole irregularities. This arrangement helps to calculate $\Delta\rho$. i.e. correction for mudcake and borehole effects which can be added to long spacing detector response to calculate formation density (Bassiouni 1994).

In neutron logs, neutrons are emitted into the formation. They are slowed down by elastic and inelastic scattering. When sufficiently slowed, some of them are absorbed and thus, capturing nuclei emit gamma rays. Some of the unabsorbed neutrons are also deflected back towards the detectors. Thus, based on the tool configuration, detectors can either detect gamma rays or neutrons. The elements that mainly slow down the neutrons are the hydrogen nuclei as they are roughly equal in mass compared to a neutron. With one collision with hydrogen nuclei, it loses 50% of its energy. Therefore, the neutron log mainly responds to hydrogen concentrated in pore fluids and thus responds to porosity (Bassiouni 1994).

The interpretation of both density and neutron logs are effected by uncertainties in lithology, fluid type, and saturation. In unconventional reservoirs, grain densities also need to be corrected for TOC. To reduce the uncertainty and get a better estimate of porosity, different logs like gamma ray, resistivity, neutron, and density are combined and variables like Vclay, fluid saturations and porosity are solved simultaneously. The log porosity in this study was calculated using the standard integrated workflow in a commercial software.

2.2.2 TOC Calculation

Total organic carbon (TOC) as measured in the laboratory is widely used to evaluate unconventional reservoirs. A wide array of log based methods are available to calculate TOC. Passey et al. (1990) is one of the most commonly used methods. It is also known as "Δlog R" method. In the original paper, the method was applied using sonic and resistivity logs. But, density and neutron data can also be used. Different equations used to calculate TOC using different log sets are given below:

$$\Delta\text{LogR} = \log\left(\frac{\text{RESD}}{\text{RESDbase}}\right) + 0.02 * (\text{DTC} - \text{DTCbase})$$

$$\text{TOCs} = \text{SF1s} * (\Delta\text{logR} * 10\text{^}(0.297 - 0.1688 * \text{LOM})) + \text{SO1s}$$

Where RESD is the deep resistivity in any zone (ohm-m), RESDbase is the deep resistivity baseline in non-source rock (ohm-m), DTC is the compressional sonic log reading (usec/ft.), DTCbase is the sonic baseline in the non-source rock (usec/ft.), LOM is the level of organic maturity (unitless), SF1s and SO1s are scale factor and scale offset to calibrate to the lab values of TOC. Similar equations for density and neutron logs are given below.

$$\Delta\text{LogR} = \log\left(\frac{\text{RESD}}{\text{RESDbase}}\right) - 2.5 * (\text{DENS} - \text{DENSbase})$$

$$\text{TOCd} = \text{SF1d} * (\Delta\text{logR} * 10\text{^}(0.297 - 0.1688 * \text{LOM})) + \text{SO1d}$$

$$\Delta\text{LogR} = \log\left(\frac{\text{RESD}}{\text{RESDbase}}\right) + 4.0 * (\text{PHIN} - \text{PHINbase})$$

$$\text{TOCn} = \text{SF1n} * (\Delta\text{logR} * 10\text{^}(0.297 - 0.1688 * \text{LOM})) + \text{SO1n}$$

Where RESD is the deep resistivity in any zone (ohm-m), RESDbase is the deep resistivity baseline in non-source rock (ohm-m), DENS is the density log reading against the source rock, DENSbase is the baseline density log reading against non-source rock, PHIN is the neutron log reading against source rock, PHINbase is the baseline neutron log reading against non-source rock, LOM is the level of organic maturity (unitless), SF1d, SO1d, SF1n and SO1n are scale factors and scale offsets to calibrate to lab values of TOC.

LOM typically ranges from 6 to 14. Default LOM for a gas shale is 8.5 and for an oil shale is 10.5. Elzarka and Younes (1987) show how LOM values can be derived based on vitrinite reflectance values. In the current study, resistivity, neutron, and

density logs were available and thus the above four equations were used for TOC calculation. Laboratory measured TOC values were also available to calibrate the modelled TOC logs.

2.3 Data Mining and Analytics

2.3.1 Overview

Commercial and scientific data collection and storage has increased tremendously in the last decade. For instance, Yahoo has petabytes of web data, Facebook has more than one billion users, and Amazon records several million items every day. The storage devices like disk drives, server systems, etc. have become ultra-cheap leading to a spike in the data collection. The ideology is to collect whatever data you can, whenever you can and the expectation is that the gathered data may be of immediate use or in future for a purpose not envisioned currently.

Thus, a new field has emerged called Data Mining and Analytics that consists of people that mine databases of exhaustive data and discover patterns and models that are valid, useful, unexpected, and understandable. In other words, data mining is non-trivial extraction of implicit, previously unknown, and potentially useful information from the data. A typical workflow for data mining process is shown in Figure 3.

Many times, gathered data has noise due to many factors which are beyond control. For instance, when taking measurements in the lab, humidity, temperature, human and machine errors can lead to different values of a property on the same sample. Thus, first step in data mining, is data preprocessing, where data needs to be checked for outliers, quality, redundant, un-useful and missing values.

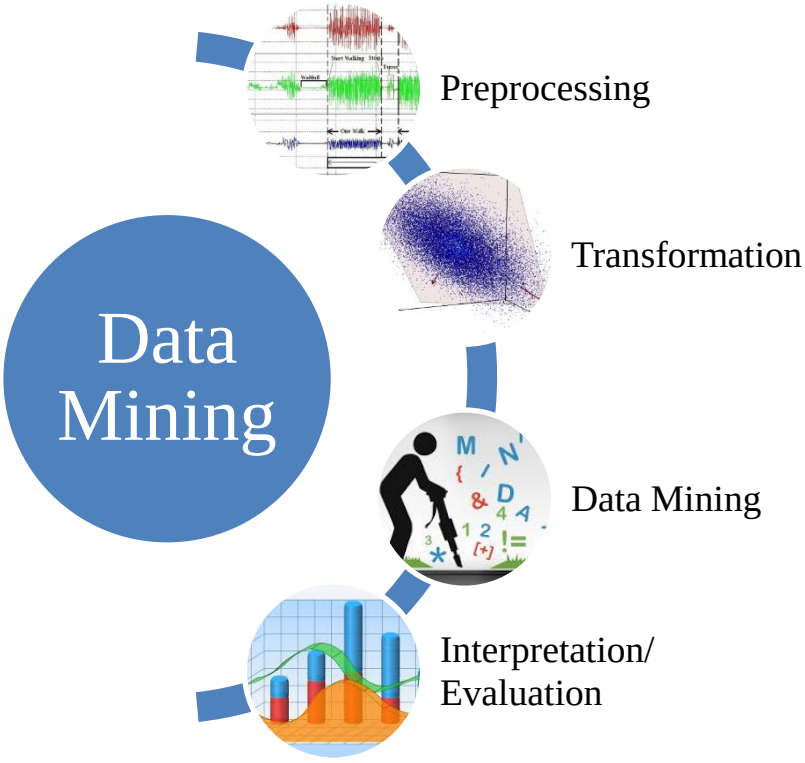

Figure 3: Data Mining Workflow

The next step is transformation which basically involves removing bias from the samples. It also includes reducing dimensionality of the data so that it becomes easier to process. To remove the bias, all attributes are scaled and the data is normalized so that any one parameter does not dominate the results. In this study, we used petrophysical measurements like porosity, TOC, clay, carbonate, and quartz content to define different rock types. Porosity and TOC generally vary between 2-15 % whereas mineralogical compositions vary between 0-100%. Thus, to prevent mineralogical compositions from dominating the results, all attributes are normalized between their respective minima and maxima.

Principal Component Analysis (PCA) is used to reduce the dimensionality of the data. The idea behind PCA is to identify directions in multidimensional space that

contain most of the variations observed in the data. Principal components are linear combination of different input parameters (TOC, porosity, mineralogy in this case). In general, the first few principal components explain most of the variance in the data. Thus, instead of using 5 variables (such as TOC, porosity, quartz, clays, and carbonates) for clustering, it is sufficient if we use first three to four principal components.

The third step in data mining workflow is to discover information using various data mining and analytic techniques. The data mining tasks generally consists of following: Classification, Clustering, Association, Regression, and Anomaly detection (Tan et al. 2006). In Classification, existing records or attributes are grouped into several classes and new data is assigned to any one of the classes depending on a measure of proximity. For instance, psychological evaluations of people can be used to assign them to different groups with increasing tendencies of criminal intent. In Clustering, based on a measure of similarity, data points are divided into many clusters. The points in the same cluster are more similar to each other than to the data points in different clusters. For instance, fracture dimensions, reservoir properties, etc. can be used to cluster wells into two categories namely good producers and poor producers. In Association, the relationships between different attributes are studied and occurrence of one is predicted based on the occurrence of other. For example, data from a supermarket can be analyzed to identify if someone buys milk, how likely he/she is to buy eggs as well. In Regression, a value of a given continuous variable is predicted based on the values of other variables, assuming a linear or nonlinear model of dependency. For instance, prediction of stock prices based on historical data. Finally, in Anomaly

detection, data is analyzed to determine significant deviations from normal behavior; for example, using credit card transactions to analyze fraud detection.

The fourth step is to analyze the results using various visual mechanisms along with prior knowledge to make meaningful conclusions. There are several visual techniques available like cross-plots, box plots, rose or pie diagrams, etc.

Not all algorithms are applicable to all situations. Selection of data mining algorithm should be carefully evaluated based on objective, domain expertise and data availability (Tan et al. 2006). In this study, Principal Component Analysis (PCA) was used to reduce the dimensionality of the data. Clustering algorithms namely K-means and Self Organizing maps (SOM) were used to define different rock types, and classification algorithm like Support Vector Machines (SVM) was used to upscale rock types from cores to logs. These techniques are discussed in detail in the following sections.

2.3.2 Principal Component Analysis (PCA)

PCA is used to reduce dimensionality of a dataset with a large number of correlated attributes (Pearson 1901, Hotelling 1933). Graphically, PCA rotates the original axis of the data to the direction having maximum variance (Figure 4). New attributes are created as a result which are linear combination of existing variables. These new attributes are orthogonal and unrelated to each other. Thus, only a few of them can explain the maximum variability in the data. Therefore, instead of dealing with large number of correlated attributes, a few principal components can be used which significantly decreases the processing time and increases accuracy.

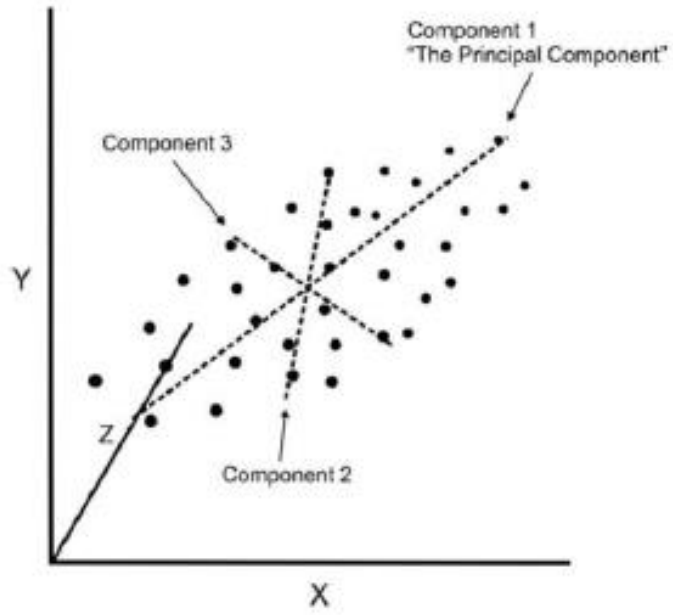

Figure 4: Graphical representation of the axis rotation during PCA (Srivastava 2016)

Mathematically, the principal components are the eigenvector of the covariance matrix of the original attributes. The covariance matrix of $X_{a \text{ by } b}$ is given by

$$C_X = \frac{1}{b} X X^T$$

The principal component (P) can be given by,

$$P = E^T X$$

Where E is the eigenvector for the covariance matrix. Each principal component is a linear combination of original attributes with different weights. The higher the weight, implies higher the importance of that component. In practice, it is more practical to use correlation matrix instead of covariance matrix. This removes the units of measure dependency by scaling the variables to same range of values. The main

assumption in PCA is that different attributes are linearly correlated. Thus, it cannot account for non-linear relationships.

2.3.3 K-means Clustering

It is one of the most popular clustering algorithms (Lloyd 1957, Macqueen 1967). It requires a predefinition of the number of clusters required which is sometimes seen as a disadvantage. However, data variability can be exploited to overcome this drawback. The optimum number of clusters can be chosen based on inter-cluster variance and intra-cluster variance plot shown in Figure 5. Intra-cluster variance refers to the variance between data points in the same cluster. It is also known as sum-of-squares within (SSW) all clusters. It is given by,

$$SSW = \sum_{i=1}^{g} \sum_{j=1}^{ni} (x_{ij} - \overline{x_i})'(x_{ij} - \overline{x_i})$$

Here, x_{ij} refers to a data point within a cluster and $\overline{x}$ is the mean of the cluster. Inter-cluster variance refers to the variance between data points of different clusters. It is also known as sum-of-squares between clusters. It is given by,

$$SSB = \sum_{i=1}^{g} n_i(\overline{x_i} - \bar{x})'(\overline{x_i} - \bar{x})$$

Here, $\overline{x_i}$ is the mean of any one cluster and $\bar{x}$ is the mean of all the clusters. The point at which SSW and SSB clusters start flattening out defines the optimum number of clusters as after that point, increasing the number of clusters does not significantly improve the rock typing definition.

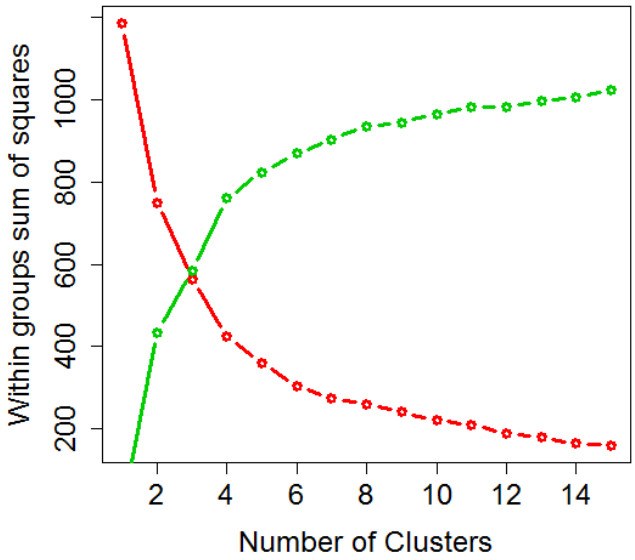

Figure 5: K-Means can create multiple scenarios with different number of clusters. In each case, it identifies the intra-cluster variance (red curve) and inter-cluster variance (green curve). The point at which the curves start flattening out defines the optimum number of clusters.

K-means clustering typically consists of four steps. The first step is to choose the number of clusters. One way to do it is through the SSW-SSB method as explained above. After choosing the number of clusters, cluster centroids are randomly assigned in the data. In the second step, the points closest to each centroid are assigned to that group. In other words, SSW (sum-of-squares within a cluster) is minimized. In the third step, cluster means are reassigned. For each cluster, centroid is assigned as the mean of the observations belonging to that group. In Step 4, the steps 2 and 3 are repeated until convergence is achieved, i.e. centroids do not change with successive iterations. Figure 6 (Guido 2016) shows the schematic of K-means clustering in which three clusters were identified.

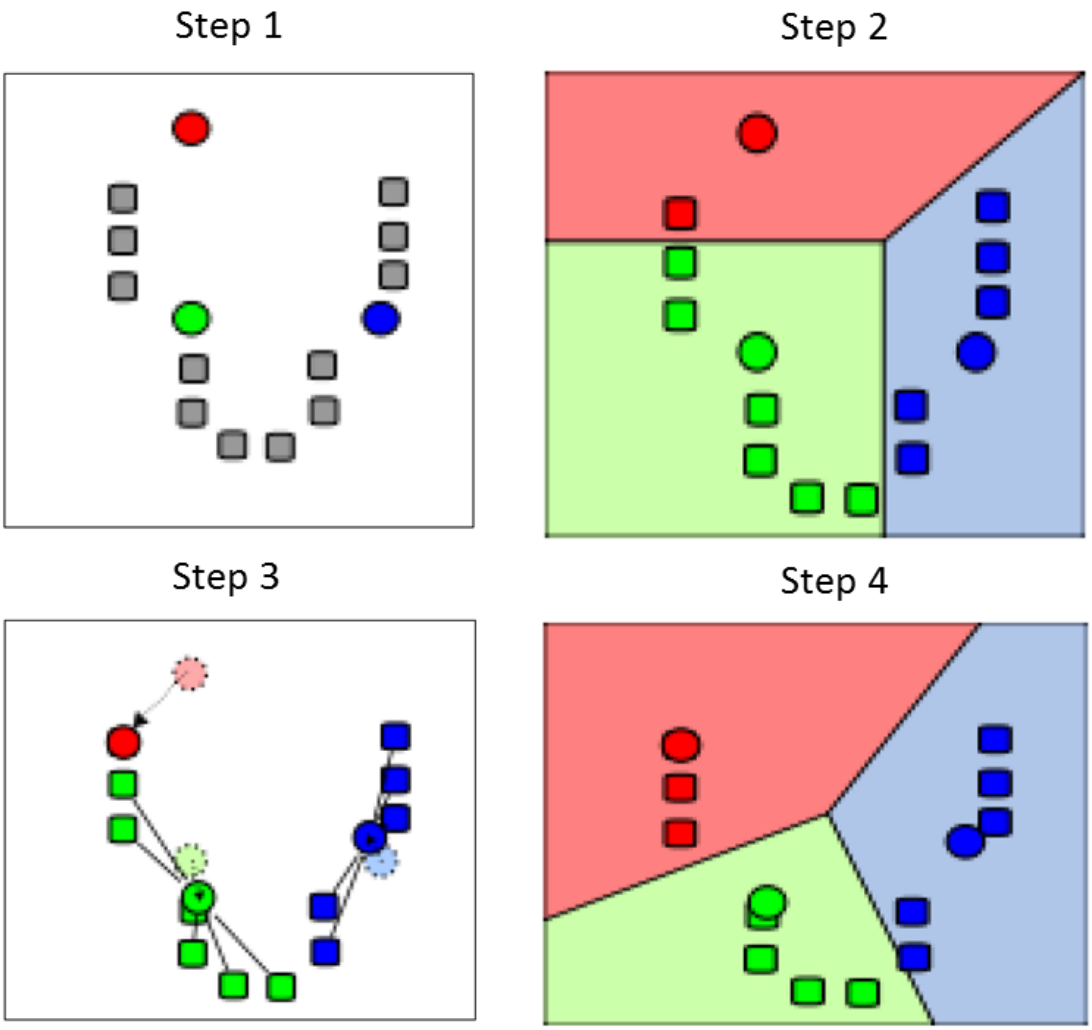

Figure 6: Schematic of K-means clustering (Guido 2014)

2.3.4 Self-Organizing Maps (SOM)

SOM (Kohonen and Honkela 2007, Chon and Park, 2008) is an unsupervised classification algorithm which is a simpler form of neural nets. A self-organizing map is a lower (usually 2D) dimensional representation of a multi-dimensional dataset. It can be very useful for finding patterns in the data like common features in well logs or cores.

The SOM network is created from a 2D lattice of nodes. Each node has specific topological position (x, y location in the lattice) and contains a vector of weights of the same dimension as the input vectors. Figure 7 shows a schematic of a 2D lattice of nodes. Each node has three vector weights basically percentages of blue, green, and red. This is a training grid which is used for generating SOM (Pang 2003).

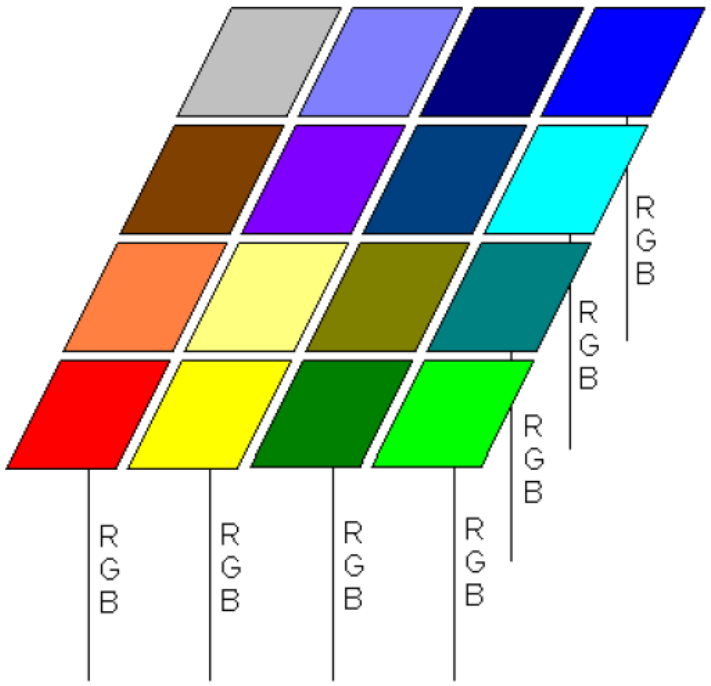

Figure 7: A 4X4 Training SOM Grid. Each node has three vectors basically percentages of blue, green, and red (Pang 2003).

The data is generally randomly distributed as shown in Figure 8 (Pang 2003). This is also called the latent space. The algorithm randomly selects a node from data grid (latent space) and tries to find the closest match from the training grid. The closest match for any data point is termed Best Matching Unit (BMU). The BMU is identified by minimizing the Euclidean distance as shown below,

$$Dist = \sqrt{(R_{data} - R_{training})^2 + (G_{data} - G_{training})^2 + (B_{data} - B_{training})^2}$$

Where R, G and B represent percentages of red, green, and blue.

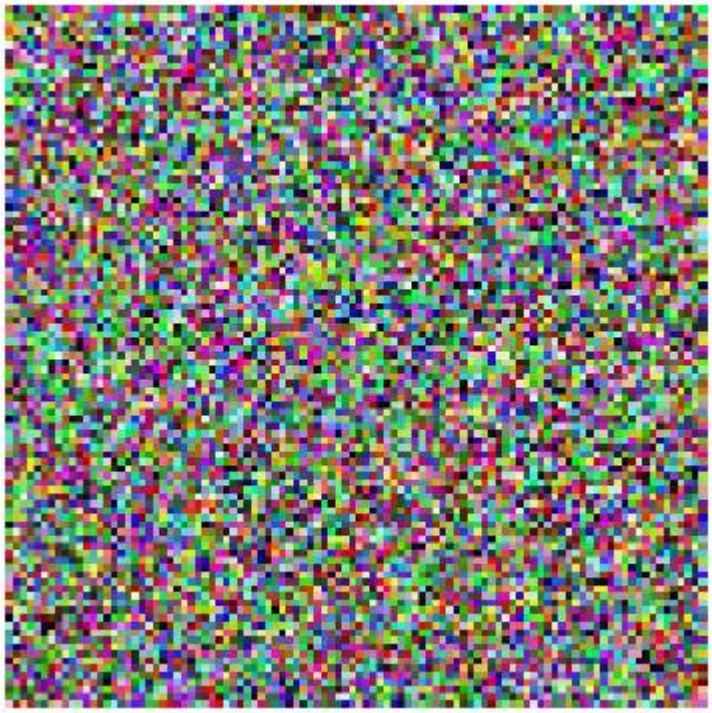

Figure 8: Raw data to be clustered using SOM (Pang 2003)

Once the best matching unit is identified, the region around the node in the data grid is selectively optimized to resemble more closely the BMU. The nodes in the neighborhood are modified within a neighborhood radius which can be adjusted based on user's need (Figure 9). The modification of the weights of the neighboring nodes is done using an equation,

$$\begin{bmatrix} R \\ G \\ B \end{bmatrix}_{New} = \begin{bmatrix} R \\ G \\ B \end{bmatrix}_{old} + \alpha \left[\begin{bmatrix} R \\ G \\ B \end{bmatrix}_{BMU} - \begin{bmatrix} R \\ G \\ B \end{bmatrix}_{Old} \right]$$

Where α is the neighborhood weight and it usually decreases as you go farther from the central node (Figure 9).

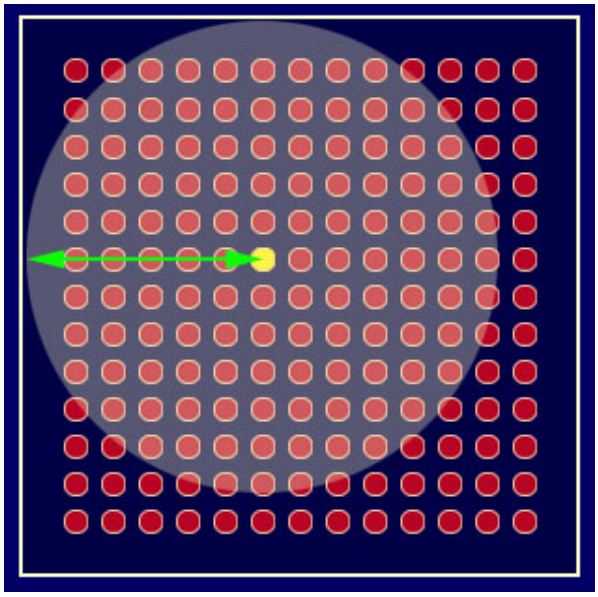

Figure 9: Schematic of neighborhood radius. The neighborhood weighing factor, α, decreases as you go farther from the central node (Pang 2003).

This process is repeated for all the nodes of the data grid and after multiple iterations the data grid starts unveiling clusters. The process is stopped when convergence is reached that is iterations does not change the latent space as shown in Figure 10 (Pang 2003).

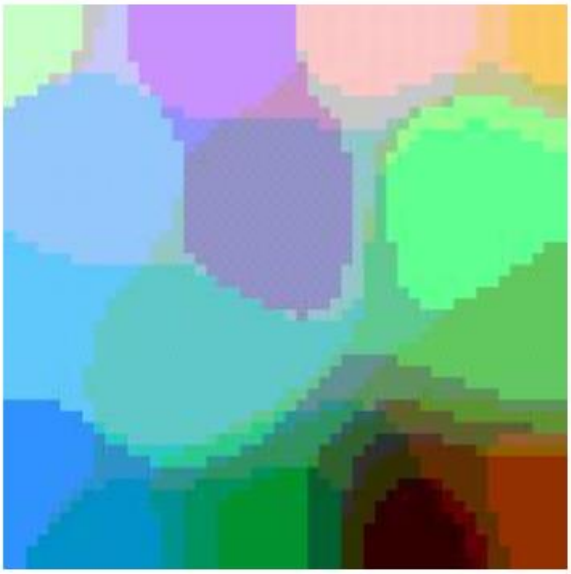

Figure 10: Post convergence latent space or data grid (Pang 2003)

2.3.5 Support Vector Machines (SVM)

SVM (Cortes and Vapnik 1995) is a classification algorithm mainly suited for binary classification or 2-class problems but it can be used for multi-class problems as well. The mathematical details are described in Steinwart and Christmann (2008). A training dataset consists of data points with different attributes where the class for each data point is already known. For instance, in case of rock typing, different data points can represent different core depths. The attributes can be TOC, porosity, mineralogical fractions, etc. The corresponding classes can be Rock Type 1, Rock Type 2, etc.

SVM algorithm plots the data in multiple dimensions and tries to identify boundaries called hyperplanes between different classes. Examples of hyper-planes are shown in Figure 11 (Thornton 2017) for both linear and non-linear classifications between the blue- and the red-colored points.

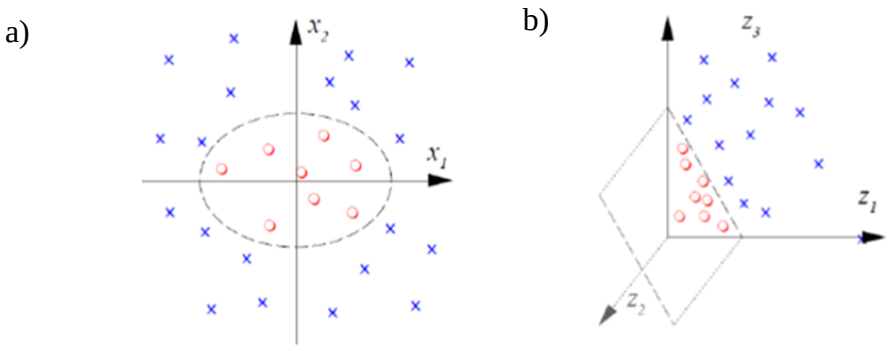

Figure 11: Examples of hyperplane in SVM. The separation between different clusters is termed a hyperplane and its geometry can be linear, polynomial, or radial. a) shows an example of radial hyper plane. b) shows an example of linear hyperplane (Thornton 2017)

A hyperplane can be chosen in many ways as shown in Figure 12 (Opencv 2017). Selection of an optimal hyperplane becomes critical. It should be farthest from the training observations.

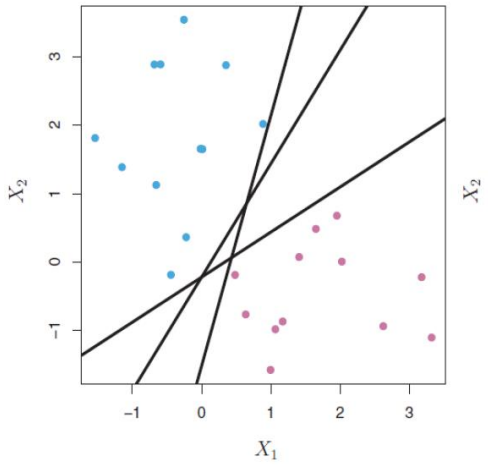

Figure 12: Different hyperplanes possible between two classes (Opencv 2017)

The training observations closest to the hyperplane are called support vectors. Optimal hyperplane is selected based on "Maximal margin classifier" principle i.e. hyperplane should be farthest away as possible from support vectors (Figure 13).

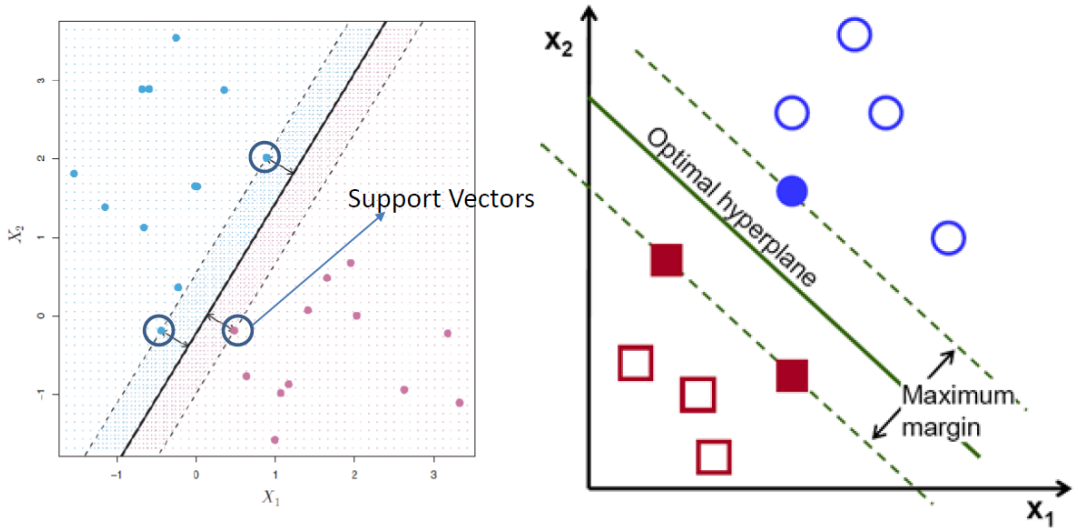

Figure 13: Optimal hyperplane selection (Opencv 2017)

Once optimal hyperplane is selected, algorithm calculates the distance of each data point in the test dataset and assigns it to one of the classes. This algorithm was used to upscale data from core to logs.

2.4 Rock Typing Workflow

Figure 14 shows the rock typing workflow. The first step in the workflow is to prepare a comprehensive database of laboratory data like TOC, porosity, mineralogy, etc. These data were selected as these represent the most commonly done measurements in the lab. These measurements have high accuracy and lower associated errors. Finally, they explain the maximum variance in the data and are sufficient to distinguish different rock types.

In the next step, key parameters are determined for rock typing and clustering algorithms like K-means and Self Organizing maps are used to define rock types. In the third step, clustering results are analyzed to ensure petrophysical relevance. In fourth step, once rock types are defined at the core level, a classification technique called SVM or Support Vector Machines, is used to upscale the rock types at the log level. Finally, in fifth step, rock types are populated in many wells and correlated with production data.

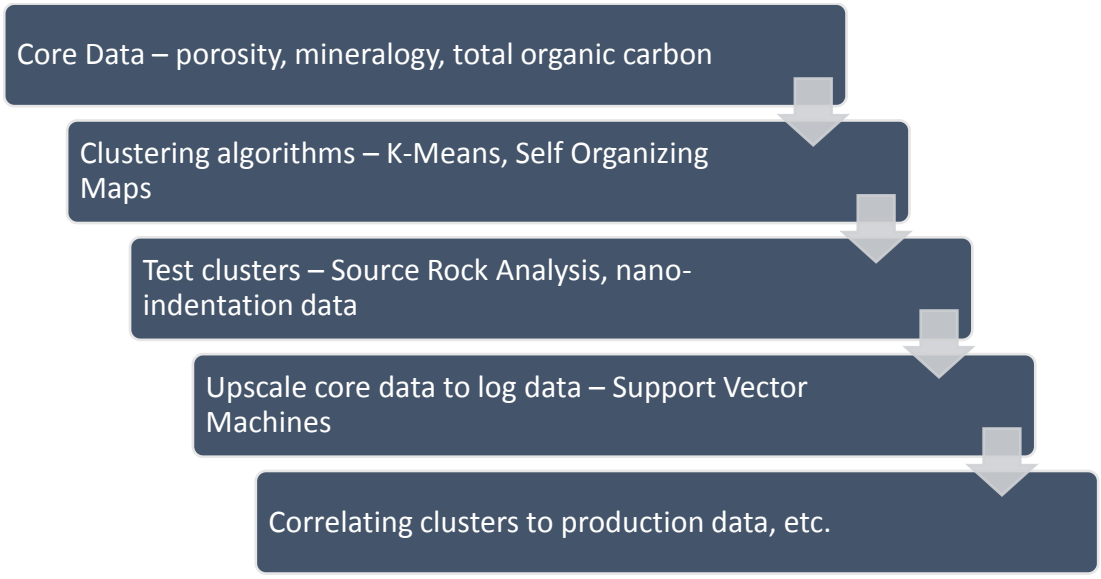

Figure 14: Rock Typing Workflow

This workflow is unique and extensive. First, two independent techniques like K-Means and SOM are used to predict rock types. Second, the upscaling of core based rock types to log based rock types using SVM is new and very effective. Finally, a strong correlation is seen between rock types and production data which makes the workflow practically useful.

Chapter 3: Barnett Formation

3.1 Study Area Description

Barnett is one of the prominent shale gas plays in US. Figure 15 shows the Barnett shale play (Pollastro et al. 2007). It is a Mississippian shale located in the Delaware and Fort Worth basins in North Texas. It has produced more than 69 MMbbl oil, and 19.2 Tcf gas so far (based on drilling info, checked Dec 16, 2016). It varies in thickness between 100 to 700 ft. (Kinley 2008). The depths of Barnett formation vary between 7,000-18,000 ft. (Kinley 2008). Barnett is slightly over-pressured with average pressure gradient of 0.52 psi/ft. (Slatt et al. 2008).

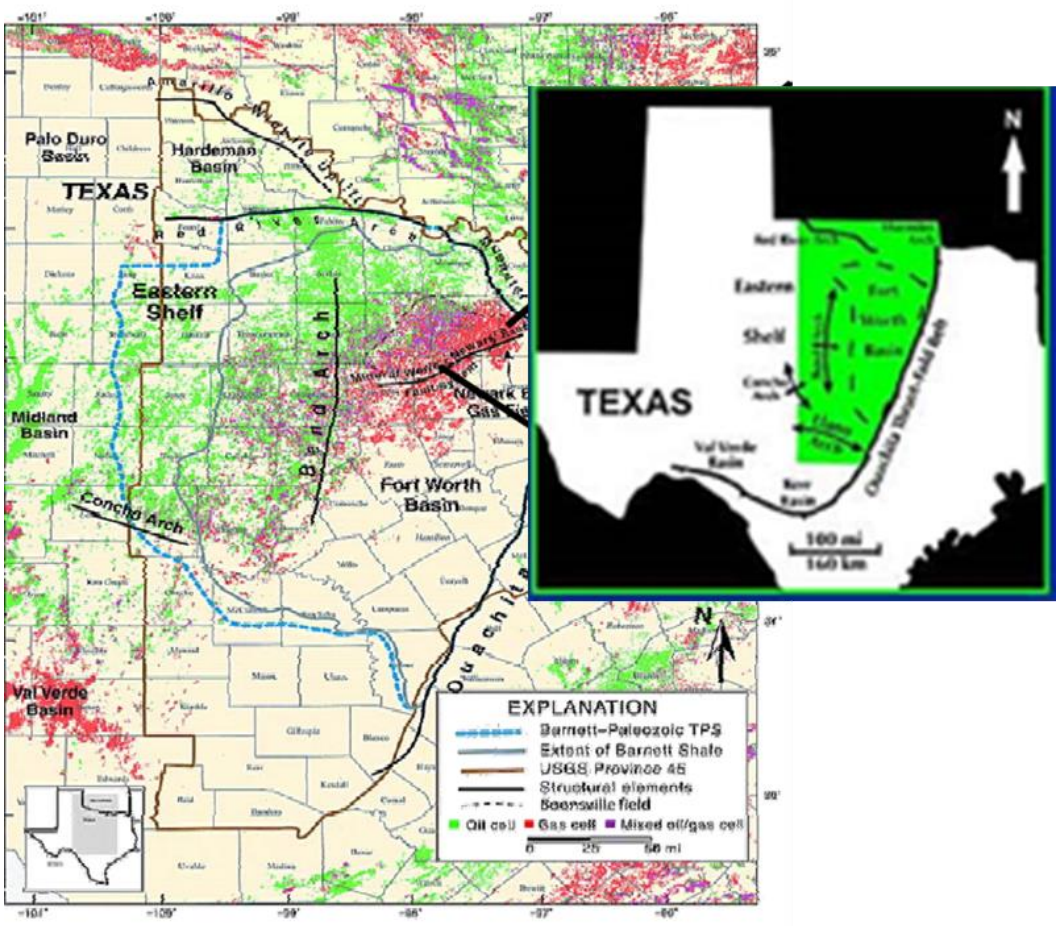

Figure 15: Barnett shale play extent (Pollastro et al. 2007)

Figure 16 shows the north-south and west-east cross-sections through the Fort Worth basin (Bruner and Smosna 2011). Barnett was deposited during Paleozoic in a back-arc setting. Barnett play consists of upper Barnett, lower Barnett and Forestburg limestone. Lower Barnett lies directly over regional angular unconformity. The Forestburg limestone separates the upper and lower Barnett shale members. It is quite thick in the north (~200 ft.) and thins towards south (few feet).

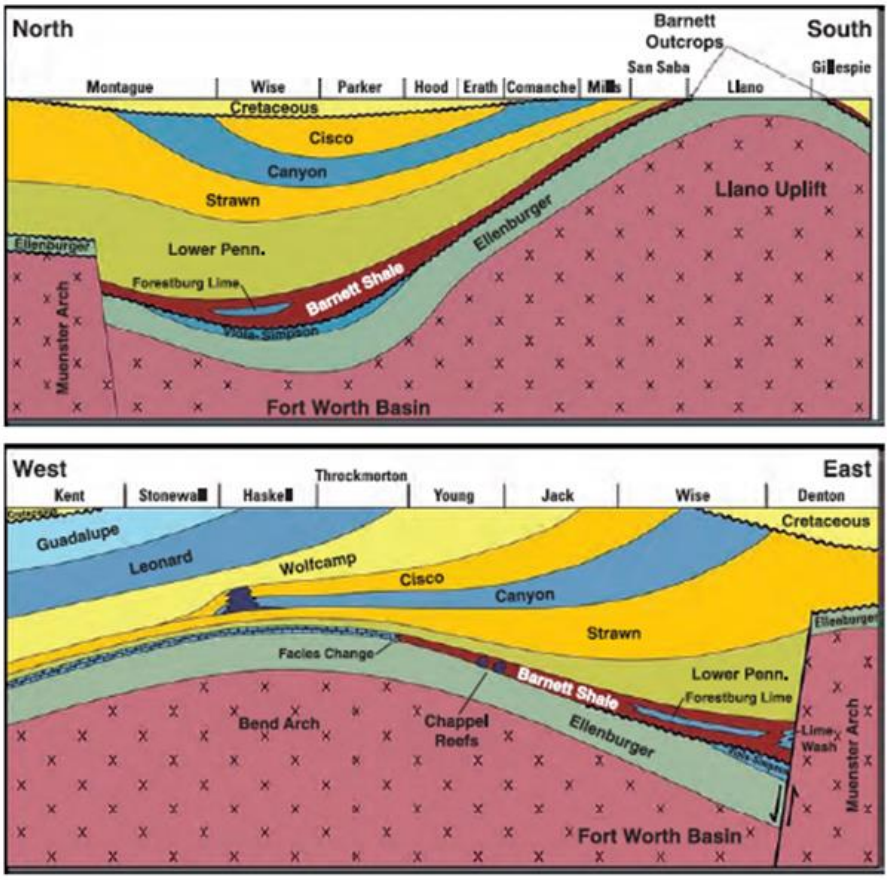

Figure 16: North-south and west-east cross-sections through Fort Worth Basin, illustrating the structural position of Barnett formation between Muenster arch, Bend arch and Llano uplift (Bruner and Smosna 2011)

Singh (2008) identified 10 different lithofacies in Barnett. They were namely siliceous non-calcareous mudstone, siliceous calcareous mudstone low calcite, siliceous

calcareous mudstone high calcite, silty-shale, phosphatic deposits, limy mudstone, dolomitic mudstone, calcareous laminae, concretions, and fossiliferous deposits. Out of these, lithofacies 1, 2, 3 and 6 are dominant and are responsible for majority of the petrophysical variation. Majority of the cored interval also consists of these four lithofacies. Lithofacies 1 and 2 are associated with high TOC and high porosity. On the other extreme, Lithofacies 6 is very tight with little porosity and very low TOC.

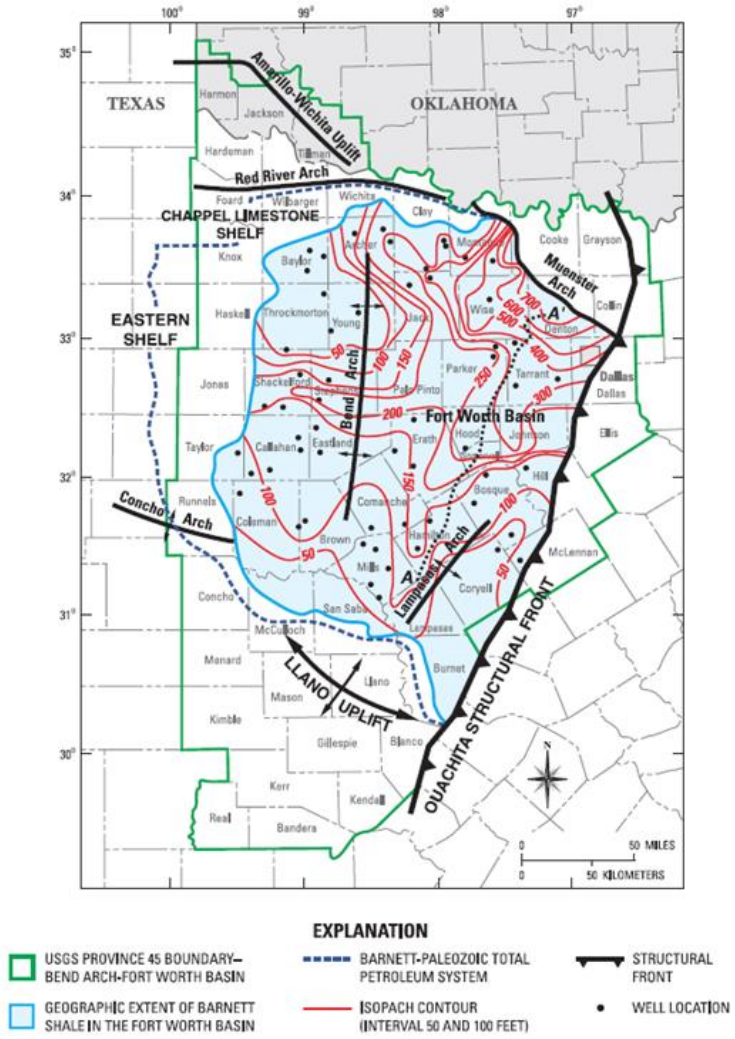

Figure 17: Isopach map for Barnett. Contour interval equals 50. (Bruner and Smosna 2011). The north-eastern and eastern portions of the play have the greatest thickness.

Figure 17 shows the isopach map for Barnett (Bruner and Smosna 2011). The north-eastern and eastern portions of the basin have the highest thickness. Figure 18a shows the TOC map for Barnett (Sarmiento et al. 2013). The TOC map shows that majority of the play (including the thick eastern and north-eastern parts) are very low in TOC. Southern part of the basin has the highest TOC. Figure 18b shows the vitrinite reflectance map and thus shows the maturity of the Barnett play (Sarmiento et al. 2013). Majority of the high TOC region lies in immature window. The thick eastern and north-eastern parts of the basin lie in the gas maturity window. This explains the high gas potential of the Barnett play.

a) b)

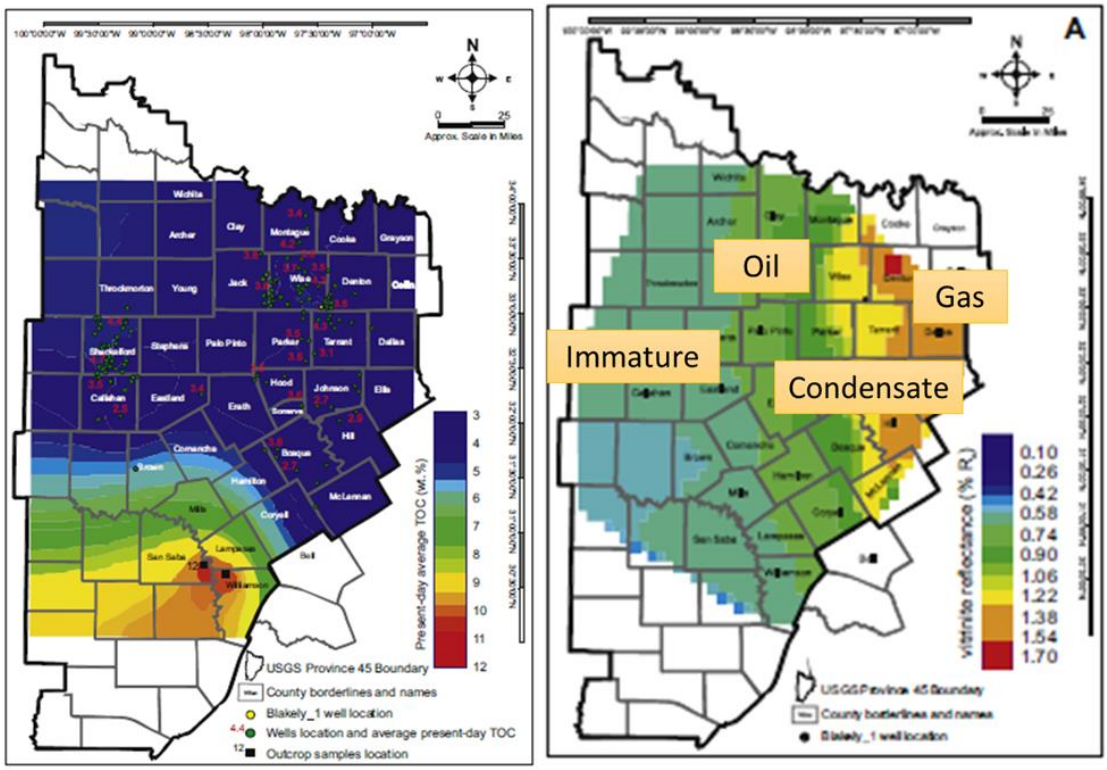

Figure 18: a) TOC distribution map of the Barnett formation (Sarmiento et al. 2013). Fig. 11 b) - Vitrinite reflectance map indicating thermal maturity across the play. Values <0.55 %Ro are considered immature, 0.55 – 1.15 are oil prone, 1.15 – 1.4 are condensate prone and values >1.4 are dry gas prone (Sarmiento et al. 2013).

Figure 19 shows the cumulative gas production bubble map of the Barnett formation. The bubble plot affirms that eastern, north-eastern, and south-eastern portions of the Bakken play have the greatest producing wells. These areas are characterized by thick shales (Figure 17), gas maturity window (Figure 18b) and high production (Figure 19). Thus, these are the sweet spots of Barnett shale play.

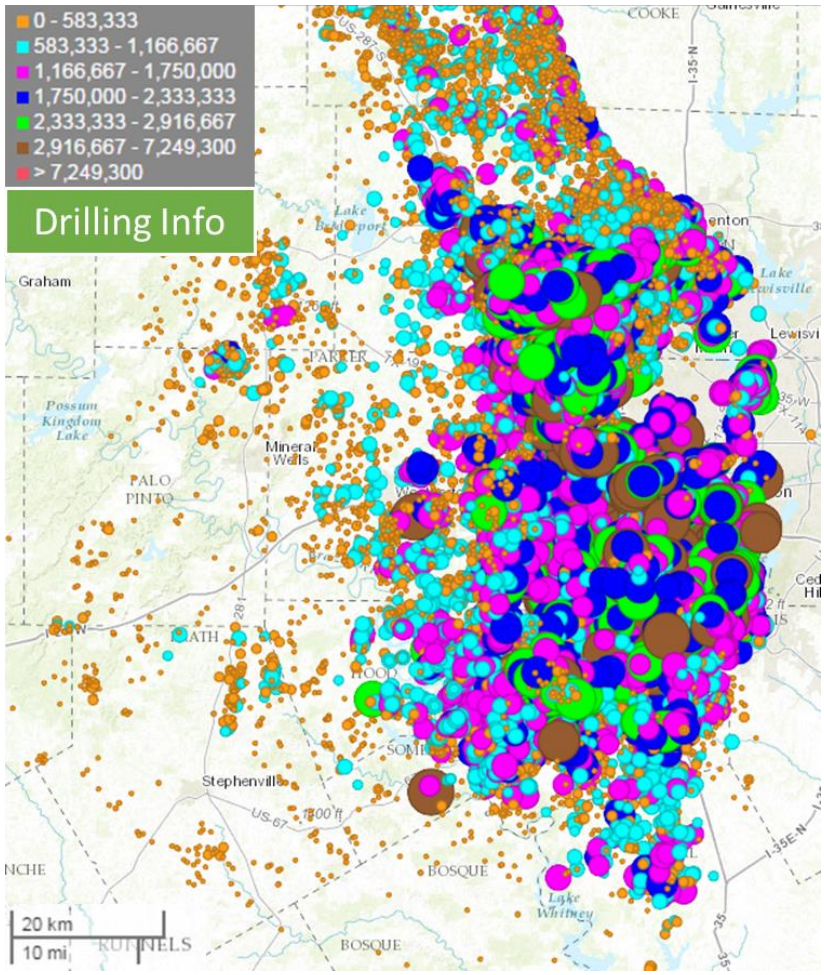

Figure 19: Gas production bubble maps for Barnett shale play. Area concentrated with larger bubbles defines the "sweet spot."

Figure 20 shows the wells having the core and the log data which were used for rock typing. Three wells had core data (shown as red bubbles) which were in over-mature, gas rich, stratigraphically thick part of the Barnett shale play. Core data was

available for 211 plugs in these 3 wells. Only gamma ray and resistivity logs were available for 2 wells (out of the three wells having the core data). Thus, gamma ray and resistivity logs were used for upscaling from core to log level.

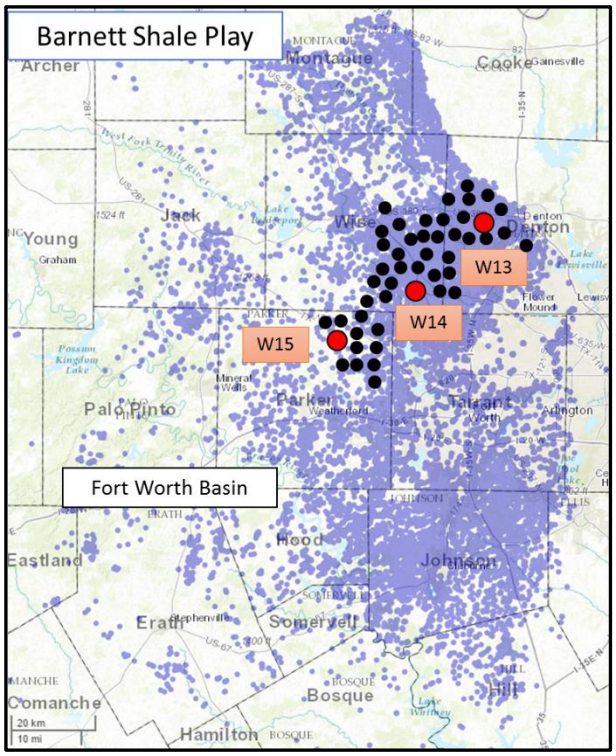

Figure 20: Wells with core and log data for rock typing. 3 wells (red bubbles) had core data which mainly lie in over mature, gas rich, stratigraphically thick part of the Barnett shale play. Core data were available for 211 plugs. Additional 44 wells (shown as black bubbles) were taken for correlation of rock types with production data. They did not have the core data but had the required logs.

3.2 Core-Derived Rock Typing

The five petrophysical measurements from core data namely porosity, TOC, clay, quartz, and carbonate content were used for defining rock types in Barnett. PCA was applied to reduce dimensionality of the clustering problem. Figure 21 shows that the first three principal components explain more than 85% of the variance in the data.

Thus, instead of using 5 variables, it is sufficient to use the first three principal components.

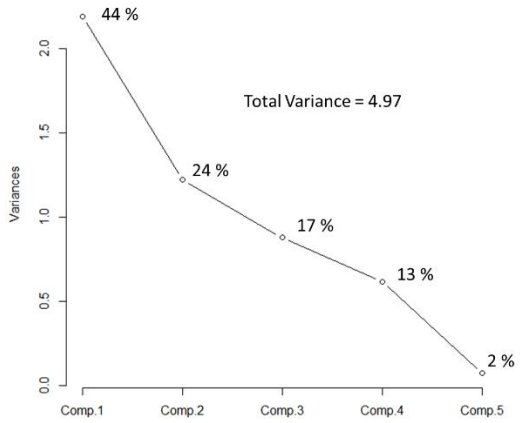

Figure 21: Principal Component Analysis results. The percentage variance explained by each component is listed in the figure. The first three principal components explain more than 85% of the variance in the data.

The optimum number of rock types were defined to be three based on the SSW-SSB method. The results are shown in Figure 22. K-Means and SOM clustering techniques were used to define rock types. K-means and SOM gave very similar results. Different rock types and their characteristics are shown in Figure 23.

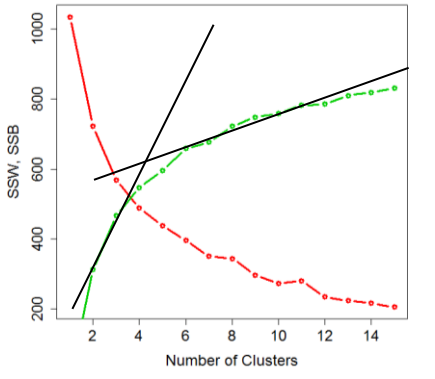

Figure 22: K-Means creates multiple scenarios with different number of clusters. In each case, it identifies the intra-cluster variance (red curve) and inter-cluster variance (green curve). The elbow effect represents change in slope. The elbow effect occurs around 3 clusters which represents the optimum number of clusters.

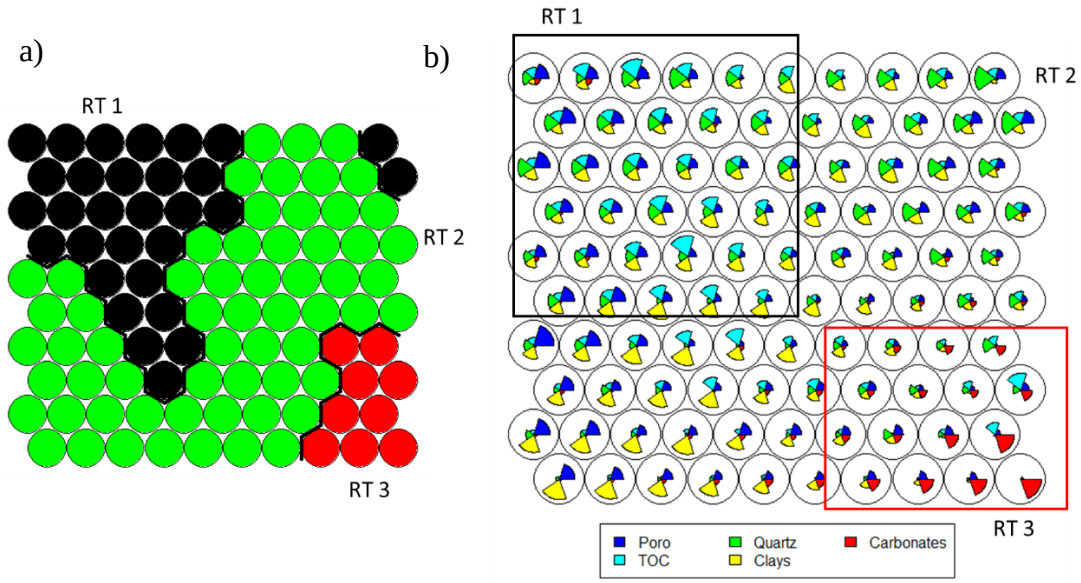

Figure 23: a) Clusters created on a SOM map b) Rose diagram (or pie diagram) shows the petrophysical properties distribution for different rock types/clusters. The size of the pie is proportional to the value of the petrophysical property. Rock Type 1 has high TOC and porosity while Rock Type 3 has high carbonates and low porosity and TOC.

The different rock types were analyzed for their petrophysical relevance. While porosity is a direct indicator of storage potential, TOC is the total organic content and S1 signifies the amount of movable hydrocarbons in the core. High values of TOC and S1 peaks generally indicate higher source rock potential. The other key parameter governing the production from a well in unconventional shale reservoirs is the brittleness of the rock. Mineralogy from FTIR may be utilized as indicators of brittleness. Minerals like quartz are very brittle while on the other hand, clay minerals are ductile.

The parameters governing storage and source potential for different rock types in Barnett are shown in Figure 24. Rock Type 1 has the high storage and source

potential. Rock Type 2 has high storage (porosity) but low TOC (source potential). Rock Type 3 has low porosity and TOC.

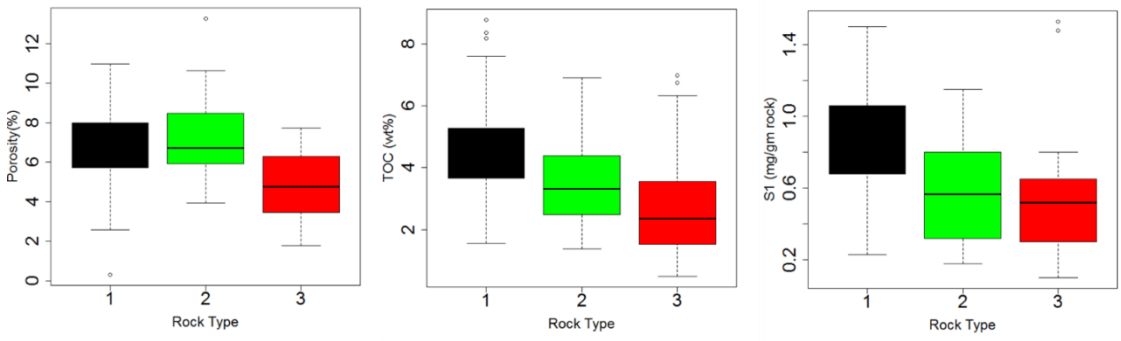

Figure 24: Parameters governing storage and source potential in Barnett. Clearly, Rock Type 1 has the high storage and source rock potential. Rock Type 2 has high storage (porosity) but low TOC (source potential). Rock Type 3 has low porosity and TOC.

The average mineral content for different rock types in Barnett are shown in Figure 25. Rock Type 1 has high quartz content and is likely the most brittle of the three rock types. Coupled with high storage and source rock potential, this rock type is expected to have the largest impact on production. Rock Type 2 is the most ductile of the three rock types due to highest clay content.

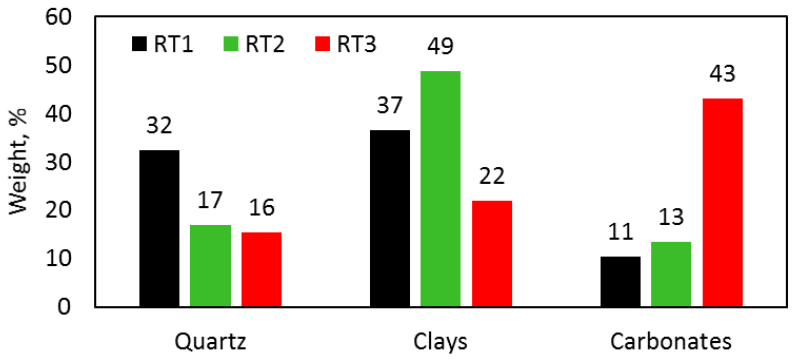

Figure 25: Average mineral content for different rock types in Barnett. Rock Type 1 has high quartz content. It is more brittle compared to the other two rock types. Rock Type 2 has the highest clay percentage and is the most ductile of the three rock types.

Kale et al. (2010) worked on a part of the same dataset used in this study. They came up with three petrofacies. In their study, Petrofacies 1 represented calcite lean (<10 wt. %), high quartz, high clays, high porosity, and high TOC facies. Petrofacies 2 represented moderate calcite content (10-25 wt. %), high porosity, moderate clays and quartz, and low TOC facies. Petrofacies 3 was calcite rich, and low porosity and TOC. The results obtained by Kale et al. (2010) are similar to the results of this study. Also, they were able to group 10 lithofacies identified by Singh (2008) and come up with three broad lithofacies groups, quite distinct from each other. These broad lithofacies groups were basically equivalent to the three petrofacies identified from core measurements. Thus, the three petrofacies were both geologically and petrophysically relevant.

Mercury injection capillary pressure data were also available for 100 core plugs in this study. The capillary pressure curves for most of the samples were interpreted to lie in one of the three broad categories. The average petrophysical properties of the three categories were comparable to the properties of the three rock type groups.

Incremental and cumulative mercury intrusion plots, normalized by helium pore volume, for the three rock types are shown in Figure 26. The cumulative intrusion plot in Rock Type 1 samples which had high storage and source rock potential, shows that the ratio of mercury to helium volume varies between 0.65 to 0.80. In Rock Type 2 samples, this ratio varies between 0.40 to 0.60 and it varies between 0.30 to 0.45 for Rock Type 3 samples. It may mean that the connected pore volume decreases as we go from Rock Type 1 to Rock Type 2 and Rock Type 3. It is interesting to note that both

rock types 1 and 2 had similar range of helium porosity but Rock Type 2 has much lower connectivity then Rock Type 1.

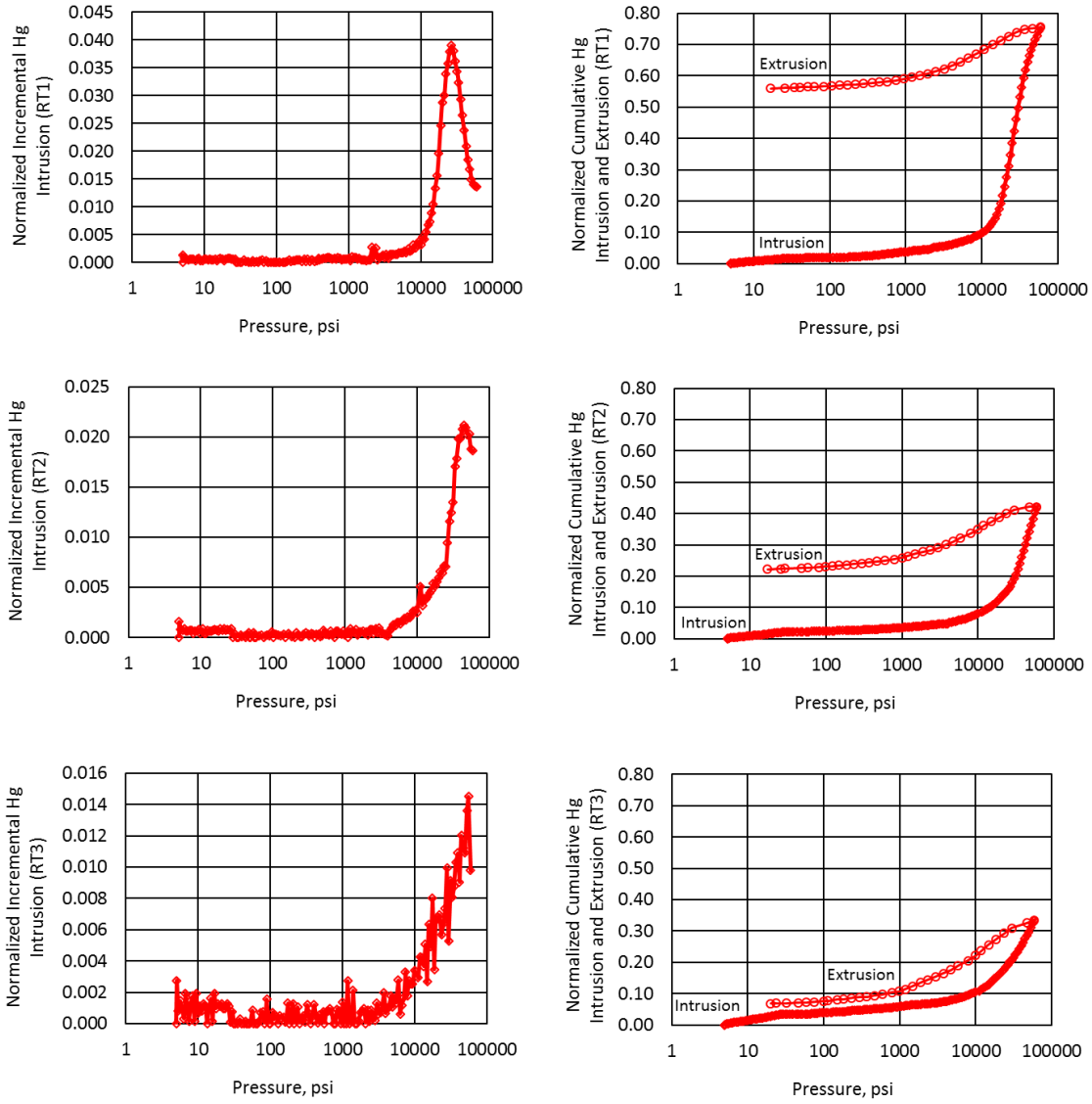

Figure 26: Representative normalized incremental and cumulative mercury intrusion plots for the three rock types in Barnett. Pore volume connectivity decreases from Rock Type 1 to Rock Type 2 to Rock Type 3. Rock Type 3 is very tight and does not have an inflection point as shown by monotonously increasing incremental intrusion curve.

The shape of the capillary pressure curves is also different for the three categories or rock types. In Rock Type 3 samples, the incremental injection curve

increases monotonically without reaching a plateau or an inflection point even at 60,000 psia. This shape is characteristic of very tight rocks where the dominant pore size may be smaller than 3 nm. The cumulative intrusion plots in both Rock Type 1 and Rock Type 2 exhibit considerable hysteresis between saturating and desaturating curves, implying that not all the mercury that enters the sample during the intrusion cycle comes out when the pressure is released during the extrusion cycle. This is a sign of real Hg intrusion into the sample and storage potential

However, in Rock Type 3, cumulative intrusion curves in Rock Type 3 exhibit almost overlapping saturating and desaturating curves. The lack of hysteresis between saturating and desaturating curves is a sign of false intrusion/blank effect due to sample and Hg compression at high pressures. Samples exhibiting this type curve have high calcite content and very low porosity.

In Rock Type 1 and Rock Type 2 samples, the capillary pressure curve exhibit a distinct maximum before 60,000 psia. For Rock Type 1 samples, the average dominant pore throat size is 8 nm while for Rock Type 2 samples, it is 4 nm. Thus, Rock Type 1 samples have the highest permeability. Rock Type 2 samples may be effected by presence of higher clay fraction.

Kale et al. (2010) also did an independent MICP data study and grouped different plugs based on capillary pressure curve characteristics. These groups were then tied back to the different petrofacies. They concluded that Petrofacies 1 and 2 samples had high hysteresis and showed high connectivity. Petrofacies 3 samples (calcite rich facies) showed low connectivity and negligible hysteresis. Thus, results in this study were similar to their study.

3.3 Extending Core-Based Classification to Well Logs

In Barnett play, gamma ray and resistivity were the only logs available in two out the three wells which had the core data. Thus, these two logs were used for upscaling. Figure 27 shows the distribution of gamma ray and resistivity for different rock types. Rock Type 1 had high gamma ray and high neutron porosity consistent with high TOC and high porosity measured in the lab. Rock Type 3, on the other hand, had lowest neutron porosity consistent with lowest helium porosity measured in the lab.

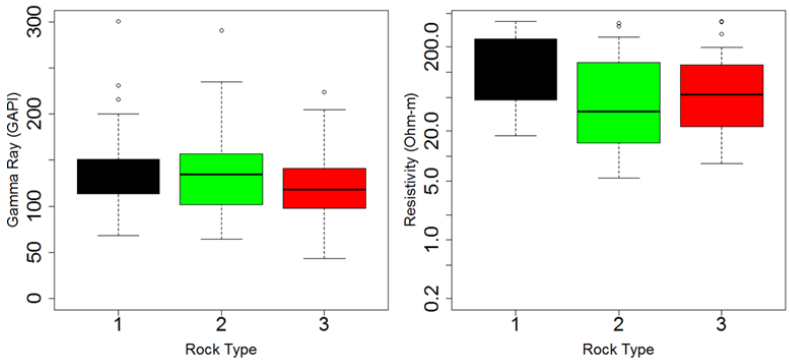

Figure 27: Gamma ray and resistivity distribution for different rock types in the Barnett formation. Rock Type 1 shows high gamma ray and resistivity due to high TOC.

To do the upscaling, log data were extracted corresponding to depths where core data were available. The core-based rock types were derived from K-means and SOM clustering. This then constituted the training data for the Support Vector Machines (SVM) classification algorithm. A test was done where different SVM models were tested like linear, polynomial, and radial. A large part of the training dataset was used to train the model and then the prediction was made on a small portion of the training dataset. The efficiency or accuracy of a model was gauged by the fact if the model could predict the same rock types from log data as were obtained from the core-based

clustering. Radial SVM model gave the best results and therefore, was used for prediction. The trained model was. used to predict rock types in uncored wells and remaining section of the cored wells where core data were not available. The rock type logs for the two sample wells (W13 on left, W14 on right) are shown in Figure 28. The lower Barnett is richer in Rock Type 1. Thus, the lower Barnett has higher TOC and quartz compared to upper Barnett. The rock type logs for other wells are shown in Appendix B.

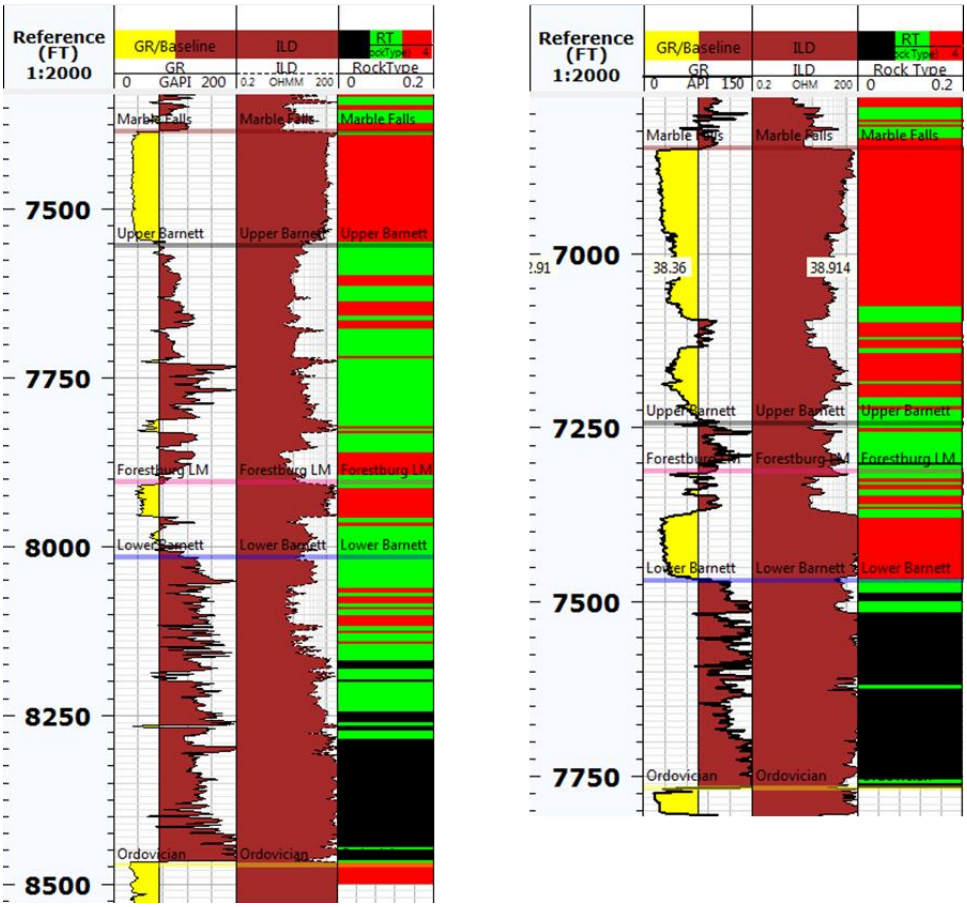

Figure 28: Rock type logs (track 3; black=Rock Type 1, green=Rock Type 2, and red=Rock Type 3) for two sample wells (W13 on left, W14 on right) in Barnett. The lower Barnett is richer in Rock Type 1. Thus, lower Barnett has higher TOC and quartz compared to upper Barnett.

3.4 Relating rock types to Production Data

Kale et al. (2010) compared the production data in the two wells where rock typing study was carried out. They identified that Well A had thick continuous Petrofacies 1 layers, much higher Net to Gross (NTG) (83.7 % of Petrofacies 1) compared to Well B which had thinner Petrofacies 1 layers interspersed with Petrofacies 2 and 3 layers. The NTG in Well B was also considerably lower (51.7 % of Petrofacies 1). The production in Well A was observed to be 42% higher than Well B possibly because of this different distribution of Petrofacies. A more exhaustive correlation of the production data was carried out for this study to validate the practical utility of the rock typing exercise.

Rock Type 1 had high storage and source rock potential in the Barnett formation. Additionally, it was also the most brittle of the three rock types. Thus, Rock Type 1 is expected to be the key driver in production. A Rock Type 1 ratio (RTR) was created by dividing the Rock Type 1 thickness with the gross thickness (i.e. RT1+RT2+RT3) for all the wells. This was correlated with normalized production.

The spatial locations of wells for which rock types were upscaled are shown in Figure 20. All the wells were vertical wells. Figure 29 shows the comparison of RTR with normalized production. Normalized production here refers to first 24 months' cumulative gas normalized by the zone thickness. A strong positive correlation suggests that Rock Type 1 is the key rock type controlling the production.

A sensitivity study was done to compare 12 months, 24 months and cumulative production (average well life 11 years) as shown in Figure 30. Almost perfect correlation between 12 months and 24 months' production suggest that likely the wells are still in transient phase and interference effects between adjacent fractures and wells

have not kicked in. Also, high correlation coefficients between different production metrics suggest that any one metric could be used for production correlation.

The set of wells lying along the green trend line show high productivity while wells lying along red trend line show relatively lower productivity. The wells having high productivity are from different counties; namely, Denton, Wise and Parker. The commonality among these high productivity wells is that they were all completed by one operator. The wells lying along the red trend line were completed by other operators. Thus, it appears that the reason for multiple trends in Figure 29 can be attributed to different completion practices used by various operators.

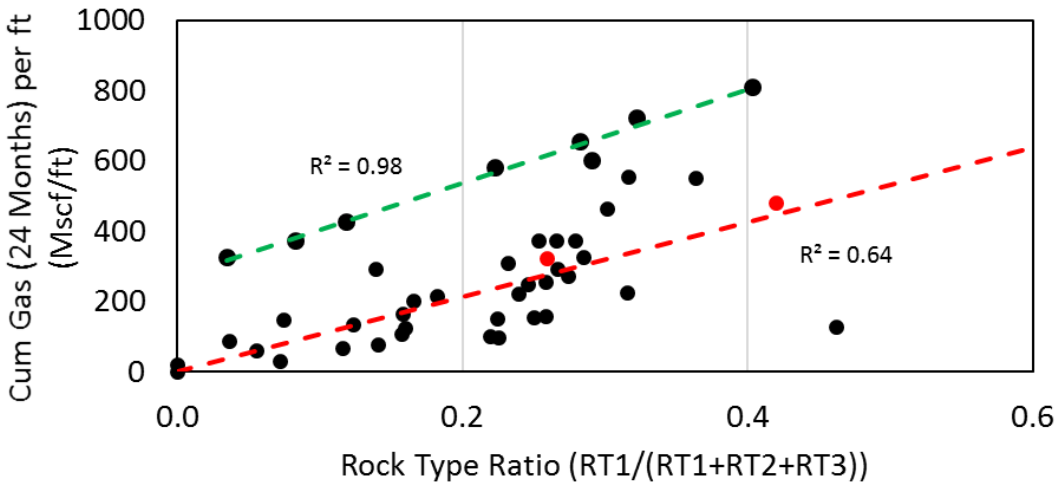

Figure 29: Normalized production correlated with the Rock Type Ratio (RTR) in Barnett. A strong positive correlation suggests Rock Type 1 is the key rock type controlling the production. The set of wells lying along the green trend line show high productivity while wells lying along red trend line show relatively lower productivity. The commonality among these high productivity wells is that they were all completed by one operator. Thus, it appears that the reason for multiple trends in the figure can be attributed to different completion practices used by various operators.

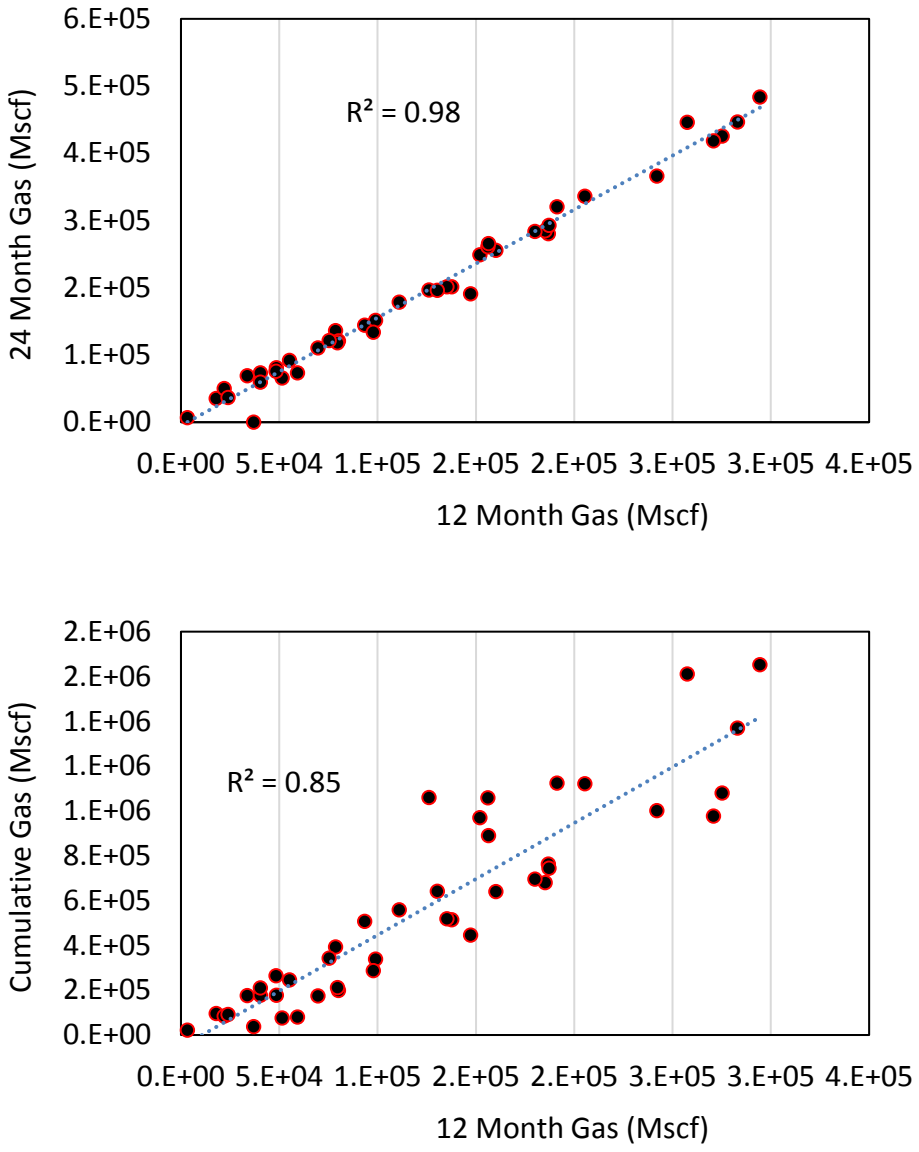

Figure 30: Comparison of different production metrics namely 12 months' gas production, 24 months' gas production and cumulative gas production (average well life 11 years). Almost perfect correlation between 12 months and 24 months' production suggest that likely the wells are still in transient phase and interference effects between adjacent fractures and wells have not kicked in. Also, high correlation coefficients between different production metrics suggest that anyone could be used for production correlation.

Chapter 4: Eagle Ford Formation

4.1 Study Area Description

Eagle Ford is one of the most prominent shale plays in US. It is late Cretaceous in age with more than 1.5 billion barrels oil, and 4.2 Tcf gas produced so far (based on drilling info, checked Dec 16, 2016). It varies in thickness between 150 to 450 ft. (Callantine 2010). The depths of Eagle Ford formation vary from 7,000 ft. to 12,000 ft. (CLR 2010). Eagle Ford is slightly over-pressured with pressure gradient varying from 0.4 to 0.7 psi/ft. (CLR 2010). It has 4 different basins namely Maverick, Hawkville, San Marcos and East Texas. Traditionally, some experts do not consider East Texas basin as a part of Eagle Ford play due to its very high clay content compared to rest of the Eagle Ford. Figure 31 (Tuttle 2010) shows the Eagle Ford shale play.

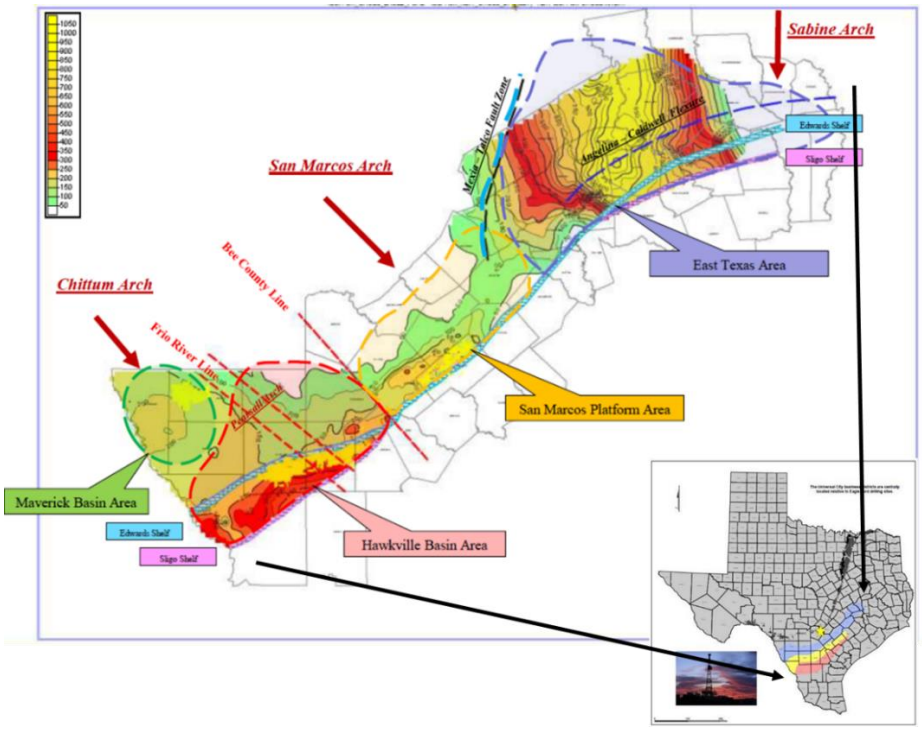

Figure 31: Eagle Ford shale play. The figure shows the four major basins in Eagle Ford namely Maverick, Hawkville, San Marcos and East Texas (Tuttle 2010).

Figure 32 shows the depositional environment for Eagle Ford (Breyer et al. 2012). The sediment influx is evident from north-east. East Texas basin has mainly deltaic deposits. This is primarily the reason for higher clay fraction in this basin. Marine shelf and slope deposits are evident as one moves towards central, western, and southern parts of the play. The marine deposits are very rich in carbonates. The slope deposits are deeper compared to shelf deposits and are expected to have higher maturity than the northern shelf deposits.

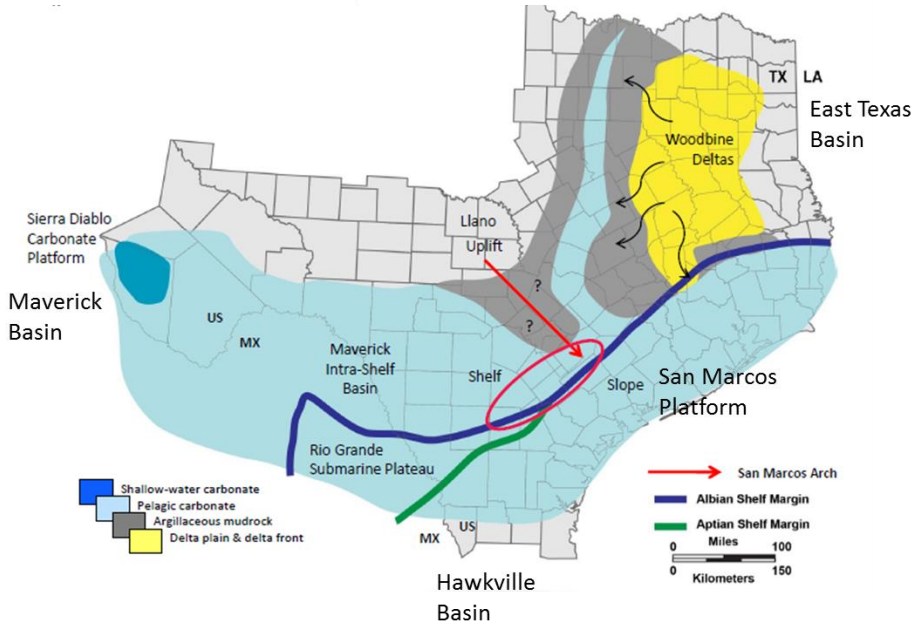

Figure 32: Depositional environment for Eagle Ford (Breyer et al. 2013). The sediment influx is evident from north-east. East Texas basin has mainly deltaic deposits. The other three basins have marine shelf and slope deposits and are rich in carbonates.

Figure 33 shows the isopach thickness map for Eagle Ford play (EOG 2010). The blue color represents thickness of 350 ft. The orange color represents lower thickness of 30 ft. The thickness increases as one goes seaward. Figure 34 shows the TOC maps for upper and lower Eagle Ford (Tian 2014). The TOC maps are only

available for a part of the Eagle Ford play. The red color represents high TOC and blue color represents low TOC. Generally, lower Eagle Ford is more rich in TOC. The TOC varies from 1 to 6 % in upper Eagle Ford and from 2 to 12 % in lower Eagle Ford. It is evident from Figure 33 and Figure 34 that thicker parts of the Eagle Ford play are associated with higher TOC.

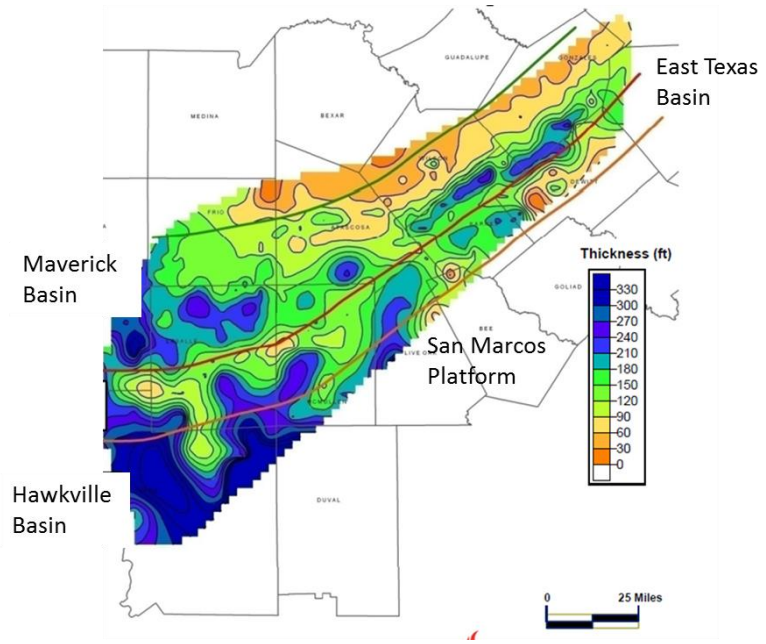

Figure 33: Isopach thickness map for Eagle Ford play (EOG 2010). The blue color represents greater thickness of 350 ft. The orange color represents lower thickness of 30 ft. The thickness increases as one goes seaward.

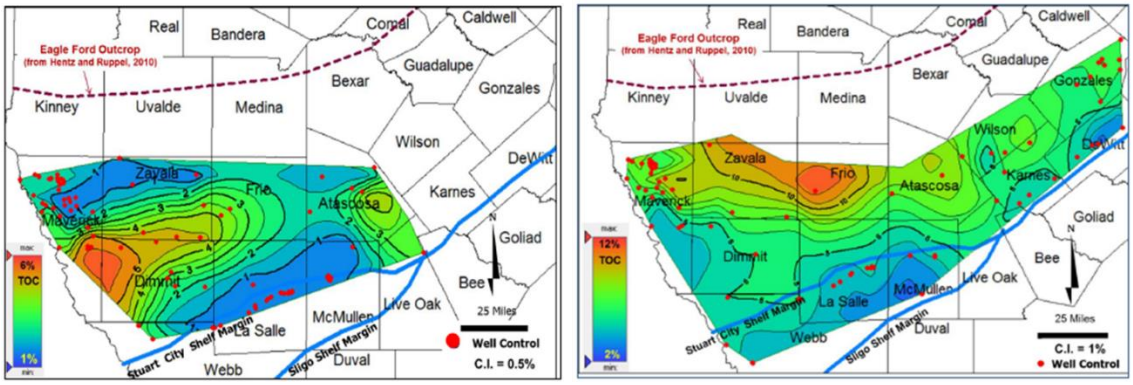

Figure 34: (Left) TOC map for upper Eagle Ford. (Right) TOC map for lower Eagle Ford (Tian 2014). The TOC map is available only for a part of the play.

Figure 35 shows the oil, gas, and condensate regions in the Eagle Ford play (Tuttle 2010). Slope deposits are deeper and expected to be more mature compared to the northern shelf deposits. Thus, as one goes north, maturity decreases and there is a transition from gas to oil.

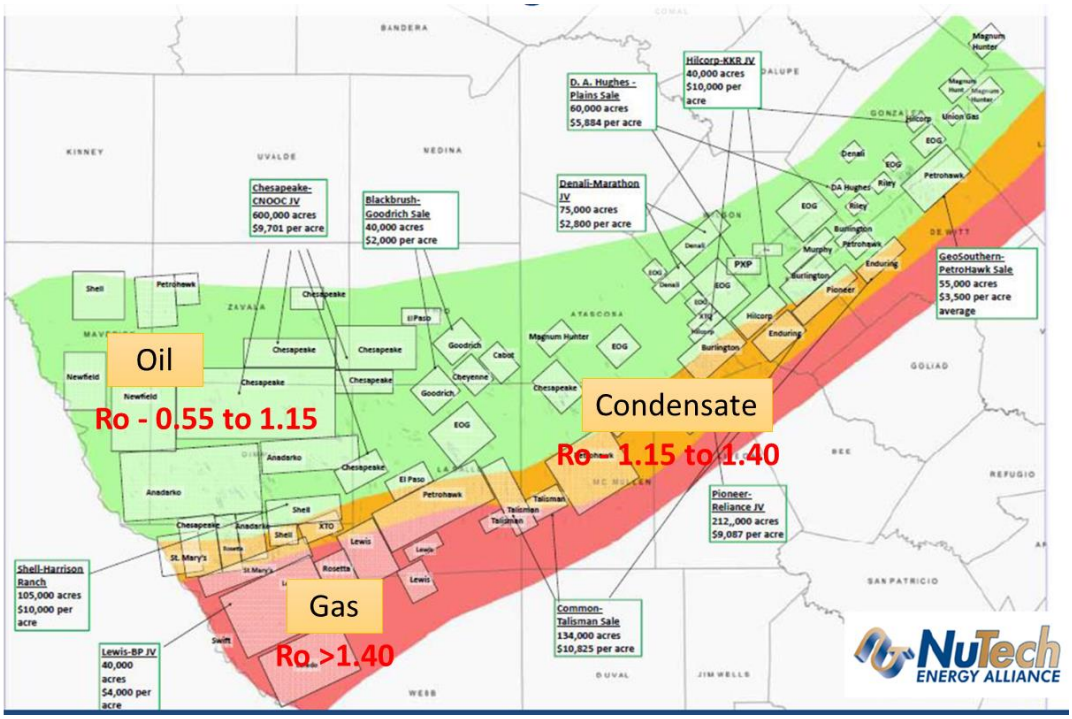

Figure 35: Oil, gas, and condensate regions in the Eagle Ford play (Tuttle 2010).

The oil and gas production bubble maps are shown in Figure 36. The bubble maps show that southern part of the play is more gas prone and northern part of the play is more oil prone. The bubble maps also show that the western and northern parts of the play contain highest oil production wells. These areas are characterized by thick shales (Figure 33), high TOC (Figure 34) and oil maturity window (Figure 35) and high production (Figure 36). Thus, these are also the sweet spots of Eagle Ford play.

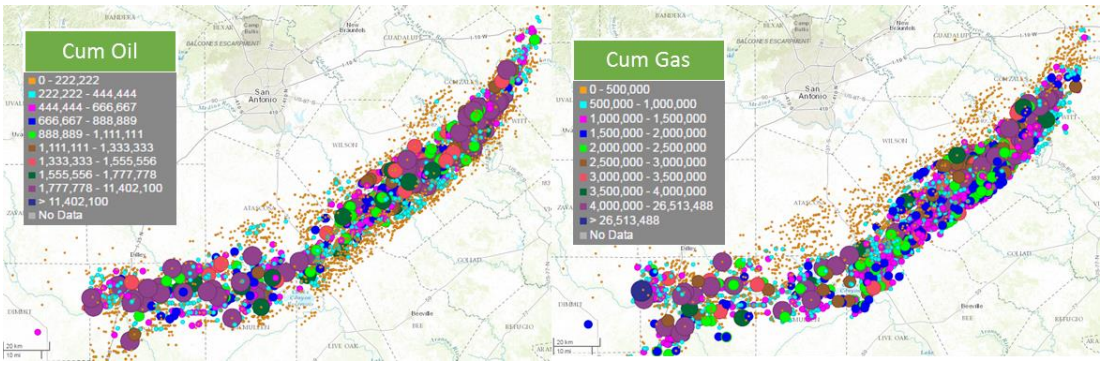

Figure 36: Cumulative oil and gas production bubble maps for Eagle Ford formation. Areas having larger bubbles represent sweet spots in Eagle Ford.

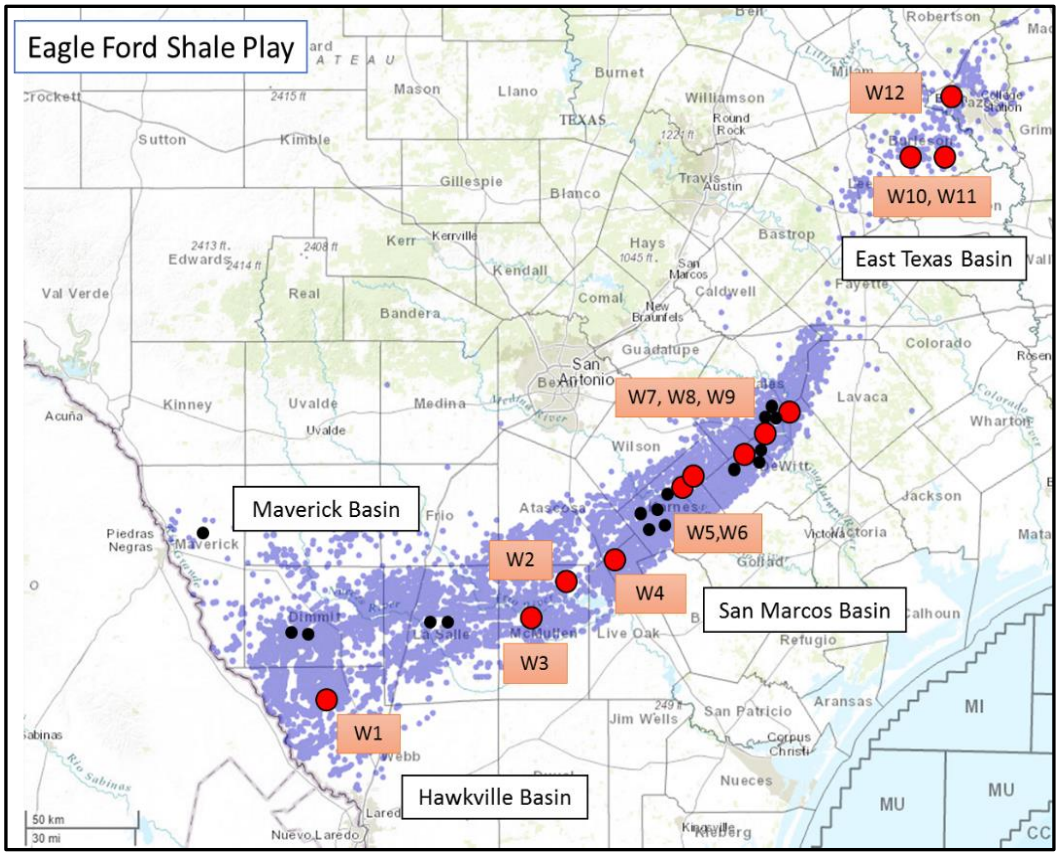

Figure 37: Wells with core and log data for rock typing. 12 wells had core data (shown as red bubbles). They are spread throughout the Eagle Ford play but were mainly limited to the condensate window. Core data were available for 263 depth points. An additional 17 wells (shown as black bubbles) were taken for correlation of rock types with production data. They did not have core data but had the required logs.

Figure 37 shows the wells having the core data (red bubbles) which were used for rock typing. Twelve wells were available which spread throughout the Eagle Ford play but were mainly limited to the condensate window. Core data were available for 263 plugs in these 12 wells. Out of the 12 wells which had core data, triple combo logs were available in only 3 wells while 3 more wells had gamma ray and resistivity. Thus, gamma ray and resistivity logs were used for upscaling from core to log level.

4.2 Core-Derived Rock Typing

Five petrophysical measurements from core data namely porosity, TOC, clay, quartz and carbonate content were used for defining rock types. PCA was done to reduce dimensionality of the clustering problem. Figure 38 shows that the first three principal components explain around 90% of the variance in the data. Thus, instead of using 5 variables, it is sufficient to use first three principal components.

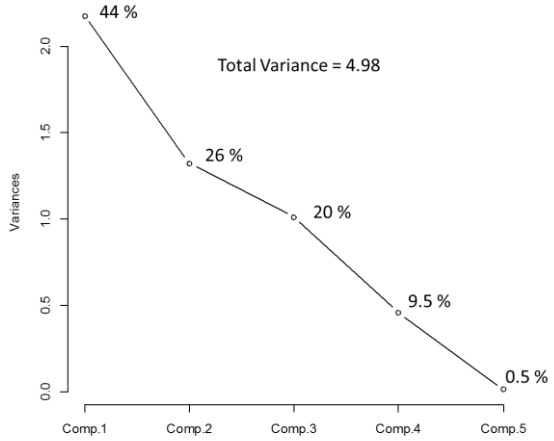

Figure 38: Principal Component Analysis results. The percentage variance explained by each component is listed in the figure. The first three principal components explain around 90% of the variance in the data.

The optimum number of rock types were defined to be three based on the SSW-SSB method. The results are shown in Figure 39. K-Means and SOM clustering

techniques were used to define rock types. K-means and SOM gave very similar results. Different rock types and their characteristics are shown in Figure 40.

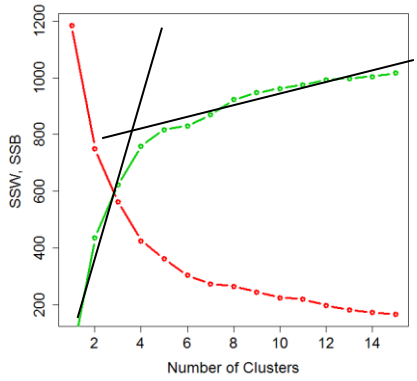

Figure 39: K-Means creates multiple scenarios with different number of clusters. In each case, it identifies the intra-cluster variance (red curve) and inter-cluster variance (green curve). The elbow effect represents change in slope. The elbow effect occurs around 3 clusters which represents the optimum number of clusters.

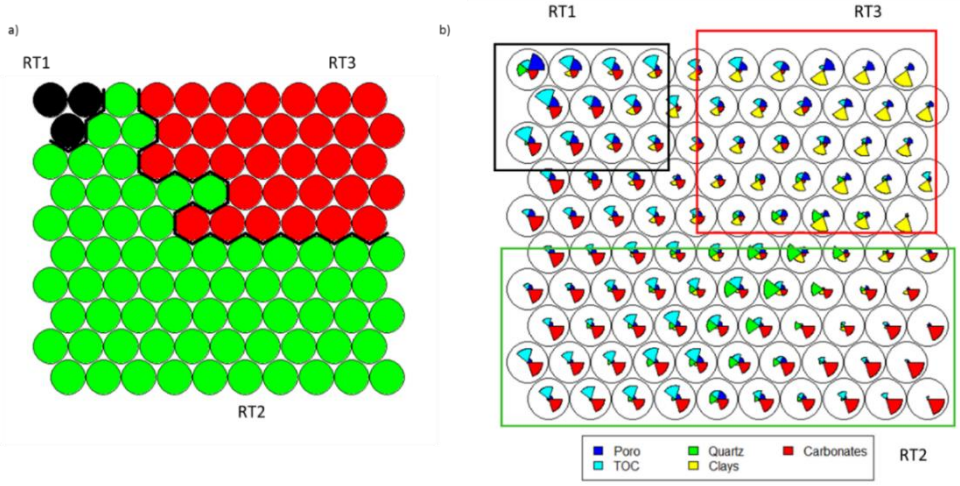

Figure 40: a). Clusters created on a SOM map b) Rose diagram (or pie diagram) shows the petrophysical properties distribution for different rock types/clusters. The size of the pie is proportional to the value of the petrophysical property. Rock Type 1 has high TOC and porosity while Rock Type 3 has high clays and low TOC.

The parameters governing storage and source potential for different rock types in Eagle Ford are shown in Figure 41. Clearly, Rock Type 1 has the highest porosity, TOC and S1 values. Rock Type 1 has the highest storage and source potential.

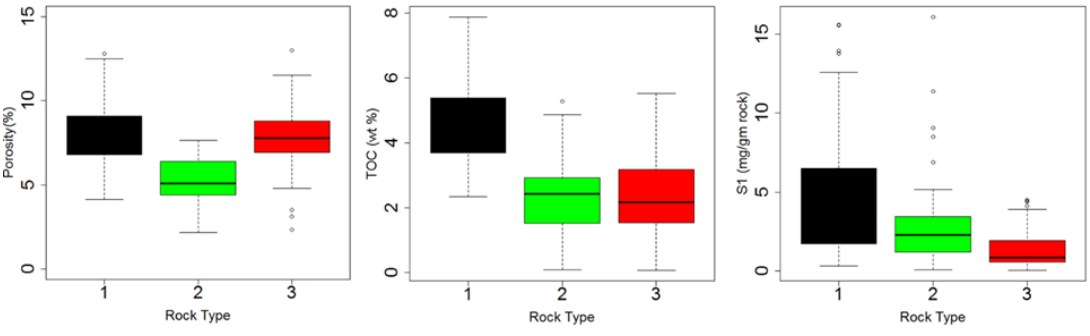

Figure 41: Parameters governing storage and source potential in Eagle Ford. Clearly, Rock Type 1 has the highest porosity, TOC and S1 value, Rock Type 1 has the highest storage and source potential.

The average mineral content for different rock types in Eagle Ford is shown in Figure 42. All rock types have little quartz and thus cannot be differentiated based on quartz content for brittleness. However, Rock Type 3 has the highest clay percentage. Wells 10, 11 and 12 (Figure 37) are rich in Rock Type 3. These wells lie in detrital deltaic deposits. This explains why these wells are different and clay rich compared to other wells in carbonate rich marine shore/shelf deposits. The Rock Type 3 has high porosity but very small TOC/S1. Thus, Rock Type 3 is ductile and has poor source rock potential.

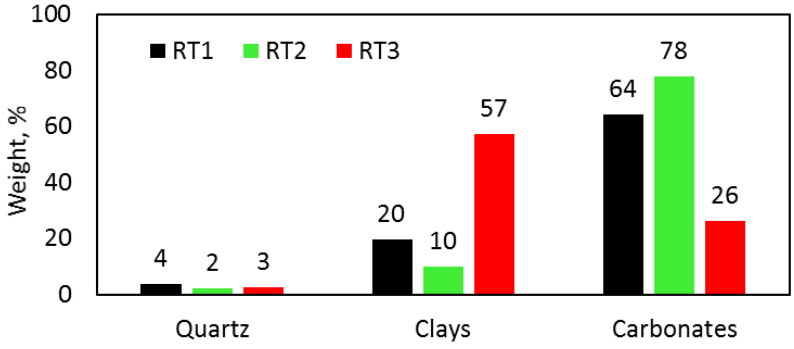

Figure 42: Average mineral content for different rock types in Eagle Ford. Rock Type 3 has high clay content. Wells rich in Rock Type 3 lie in the East Texas basin. This rock type has high porosity but poor source rock potential.

Mercury injection capillary pressure data were also available for 220 core plugs. The capillary pressure curves for most of the samples were interpreted to lie in one of the three broad categories. The average petrophysical properties of the three categories were comparable to the three rock types.

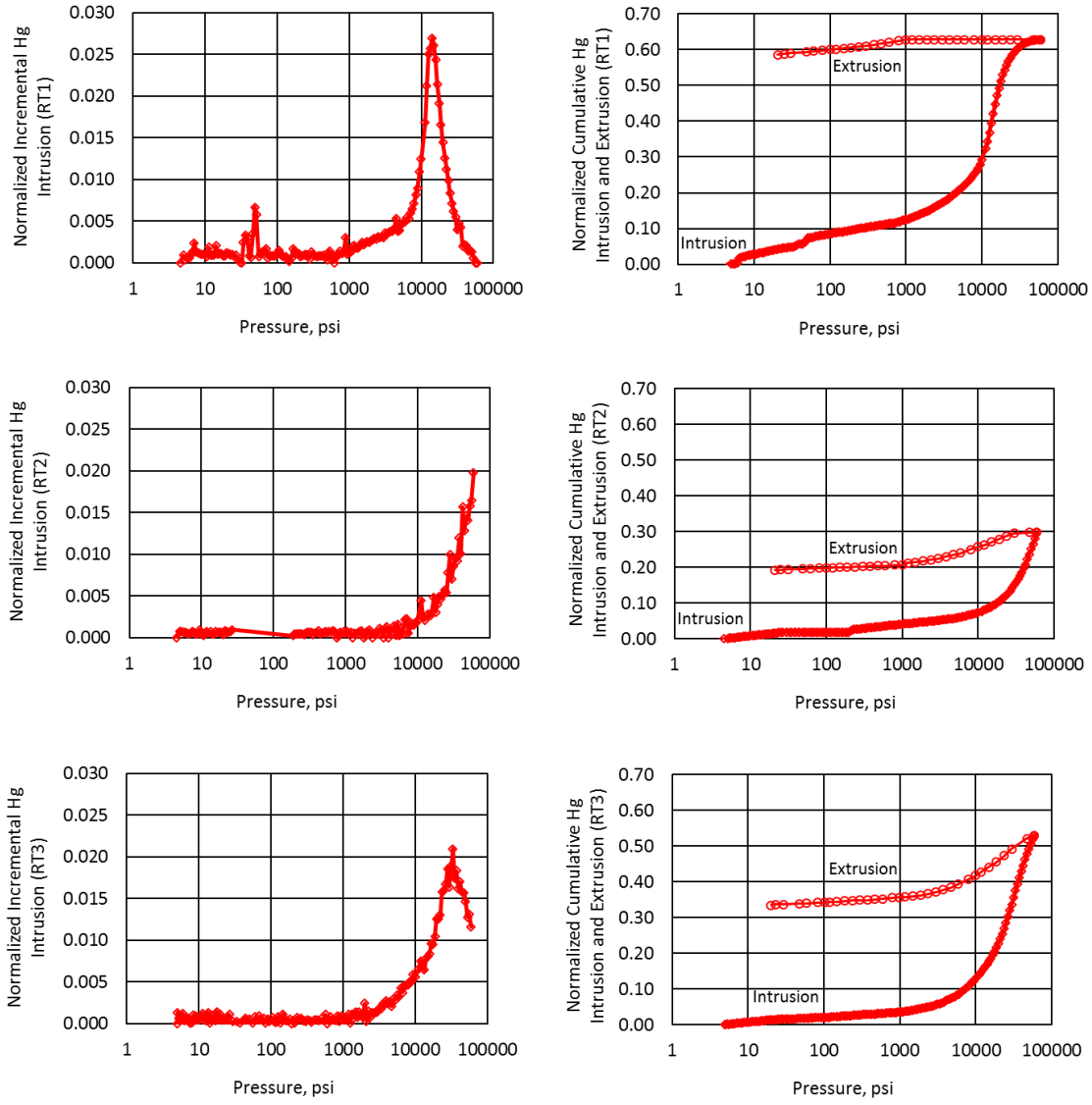

Figure 43: Representative normalized incremental and cumulative mercury intrusion plots for the three rock types in Eagle Ford. Pore volume connectivity decreases from Rock Type 1 to Rock Type 3 to Rock Type 2. Rock Type 2 is very tight and does not have an inflection point as shown by monotonously increasing incremental intrusion curve.

Incremental and cumulative mercury intrusion plots, normalized by helium pore volume, for the three rock types are shown in Figure 43. Because of normalization, intrusion scale varies between 0 and 1. The normalization helps to determine connectivity of the sample. In Rock Type 1 samples, which had the highest storage and source rock potential, the cumulative intrusion plot shows that the ratio of mercury to helium volume varies between 0.6 to 0.75. In Rock Type 3 samples, this ratio varies between 0.5 to 0.65 and it varies between 0.3 to 0.4 for Rock Type 2 samples. Thus, it shows that the connected pore volume decreases from Rock Type 1 to Rock Type 3 and Rock Type 2. It is interesting to note that both rock types 1 and 3 have similar range of helium porosity but Rock Type 3 has lower connectivity then Rock Type 1.

The shapes of the capillary pressure curves also clearly distinguish the three rock types. In Rock Type 2 samples, the curve injection increases monotonously without reaching a plateau or an inflection point even at 60,000 psia. At 60,000 psia, equivalent pore size which the mercury could pass through is 3 nm. This shape is characteristic of very tight rocks where the dominant pore size may be smaller than 3 nm.

The incremental capillary pressure curves exhibit a distinct maximum before 60,000 psia for Rock Type 1 and Rock Type 3 samples. The inflection point defines the dominant pore throat. A larger value of the dominant pore throat means higher permeability. For Rock Type 1 samples, the average dominant pore throat size was 13 nm while for Rock Type 3 samples, it was 5 nm. Rock Type 1 samples had the highest permeability. Rock Type 3 samples may be effected by presence of higher clay fraction.

4.3 Extending Core-Based Classification to Well Logs

The next step was to extend the core-based classification to well log data. This is necessary because in general, not all intervals within a well are cored and additionally, it may be necessary to determine the distribution of rock types in uncored wells. The logs were only available for vertical pilot holes and thus, there was an inherent assumption that properties do change as you go away from wellbore. In Eagle Ford, gamma ray and resistivity logs were available for six out of the twelve wells which had the core data. Thus, these two logs were used for upscaling. The distributions of gamma ray and resistivity for different rock types are shown in Figure 44. Rock Type 1 and Rock Type 3 both show high gamma ray possibly due to high TOC and high clays, respectively. Also, Rock Type 1 shows a high resistivity due to high oil saturation and Rock Type 3 shows a lower resistivity due to high water saturation and high clays. Thus, core and log data are consistent with each other.

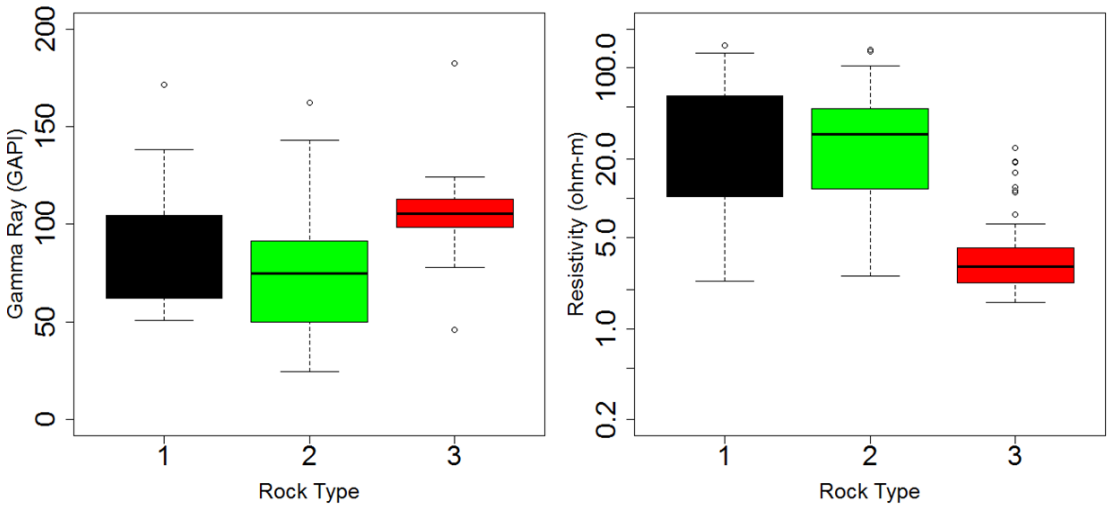

Figure 44: Gamma ray and resistivity distribution for different rock types in the Eagle Ford from the depth points at which both core and log data were available.

The trained SVM model was used to predict rock types in uncored wells and remaining section of the cored wells where core data were not available. The rock type logs for two sample wells (W10 on left, W6 on right) in the Eagle Ford are shown in Figure 45. W10 is in East Texas basin and is very rich in Rock Type 3. W6 is in San Marcos basin and is rich in Rock Type 1. W6 is expected to have a better production rate than W10. The rock type logs for other wells in Eagle Ford are shown in Appendix A. These include wells which had both core and log data, and wells which only had log data.

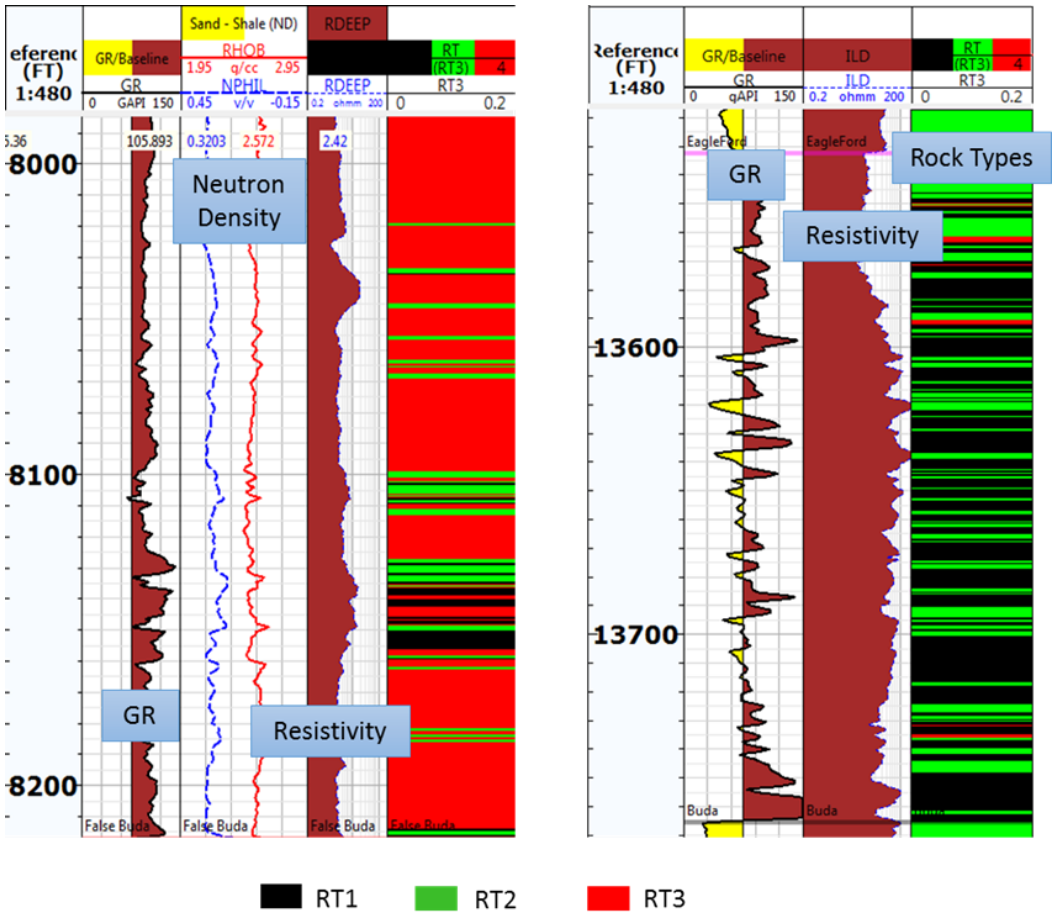

Figure 45: Rock type logs (track 4; black=Rock Type 1, green=Rock Type 2, and red=Rock Type 3) for two sample wells (W10 on left, W6 on right) in Eagle Ford. W10 is located in East Texas basin and is very rich in Rock Type 3. W6 is located in San Marcos basin and is rich in Rock Type 1.

Next, an innovative method was devised to check the quality of populated rock type logs and asses the robustness of the SVM algorithm. Since, the triple combo logs were available for three wells, porosity and TOC logs were modelled using resistivity, gamma ray, neutron and density logs. The triple combo logs and the calculated porosity and TOC logs for Well 10 and Well 6 are given in Figure 46. The methodology has been described in 2.2 Log Analysis section.

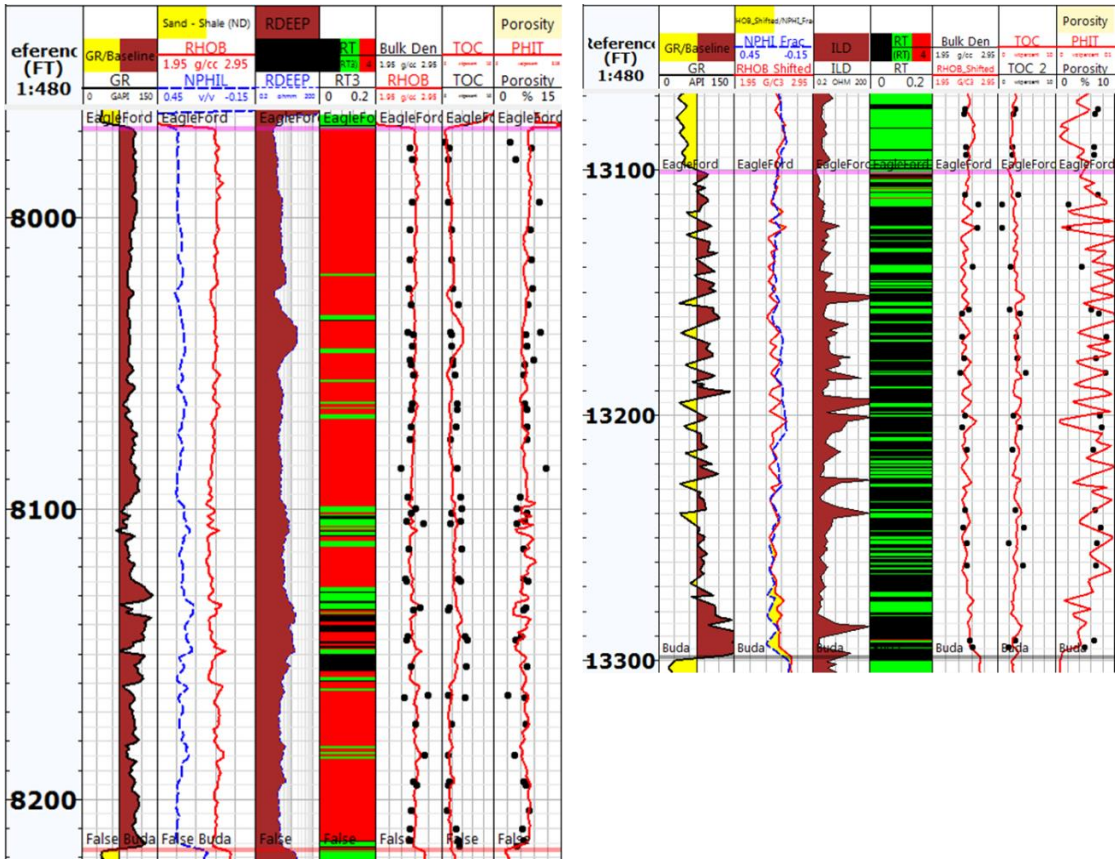

Figure 46: Calculated logs (rock types in track 4; black=Rock Type 1, green=Rock Type 2, and red=Rock Type 3) namely porosity and TOC logs for two sample wells (Well 10 on left, W6 on right). The red curve represents the modelled curves. The black filled circles represent the core measurements that were used for calibration.

Box plots were created to see the distribution of calculated TOC and porosity based on the rock type log. The box plots are shown in Figure 47. The results reassert

the conclusion based on core-derived rock types (Figure 41). Rock Type 1 has the highest source rock and storage potential. Rock Type 3 though has a high porosity but lacks TOC. This cross-check validates the rock type upscaling method and lends credibility to further analysis with the production data.

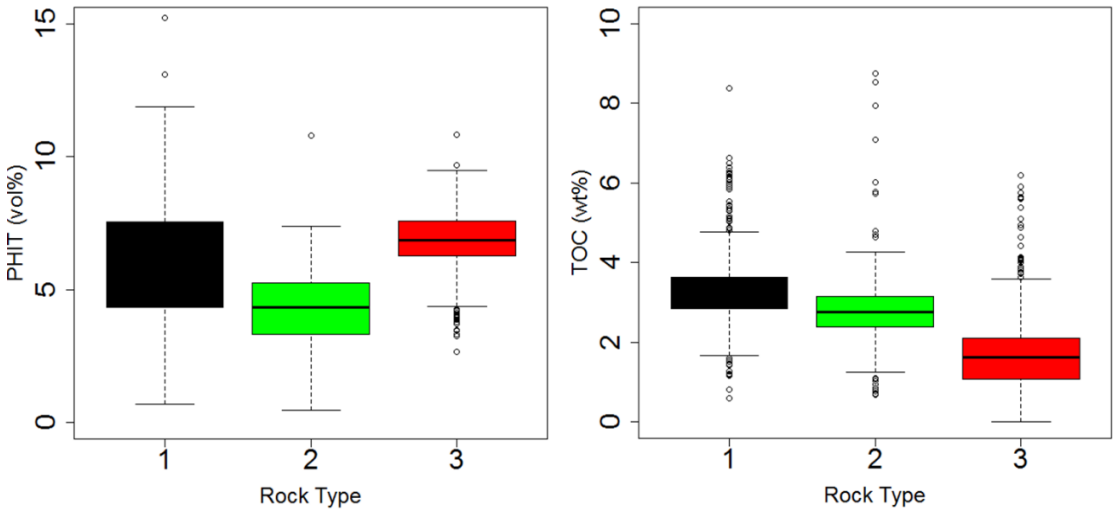

Figure 47: Box plots showing distribution of calculated TOC and porosity logs based on populated rock type log. The distributions reassert the conclusions based on core derived rock types.

4.4 Relating rock types to Production Data

In Eagle Ford, Rock Type 1 had the highest storage and source rock potential. Thus, Rock Type 1 is expected to be the key driver of the production. A Rock Type 1 ratio (RTR) was created by dividing the Rock Type 1 thickness with the gross thickness (i.e. RT1+RT2+RT3) for all the wells. This was then correlated with normalized production. The positive correlation between the two validates the robustness and practical utility of the rock typing exercise. It also highlights the value that can be generated by doing such an exercise in unconventional reservoirs.

The spatial locations of the wells for which rock types were upscaled are shown in Figure 37. Red represents wells with cores and black represents additional wells which did not have the core data. All the wells were horizontal wells and their lateral length varied from 600 to 6000 ft. To make a fair comparison, the production was normalized by the lateral length. The comparison of RTR with normalized production is shown in Figure 48. Normalized production here refers to first 24 months' cumulative barrel of oil equivalent (BOE) normalized by the lateral lengths. A strong positive correlation suggests that Rock Type 1 is the key rock type controlling production. There are some outliers which are expected due different completion treatments, etc.

Comparison of different production metrics namely 6 months' BOE, 24 months' BOE and cumulative BOE (average well life 5 years) is shown in Figure 49. Very high correlation coefficients between different production metrics suggest that anyone could be used for production correlation.

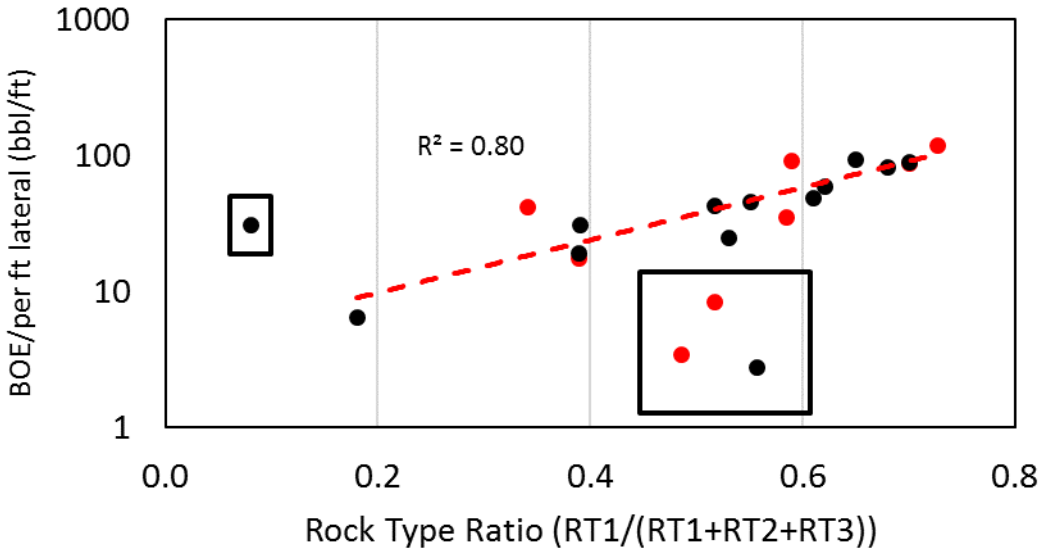

Figure 48: Normalized production correlated with the Rock Type Ratio (RTR). A strong positive correlation suggests Rock Type 1 is the key rock type controlling the production. The correlation of fit does not include points inside black boxes.

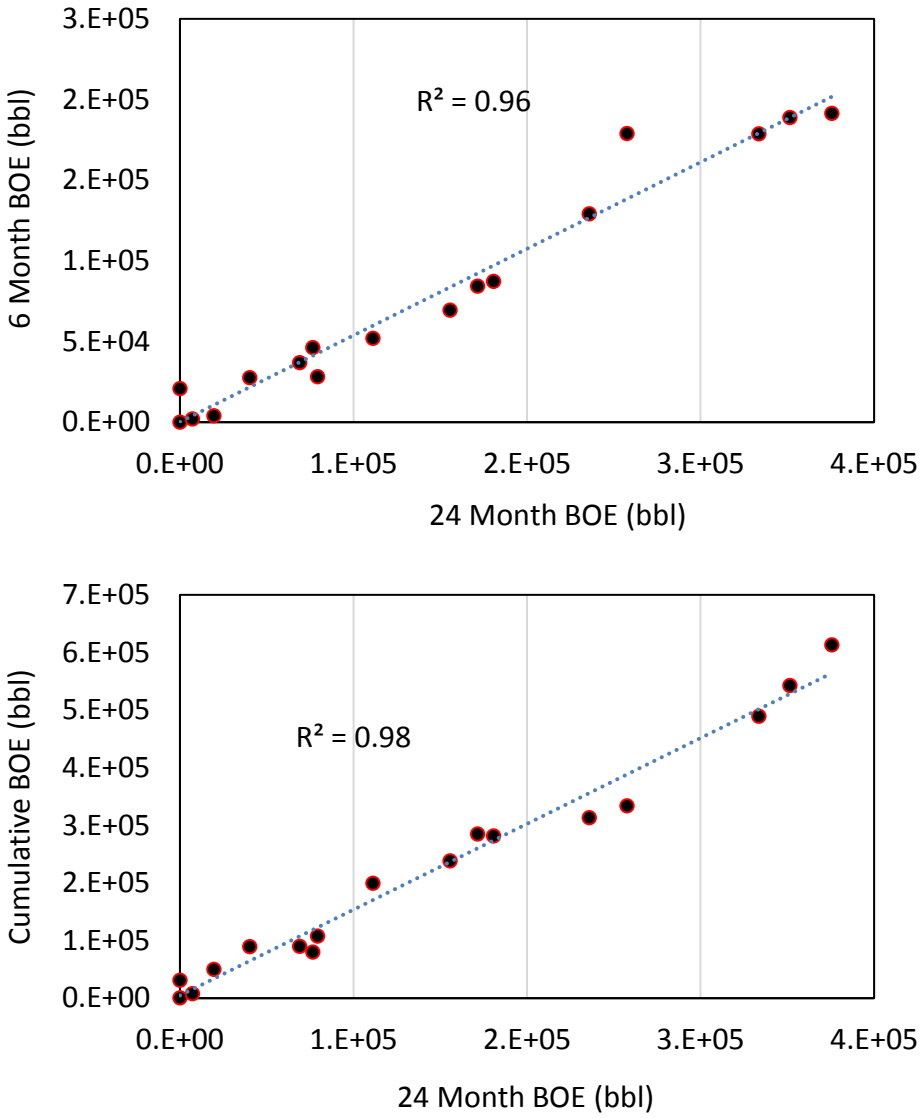

Figure 49: Comparison of different production metrics namely 6 months' BOE, 24 months' BOE and cumulative BOE (average well life 5 years). Very high correlation coefficients between different production metrics suggest that anyone could be used for production correlation.

Chapter 5: Woodford Formation

5.1 Study Area Description

The Woodford formation is a Devonian-Mississippian shale located in the Anadarko, Arkoma and Ardmore basins in Oklahoma and Texas. The Woodford formation extent and distribution is given in Figure 50 (Jarvie 2008, Lantana 2013). It has produced more than 87 MMbbl oil, and 4.6 Tcf gas so far (based on drilling info, checked Dec 16, 2016). It varies in thickness between 150 to 400 ft. (CLR 2010). The depths of Woodford formation vary between 4,800 to 10,000 ft. (CLR 2010). Woodford formation is over-pressured with pressure gradient varying between 0.60-0.65 psi/ft. (CLR 2010).

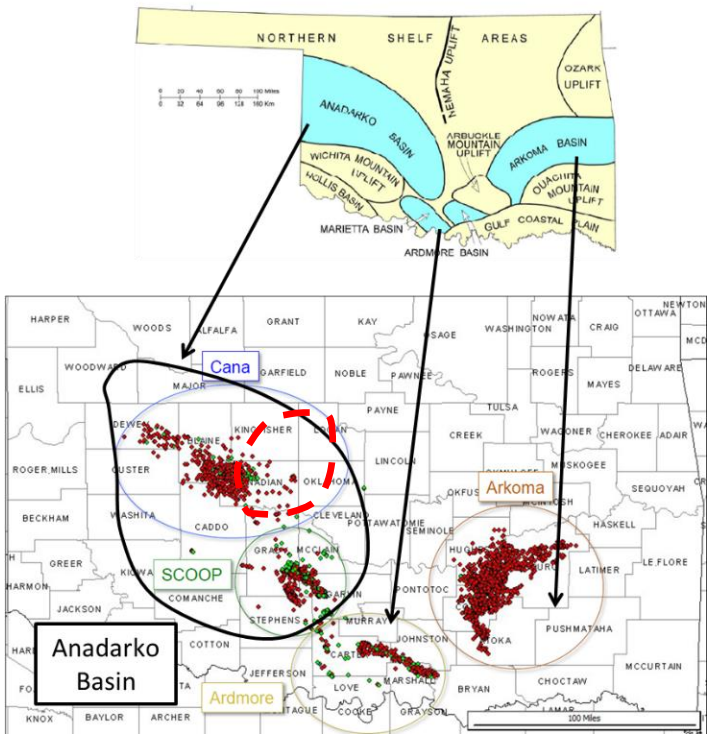

Figure 50: Woodford formation extent with the SCOOP play marked in black and the STACK play marked in red (Jarvie 2008; Lantana 2013)

Woodford formation was deposited in the Devonian, around 360 million years ago, (MYA). It was deposited as organic rich shale in an ancient seaway. The low oxygen environment facilitated preservation of oil prone organic matter. In early Pennsylvanian, plate collision resulted in formation of Anadarko, Ardmore and Arkoma basins. In late Pennsylvanian, there was rapid subsidence and sedimentation. It was during this period that majority of the overlying sandstone reservoirs were deposited. By early Permian, oil generation and migration into overlying conventional reservoirs had started. The entire depositional sequence is shown in Figure 51 (CLR 2010).

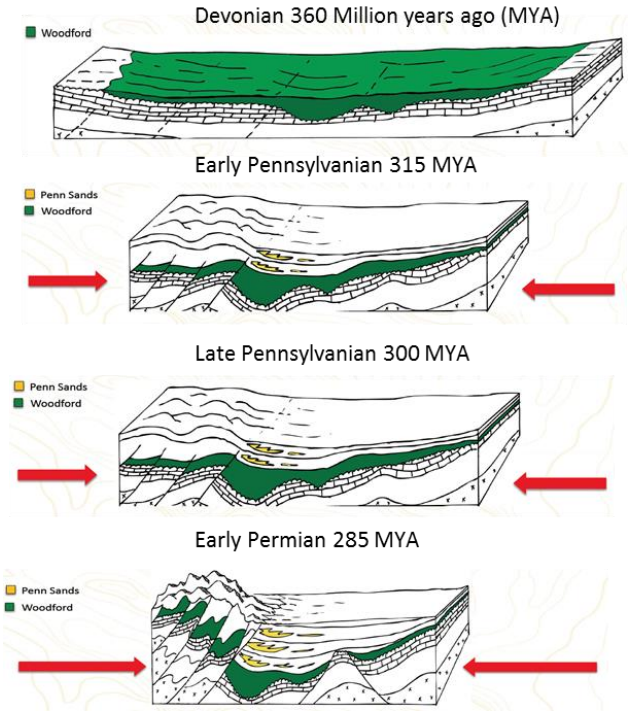

Figure 51: Deposition of Woodford formation (CLR 2010). Woodford was deposited in the Devonian in ancient seaway.

The common lithologies found in Woodford formation are black shale, chert, sandstone, siltstone and dolostone. The most productive lithologies are siliceous and include cherts and cherty black shales. Siliceous formations in Woodford are highly brittle and contain natural fractures. Chert and quartz in Woodford have different

sources and distributions. Quartz is detrital while chert is biogenic and represents siliceous radiolaria. Chert deposits are organic rich and where they are thermally mature, they form optimum exploration targets.

Figure 52 shows the isopach map for Anadarko basin (Caldwell and Johnson 2013). Anadarko basin has thickest Woodford formation among the three basins. Isopach maps for Ardmore and Arkoma basins could not be found in the literature.

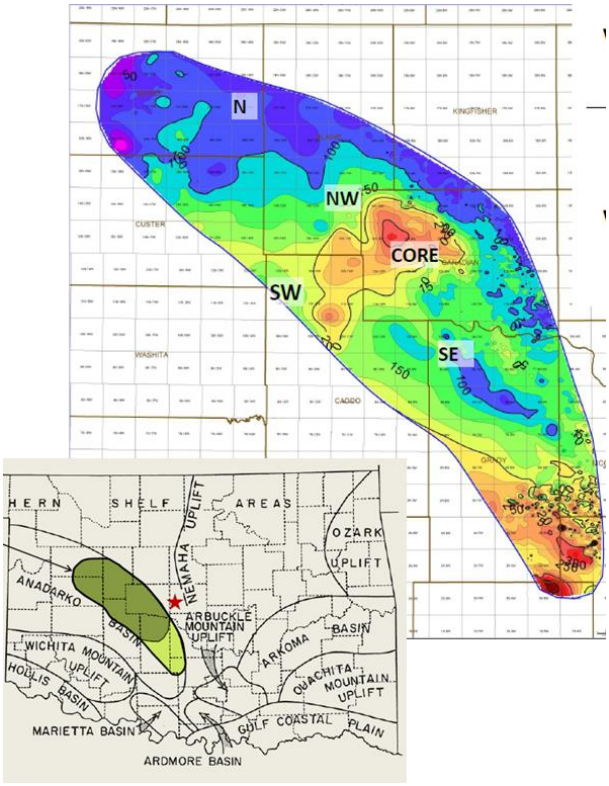

Figure 52: Isopach map for Anadarko basin, Woodford (Caldwell and Johnson 2013).

Figure 53 and Figure 54 show the TOC and vitrinite reflectance map for Woodford formation, respectively (Comer 2005). The TOC map shows that Anadarko basin has the highest TOC and the vitrinite reflectance map shows that Anadarko basin lies in oil maturity window. Thus, Anadarko basin is likely to have the best oil

production in Woodford shale play. South Central Oklahoma Oil Province (SCOOP) and Sooner Trend Anadarko Basin Canadian and Kingfisher Counties (STACK), the most prolific Woodford regions lie in the Anadarko basin.

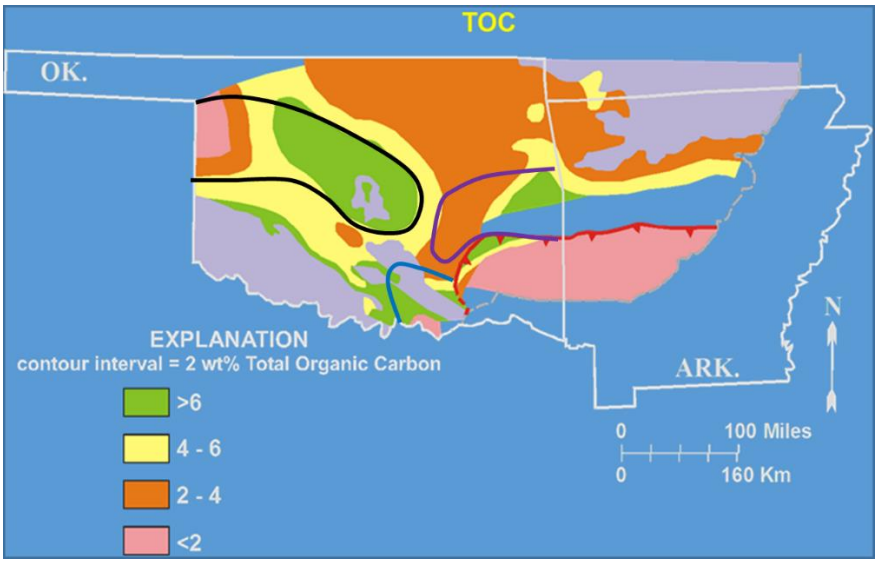

Figure 53: TOC map for Woodford formation. Anadarko basin has the highest TOC among the three basins: Anadarko (outlined as black), Arkoma (outlined as purple) and Ardmore (outlined as blue). (Comer 2005)

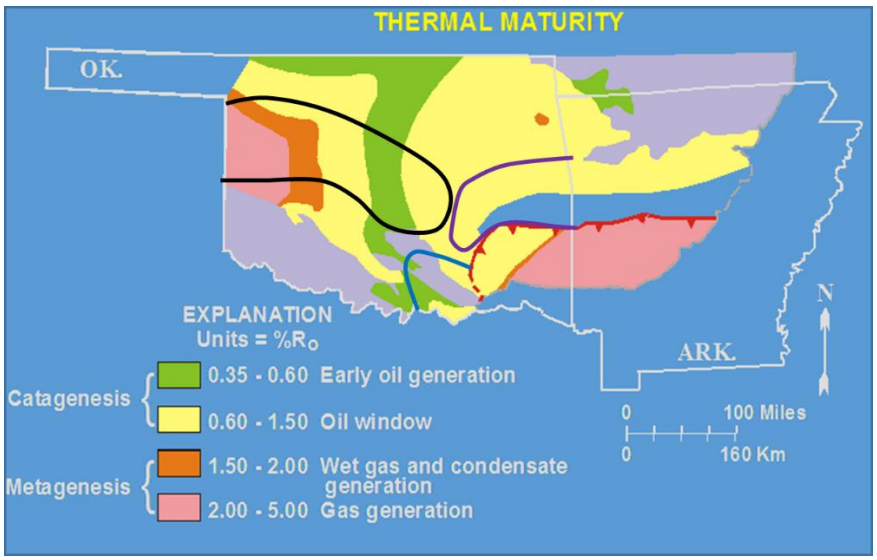

Figure 54: Vitrinite reflectance map for Woodford formation. Majority of the Anadarko (outlined as black) and Arkoma (outlined as purple) basins are in oil maturity window. Ardmore basin (outlined as blue) is comparatively immature (Comer 2005).

Figure 55 shows the cumulative oil production bubble map for Woodford play. It affirms that Anadarko basin has the highest production. This area is characterized by thick shales (Figure 52), high TOC (Figure 53), oil maturity window (Figure 54) and high production (Figure 55). The Anadarko basin is in general a high potential area in the Woodford play. More specifically, SCOOP (South Central Oklahoma Oil Province) and STACK (Sooner Trend Anadarko Basin Canadian and Kingfisher Counties) areas inside Anadarko basin are the sweet spots of Woodford play. The operators are interested in these two areas because of two major reasons. First, they have a relatively higher liquid content compared to rest of the basin and second, the water cut in these regions is very low compared to rest of the basin. A recent ruling in Mar 2016 mandated a reduction in the number of injection wells in several counties of Oklahoma by 40% due to impending danger of induced earthquakes. Thus, with strong regulations against water injection, operators are particularly interested in SCOOP and STACK areas due to their low water cut.

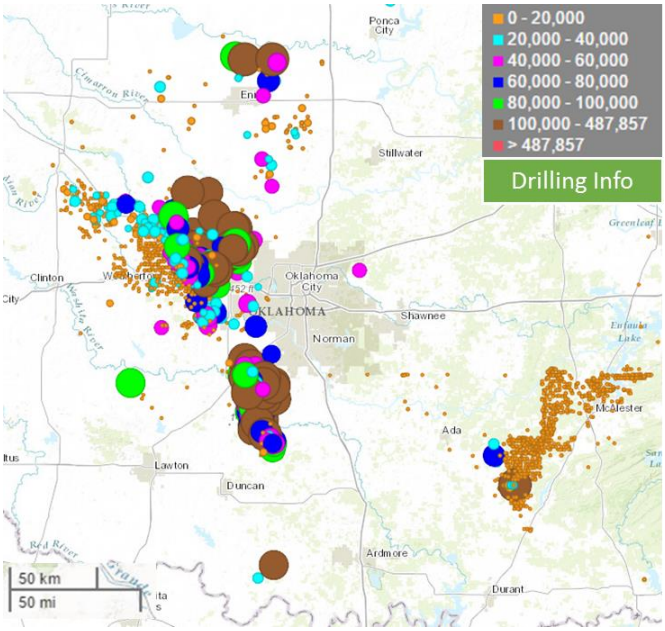

Figure 55: Oil production bubble map for Woodford play.

Figure 56 shows the wells having the core and log data and which were used for rock typing. Seven wells were available which had core data and majority of them were in Anadarko basin. Core data were available for 411 plugs in these 7 wells. Triple combo logs were available in all 7 wells. Thus, gamma ray, resistivity, neutron, and density logs were used for upscaling logs from core to log level.

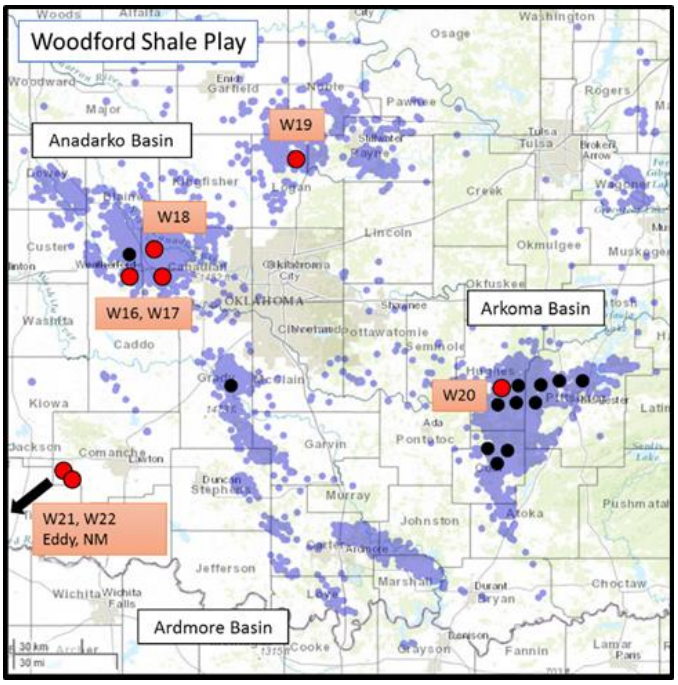

Figure 56: Wells with core and log data for rock typing. 7 wells had core data (shown as red bubbles) and most of which were in Anadarko basin. Core data were available for 411 depth points. Additional 12 wells (shown as black bubbles) had triple combo logs but no core data. Rock type logs were populated in these 12 wells for correlation with production data.

5.2 Core-Derived Rock Typing

The same five petrophysical measurements from core data namely porosity, TOC, clay, quartz, and carbonate content were used for defining rock types in Woodford, as were used in Eagle Ford and Barnett. PCA was done to reduce dimensionality of the clustering problem. Figure 57 shows that the first three principal components explain

more than 90% of the variance in the data. Thus, instead of using 5 variables, it is sufficient to use first three principal components. The optimum number of rock types were defined to be three based on the SSW-SSB method. The results are shown in Figure 58.

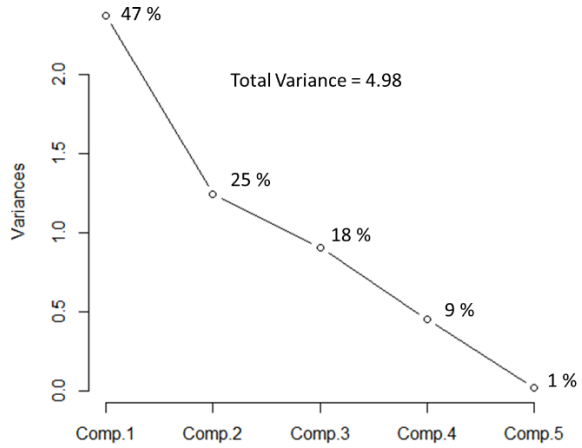

Figure 57: Principal Component Analysis results. The percentage variance explained by each component is listed in the figure. The first three principal components explain more than 90% of the variance in the data.

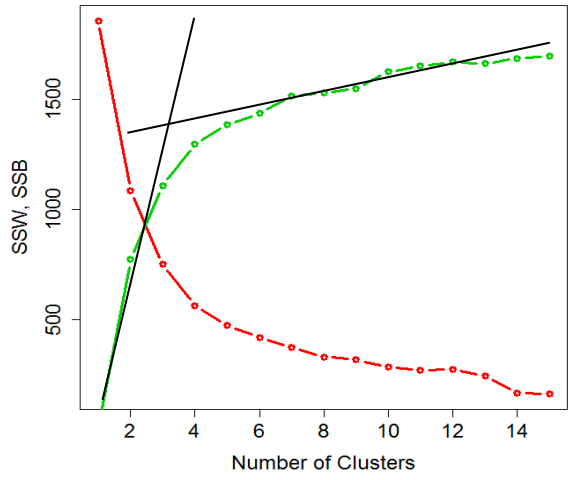

Figure 58: K-Means creates multiple scenarios with different number of clusters. In each case, it identifies the intra-cluster variance (red curve) and inter-cluster variance (green curve). The elbow effect represents change in slope. The elbow effect occurs around 3 clusters which represents the optimum number of clusters.

Next, K-Means and SOM clustering techniques were used to define rock types. Different rock types and their characteristics are shown in Figure 59. The parameters governing storage and source potential for different rock types in Woodford are shown in Figure 60.

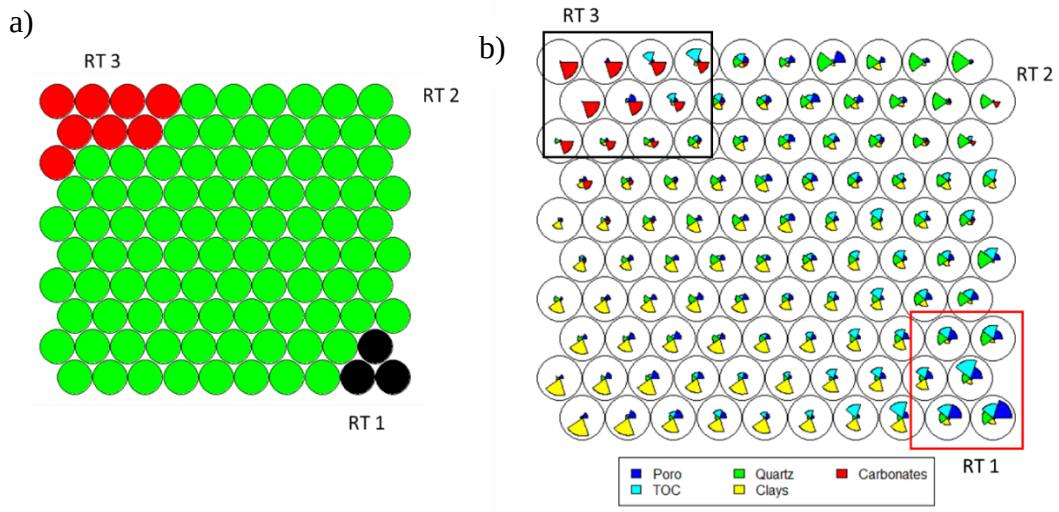

Figure 59: a) Clusters created on a SOM map b) Rose diagram (or pie diagram) shows the petrophysical properties distribution for different rock types/clusters. The size of the pie is proportional to the value of the petrophysical property. Rock Type 1 shows high porosity and TOC while Rock Type 3 shows high carbonates, low porosity, and TOC.

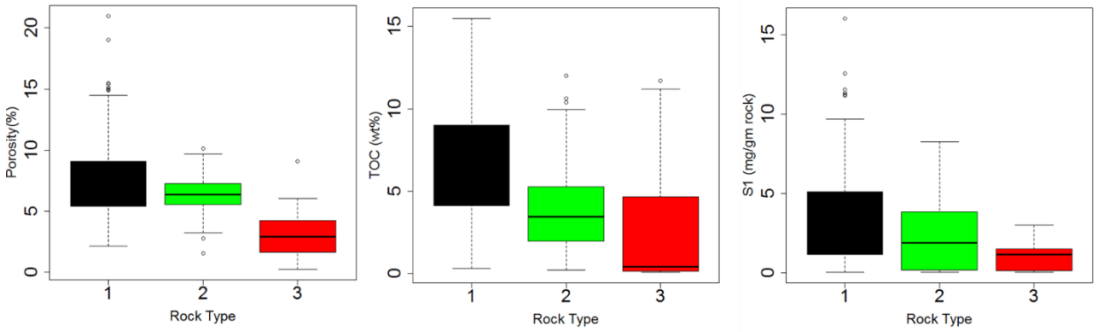

Figure 60: Parameters governing storage and source potential in Woodford. Rock Type 1 has the highest storage and source rock potential.

Rock Type 1 has the highest storage and source potential. The average mineral content for different rock types in Woodford are shown in Figure 61. Rock Type 1 has

high quartz content and is likely the most brittle of the three rock types. Again, it is expected to have the largest impact on production.

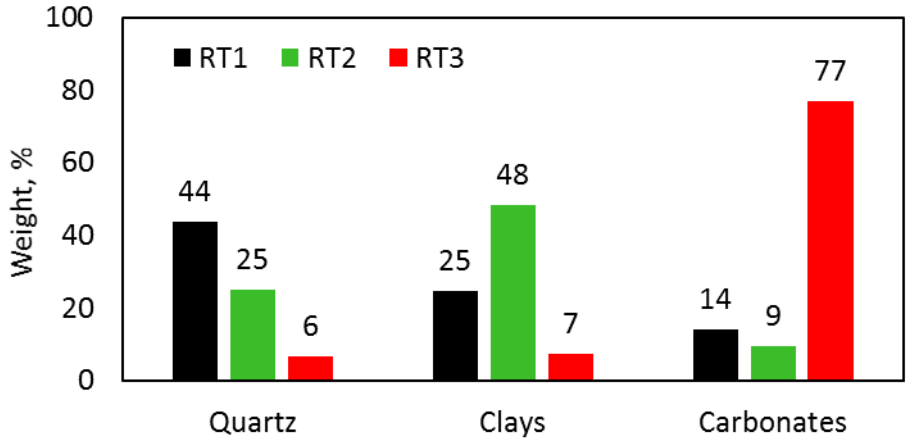

Figure 61: Average mineral content for different rock types in Woodford. Rock Type 1 has high quartz content. It is more brittle compared to other two rock types. Rock Type 2 has the highest clay percentage and is the most ductile of the three rock types.

Mercury injection capillary pressure data were also available for 112 core depths. Incremental and cumulative Hg intrusion plots, normalized by helium pore volume, for the three rock types are shown in Figure 62.

In Rock Type 1 samples, the cumulative intrusion plot shows that the ratio of mercury to helium volume varies between 0.65 to 0.80. In Rock Type 2 samples, this ratio varies between 0.50 to 0.65 and it varies between 0.40 to 0.55 for Rock Type 3 samples. This shows the connected pore volume decreases as we go from Rock Type 1 to Rock Type 2 and Rock Type 3.

In Rock Type 3 samples, the incremental intrusion curve increases monotonically without reaching a plateau or an inflection point even at 60,000 psia. Rock type 3 samples were very tight, characterized by high carbonate percentage and a higher grain density.

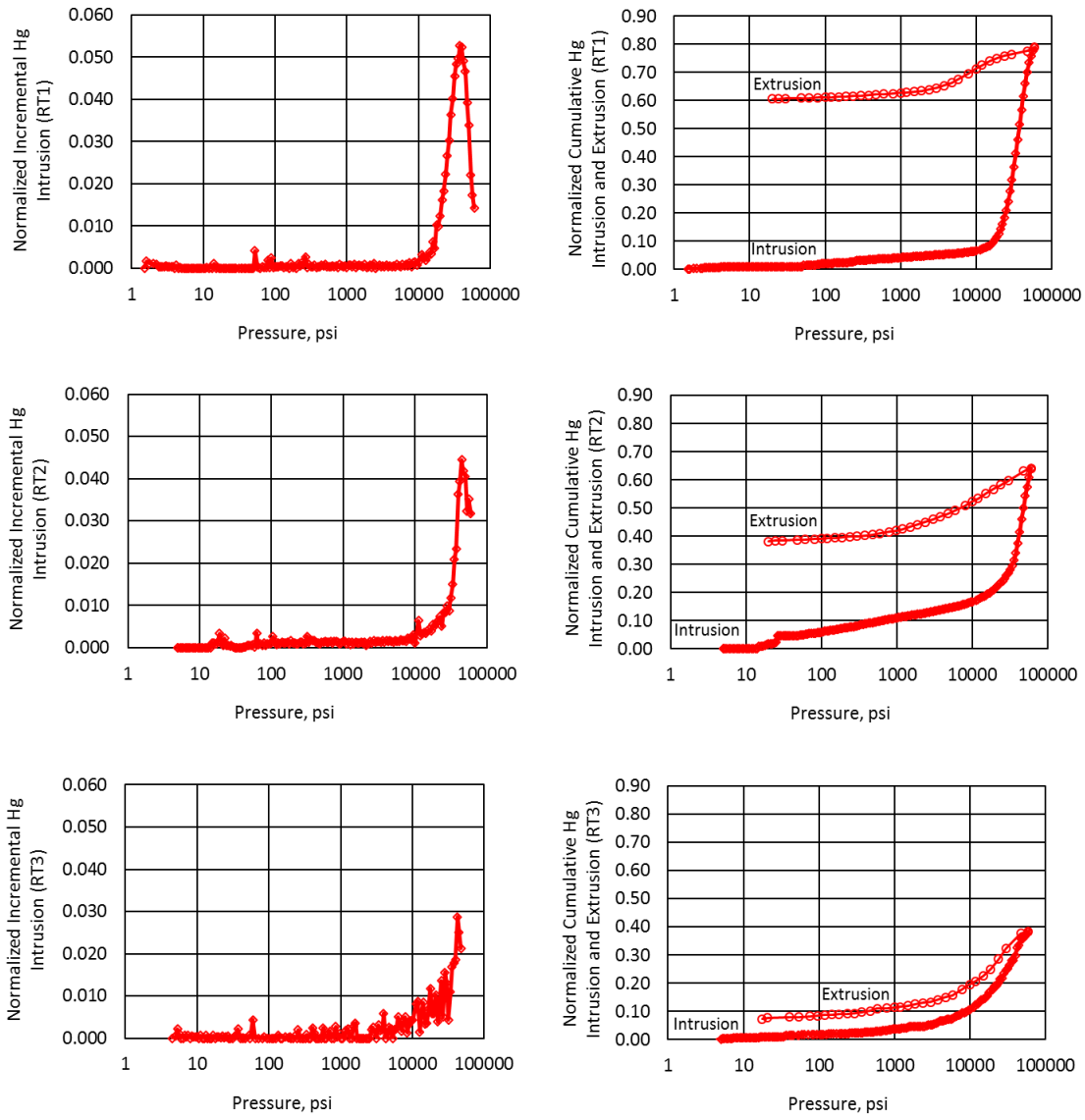

Figure 62: Representative normalized incremental and cumulative mercury intrusion plots for the three rock types. Rock Type 1 has the highest dominant pore throat size and highest connected volume. On the other end, Rock Type 3 shows signs of false intrusion and has lowest connected volume.

The cumulative intrusion plots in both Rock Type 1 and Rock Type 2 exhibit considerable hysteresis between saturating and desaturating curves, implying real Hg intrusion into the sample. The almost overlapping saturating and desaturating curves in Rock Type 3 may be indicative of false intrusion. The average dominant pore throat

size is 6 nm for Rock Type 1 samples, while for Rock Type 2 samples, it is 4 nm. Thus, Rock Type 1 samples have the highest permeability. Rock Type 2 samples may be effected by presence of higher clay fraction.

5.3 Extending Core-Based Classification to Well Logs

In the Woodford, triple combo logs were available for all the seven wells that had core data. Again, the logs were only available for vertical pilot holes and thus, there was an inherent assumption that properties do change as you go away from wellbore. The gamma ray, neutron, density, and resistivity logs were used for upscaling. Figure 63 shows the distribution of gamma ray, neutron porosity and density logs for different rock types. The logs were consistent with the core data and were found adequate for upscaling the rock types.

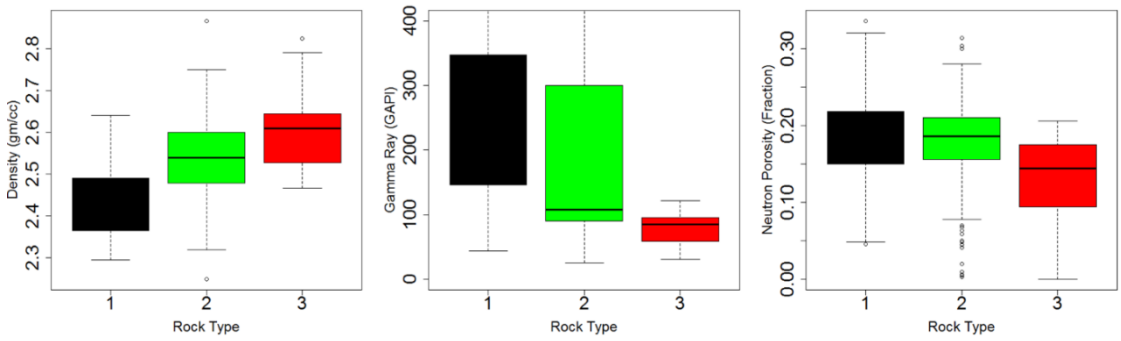

Figure 63: Gamma ray, density, and neutron logs distribution for different rock types in Woodford. Rock Type 1 has low density, high gamma ray and high neutron porosity consistent with high TOC and high lab measured porosity. Rock Type 3, on the other hand, has highest density and lowest neutron porosity consistent with high carbonates in lab measured mineralogy.

To do the upscaling, following the same procedure as in Eagle Ford and Barnett, log data were extracted corresponding to depths where core data were available. The trained the SVM model was used to predict rock types in uncored wells and remaining

section of the cored wells where core data were not available. Figure 64 shows the rock type logs for two sample wells (W16 on left, W18 on right). The rock type logs for the remaining wells are given in Appendix C.

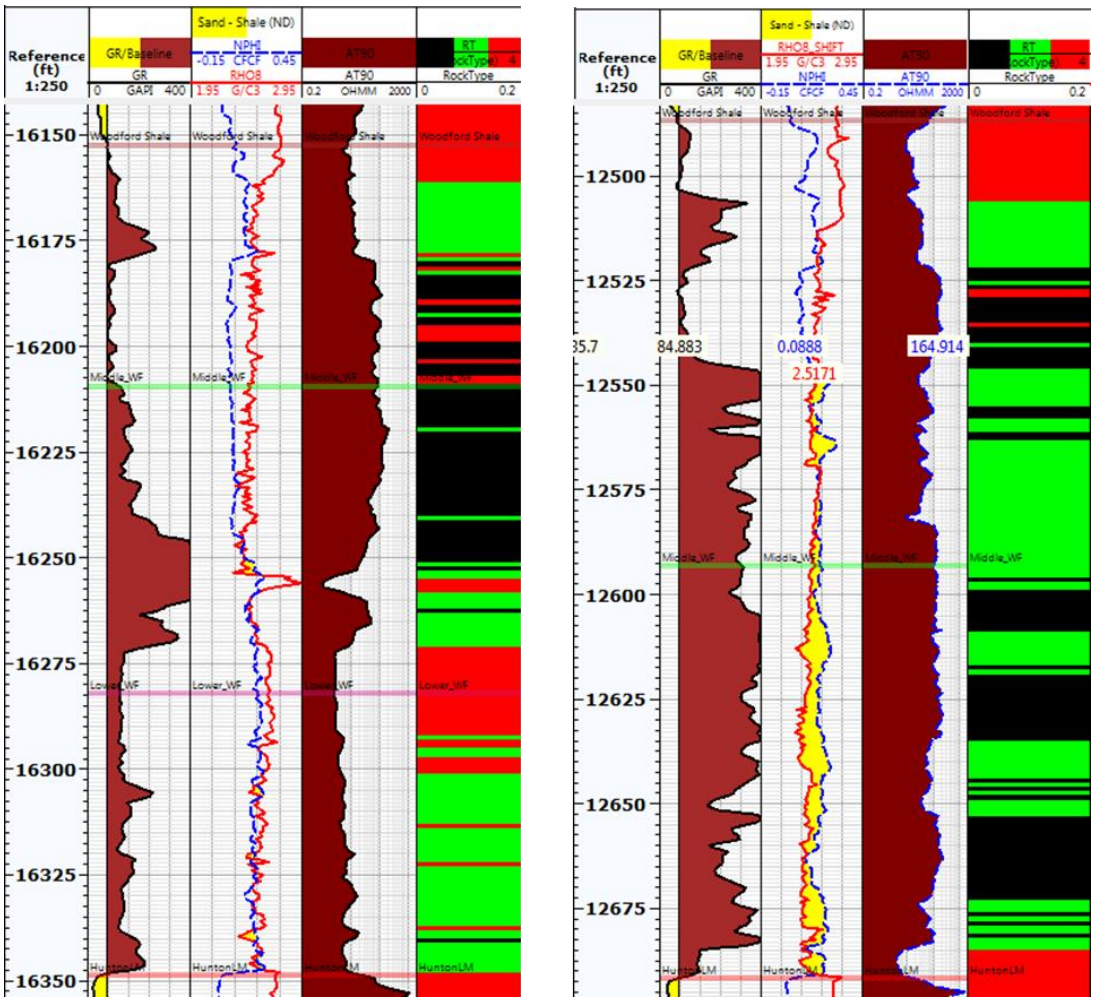

Figure 64: Rock type logs (track 4; black=Rock Type 1, green=Rock Type 2, and red=Rock Type 3) for two sample wells (W16 on left, W18 on right) from the Woodford formation.

The quality of populated rock type logs was checked and the robustness of the SVM algorithm was assessed. Since, the triple combo logs were available for all seven wells, porosity and TOC logs were modelled using resistivity, gamma ray, neutron, and

density logs. The triple combo logs and calculated porosity and TOC logs for Well 16 and Well 18 are given in Figure 65.

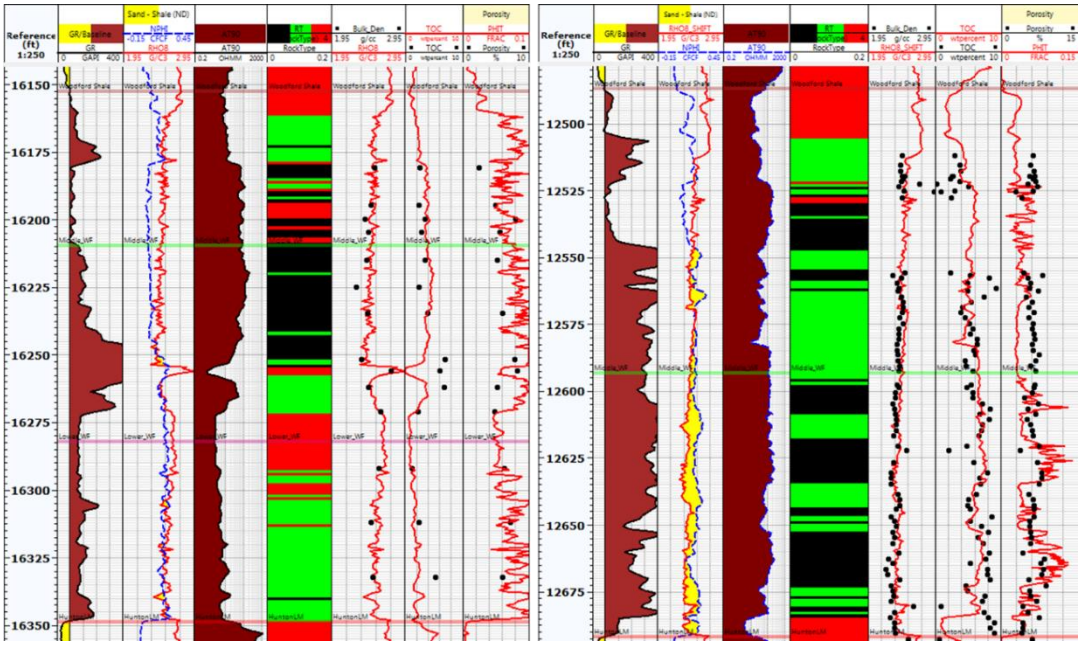

Figure 65: Calculated logs (rock types in track 4; black=Rock Type 1, green=Rock Type 2, and red=Rock Type 3) namely porosity and TOC logs for two sample wells (Well 16 on left, W18 on right). The red curve represents the modelled curves. The black filled circles represent the core measurements that were used for calibration.

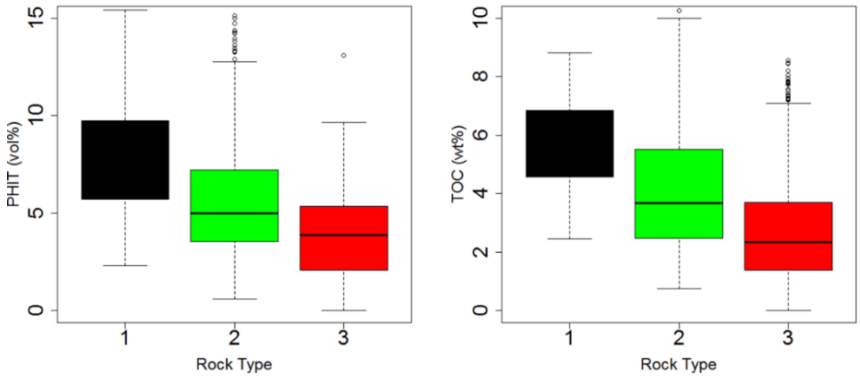

Figure 66: Box plots showing distribution of calculated TOC and porosity logs based on populated rock type log. The distributions reassert the conclusions based on core derived rock types.

Box plots (Figure 64) were created to show the distribution of calculated TOC and porosity based on the rock type log. The results reassert the conclusion based on

core derived rock types (Figure 60). Rock Type 1 has the highest source rock and storage potential followed by Rock Type 2 and Rock Type 3. This cross-check validates the rock type upscaling method and lends credibility to further analysis with production data.

5.4 Relating rock types to Production Data

Same exercise was carried in Woodford wells. Figure 56 shows the location of the wells. Some of the wells were horizontal, some were vertical. Figure 67 shows the comparison of RTR with normalized production. Vertical well production was normalized by zone thickness and horizontal well production by lateral length. A positive correlation between normalized production and RTR is evident.

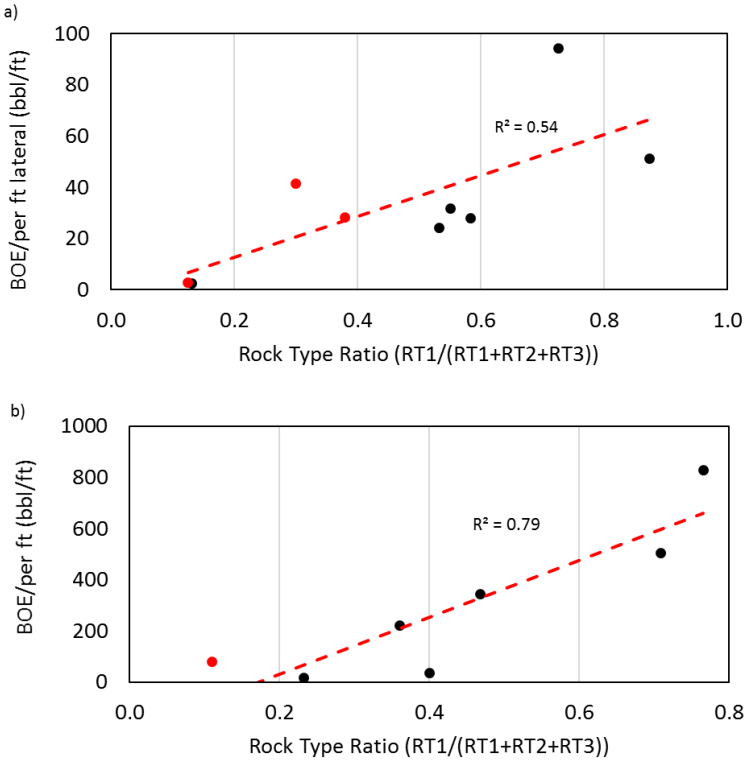

Figure 67: Normalized production correlated with the Rock Type Ratio (RTR). a) Correlation plot for horizontal wells. b) Correlation plot for vertical wells. A positive correlation on both the plots suggests that Rock Type 1 is the key rock type controlling the production.

Comparison of different production metrics namely 12 months' BOE, 24 months' BOE and cumulative BOE (average well life 7 years) is shown in Figure 68. Very high correlation coefficients between different production metrics suggest that anyone could be used for production correlation.

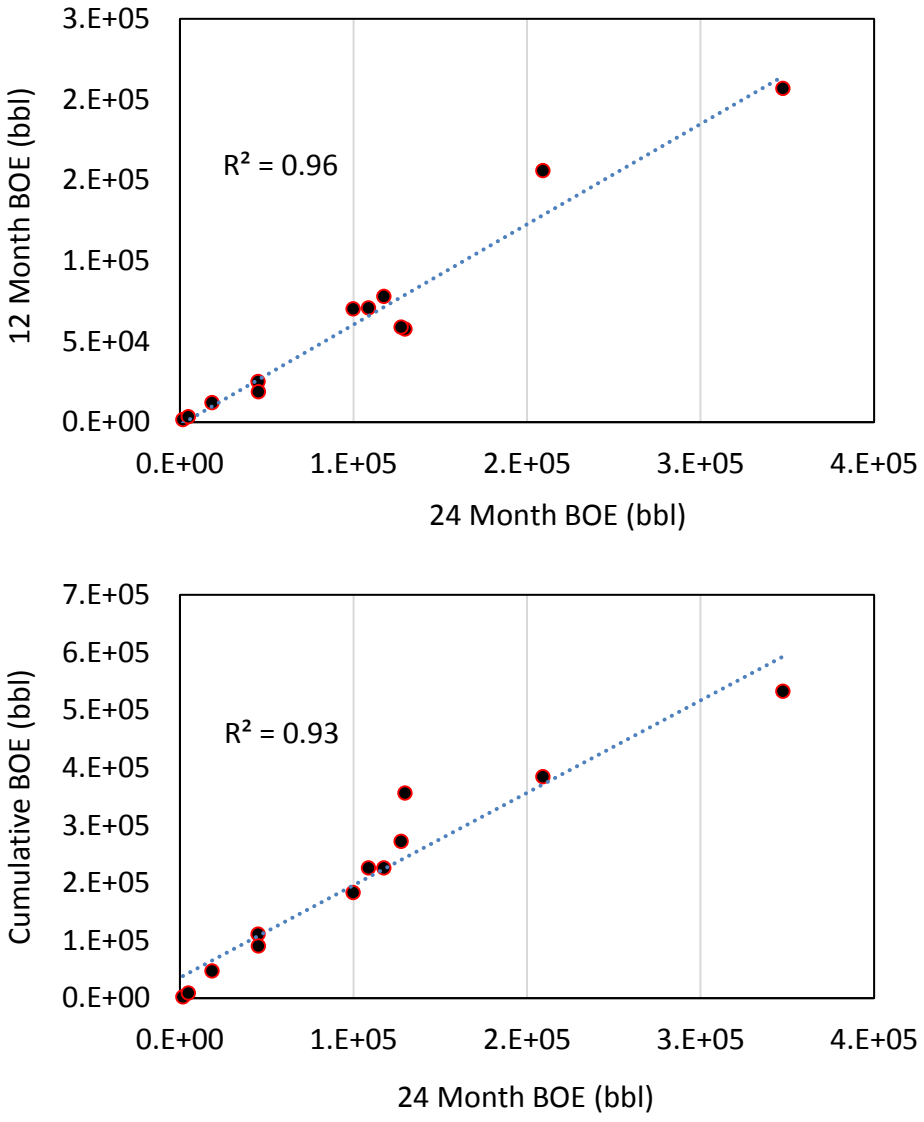

Figure 68: Comparison of different production metrics namely 12 months' BOE, 24 months' BOE and cumulative BOE (average well life 7 years). Very high correlation coefficients between different production metrics suggest that anyone could be used for production correlation.

Chapter 6: Wolfcamp Formation

6.1 Study Area Description

The Wolfcamp formation is mainly located in the Permian basin in Texas and New Mexico. It is a late Cretaceous shale. It has produced more than 962 million barrels oil, and 4.2 Tcf gas so far (based on drilling info, checked Dec 16, 2016). The average thickness is around 2000 ft. (Wilson et al. 2016). The depths of Wolfcamp formation range from 5,500 to 11,000 ft. (Pioneer 2013). Wolfcamp is over-pressured with pressure gradient varying between 0.55-0.70 psi/ft. (Pioneer 2013). Figure 69 shows the Wolfcamp shale play (Cortez 2012).

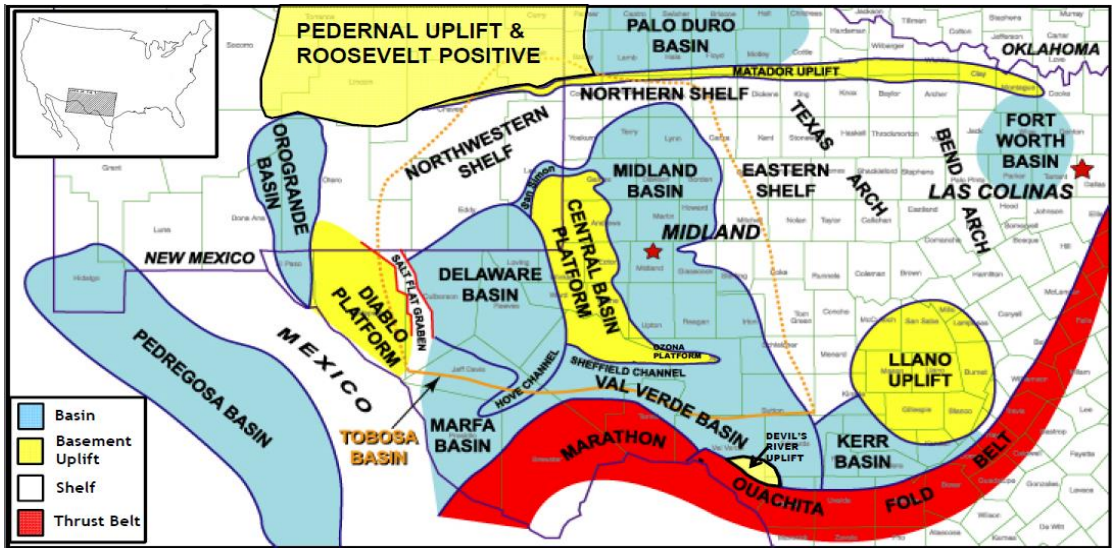

Figure 69: Major basins in the Texas and New Mexico areas (Pioneer 2014). The two major basins namely Delaware and Midland together form Permian basin. The Wolfcamp formation in the Permian basin forms the Wolfcamp shale play (Cortez 2012).

The Permian basin is an asymmetric basin. It underwent active subsidence and increased levels of shale, limestone, and arkosic sand deposition from Mississippian to early Permian time (Heckel 1986). Intricate faulting and differential rates of subsidence

produced several sub-basins namely the Delaware basin, the Central basin platform and the Midland basin. The area is marked by extreme stratigraphic discontinuity which has been a major concern for the oil and gas operators in this region. Figure 70 shows the stratigraphic column and Figure 71 shows the regional cross-section (Cortez 2012). In the Delaware basin, Wolfcamp formation is being targeted with horizontal wells and is commingled with Bone Spring sands. In the Midland basin, the combination of Wolfcamp and Spraberry is being exploited.

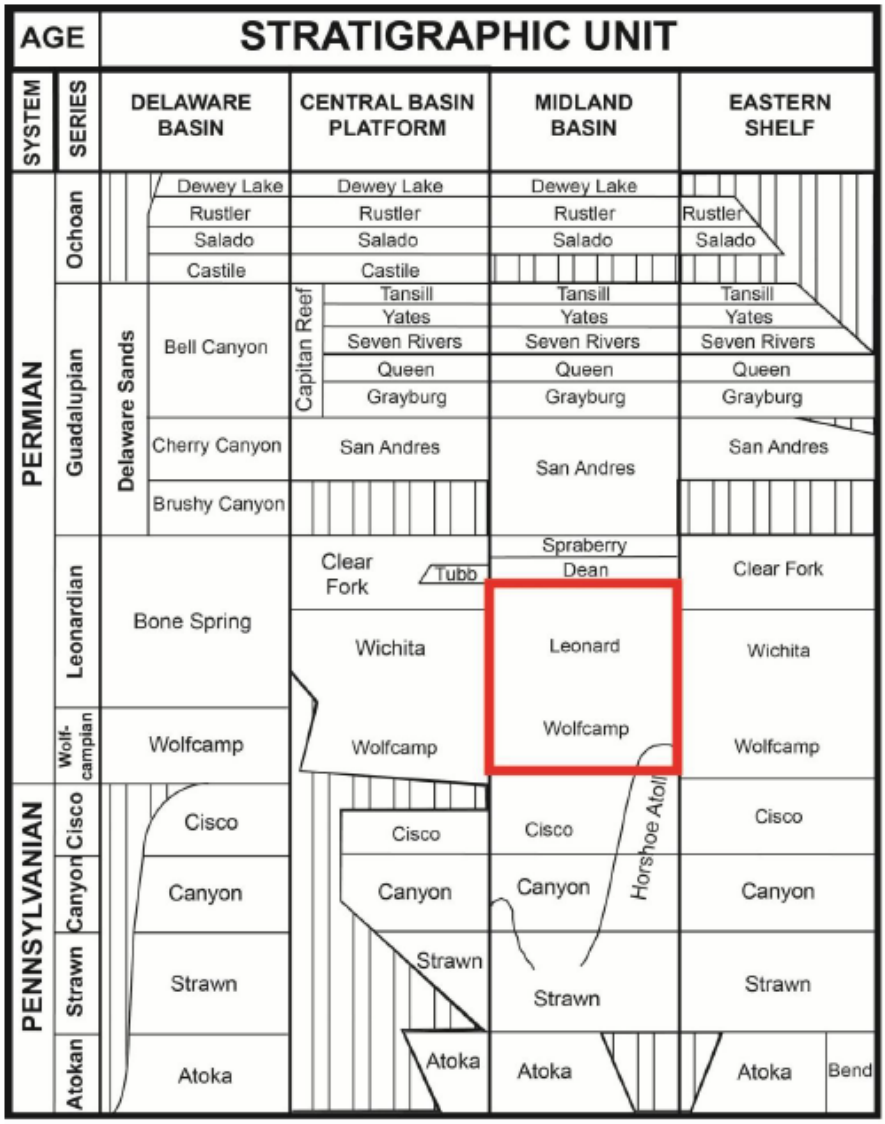

Figure 70: Stratigraphic column of the Permian Basin (Cortez 2012).

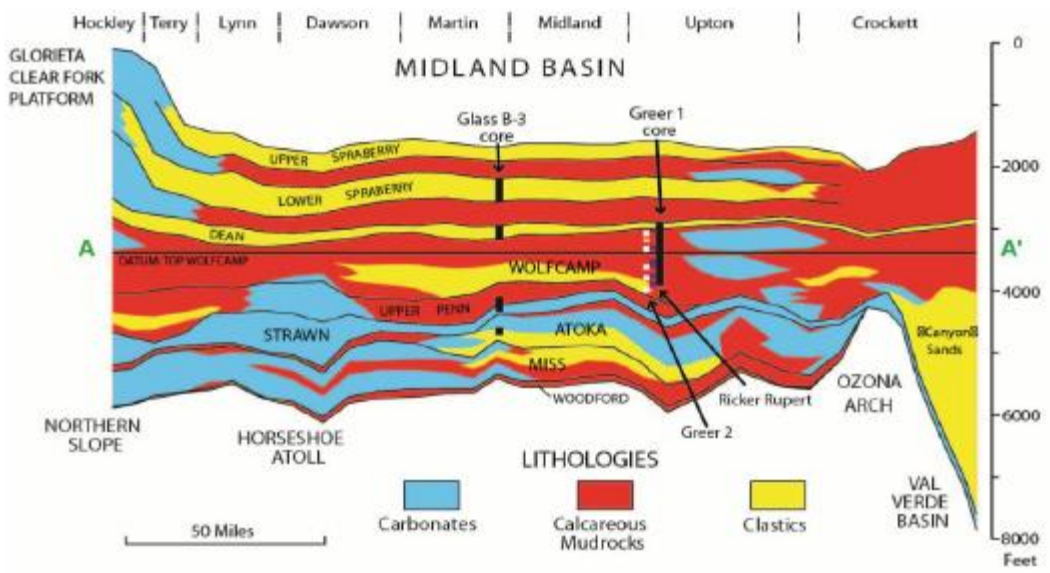

Figure 71: The regional cross-section A-A' showing stratigraphy and lithology across the Permian basin (Cortez 2012).

Lower Permian (Wolfcamp and Leonard shales) in Midland basin were deposited in an intra-cratonic deep water basin surrounded by shallower carbonate platforms (Hamlin and Baumgardner 2012). The depositional systems alternated between siliclastic, turbidite systems to hemipelagic, calcareous systems. The sediment transport to the basin was controlled by changes in sea-level. During high stand, platforms were submerged and acted as carbonate factories. The sediment influx to the basin was mainly carbonate derived from the platforms and hemipelagic clay and silt. On the contrary, during low stand, carbonate platforms were exposed and sediment influx to the basin comprised of siliclastic sediments.

The lithologic description of Wolfcamp formation in Midland basin is given by Cortez (2012). He identified four different facies from core descriptions. They were namely siliceous mudrock, calcareous mudrock, muddy carbonate-clast conglomerates and skeletal grainstone. Siliceous mudrock has an average clay content of 40%. The

clay type is mainly illite. The remaining mineralogy consists of carbonate, quartz, feldspar, pyrite, and apatite. Carbonate content is generally less than 20 wt.%. Calcareous mudrock are like siliceous mudrock but are a shade lighter due to increased carbonate content (>20 wt.%). These rocks are also organically less rich compared to siliceous mudrock. Muddy conglomerates were deposited as debris flows and have a very high carbonate content (~ 62 wt.%). Lastly, skeletal grainstone are turbidite deposits. These rocks have little clay (~ 8 wt.%) and low TOC. These rocks contain significant amount of diagenetic quartz which can exceed 50 wt.% (Cortez 2012).

The first two facies namely the siliceous mudrock and calcareous mudrock are the dominant facies. They have few sedimentary structures and high TOC compared to the other two facies. TOC varies inversely with carbonates as carbonates are detrital and non-biogenic (Hamlin and Baumgardner 2012).

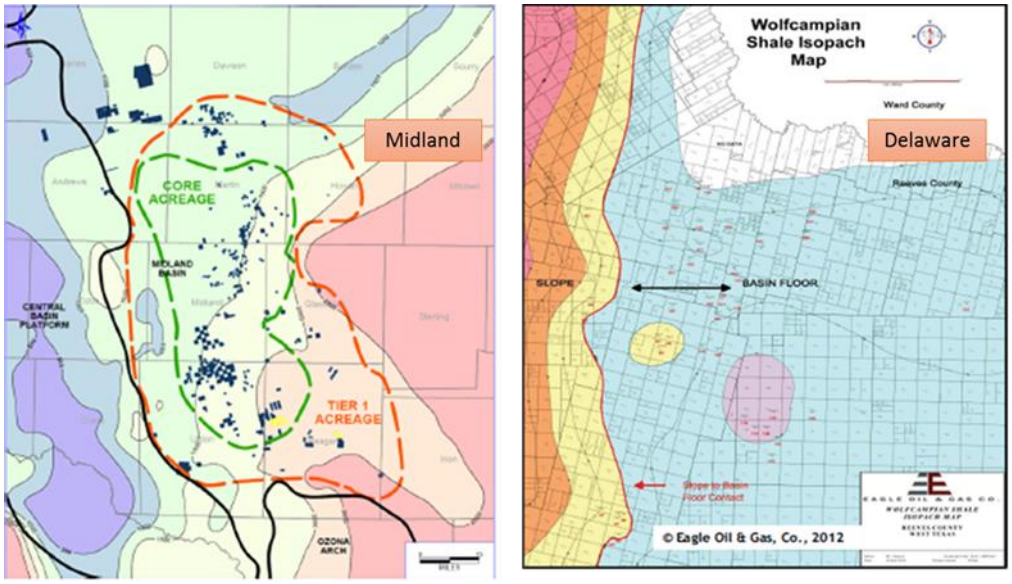

Figure 72: (Left) Isopach map for Wolfcamp in Midland basin. The polygon marked by green dashed curve represents thickest Wolfcamp formation in Midland basin. (Right) Isopach map for Wolfcamp in the Delaware basin. Orange and yellow shaded areas have thicker Wolfcamp compared to the blue shaded area (Parsley 2014).

Figure 72 shows the isopach maps for Wolfcamp formation in the Permian basin (Parsley 2014). The maps show that western part of the Delaware basin and central region of the Midland basin have the thickest Wolfcamp formation. Figure 73 shows the vitrinite reflectance map for Wolfcamp formation (Holmes and Dolan 2014). It is evident that Delaware basin may be partly gas prone while Midland basin is entirely oil prone.

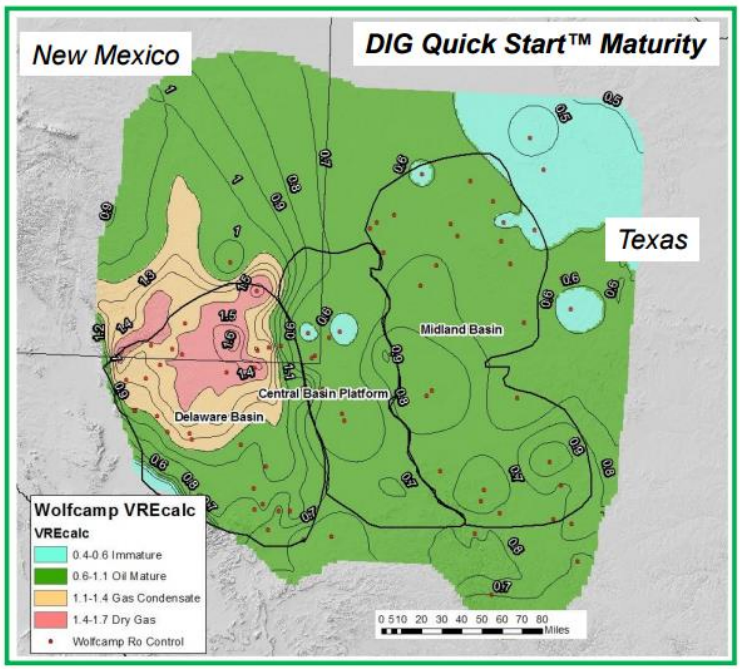

Figure 73: Vitrinite reflectance map for Wolfcamp formation (Holmes and Dolan 2014). It shows that part of Delaware basin is in gas/condensate maturity region while Midland basin is entirely in oil maturity region.

Figure 74 shows the oil and gas production bubble maps for Wolfcamp formation. The oil bubble plot shows that the highest oil production occurs in Midland Basin which lies in the oil maturity window (Figure 73). This area lies in the core area that is thickest part of the Midland Basin (Figure 72 Left). The gas bubble plot indicates that majority of the gas production is limited to Delaware basin which is in the gas

maturity window (Figure 73). The production is highest in the western part of the basin which is thickest part of the Delaware basin (Figure 72 Right). Thus, the isopach map, vitrinite reflectance map and production data map, are consistent with each other and can be used to determine the sweet spots in the Wolfcamp shale play.

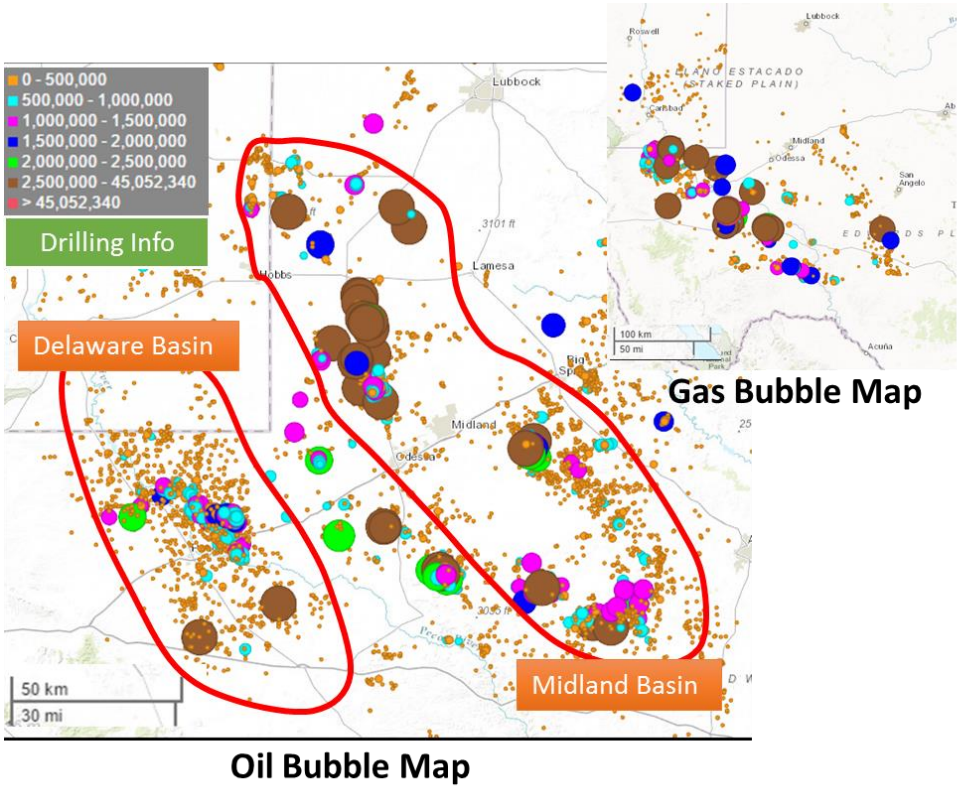

Figure 74: Oil and gas production bubble maps for Wolfcamp formation. The oil bubble plot shows that the highest oil production occurs in Midland Basin which lies in the oil maturity window (Figure 70). The gas bubble plot indicates that majority of the gas production is limited to Delaware basin which is in the gas maturity window (Figure 70).

Figure 75 shows the wells having the core and log data which were used for rock typing. Three wells were available all of which were in the Midland basin. Core data were available for 212 plugs in these 3 wells. Only gamma ray and neutron porosity logs were available in all the three wells. Thus, these two logs were used for upscaling rock types from core to log level.

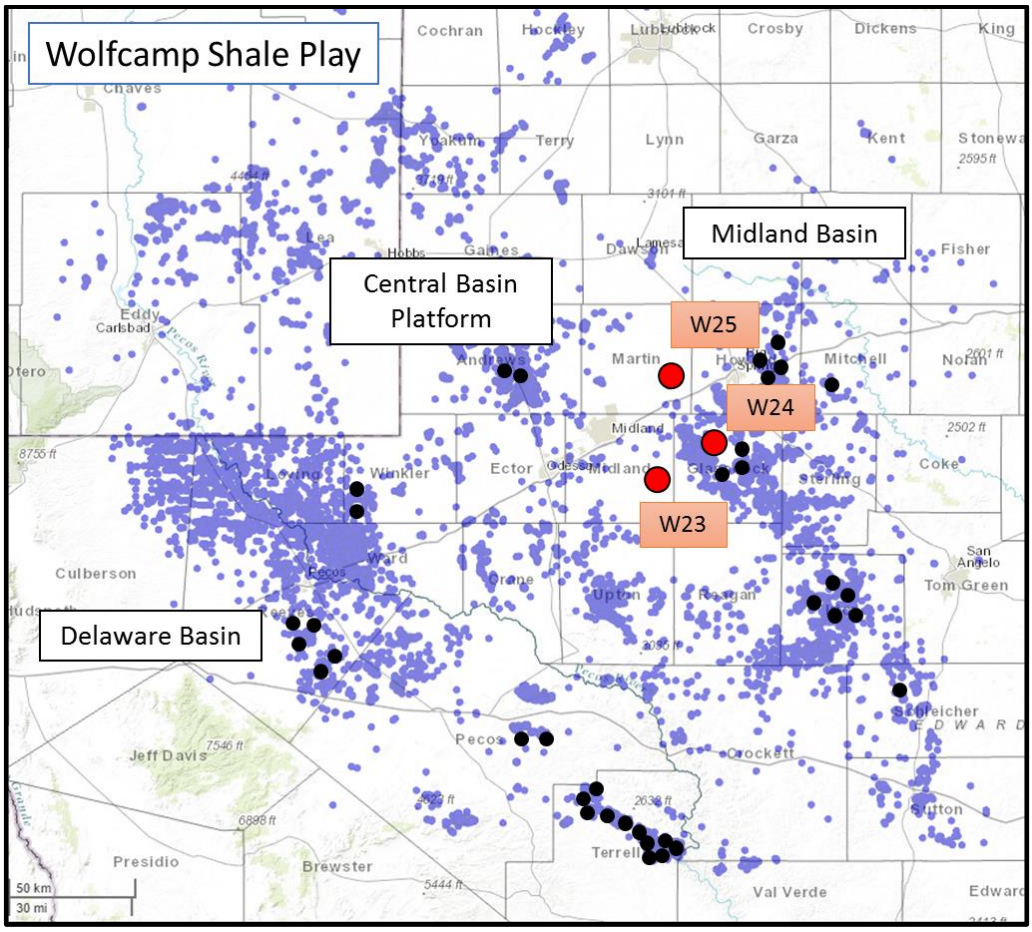

Figure 75: Wells with core and log data for rock typing. 3 wells had core data (shown as red bubbles) and all of them are in Midland Basin. Core data were available for 212 depth points. Additional 39 wells (shown as black bubbles) had logs but no core data. Rock type logs were populated in these 39 wells for correlation with production data.

6.2 Core-Derived Rock Typing

Six petrophysical measurements from core data namely porosity, TOC, V_p/V_s, clay, quartz, and carbonate content were used for defining rock types in Wolfcamp. PCA was done to reduce dimensionality of the clustering problem. Figure 76 shows that the first three principal components explain more than 86% of the variance in the data. Thus, instead of using 6 variables, it is sufficient to use first three principal components.

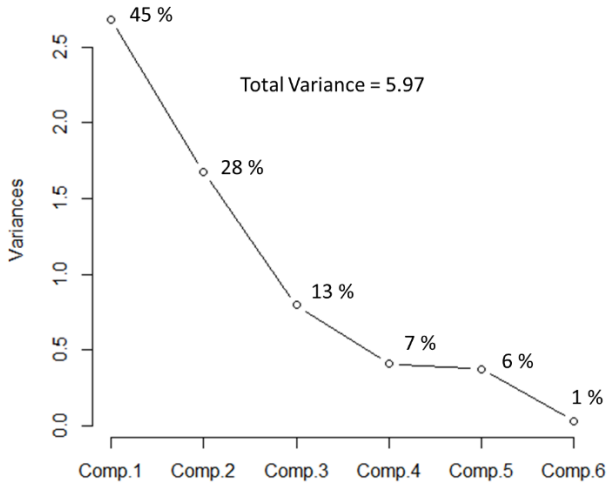

Figure 76: Principal Component Analysis results. The percentage variance explained by each component is listed in the figure. The first three principal components explain more than 86% of the variance in the data.

The optimum number of rock types were defined to be three based on the SSW-SSB method. The results are shown in Figure 77. K-Means and SOM clustering techniques were used to define rock types. Different rock types and their characteristics are shown in Figure 78.

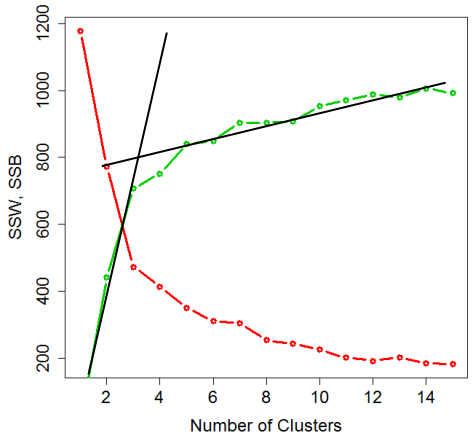

Figure 77: SSW-SSB plot. The elbow effect occurs around 3 clusters which represents the optimum number of clusters.

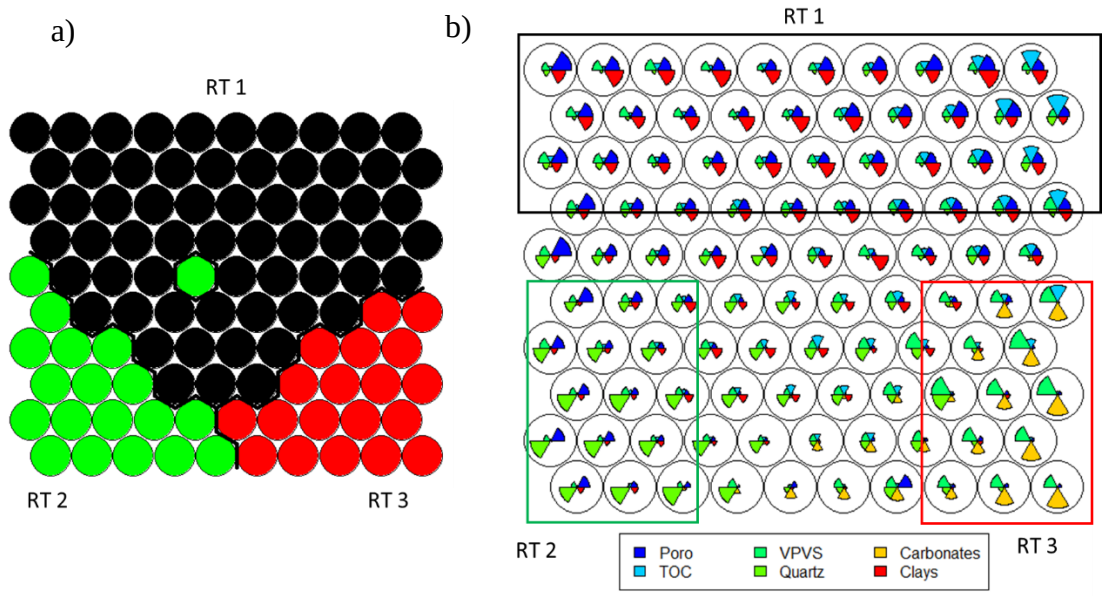

Figure 78: a) Clusters created on a SOM map b) Rose diagram (or pie diagram) shows the petrophysical properties distribution for different rock types/clusters. Rock Type 1 shows high porosity, high TOC, and high clay fraction while Rock Type 3 shows high carbonates, low porosity, and low TOC.

The parameters governing storage and source potential for different rock types in Wolfcamp are shown in Figure 79. Rock Type 1 has the highest porosity, TOC and S1 values. Based on Figure 79, Rock Type 1 has the highest storage and source potential followed by Rock Type 2 and then Rock Type 3. The average mineral content for different rock types in Wolfcamp are shown in Figure 80. Rock Type 1 has high clay content and is likely the most ductile of the three rock types.

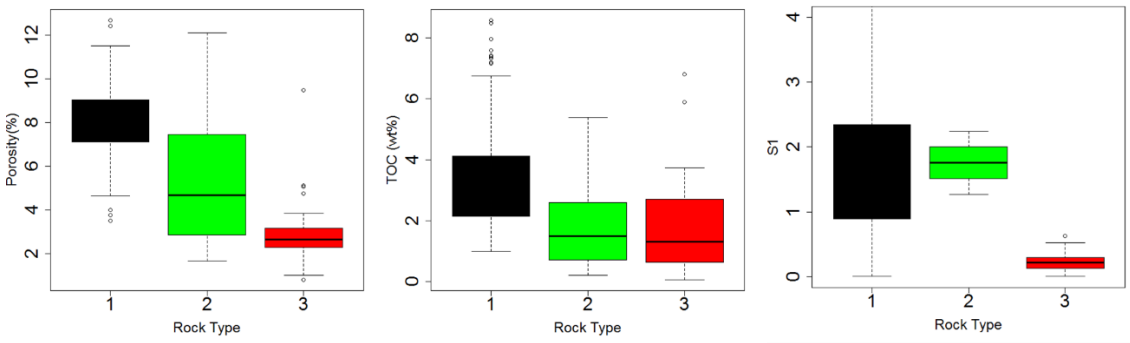

Figure 79: Parameters governing storage and source potential in Wolfcamp. Again, Rock Type 1 has the highest storage and source rock potential.

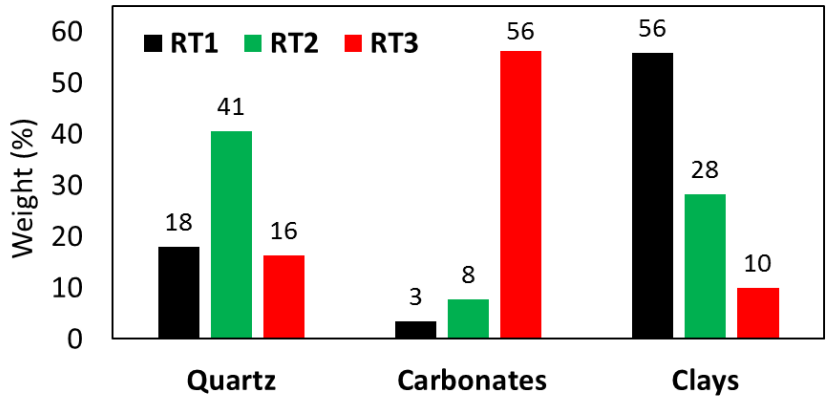

Figure 80: Average mineral content for different rock types in Wolfcamp. Rock Type 2 has high quartz content. It is more brittle compared to other two rock types. Rock Type 1 has the highest clay percentage and is thought to be the most ductile of the three rock types.

Rock Type 2 has the highest quartz percentage. This suggests that Rock Type 2 is very brittle and can fracture easily. Rock Type 2 may play a key role in governing fracture growth and initiation. Wells having higher proportion of Rock Type 2 may need smaller and farther spaced perforations compared to wells that lack Rock Type 2. This behavior is different from previous shale plays where the most productive rock type was also the most brittle, based on mineralogy data.

Ultrasonic measurements can also be used to infer brittleness. Compressional wave velocity (V_p), shear wave velocity (V_s) and bulk density (ρ) can be used to calculate Poisson's ratio (υ) and Young's modulus (E) using following formulas.

$$v = 0.5 * \left[\frac{\left(\frac{V_p}{V_s}\right)^2 - 2}{\left(\frac{V_p}{V_s}\right)^2 - 1}\right]$$

$$E = \frac{\rho v_s^2 * (3v_p^2 - 4v_s^2)}{v_p^2 - v_s^2}$$

The assumption in the above calculations is that rock is isotropic. However, it is well known that shales are anisotropic and thus, above calculations may not be representative of the actual rock. To validate the calculations, Young's modulus values calculated from ultrasonic measurements were compared to actual Young's modulus measurements made on the rock samples using nano-indentation. The comparison between the two is shown in Figure 81. The figure shows that ultrasonic measurements can be used to predict representative rock properties.

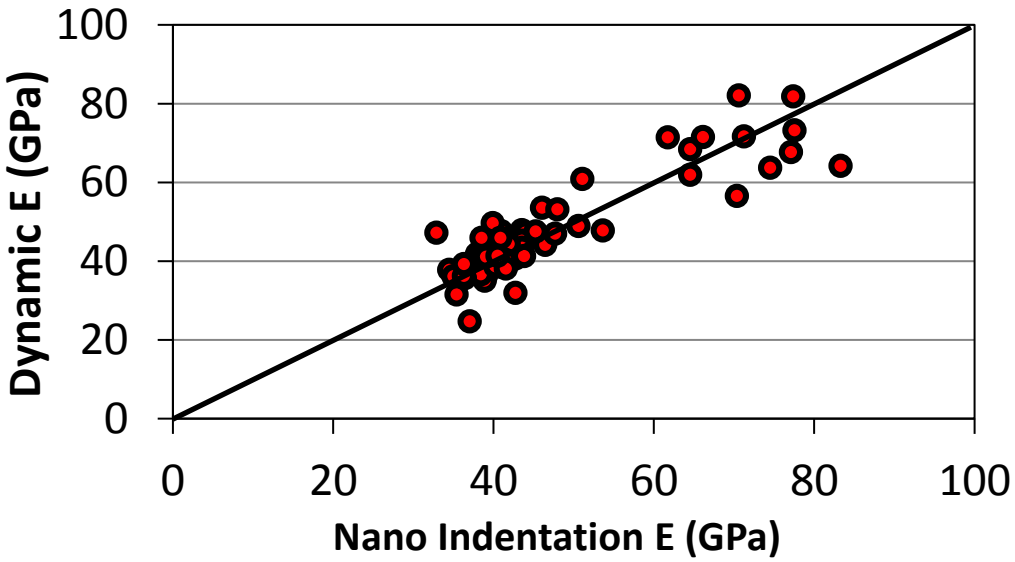

Figure 81: Young's modulus values calculated from ultrasonic measurements compared against actual Young's modulus measurements on Wolfcamp samples using nanoindentation. The 1:1 line is shown as black line.

The cross-plot between Young's modulus and Poisson's ratio can differentiate brittle and ductile rocks. Brittle rocks are characterized by low Poisson's ratio and high Young's modulus. The cross-plot for the three rock types is shown in Figure 82. Rock Type 2 shows high Young's modulus and low Poisson's ratio and appears to be the most brittle of the three rock types. Thus, mineralogy and ultrasonic measurements both indicate that Rock Type 2 is the most brittle rock type.

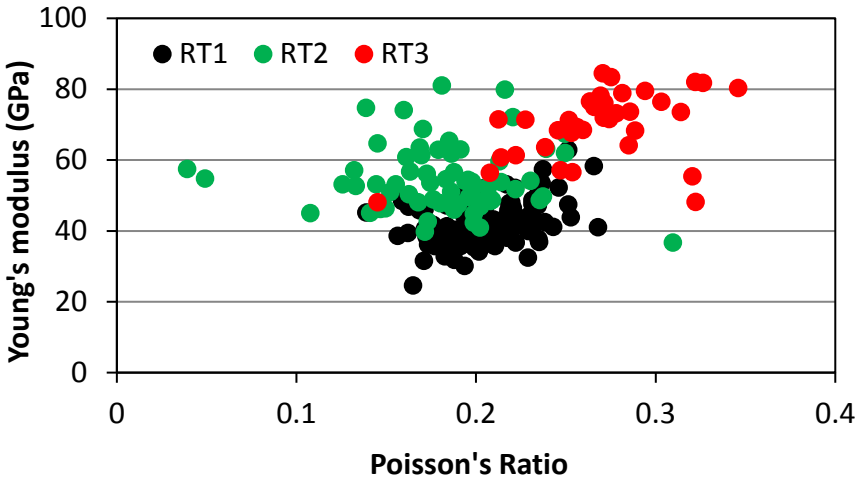

Figure 82: Cross-plot of Young's modulus and Poisson's ratio obtained from ultrasonic measurements. Rock Type 2 shows high Young's modulus and low Poisson's ratio and appears to be the most brittle of the three rock types.

Mercury injection capillary pressure data were also available for 156 core plugs. Incremental and cumulative Hg intrusion plots, normalized by helium pore volume, for the three rock types are shown in Figure 83. The cumulative intrusion plot for Rock Type 1 samples show that the ratio of mercury to helium volume varies between 0.65 to 0.85. In Rock Type 2 samples, this ratio varies between 0.55 to 0.75 and it varies between 0.25 to 0.45 for Rock Type 3 samples. The connected pore volume decreases as we go from Rock Type 1 to Rock Type 2 and Rock Type 3.

Rock Type 3 samples were characterized by monotonically increasing incremental intrusion curve without an inflection point even at 60,000 psia. This shape is characteristic of very tight rocks where the dominant pore size may be smaller than 3 nm. These samples are characterized by high carbonate percentage and a higher grain density.

The cumulative intrusion plots in both Rock Type 1 and Rock Type 2 exhibit considerable hysteresis between saturating and desaturating curves, implying actual

intrusion. However, in Rock Type 3, cumulative intrusion curves in Rock Type 3 exhibit almost overlapping saturating and desaturating curves. Lack of hysteresis between saturating and desaturating curves implied false intrusion.

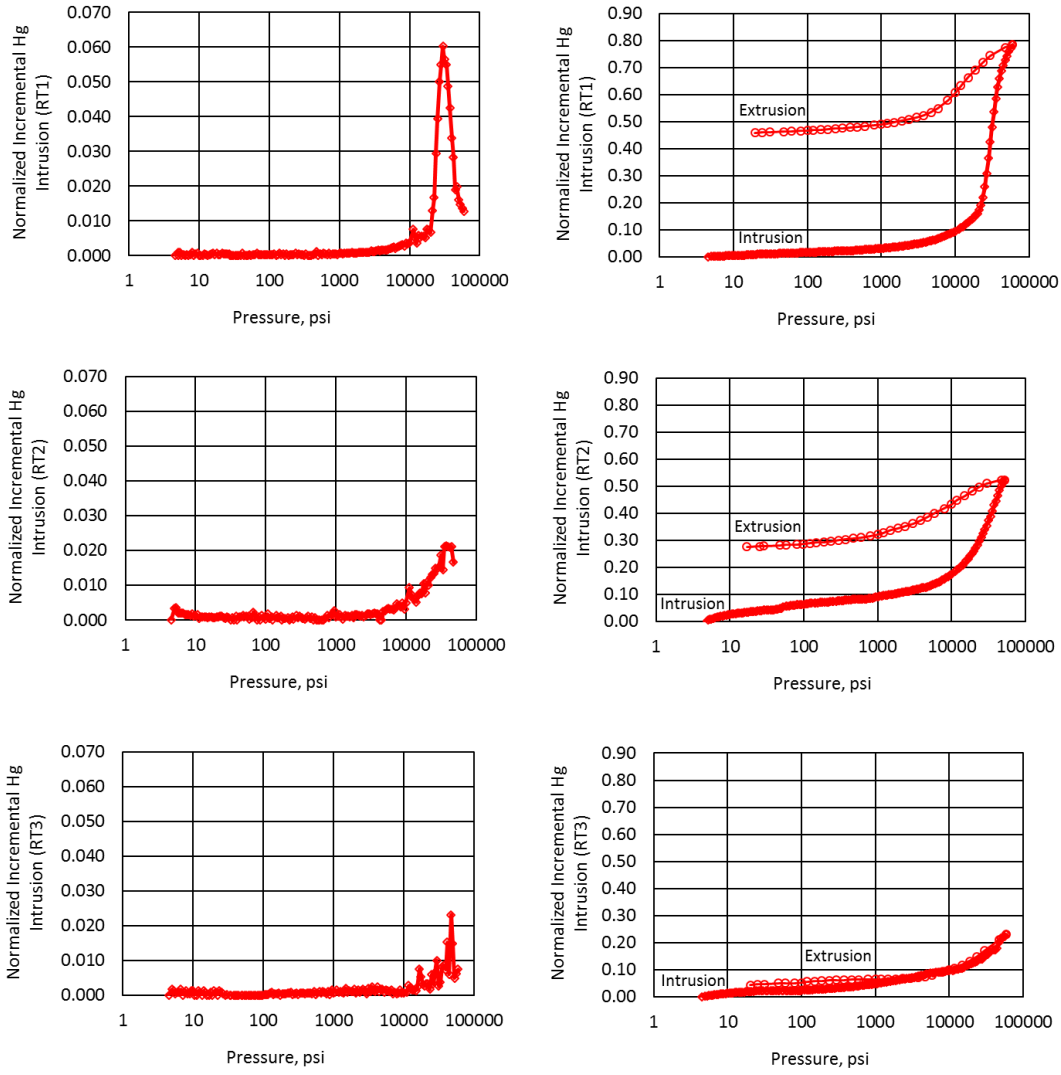

Figure 83: Representative normalized incremental and cumulative mercury intrusion plots for the three rock types in Wolfcamp. Rock Type 1 has the highest dominant pore throat size and highest connected volume. On the other end, Rock Type 3 shows signs of false intrusion and has lowest connected volume.

For Rock Type 1 samples, the average dominant pore throat size is 5.5 nm while for Rock Type 2 samples, it is 4 nm. Thus, Rock Type 1 samples have the highest

permeability. As discussed before, Rock Type 2 samples may be affected by presence of clay.

6.3 Extending Core-Based Classification to Well Logs

In Wolfcamp, gamma ray and neutron porosity logs were available for all three wells that have core data; these two logs were used for upscaling. Figure 84 shows the distribution of gamma ray and neutron porosity logs for different rock types. Rock Type 1 is associated with the highest neutron porosity and highest gamma ray values. This corresponds well with results from the analysis of core data where Rock Type 1 is characterized by the highest helium porosity, clay fraction and TOC. The logs were consistent with the core data and were found adequate for upscaling the rock types.

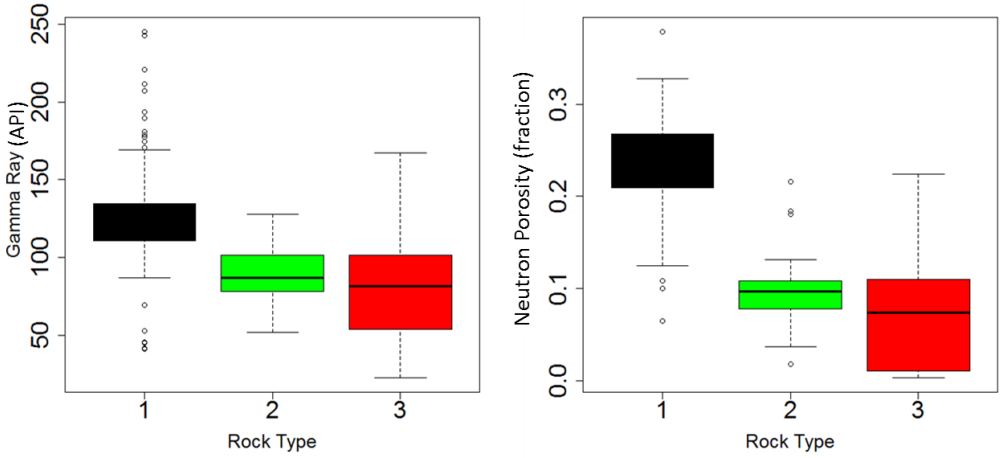

Figure 84: Gamma ray and neutron porosity distribution for different rock types. This data corresponds to depths where both log values and core measurements are available. Rock Type 1 has highest neutron porosity and highest gamma ray. This corresponds well with the core data because Rock Type 1 also had highest helium porosity, clay fraction and TOC from core analysis. Both clay fraction and TOC contribute to high GR.

To do the upscaling, following the same procedure as in previous three shale plays, log data were extracted corresponding to depths where core data were available.

The trained SVM model was used to predict rock types in uncored wells and remaining section of the cored wells where core data were not available. Figure 85 shows the rock type logs for two sample wells (W23 on left, W24 on right). The rock type logs for the remaining wells are given in Appendix D.

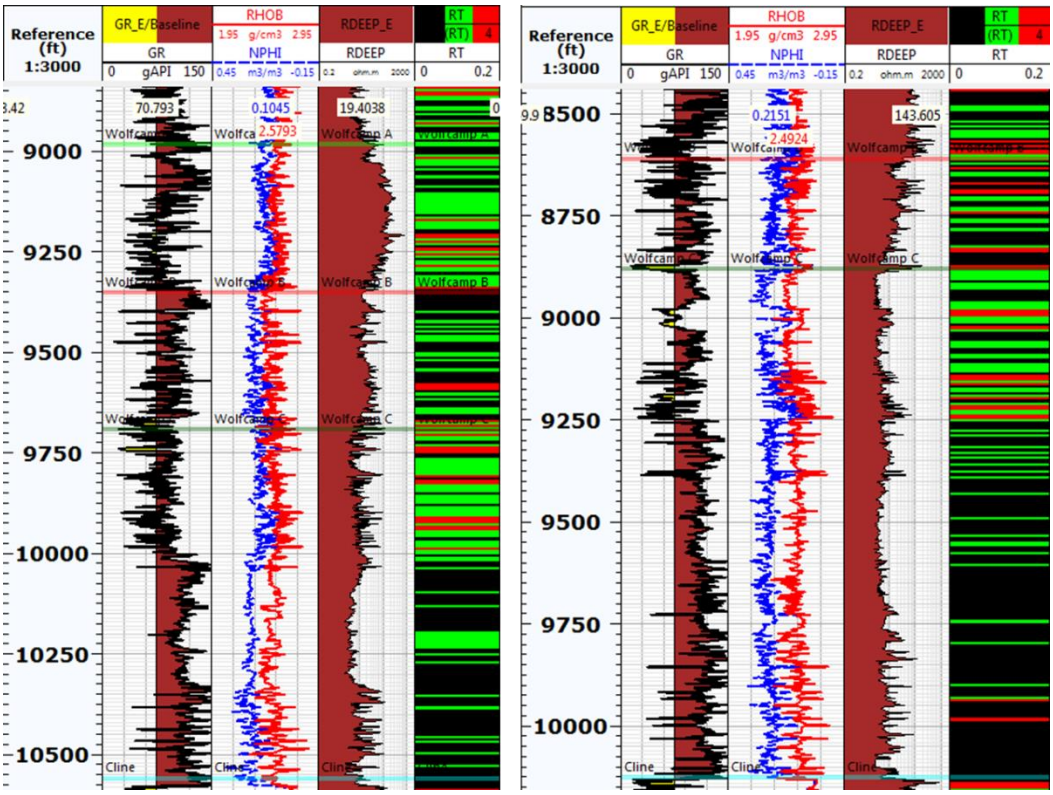

Figure 85: Rock type logs (track 4; black=Rock Type 1, green=Rock Type 2, and red=Rock Type 3?) for two sample wells (W23 on left, W24 on right) in Wolfcamp.

The quality of populated rock type logs was checked and the robustness of the SVM algorithm was assessed. The triple combo logs were available for two wells. The porosity and TOC logs were modelled using resistivity, gamma ray, neutron, and density logs. The triple combo logs and calculated porosity and TOC logs for Well 23 and Well 24 are given in Figure 86.

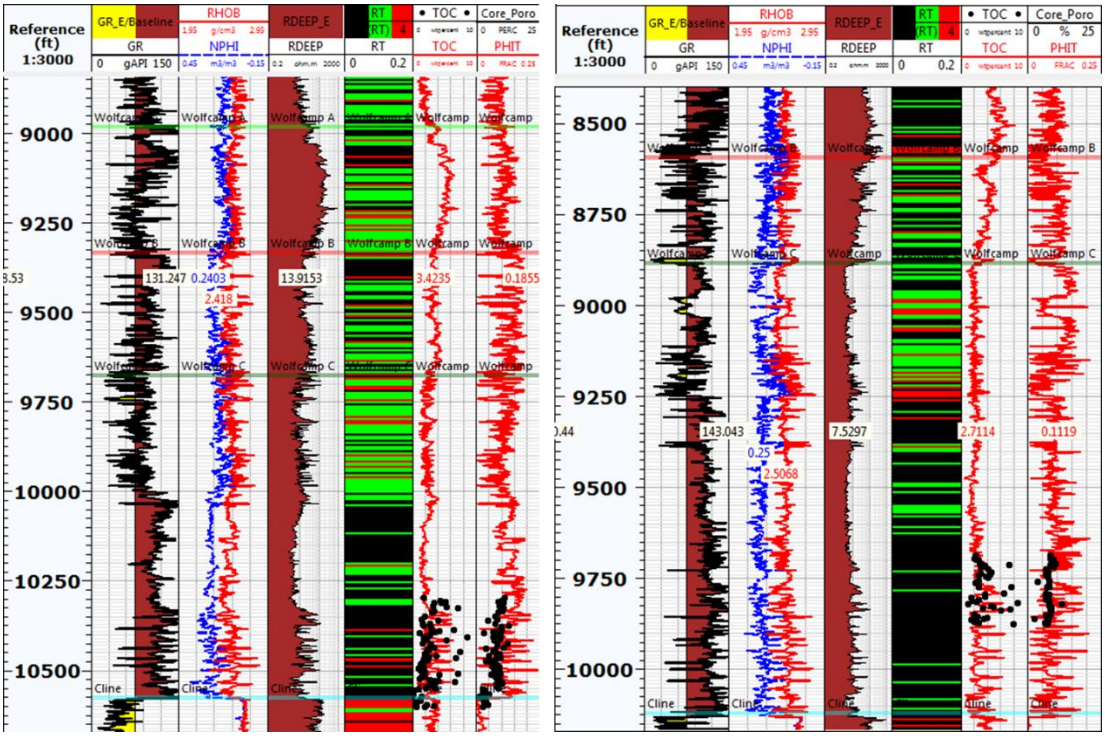

Figure 86: Calculated logs (rock types in track 4; black=Rock Type 1, green=Rock Type 2, and red=Rock Type 3) namely porosity and TOC logs for two sample wells (Well 23 on left, Well 24 on right). The red curve represents the modelled curves. The black filled circles represent the core measurements used for calibration.

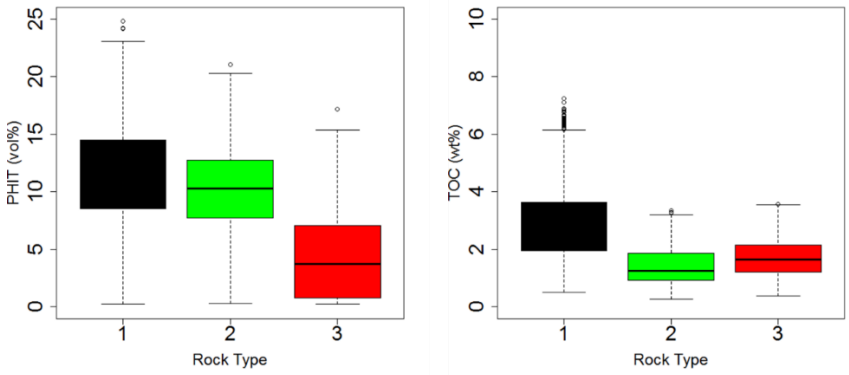

Figure 87: Box plots showing distribution of calculated TOC and porosity logs based on populated rock type log. The distributions confirm the conclusions based on core derived rock types.

Box plots (Figure 87) were created from the calculated TOC and porosity based on the rock type log. The results confirm the conclusions based on core derived rock

types (Figure 79). Rock Type 1 has the highest source rock and storage potential followed by Rock Type 2 and Rock Type 3. This cross-check validates the rock type upscaling method and lends credibility to further analysis with production data.

6.4 Relating rock types to Production Data

Figure 75 shows the location of the Wolfcamp wells. All the wells considered in Wolfcamp were vertical wells. Figure 88 shows the comparison of RTR with normalized production. Vertical well production was normalized by zone thickness. A positive correlation between normalized production and RTR is evident. Different linear trends are likely due to different completion practices used by various operators.

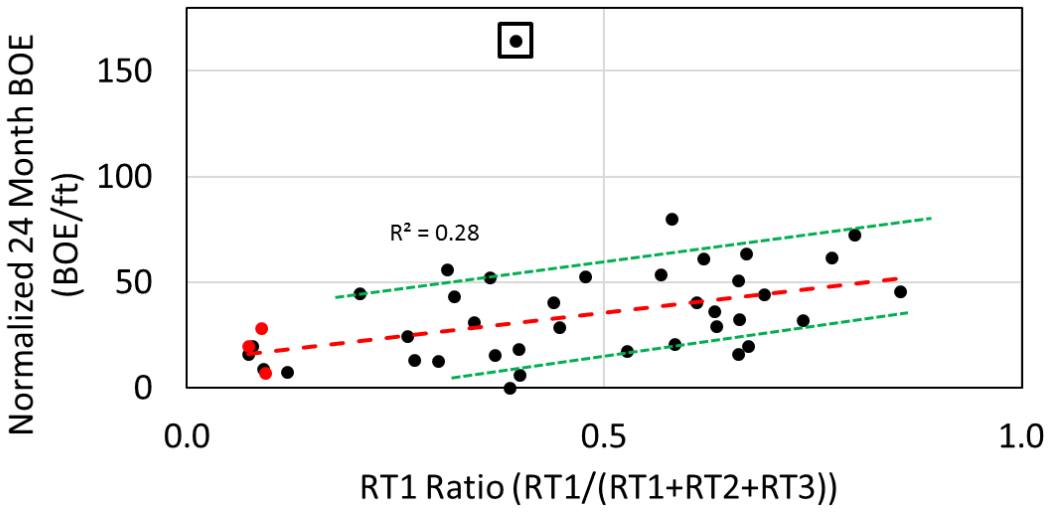

Figure 88: Normalized production correlated with the Rock Type Ratio (RTR). A positive correlation suggests that Rock Type 1 is the key rock type controlling the production. Outlier in the black box are not included in the correlation coefficient.

In the Delaware basin, the Wolfcamp formation is produced commingled with Bone Spring sands. In the Midland basin, the combination of Wolfcamp and Spraberry is being exploited. Fracture analysis to map the extent of fracturing and whether it pierced the overlying Dean or Spraberry formations, was not carried out. Thus, the

production plot may be affected by commingled production. The spread in the cross-plot can also be explained based on commingled production from Spraberry and Dean, which have not been accounted for in the RTR; but, still, a general positive trend suggests Rock Type 1 is sensitive to production which validates the rock typing exercise.

Chapter 7: Microstructure Analysis of Different Rock Types

The unconventional shale rocks have a very complex microstructure due to abundance of different type of minerals, a variety of organic matter and complex diagenetic and alteration history. The macroscopic properties are a complex interplay of these different influences and leads to diversity and heterogeneity within and between different shale plays. Thus, any rock typing exercise cannot be complete without understanding the microstructural controls behind different rock types. This chapter focusses on identifying microstructural controls behind different rock types using Scanning Electron Microscope (SEM) images and tying the images back to the macroscopic data.

Different researchers have proposed different terminology for the type of pores that can be distinguished on SEM images. Schieber (2010) suggested three categories for pore types based on his study of six shale successions. The three categories were phyllosilicate framework (PF) pores, carbonate dissolution (CD) pores and the organic matter (OM) pores. The phyllosilicate framework pores are generally low aspect ratio (Figure 89) and associated with clays. These pores are stress sensitive and range in size from 5 nm to 1000 nm. The carbonate dissolution pores are formed at the boundaries of carbonate minerals. They are formed during diagenesis when phenolic and carboxylic acids are generated during maturation of the kerogen. These acids dissolve the carbonate minerals and generate porosity at the boundaries. These pores generally have low aspect ratios (Figure 89) and vary in size from 50 nm to 1000 nm. Finally, the organic pores are generated during maturation and thermal cracking of the kerogen which is consumed in the process and generates porosity as a byproduct. These pores are generally elliptical, circular or irregular shaped with high aspect ratio (Figure 89).

Thus, these pores are orders of degree less stress sensitive then the PF or CD pores. These pores are also smaller in size and vary from 10 to 100 nm. Organic pores can be further categorized into three categories namely, intra-particle, inter-particle and crystalline pores in pyrite framboids. Loucks et al. (2009) observed the different type of organic nano-pores in Mississippian Barnett shale samples. Curtis et al. (2012) has shown that in addition to the above general categories of pores, pores are also associated with other minerals like pyrite, phosphates, etc.

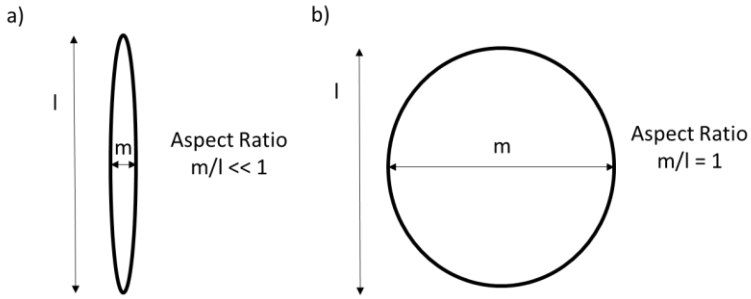

Figure 89: a) Low aspect ratio pore, where major axis of the pore is much larger than the minor axis. Low aspect ratio pores are particularly stress sensitive. b) High aspect ratio pore. The major and minor axis of the pore are similar in length. These pores are comparatively stress resistant.

In this study, SEM images were taken for different rock types in the four shale plays. The images for different shale plays in Figure 90 show the occurrence of different pore-types. Even though, the images show that all shale plays contain all the pore-types but the fraction of each varies spatially both within and between shale plays which makes them so unique and heterogeneous. For instance, in Barnett SEM image shown in the Figure 90, 3 % of the porosity existed in the purely organic pore and 40% of the porosity existed in purely inorganic pore. Remaining 57 % of the porosity existed in mixed pores, where pore lining comprises of both organic surfaces like kerogen and inorganic mineral surfaces. The corresponding numbers for Eagle Ford image were 22.5

% for organic pores, 8.5 % for inorganic pores and 69% for mixed pores, respectively. The numbers for Woodford image were 9% for organic pores, 22.5 % for the inorganic pores and 68.5% for the mixed pores, respectively. Thus, Figure 90 shows the huge variability between different shales at the micro-structure level.

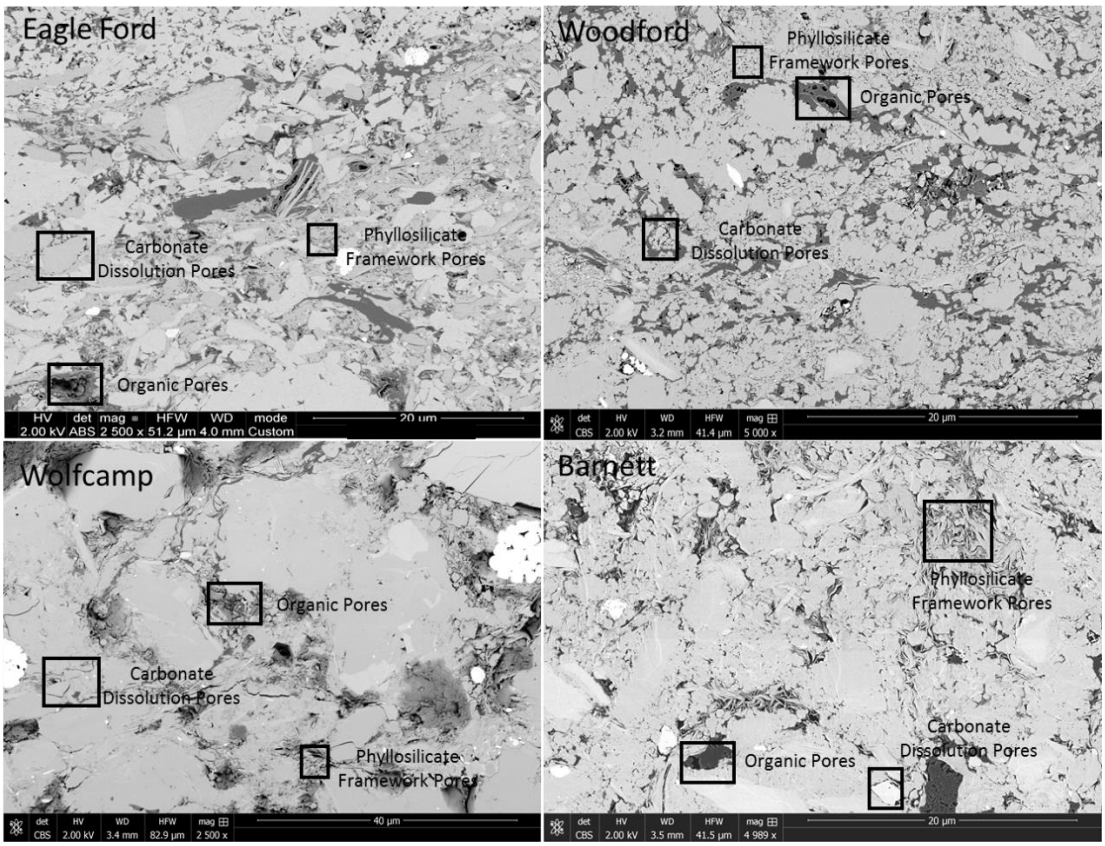

Figure 90: SEM images from different shale plays showing abundance of different types of pores. In Barnett SEM image, 3 % of the porosity existed in the purely organic pore and 40% of the porosity existed in purely inorganic pore. Remaining 57 % of the porosity existed in mixed pores, where pore lining comprises of both organic surfaces like kerogen and inorganic mineral surfaces. The corresponding numbers for Eagle Ford image were 22.5 % for organic pores, 8.5 % for inorganic pores and 69% for mixed pores, respectively. The numbers for Woodford image were 9% for organic pores, 22.5 % for the inorganic pores and 68.5% for the mixed pores, respectively. Thus, the figure shows the huge variability between different shales at the micro-structure level.

It is only logical to assume that different proportions of these different pore types lead to different macroscopic properties. For instance, the pore-types that have the

highest volumetric fraction are more likely to be connected and thus, control properties like wettability and permeability. This conclusion is again based on the fact that all shale plays have different pore types exhibiting different wettabilities. Phyllosilicate pores are generally water wet unless they are filled with organic matter in which case these pores might show an oil wet character. On the other hand, organic pores are generally considered oil wet.

The above classification and generalization holds true but there are notable exceptions. One has already been mentioned, that phyllosilicate pores are generally water wet unless filled with organic matter which might make them more oil wet. Schieber (2010) showed that in shales with comparatively low TOC (<7 wt. %), the phyllosilicate pores are open, connected and free of organic matter. But, at higher TOC values, these pores are filled with kerogen and bitumenite.

Another notable exception was pointed out by Curtis et al. (2012) who pointed it out that an important factor deciding the aspect ratio of organic pores is whether kerogen is matrix supported or pressure supported. Kerogen is soft and ductile (Kumar et al. 2012, Shukla et al. 2013). If kerogen is pressure shadowed by larger resistant grains, the pores tend to be high aspect ratio. On the other hand, if kerogen supports the stress, the stress tends to close the pores or make them low aspect ratio. Other reasons for low aspect ratio pores in the organic matrix is organic matter shrinkage and fracturing inside organic macerals because of maturation (Lopez 2016). Figure 91 shows few examples of low aspect ratio pores inside organic matter.

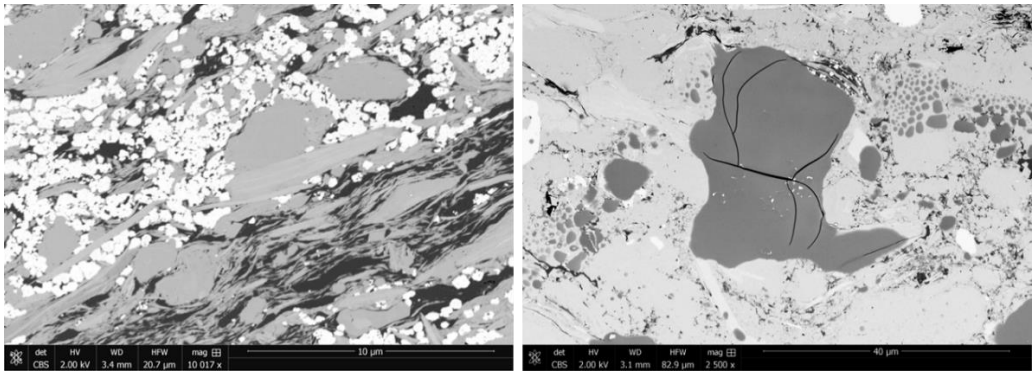

Figure 91: SEM images from the Woodford formation in late condensate window. (Left) Example showing organic matter filling of the phyllosilicate pores and high aspect ratio organic pores. (Right) Fractures inside organic matter occur most likely due to maturation process. This fracture is not likely due to sample preparation as it is limited inside the organic maceral.

The organic pore development is dependent on many other variables like kerogen type, localized compaction, presence of water for hydrous pyrolysis, etc. (Curtis et al. 2011, Curtis et al. 2012). Figure 92 shows examples where adjacent organic macerals that have experienced similar thermal histories have completely different organic pore development. Porosity in shales is a complex function of TOC, thermal maturity, mineral content, texture, relative arrangement of different matrix components, diagenetic and stress history, etc.

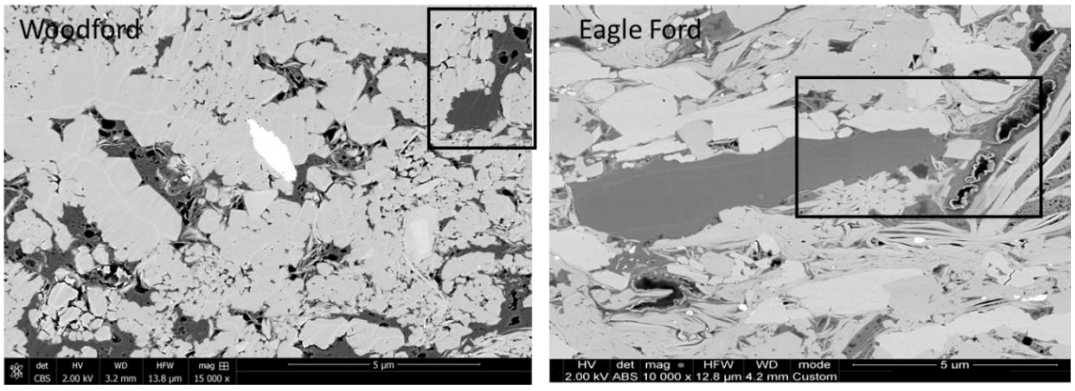

Figure 92: The highlighted area in both shale samples show adjacent organic macerals that have experienced similar thermal histories but one has organic pores while the other has no porosity.

Determining individual petrophysical properties on first principle basis is not only difficult but highly dependent on local conditions. At the same time, this highlights the importance of rock typing in unconventional reservoirs as it integrates all the available data and collectively identifies clusters having different macroscopic properties (which are a result of complex interplay of various geological processes as described above). The rock types are easy to comprehend and are an appropriate tool for reservoir completion and development.

Rock Type 1 is the best rock type while Rock Type 3 is the worst. Figure 93 shows the best (RT1) and the worst (RT3) rock types for the different shale plays. In all the shale plays, Rock Type 1 has the highest TOC, high porosity and highest fraction of movable hydrocarbons. Rock Type 1 images shows considerably more organic matter (shown by white arrows) compared to Rock Type 3 images. Also, except Eagle Ford, in all other shale plays, Rock Type 3 has high carbonates and has a very low porosity (shown by black arrows).

In Eagle Ford, the porosity of the Rock Type 3 is high and the Rock Type 3 is rich in clays. These results are corroborated by the SEM image in the Figure 93. Finally, in Woodford and Barnett, Rock Type 1 is characterized by high quartz content. The quartz mineral grains are visible in abundance in the SEM images in Figure 93. Thus, the different rock types obtained from macroscopic petrophysical properties have completely different microstructures and are characteristically different from each other.

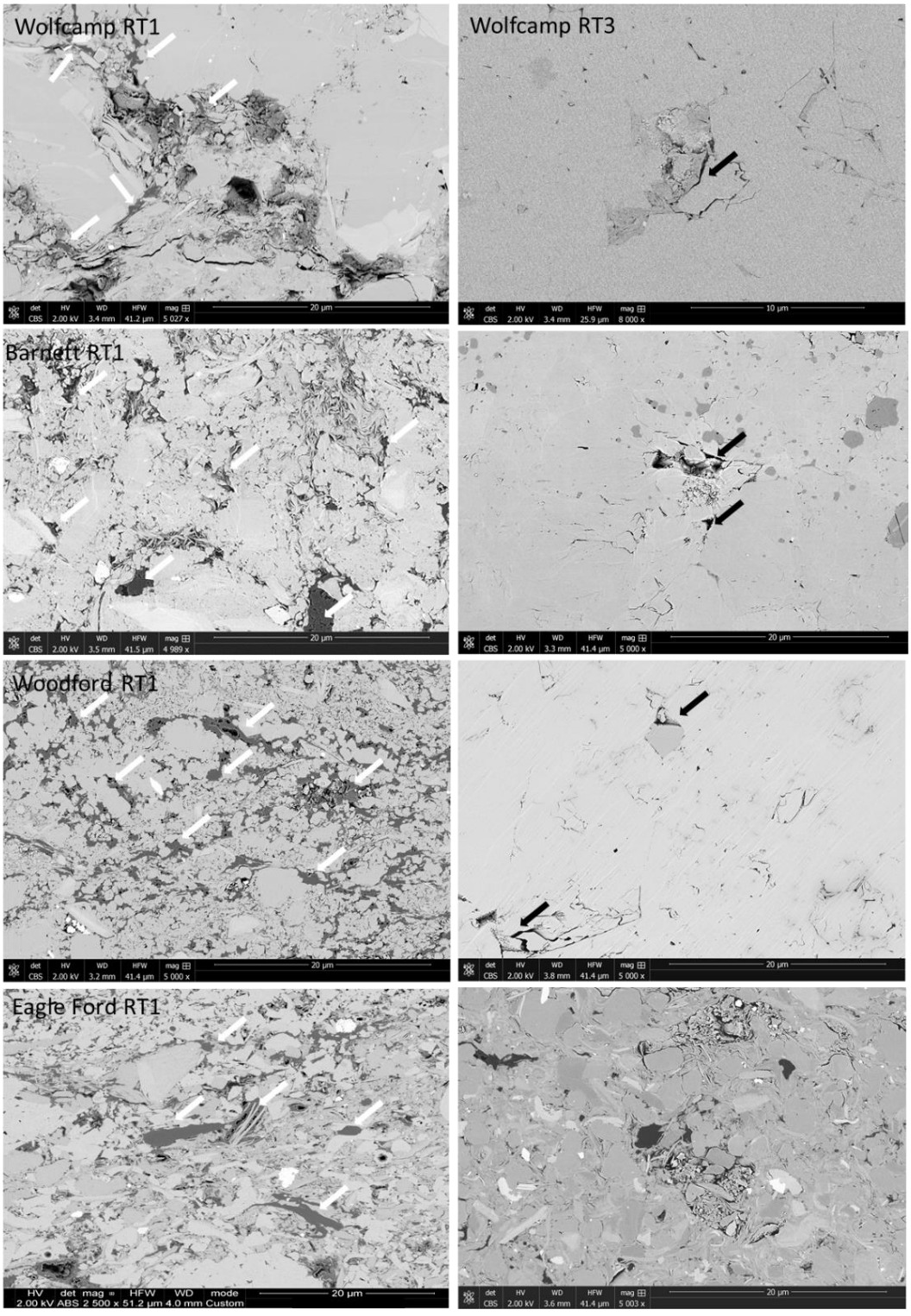

Figure 93: The best (RT1) and the worst (RT3) rock type SEM images for the different shale plays. Rock Type 1 generally has high porosity and TOC (shown by white arrows). Rock Type 3 has high carbonates, low TOC and porosity (shown by black arrows).

Intraparticle fractures are identified in quartz grains in Rock Type 3. Fractured grains are not observed in Rock Type 1 or 2 because of presence of softer more ductile materials like clays and TOC, as they deform and provide a cushion to minerals like quartz. Figure 94 shows some example images from Woodford and Barnett shale plays. These intraparticle fractures may not be real and may represent artifacts of sample preparation. However, if such fractures are formed during sample preparation, there is a possibility that some of them also exist downhole.

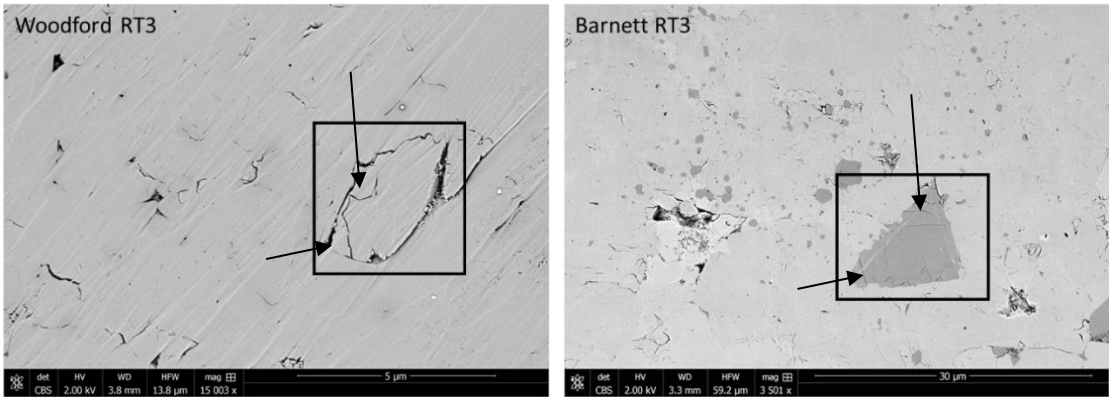

Figure 94: SEM images for Rock Type 3 samples in Woodford and Barnett showing intraparticle fractures (pointed by arrows) in quartz grains.

These intraparticle fractures are likely isolated and thus, do not contribute to enhancing permeability. The low quartz content and limited fractured grains are not statistically significant to influence permeability. Grain microfracturing is not expected in Eagle Ford due to very limited quartz and high clay percentage in Rock Type 3.

The best rock type (RT1) in all the four shale plays has high TOC and porosity. High TOC and porosity are universal characteristics of good rock types; therefore, it becomes important to identify what are the geological and microstructural controls on porosity and TOC. Starting with porosity, the three general types of pores namely phyllosilicate network, carbonate dissolution and organic are inherently related to clay

content, carbonate content and TOC, respectively. Out of these three, carbonate dissolution pores are generally isolated and form a negligible fraction. To understand which pore-type dominates porosity, cross-plots of porosity vs. TOC, clay content were analyzed. The results were verified in SEM images. The cross-plots are not expected to give strong correlations as all the three types of pores coexist and the whole process is further complicated by diagenetic history. However, it can provide a general guidance.

Figure 95 shows porosity cross-plots with TOC and clay content in Woodford samples. The TOC cross-plot shows porosity increases with increasing TOC. The phenomenon is very pronounced in Rock Type 1 at TOC values > 8%. The porosity vs. clay cross-plot also supports the above argument. It shows a slow and steady increase in porosity with clay content but Rock Type 1 samples which have high TOC lie much above the trend. These relationships are also evident in Rock Type 1 SEM images in Figure 96. Figure 96**Error! Reference source not found.** shows that the Woodford samples are dominated by organic pores.

In Figure 96, the image on the right was analyzed to separate organic from inorganic pores. The results indicate that 26% of the porosity existed in purely organic pores while only 2% of the porosity existed in inorganic pores. The remaining 72% of the porosity existed in the mixed pores.

Figure 97 shows the porosity cross-plots of porosity with TOC and clay content in the Barnett samples. Both the cross-plots show weak correlation. This is likely because in Barnett, both organic and inorganic porosities are seen in abundance and neither of them dominates. This is evident in SEM images in Figure 98. This is also evident by quantitative analysis of the image (enlarged image on the right). Only 2% of

the porosity existed in organic pores, another 8% in inorganic pores and the remaining 90% in mixed pores.

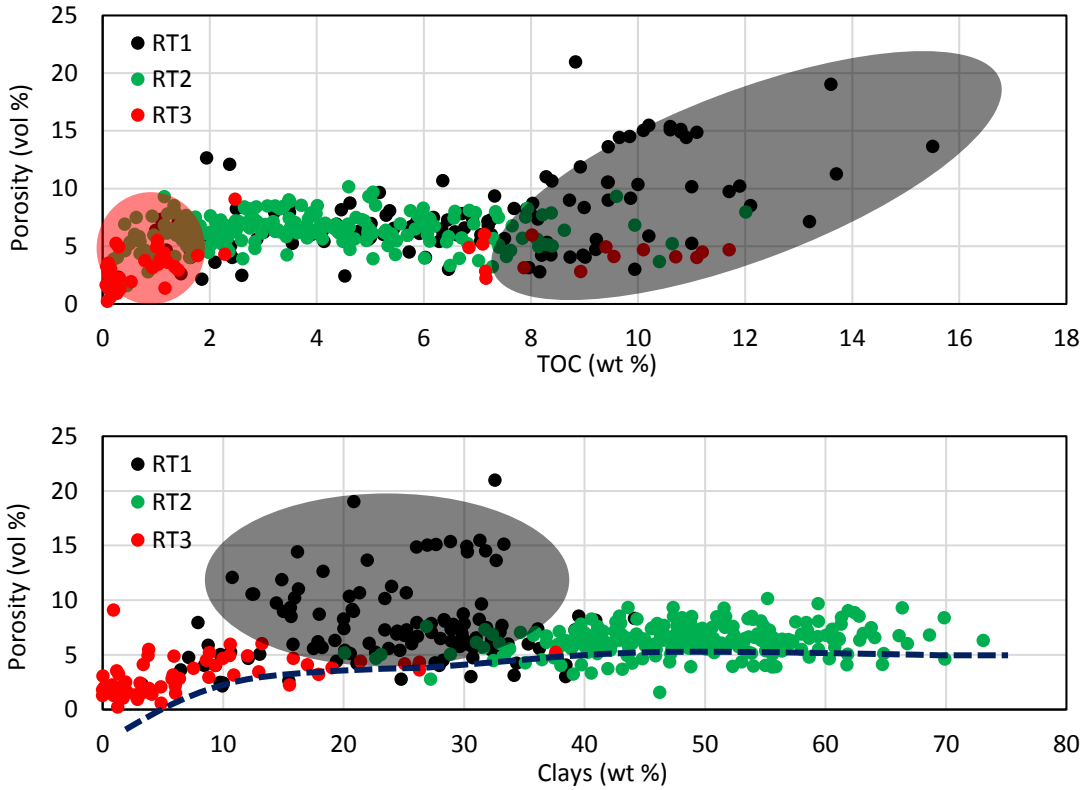

Figure 95: Porosity cross-plots with TOC and clay content in Woodford samples. The TOC cross-plot shows porosity increases with increasing TOC. The phenomenon is very pronounced in Rock Type 1 or at TOC values > 8%; at higher TOC, organic porosity dominates. The porosity vs. clays cross-plot shows a slow and steady increase in porosity with clay content but Rock Type 1 samples which have high TOC lie much above the trend.

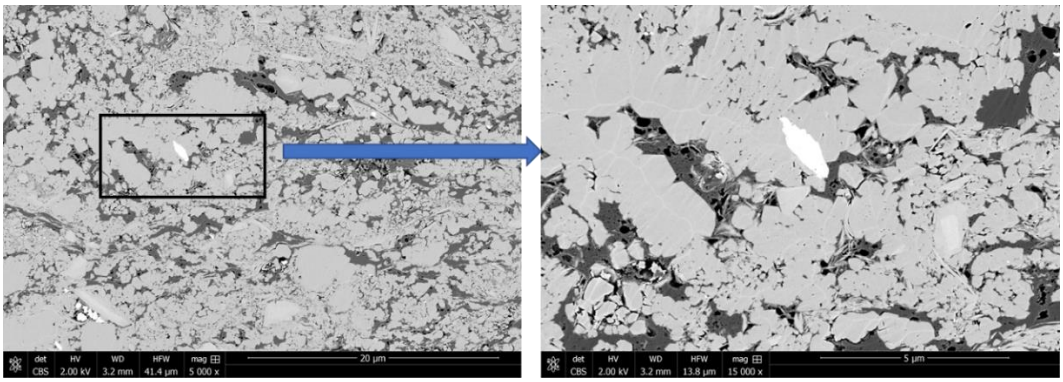

Figure 96: SEM images from Rock Type 1 in Woodford. Images show dominance of organic porosity.

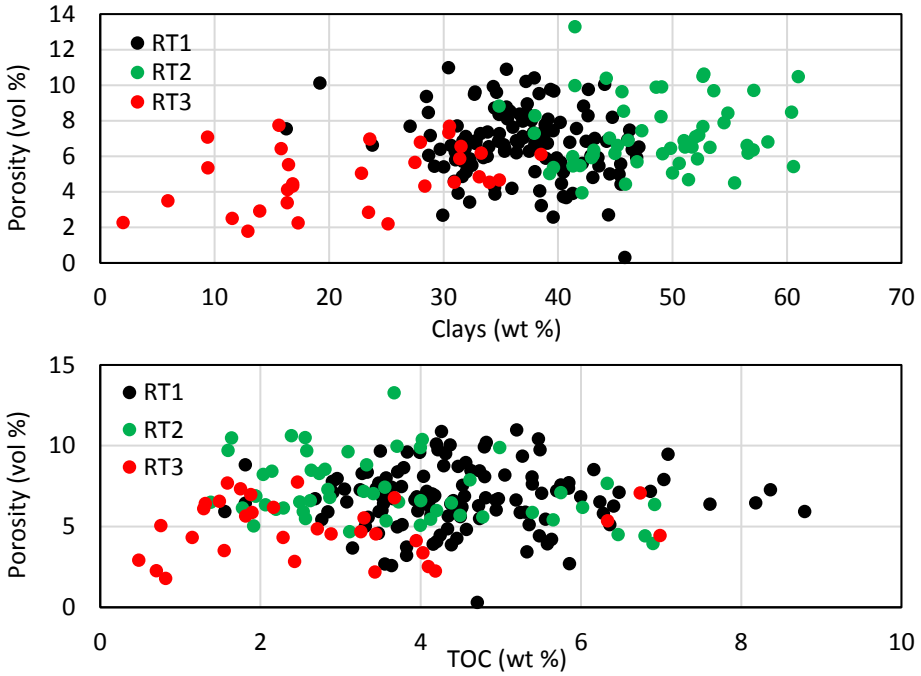

Figure 97: Porosity cross-plots with TOC and clay content in the Barnett samples. Both the cross-plots show weak correlation. This is likely because in Barnett, both organic and inorganic porosities are seen in abundance and neither of them dominates

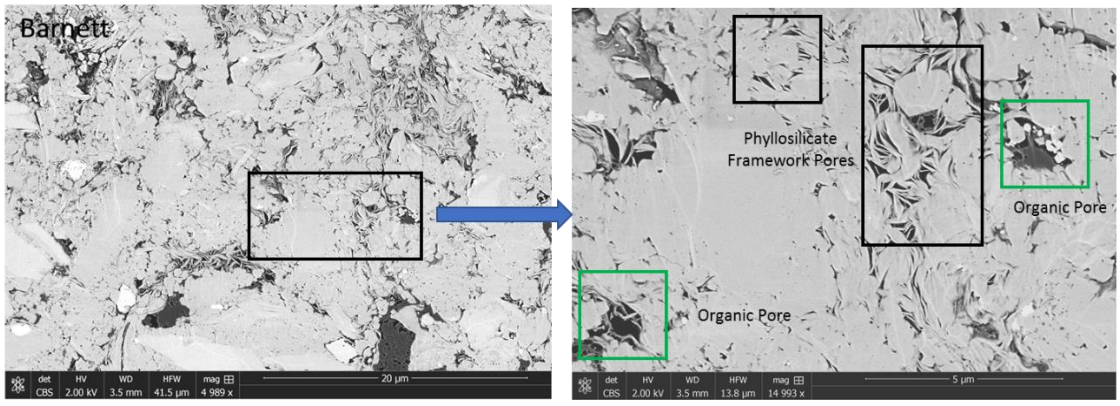

Figure 98: SEM images from Rock Type 1 in Barnett. Images show abundant organic and inorganic pores.

Figure 99 shows porosity cross-plots with TOC and clay content in Eagle Ford samples. In Eagle Ford, both the cross-plots show weak correlation. Both Rock Type 1 and Rock Type 3 has high porosity. Rock Type 1 has high TOC and low clay content

while Rock Type 3 has high clay content and low TOC. Thus, it is likely that Rock Type 1 is dominated by organic porosity and Rock Type 3 is dominated by inorganic porosity. This is evident from SEM images in Figure 100 and from core-based rock typing results in Figure 41.

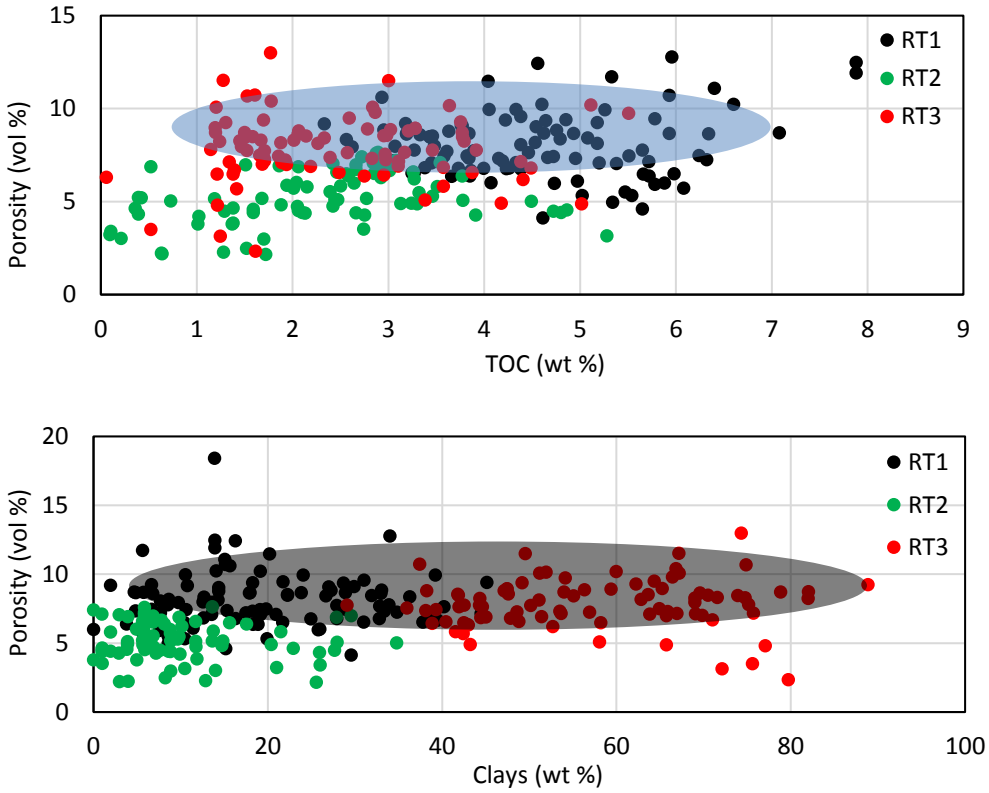

Figure 99: Porosity cross-plots with TOC and clay content in Eagle Ford formation. The behavior in Eagle Ford is similar to Barnett samples in that neither TOC nor clay fraction shows a strong correlation with porosity. Both Rock Type 1 and Rock Type 3 show high porosity.

Figure 101 shows porosity cross-plots in the Wolfcamp samples. The porosity vs. clays cross-plot suggests an increasing porosity with increasing clay content. On the other hand, there appears to be no correlation between porosity and TOC. Thus, it can be concluded that phyllosilicate network pores dominate the porosity. The results can be verified from SEM images in Wolfcamp in Figure 102. In Figure 102, the boxed area on

the left image is enlarged (right image) to clearly show the inorganic pores in the clay matrix.

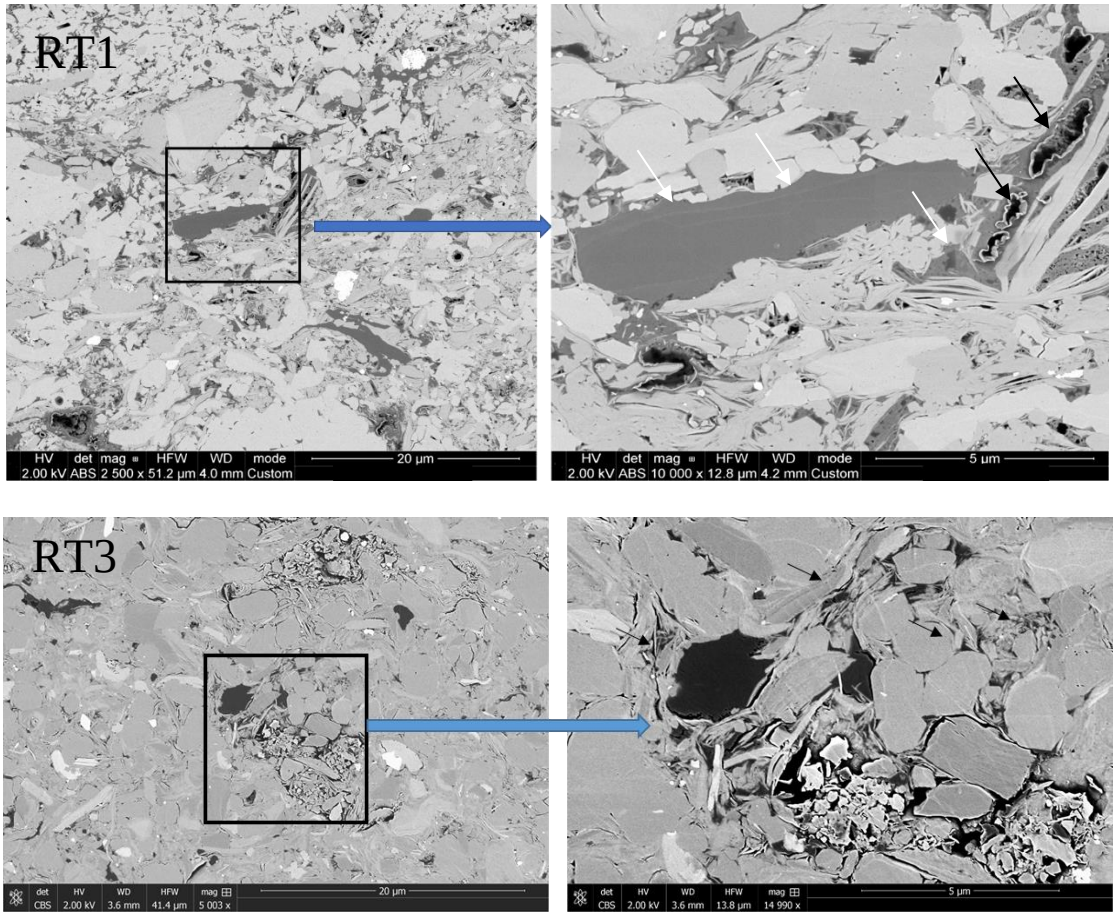

Figure 100: SEM images for Rock Type 1 (Top) and Rock Type 3 (Bottom) in Eagle Ford. Both Rock Type 1 and Rock Type 3 has high porosity. Rock Type 1 has high TOC and low clay content while Rock Type 3 has high clay content and low TOC. Images show that Rock Type 1 is dominated by organic porosity and Rock Type 3 is dominated by inorganic porosity.

A similar analysis was carried to assess the controlling factors behind TOC. The analysis of different images along with the core data suggested that TOC was generally found surrounded by quartz grains in Barnett and Woodford samples. This is consistent with geological and petrophysical analysis. The source of organics in these two plays were siliceous organisms with skeleton made of silica. On the other hand, in Wolfcamp,

organic deposition was related to clay content. The TOC in Eagle Ford was related to carbonate deposition as phytoplanktons like cocoliths are source of organic matter.

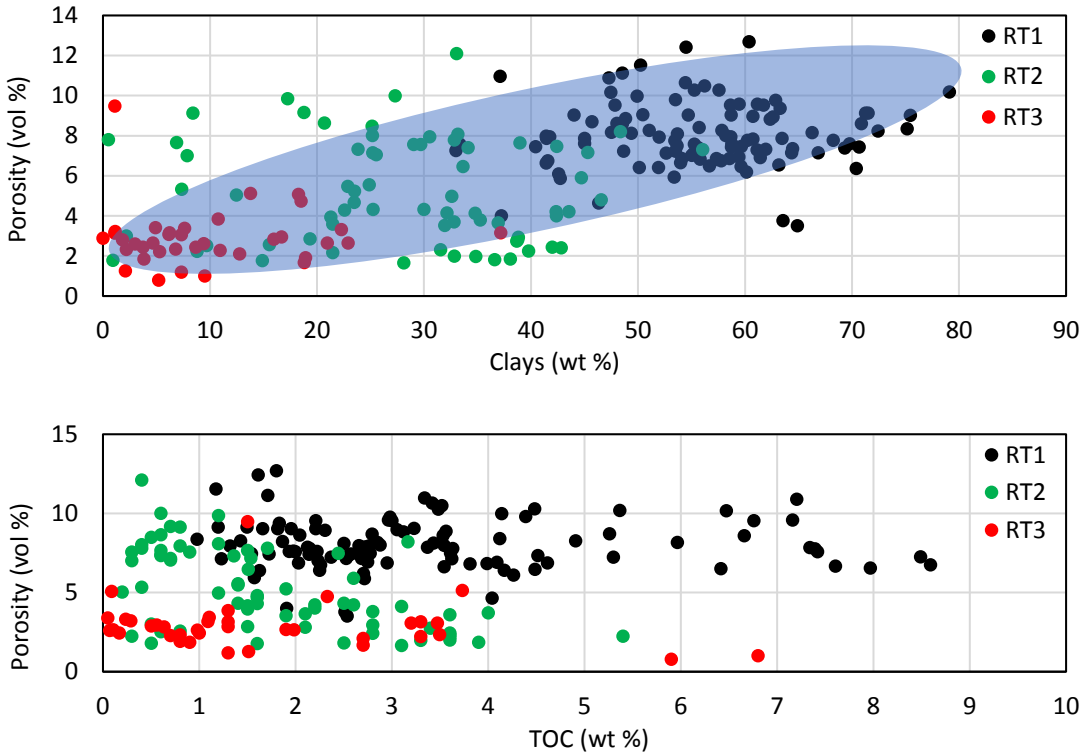

Figure 101: Porosity cross-plots in Wolfcamp formation. The porosity vs. clays cross-plot suggests an increasing porosity with increasing clay content. On the other hand, there appears to be no correlation between porosity and TOC. Thus, it can be concluded that phyllosilicate network pores dominate the porosity.

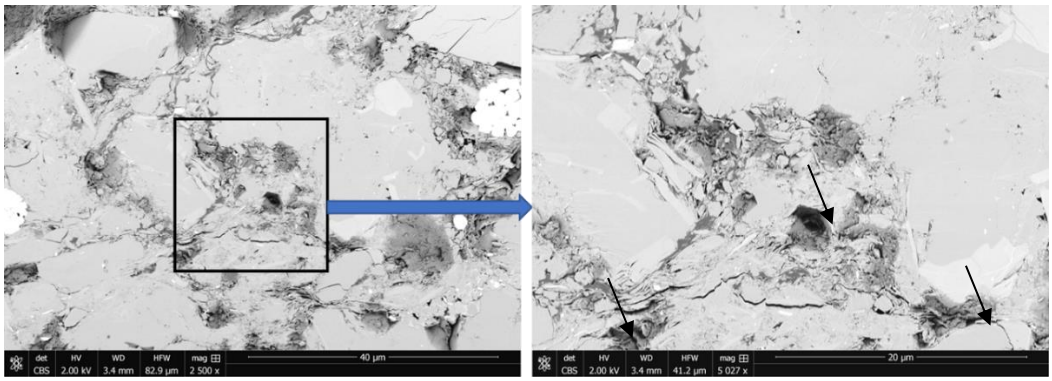

Figure 102: SEM images in Rock Type 1 in Wolfcamp formation show abundant phyllosilicate network pores. The boxed area on the left image is enlarged (right image) to clearly show the inorganic pores in the clay matrix (shown by black arrows).

Chapter 8: Conclusions

Different shale plays are very different in terms of depositional environment, lithology, microstructure, anisotropy, brittleness, source rock quantity and quality, etc. Geologists identify many lithofacies (for example, up to 10) based on the above parameters. This creates many problems for a reservoir or production engineer looking to find ideal location to drill a well and ideal zones to complete a well. These lithofacies are known only in wells having core data. These lithofacies are not easy to correlate with logs and thus, difficult to identify in wells lacking core data. Different lithofacies can have similar reservoir properties like porosity, permeability, etc. They may not necessarily represent different flow units and may not offer insights into which zones should be targeted for completion.

Due to these limitations, rock typing became an essential step in reservoir characterization workflow. Rock types identify different flow units and they tie the lithofacies to reservoir flow properties and production. Kale et al. (2010) also showed that lithofacies can be tied back to the rock types. The current study develops an integrated work flow for rock typing using lab measurements. The workflow correlates the core-based rock types with available logs and generates rock type logs. These logs show a strong correlation with the production from the wells. Data mining algorithms such as K-Means, SOM, SVM, etc. are very powerful in handling large amount of data and finding meaningful associations between different data types. The rock types were upscaled to 140 wells spanning over 20,000 ft. depth. The additional benefit is that the workflow is largely automated making the rock typing exercise rapid. The manual approach can be prohibitively time consuming.

Three rock types were identified in each of the four shale plays. The three rock types had different storage and source rock potential and different mineralogy. In general, Rock Type 1 (the best rock type) had high storage and source rock potential followed by Rock Type 2 and Rock Type 3. An exception to this was Eagle Ford shale play where Rock Type 3 had higher storage potential compared to Rock Type 2 but had poorer source rock potential. The reason for this anomaly was sampled wells belonging to two completely different depositional environments (Deltaic vs. shallow marine carbonate environments) in Eagle Ford. Deltaic deposits were terrigenous, oxidized and devoid of any organic carbon.

The three rock types also had strikingly different mineralogies. One rock type was dominated by quartz, second by carbonates and the third by clays. It was found that depending on the depositional environment, one of these three mineral groups were associated with organic carbon. For example, in the Woodford, siliceous radiolarians were responsible for the organic matter deposition; thus, in Woodford, quartz was associated with organic carbon. Therefore, Rock Type 1 had the highest quartz content among the three rock types. Similarly, in the Eagle Ford, pelagic carbonaceous organisms were responsible for organic matter deposition. Thus, Rock Type 1 had high carbonate percentage. Along the same lines, Rock Type 1 in Barnett and Wolfcamp had highest quartz and clay content, respectively.

The three rock types had characteristic mercury injection capillary pressure curves. Rock Type 1 had highest mercury to helium pore volume ratio, signaling highest connectivity. It also had high hysteresis and largest dominant pore throat radius. Rock Type 3, on the other extreme, had lowest mercury to helium pore volume ratio. It

had a monotonously increasing capillary pressure curve without any inflection point. This type of curve is characteristic of very tight rocks possibly having a dominant pore throat radius smaller than 3 nm. Rock Type 3 samples also had virtually over-lapping cumulative intrusion and extrusion curves likely indicating false intrusion. The only exception to this was Eagle Ford play where Rock Type 2 had the poorest connectivity and tight rock signature. Table 1 summarizes the characteristics for different rock types in the four shale plays studied.

Table 1: Characteristics of Different rock types (data represents 25-75 percentile).

Eagle Ford	**TOC (wt %)**	**Porosity (vol %)**	**Carbonates (wt %)**	**Clays (wt %)**	**Quartz (wt %)**	**S1 (mg/gm rock)**
Rock Type 1	3.5-5.5	7.0-9.0	55-70	10-30	0.0-6.0	2.0-6.0
Rock Type 2	1.5-3.0	4.5-6.5	70-85	5-15	0.0-4.0	1.5-3.5
Rock Type 3	1.5-3.0	7.0-9.0	15-35	45-70	0.0-4.0	1.0-2.0
Woodford	**TOC (wt %)**	**Porosity (vol %)**	**Carbonates (wt %)**	**Clays (wt %)**	**Quartz (wt %)**	**S1 (mg/gm rock)**
Rock Type 1	4.0-9.0	5.5-9.0	10-20	18-30	35-50	1.0-5.0
Rock Type 2	3.0-5.0	5.5-7.0	5-15	42-55	15-30	0.0-4.0
Rock Type 3	0.5-4.5	2.0-4.0	65-90	0-10	0-10	0.0-2.0
Barnett	**TOC (wt %)**	**Porosity (vol %)**	**Carbonates (wt %)**	**Clays (wt %)**	**Quartz (wt %)**	**S1 (mg/gm rock)**
Rock Type 1	3.5-5.5	6.0-8.0	5-15	32-40	28-36	0.7-1.1
Rock Type 2	2.5-4.5	6.0-8.0	7-18	42-52	12-20	0.3-0.8
Rock Type 3	1.5-3.5	3.5-6.0	30-55	15-30	11-20	0.3-0.7
Wolfcamp	**TOC (wt %)**	**Porosity (vol %)**	**Carbonates (wt %)**	**Clays (wt %)**	**Quartz (wt %)**	**S1 (mg/gm rock)**
Rock Type 1	2.0-4.0	7-9	0-5	50-60	12-24	1.0-2.2
Rock Type 2	1.0-2.0	3-7	0-10	20-35	35-45	1.5-1.8
Rock Type 3	1.0-2.0	2-3	45-70	5-15	5-25	0.0-0.2

The advantage of this integrated workflow is that even though different shale plays are different in so many ways, this integrated workflow identifies simple relationships between different petrophysical attributes that are more or less consistent across different shale plays. The three rock types can be easily correlated to logs and can be modelled across a shale play. They have a strong link with well productivity and can be used as tools in completion optimization. The rock type logs can aid the reservoir or production engineer in optimizing perforation intervals and number of fracture stages. Rock Type 3 is poor reservoir and may not warrant any perforation or fracturing. Rock Type 1 is the best reservoir rock. It can be selectively perforated and fractured to save cost and maximize production from a well. Other applications of the rock typing are 3D reservoir modeling, identifying sweet spots in combination with seismic attributes, new well locations, improved volumetric estimates and uncertainty and risk analysis.

It is important to highlight that rock typing exercise carried out in this study was based on extensive core, log and production data but it can be further improved by including several other parameters that effect the production. These parameters were not included because the data was not available. These parameters include geophysical attributes (for porosity, natural fractures, etc.), advanced logs (for natural fractures, water saturation, etc.), completion parameters (fracture half lengths, fracture heights, fracture conductivities, number of fracture stages, skin effects, etc.) and other reservoir parameters (pore pressures, near wellbore and far-field stresses, etc.). For instance, superior fracturing fluids provided by certain service providers increase SRV (Stimulated Reservoir Volume) for fractures leading to higher productivity. Different

operators use different proppant volumes, different fracture spacings, etc. and thus effects of completion play a major role on the productivity of the well. It was seen in the production correlation plots (Figure 29 and Figure 88) that different completion practices may show up as multiple linear trends but without completion data it is difficult to say for sure. Another example could be change of pore-pressure as we move from gas to condensate to oil maturity windows within a same shale play. The variation in pore pressure can also be due to different stress regimes. Thus, productivities may be different due differences in pore pressure regimes. To include the effects of pore pressure, one simple method is to normalize the production by pore pressure or look at well productivities instead of 24 months' production. But, bottom hole pressure data was not available in the wells.

The data that will be useful to obtain these different parameters and improve rock typing definition include seismic, micro-seismic, VSP (Vertical Seismic Profile) surveys, advanced logs like NMR, sonic, FMI (Formation Micro-imager), proppant volumes, rate and pressure transient analysis, DFIT (Diagnostic Fracture Injection Tests), MDT (Modular Dynamics Tester) measurements, etc.

All the well logs were available for the pilot vertical holes. Thus, there was an inherent assumption that the reservoir properties do not change as we move away from the wellbore. With long horizontal laterals, this assumption may not hold true and this might affect the results of production correlation with the rock types. To reduce the uncertainty, it is recommended to use logs along the horizontal wellbore for production correlation. These logs were not available for the wells used in this study.

References

Amaefule, J. O., Altunbay, M., Tiab, D., Kersey, D. G., & Keelan, D. K. 1993. Enhanced Reservoir Description: Using Core and Log Data to Identify Hydraulic (Flow) Units and Predict Permeability in Uncored Intervals/Wells. Presented at SPE Annual Technical Conference and Exhibition, 3-6 October, Houston, Texas. SPE-26436-MS. doi:10.2118/26436-MS.

Amin, S., Wehner, M., & Heidari, Z. 2016. Rock Classification in the Eagle Ford Shale through Integration of Petrophysical, Geological, and Geochemical Characterization. Presented at the 57th Annual Logging Symposium, 25-29 Jun, Reykjavik, Iceland.

Aranibar, A., Saneifar, M., & Heidari, Z. 2013. Petrophysical Rock Typing in Organic-Rich Source Rocks Using Well Logs. Presented at Unconventional Resources Technology Conference, 12-14 August, Denver, Colorado. SPE-168913. doi: 10.1190/URTEC2013-117.

Bailey, S. 2009. Closure and Compressibility Corrections to Capillary Pressure Data in Shales. Oral presentation given at the DWLS 2009 Workshop, Beyond the Basics of Capillary Pressure: Advanced Topics.

Ballard, B. D. 2007. Quantitative Mineralogy of Reservoir Rocks Using Fourier Transform Infrared Spectroscopy. Presented at SPE Annual Technical Conference and Exhibition, Anaheim, California, 11-14 November. http://dx.doi:10.2118/113023.

Bassiouni, Z. 1994. Theory, Measurement, and Interpretation of Well Logs. SPE Textbook Series Vol. 4. John Rhea Jr. Professor of Petroleum Engineering, Louisiana State U. ISBN 1-55563-056-1.

Breyer, J.A., Denne, R., Funk, J., Kosanke, T., & Spaw, J. 2013. Stratigraphy and Sedimentary Facies of the Eagle Ford Shale (Cretaceous) between the Maverick Basin and the San Marcos Arch, Texas, USA. Presented at AAPG Annual Convention and Exhibition, Pittsburgh, Pennsylvania, May 19-22, 2013.

Bruner, K., & Smosna, R. 2011. A Comparative Study of the Mississippian Barnett Shale, Fort Worth Basin, and Devonian Marcellus Shale, Appalachian Basin. DOE/NETL-2011/1478, US DOE, April, 2011.

Caldwell, C. D. & Johnson, P. G. 2013. Anadarko Woodford Shale: Improving Production by Understanding Lithologies/Mechanical Stratigraphy and Optimizing Completion Design. Oral presentation at AAPG Education Directorate Woodford Shale Forum, Oklahoma City, Oklahoma, April 11, 2013.

Callantine, S. 2010. Eagle Ford Shale Play. Investor Report, Chesapeake Energy, Oklahoma City, Oklahoma, August 2010. Web Address: http://www.commodityintelligence.com/images/2010/oct/19oct/chkoct10.pdf (Accessed 27 Mar, 2017)

Chon, T. S., & Park, Y.S. 2008. Self-Organizing Map, In *Encyclopedia of Ecology*, edited by Sven Erik Jorgensen and Brian D. Fath, Academic Press, Oxford, Pages 3203-3210, ISBN 9780080454054, http://dx.doi.org/10.1016/B978-008045405-4.00907-1.

CLR. 2010. Anadarko Woodford: The SCOOP, Internal Report, Continental Resources Limited, Oklahoma City, Oklahoma. Web Address: http://media.corporate-ir.net/media_files/irol/19/197380/CLR_Sunday_10_7_12_Anadarko_Woodford_3.pdf (Accessed 27 Mar 2017)

Coates, G. R. & Dumanoir, J. L. 1974. A New Approach to Improved Log-Derived Permeability. The Log Analyst, (January-February 1974), pp. 17.

Comer, J. B. 2005. Facies distribution and hydrocarbon production potential of Woodford Shale in the southern Midcontinent. Presented at Unconventional Energy Resources in the Southern Midcontinent Symposium, Norman, Oklahoma, Oklahoma Geological Survey, Circular 110, p. 51-62.

Corbett, P.W.M. & Potter, D.K. 2004. Petrotyping: A Basemap for Atlas for Navigating Through Permeability and Porosity Data for Reservoir Comparison and Permeability Prediction. Presented at the International Symposium of the Society of Core Analysts, 5-9 October, Abu Dhabi, UAE. SCA2004-30.

Cortes, C. & Vapnik, V. 1995. Support-vector networks. *Machine Learning*. 20 (3): Book Pg. 273–297. doi: 10.1007/BF00994018.

Cortez, M. 2012. Chemostratigraphy, Paleoceanography, and Sequence Stratigraphy of the Pennsylvanian – Permian section in the Midland basin of the West Texas, with focus on the Wolfcamp formation. MS Geology Thesis, The University of Texas at Arlington, Arlington, Texas.

Curtis, M. E., Sondergeld, C. H., Ambrose, R. J., &Rai, C. S. 2011. Microstructural investigation of gas shales in two and three dimensions using nanometer-scale resolution imaging. *AAPG Bulletin*. V. 96, No. 4, PP. 665-677. DOI: 10.1306/08151110188.

Curtis, M. E., Cardott, B. J., Sondergeld, C. H., & Rai, C. S. 2012. The Development of Organic Porosity in the Woodford Shale Related to Thermal Maturity. Presented at SPE Annual Technical Conference and Exhibition, San Antonio, Texas, 8-10 October, 2012.

Davies, D. K., Williams, B. P. J., & Vessell, R. K. 1993. Reservoir Geometry and Internal Permeability Distribution in Fluvial, Tight, Gas Sandstones, Travis Peak Formation, Texas. *SPE Reservoir Engineering*. http://dx.doi:10.2118/21850-PA.

Elzarka, M. H., & Younes, M., A., A. 1987. Generation, migration and accumulation of oil of El-Ayun Field, Gulf of Suez, Egypt. Geology Department, Faculty of Science, Alexandria University, Alexandria, Egypt. Marine and Petroleum Geology, 1987, Vol 4.

EOG Resources. 2010. South Texas Eagle Ford. Internal Report, EOG Resources, Houston, Texas (Accessed from DNA Folder Area, Eagle Ford Shale, Drilling Info on 27 Mar 2017).

Guido, S. 2014. K-Means Clustering with Scikit-Learn. Presentation uploaded on Slideshare.net. Web Address: https://www.slideshare.net/SarahGuido/kmeans-clustering-with-scikitlearn (accessed Mar 27, 2017).

Gupta, N. 2012. Multi-scale characterization of the Woodford shale in West-central Oklahoma from Scanning electron microscope to 3D seismic, PhD Thesis, Oklahoma U., Norman, Oklahoma.

Hamlin, H. S. & Baumgardner, R. W. 2012. Wolfberry Deep-Water Depositional Systems in the Midland Basin: Stratigraphy, Lithofacies, Reservoirs and Source Rocks, Report of Investigations No. 277, Bureau of Economic Geology. ISSN: 08886725.

Hay, J. L., & Pharr, G., M. 2000. *Instrumented Indentation Testing*. ASM Handbook, 232-243.

Heckel, P. H. 1986. Sea-level curve for Pennsylvanian eustatic marine transgressive-regressive depositional cycles along midcontinent outcrop belt, North America: Geology, v. 14, 330-334. Department of Geology, University of Iowa, Iowa City, Iowa.

Holmes, M., and Dolan, M. 2014. A comprehensive Geochemical and Petrophysical Integration Study for the Permian Basin. Oral presentation at the Geoscience Technology Workshop, AAPG, Houston, Texas, 4-5 September.

Hotelling, H. 1933. Analysis of a complex of statistical variables into principal components. *Journal of Educational Psychology*, 24, 417–441, and 498–520.

Jarvie, D. M., Hill, R. J., Ruble, T. E., & Pollastro, R. M. 2007. Unconventional shale-gas systems: The Mississippian Barnett Shale of North-Central Texas as one model for thermogenic shale-gas assessment: AAPG Bulletin, V. 91, P. 475–499, http://dx.doi: 10.1306/12190606068.

Junck R., & Benson D. 1973. A High-Resolution Pulse Transmission Technique for Determining Ultrasonic Velocities, *Review of Scientific Instruments*, Volume 44, pp.1044-1048.

Kale, S. 2009. Petrophysical Characterization of Barnett Shale Play, Master Thesis, Oklahoma U., Norman, Oklahoma.

Kale, S., Rai, C., & Sondergeld, C. 2010. Rock Typing in Gas Shales. Presented at SPE Annual Technical Conference, Florence, Italy, 19-22 September. SPE 134539. http://dx.doi:10.2118/134539-MS

Karastathis A. 2007. Petrophysical Measurements on Tight Gas Shale. Master Thesis, University of Oklahoma, Norman, Oklahoma.

Kenyon, W. E., P. I. Day, C. Straley, and J. F. Willemsen (1988), A three- part study of NMR longitudinal relaxation properties of water-saturated sandstones, SPE Form. Eval., 3(3), 622–636, doi:10.2118/15643-PA

Kinley, T. 2008. Hydrocarbon potential of the Barnett Shale (Mississippian), Delaware Basin, west Texas, and southeastern New Mexico. AAPG Vol (92): 967-991 http://dx.doi.org/10.1306/03240807121.

Knackstedt, M. A., Latham, S.J., Sheppard, A.P., Sok, R.M., & Kumar, M. 2010. Rock Typing Across Disciplines. Presented at SPWLA 51st Annual Logging Symposium, 19-23 June, Perth, Australia.

Kohonen, T. & Honkela, T. 2007. Kohonen network. Scholarpedia, doi:10.4249/scholarpedia.1568.

Kumar, V., Curtis, M.E., Gupta, N., Sondergeld, C.H., & Rai, C.S. 2012. Estimation of Elastic Properties of Organic Matter and Woodford Shale Through Nano-indentation Measurements. Presented at the SPE Canadian Unconventional Resources Conference, 30 Oct – 1 Nov, Calgary, Alberta, Canada.

Lantana. 2013. Woodford Shale – The changing dynamics of the Woodford Shale, Internal Report, Lantana Oil and Gas Partners, Houston, Texas. Web Address: http://lantanaog.com/play-studies/ (Accessed 27 Mar, 2017).

Law, C. 1999. Evaluating Source Rocks, Chapter 6, AAPG special volumes, Petroleum Geology/Handbook of Petroleum Geology: Exploring for Oil and Gas Traps, Pages 6-1 - 6-41, Edited by Edward A. Beaumont and Norman H. Foster.

Leiber, R. & Dunn, J. A Proposed Petrophysical Rock Typing Workflow for an Unconventional Mudstone Reservoir – Example from the Niobrara of the DJ Basin. Presented at the SPWLA 54th Annual Logging Symposium, 22-26 June, New Orleans, Louisiana.

Li, H., Hart, B., Dawson, M., & Radjef, E. 2015. Characterizing the Middle Bakken: Laboratory Measurement and Rock Typing of the Middle Bakken Formation. Presented at Unconventional Technology Conference, 20-22 July, San Antonio, Texas. SPE-178676-MS. doi: 10.2118/178676-MS.

Lloyd, S. P. 1957. Least square quantization in PCM. Bell Telephone Laboratories Paper. Published in journal much later: Lloyd., S. P. (1982). Least squares quantization in PCM. *IEEE Transactions on Information Theory*. 28 (2): 129–137. doi:10.1109/TIT.1982.1056489.

Lopez, L. A. 2016. Understanding Organic Matter Structural Changes with Increasing Thermal Maturity from Oil Shale Plays through SEM imaging. Presented at the Unconventional Resources Technology Conference, San Antonio, Texas, 1-3 Aug, 2016.

Loucks, R. G., Reed, R. M., Ruppel, S. C., & Jarvie, D. M. 2009. Morphology, Genesis, and Distribution of Nanometer-Scale Pores in Siliceous Mudstones of the Mississippian Barnett Shale. *Journal of Sedimentary Research.* V. 79, 848-861. DOI: 10.2110/jsr.2009.092.

MacQueen, J. B. 1967. Some Methods for classification and Analysis of Multivariate Observations. Proceedings of 5th Berkeley Symposium on Mathematical Statistics and Probability. University of California Press. pp. 281–297.

Merletti, G.D., Spain, D.R., Pour, R.A., & Zett, A. Understanding Depositional And Diagenetic Processes Improve Petrophysical Rock Typing Workflows in Tight Gas Reservoirs. Presented at SPWLA 55th Annual Logging Symposium, 18-22 May, Abu Dhabi, UAE.

Opencv. 2017. Introduction to Support Vector Machines. Web Address: http://docs.opencv.org/2.4/doc/tutorials/ml/introduction_to_svm/introduction_to_svm.html (Accessed Mar 27, 2017).

Pang, K. 2003. Self-Organizing Maps. Web Address: https://www.cs.hmc.edu/~kpang/nn/som.html. (Accessed 27 Mar, 2017).

Parsley. 2014. Investor Presentation: Wolfcamp, Internal Report, Parsley Energy, Austin, Texas. Web Address: http://www.parsleyenergy.com/~/media/Files/P/Parsley-Energy/reports-and-presentations/PE-investor-presentation-Sept-2014.pdf (Accessed 27 Mar, 2017).

Passey, Q. R., Creaney, S., Kulla, J. B., Moretti, F. J.,& Stroud, J. D. 1990. A Practical Model for Organic Richness from Porosity and Resistivity Logs, AAPG Bulletin, V. 74, P 1777-1794.

Pearson, K. 1901. On Lines and Planes of Closest Fit to Systems of Points in Space. Philosophical Magazine. 2 (11): 559–572. doi:10.1080/14786440109462720.

Pioneer. 2013. Investor Presentation, Wolfcamp, Internal Report, Pioneer Natural Resources, Oklahoma City, Oklahoma. Web Address: www.plsx.com/finder/publicpdf.aspx?key=CksUFGCy3EQrY1U9K2YeqQ%3D%3D. (Accessed 27 Mar, 2017).

Pioneer. 2014. The Wolfcamp Shale: Technical learnings to date and Challenges going forward, Internal Report, Pioneer Natural Resources, Oklahoma City, Oklahoma. Web Address: http://docplayer.net/38429713-The-wolfcamp-shale-technical-learnings-to-date-and-challenges-going-forward.html (Accessed 27 Mar, 2017).

Pittman E. D. 1992. Relationship of Porosity and Permeability to Various Parameters Derived from Mercury Injection – Capillary Pressure Curves for Sandstones. AAPG Bulletin Vol. 76(2): 191-198, ISSN 0149-1423.

Pollastro, R. M., Jarvie, D. M., Hill, R. J., & Adams, C.W. 2007. Geologic framework of the Mississippian Barnett Shale, Barnett-Paleozoic total petroleum system, Bend arch–Fort Worth Basin, Texas, AAPG Bulletin 91 (4): 405-436.

Rahmanian, M., Solano, N., and Aguilera, R. 2010. Storage and Output flow from Shale and Tight Gas Reservoirs. SPE 13361. Presented at SPE Western Regional Meeting, 27-29 May, Anaheim, California. SPE 133611-MS doi: 10.2118/133611-MS.

Randolph, P. L., Soeder, D. J., & Chowdiah, P. 1984. Porosity and Permeability of Tight Sands. Presented at Unconventional Gas Recovery Symposium, 13-15 May, Pittsburg, PA. SPE-12836. doi:10.2118/12836-MS.

Rebelle, M. & Bruno, L. Rock-Typing in Carbonates: A Critical Review of Clustering Methods. Presented at the Abu Dhabi International Petroleum Exhibition and Conference, 10-13 November, Abu Dhabi, UAE. SPE-171759-MS.

Rebelle, M., Umbhauer, F., and Poli, E. 2009. Pore to Grid Carbonate Rock-Typing. Presented at the International Petroleum Technology Conference, 7-9 December, Doha, Qatar. IPTC 13120.

Rushing, J. A., Newsham, K. E., & Blasingame, T. A. 2008. Rock Typing: Keys to Understanding Productivity in Tight Gas Sands. Presented at Unconventional Reservoirs Conference, 10-12 February, Keystone, Colorado. SPE-114164. doi:10.2118/114164-MS.

Sarmiento, M. F. R., Ducros, M., Carpentier, B., Lorant, F., Cacas, M. C., Fiornet, S. P., Wolf, S., Rohais, S. & Moretti, I. 2013. Quantitative evaluation of TOC, organic porosity and gas retention distribution in a gas shale play using petroleum system modeling: Application to the Barnett Shale, Elsevier. *Marine and Petroleum Geology* 45, 315-330 http://dx.doi.org/10.1016/j.marpetgeo.2013.04.003.

Schieber, J. 2010. Common Themes in the Formation and Preservation of Intrinsic Porosity in Shales and Mudstones – Illustrated With Examples Across the Phanerozoic. Presented at SPE Unconventional Gas Conference, Pittsburg, Pennsylvania, USA, 23-25 Feb, 2010.

Singh, P. 2008. Lithofacies and Sequence Stratigraphic Framework of the Barnett Shale, NorthEast Texas. Phd. Dissertation, Univ. of Oklahoma, Norman, Oklahoma.

Shukla, P., Kumar, V., Curtis, M., Sondergeld, C. H., & Rai, C. S. 2013. Nanoindentation Studies on Shales. ARMA 13-578. Presented at 47th US Rock Mechanics/Geomechanics Symposium held in San Francisco, CA, USA, 23-26 Jun 2013.

Slatt, R., Singh P., Borges, G. et al. 2008. Reservoir Characterization of Unconventional Gas Shales: Example from the Barnet Shale, Texas, U.S.A. AAPG Annual Convention, San Antonio, Texas, 20 – 23 April. Search and Discovery Article #30075.

Sondergeld C. H. & Rai C. S. 1993. A New Concept of Quantitative Core Characterization. The Leading Edge 12(7): 774-779.

Sondhi, N. 2011. Petrophysical characterization of the Eagle Ford shale, Master Thesis, Oklahoma U., Norman, Oklahoma.

Spain, D.R., & Liu, S. 2011. Petrophysical Rock Typing of Tight Gas Sands – Beyond Porosity and Saturation: Example from the Cotton Valley Formation, East Texas. Presented at SPE Middle East Unconventional Gas Conference and Exhibition, 31 Jan – 2 Feb, Muscat, Oman. SPE 142808.

Srivastava, P. 2016. Performance Prediction for Deepwater Gulf of Mexico using Data Mining, Master Thesis, Oklahoma U., Norman, Oklahoma.

Steinwart, I. & Christmann, A. 2008. Support Vector Machines, Book, *Information Science and Statistics*, ISBN: 978-0-387-77241-7 (Print) 978-0-387-77242-4 (Online).

Tan, P.N., Steinbach, M., & Kumar, V. 2006. Introduction to Data Mining. *Pearson Addison-Wesley*.

Tian, Y. 2014. Occurrence of Multiple Fluid Phases Across a Basin, in the Same Shale Gas Formation – Eagle Ford Shale Example. MS thesis, Texas A&M, College Station, Texas.

Thomeer J. H. 1983. Air Permeability as a Function of Three Pore Network Parameters. *Journal of Petroleum Technology*, 35(4): 809-814.

Thornton, C. 2017. Machine Learning – Lecture 15 Support Vector Machines. Web Address: http://users.sussex.ac.uk/~christ/crs/ml/lec08a.html (Accessed 27 Mar, 2017).

Timur, A. 1968. An Investigation of Permeability, Porosity, and Residual Water Saturation Relationship for Sandstone Reservoirs, The Log Analyst, Vol. 9, No. 4, (July-August 1968), pp. 8.

Tuttle, S. 2010. Oil Resource Plays – Examples and Technology. Geological Review, Internal Report, Petrohawk Energy Corporation, Houston, Texas (September 2010). (Accessed from DNA Folder Area, Eagle Ford Shale, Drilling Info on 27 Mar 2017).

Walls, J. D. 1982. Tight Gas Sands Permeability, Pore Structure, and Clay, *Journal of Petroleum Technology*, (1982b) 2708-2714.

Welte, D. H., 1984, Petroleum Formation and Occurrence, 2 ed.: New York, Springer-Verlag, 699 p

Williams J. L. 2008. Energy Economist: Wells and Politics, Web link: http://www.energyeconomist.com/a6257783p/archives/ee080611exp.html.

Wilson, M. J., Shaldybin, M. V., & Wilson, L. 2016. Clay Mineralogy and unconventional hydrocarbon shale reservoirs in the USA. Occurrence and interpretation of mixed-layer R3 ordered illite/smectite. Earth Science Reviews 158 (2016) 31–50, Elsevier, http://dx.doi.org/10.1016/j.earscirev.2016.04.004.

Xu, C. & Verdin, C.T. 2013. Core-Based Petrophysical Rock Classification By Quantifying Pore-System Orthogonality With a Bimodal Gaussian Density Function. Presented at International Symposium of the Society of Core Analysts, 16-19 Sep, California, USA. SCA2013-079.

Appendix A: Rock Type logs for Eagle Ford Wells

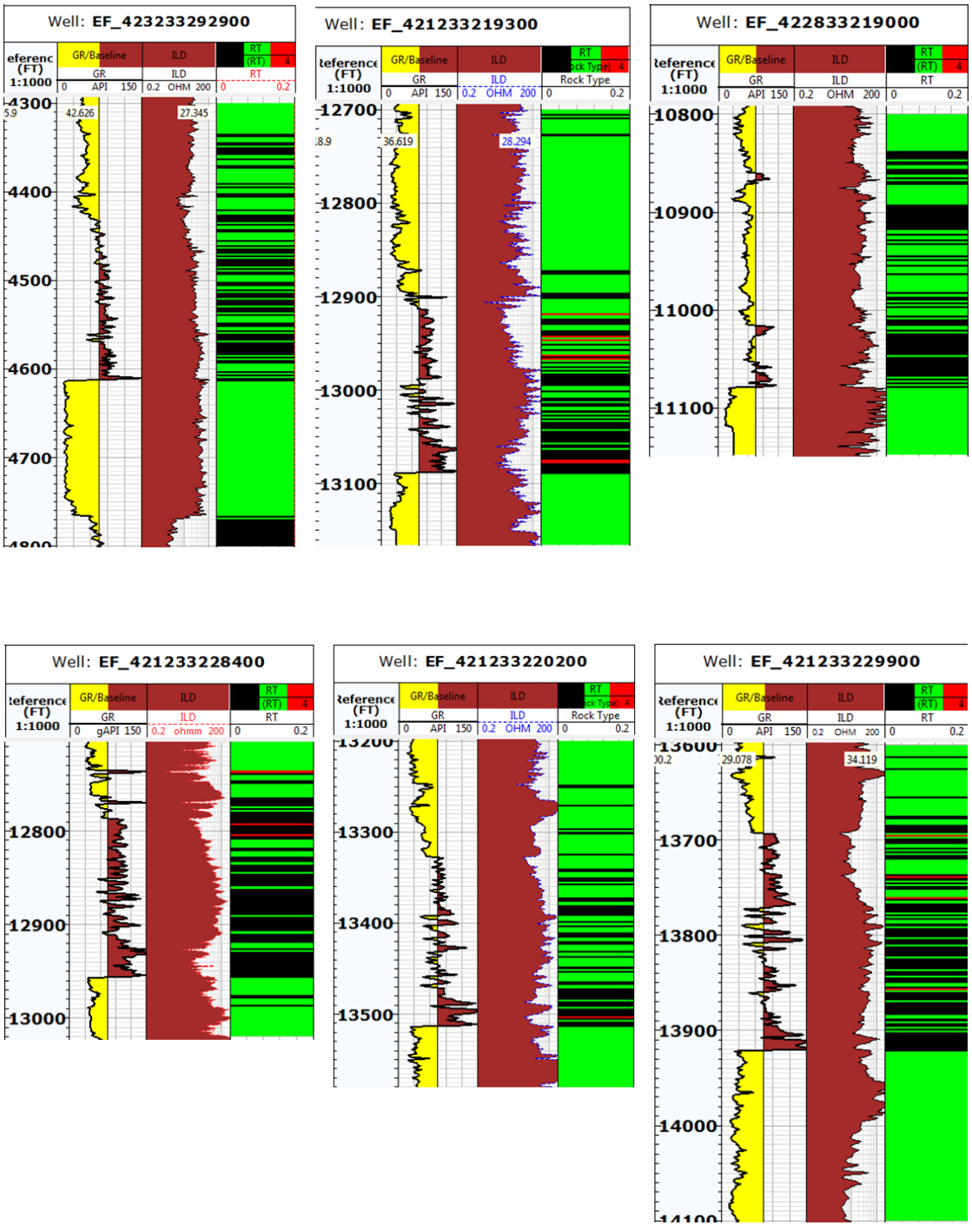

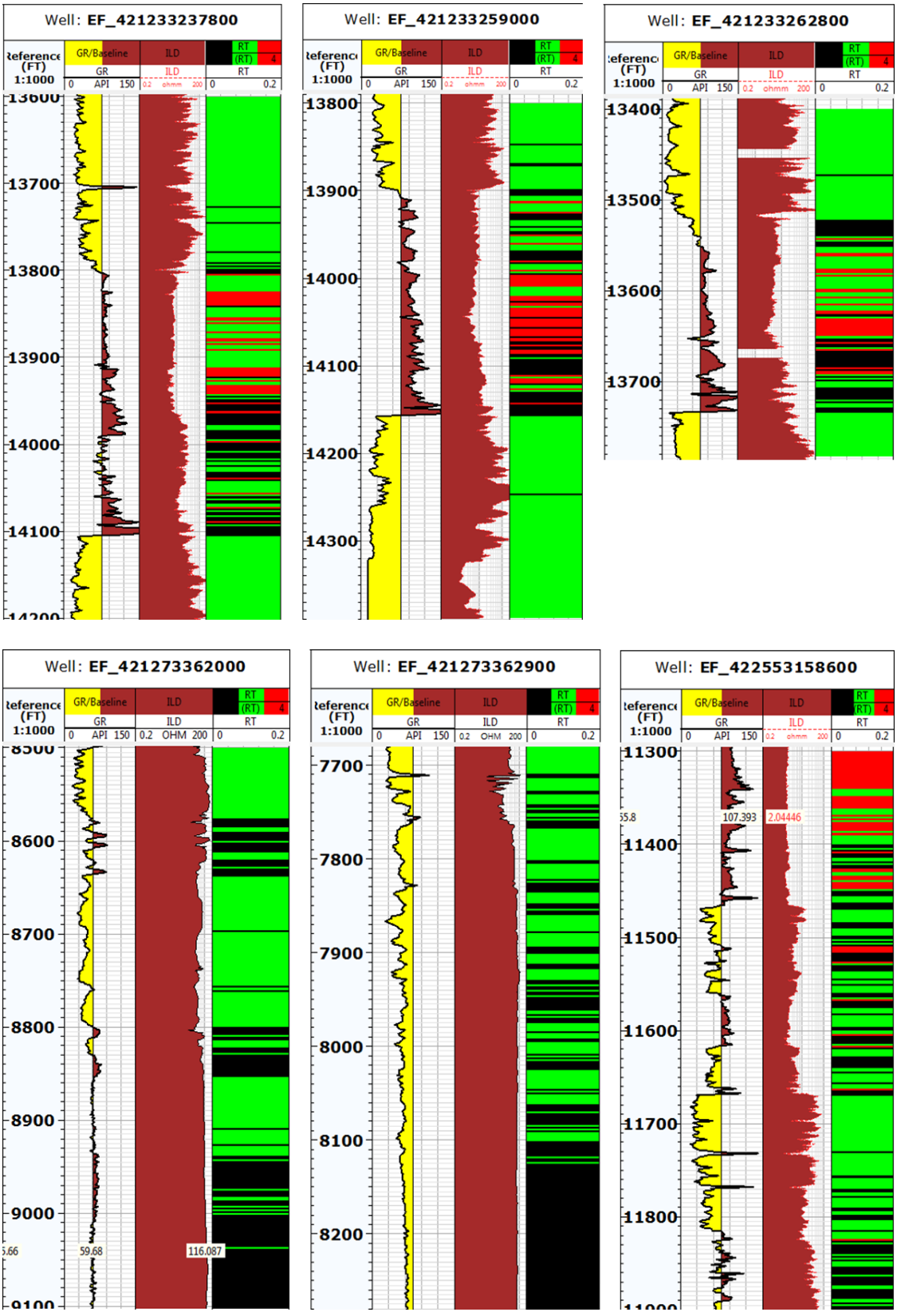
Well: EF_421233237800
Well: EF_421233259000
Well: EF_421233262800
Well: EF_421273362000
Well: EF_421273362900
Well: EF_422553158600
GR/Baseline
ILD
RT
(RT)
GR
API
OHM
1:1000
59.68
116.087
107.393
2.04446

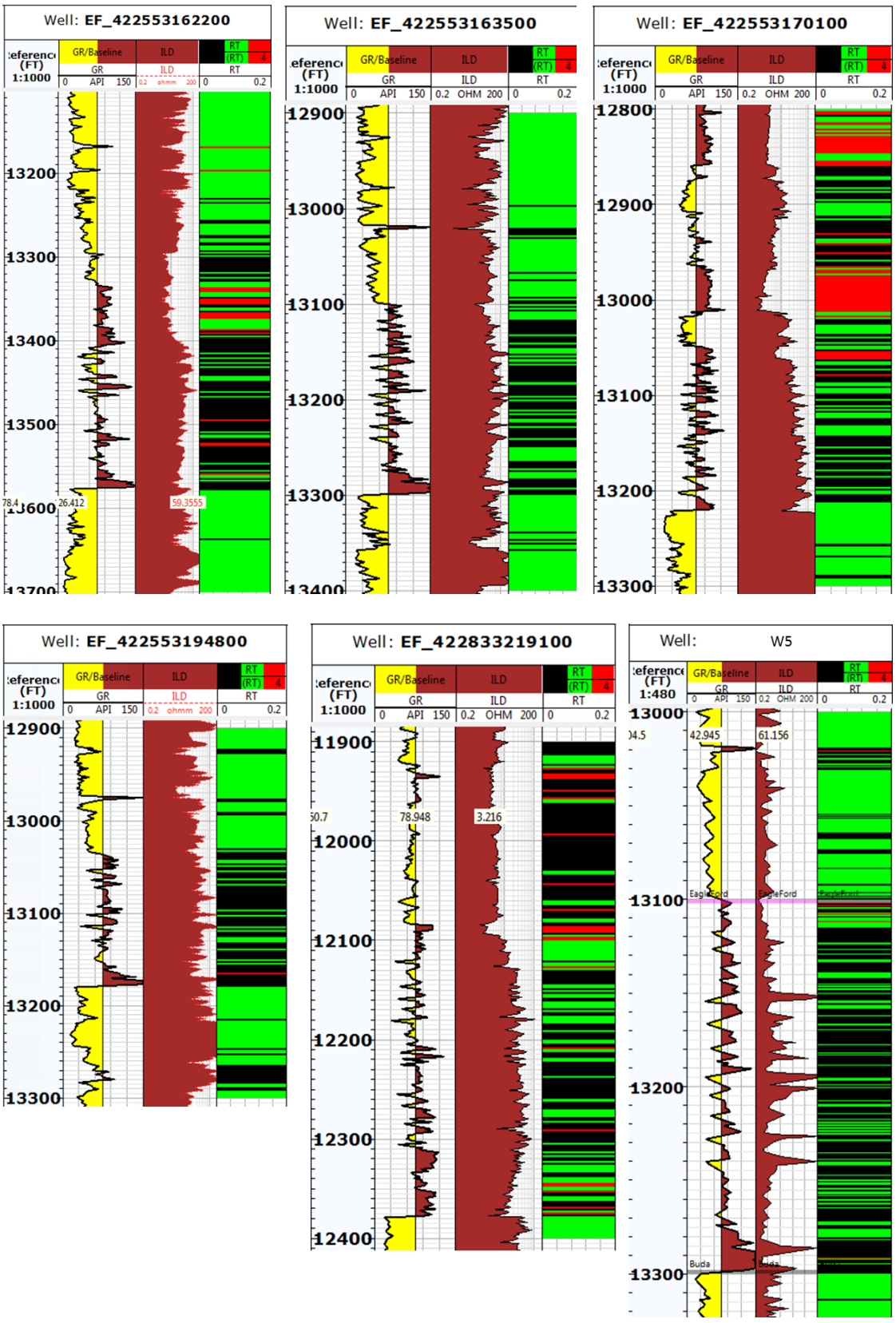
Well: EF_422553162200
Well: EF_422553163500
Well: EF_422553170100
Well: EF_422553194800
Well: EF_422833219100
Well: W5
GR/Baseline
ILD
RT
GR
ILD
RT
API
OHM
1:1000
1:480
26.412
59.3555
78.948
3.216
42.945
61.156
Buda

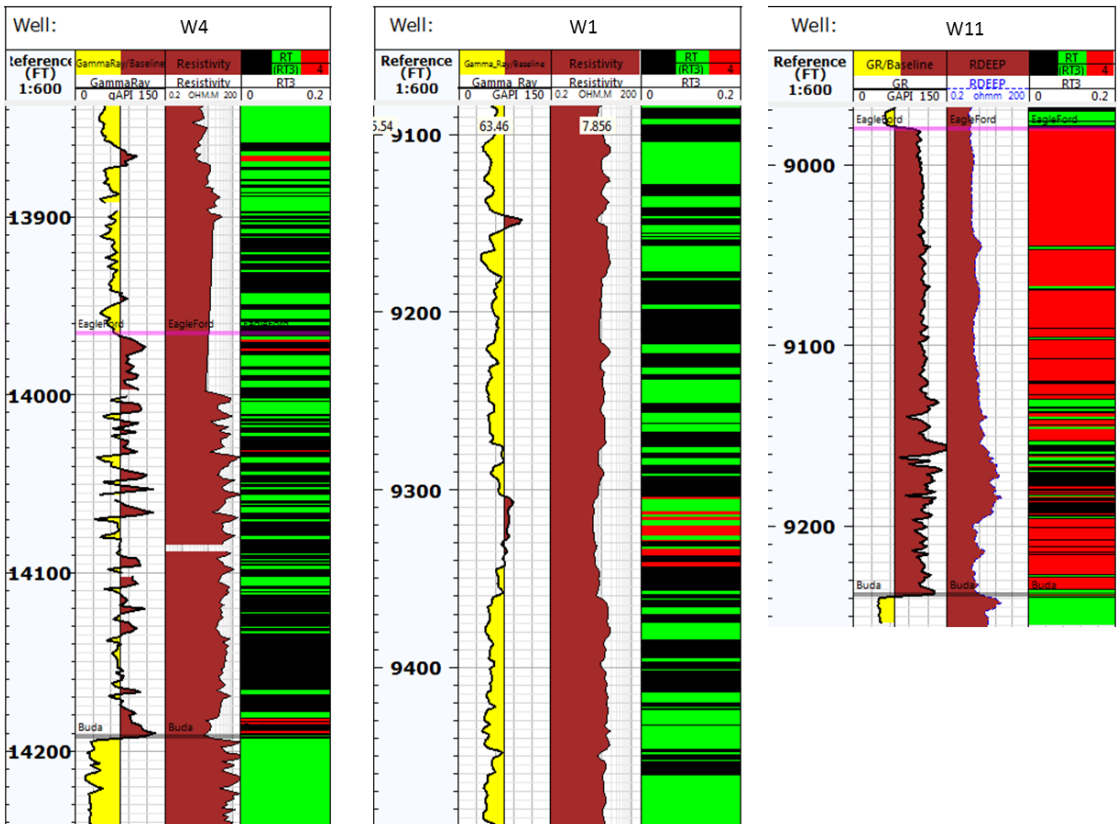
Well: W4
Reference (FT) 1:600
GammaRay/Baseline
Resistivity
RT (RT3)
GammaRay
Resistivity
RT3
0 gAPI 150
0.2 OHM.M 200
0 0.2
13900
14000
14100
14200
EagleFord
Buda
Well: W1
Reference (FT) 1:600
Gamma_Ray/Baseline
Resistivity
RT (RT3)
Gamma_Ray
Resistivity
RT3
0 GAPI 150
0.2 OHM.M 200
0 0.2
63.46
7.856
9100
9200
9300
9400
Well: W11
Reference (FT) 1:600
GR/Baseline
RDEEP
RT (RT3)
GR
RDEEP
RT3
0 GAPI 150
0.2 ohmm 200
0 0.2
9000
9100
9200
EagleFord
Buda

Appendix B: Rock Type logs for Barnett Wells

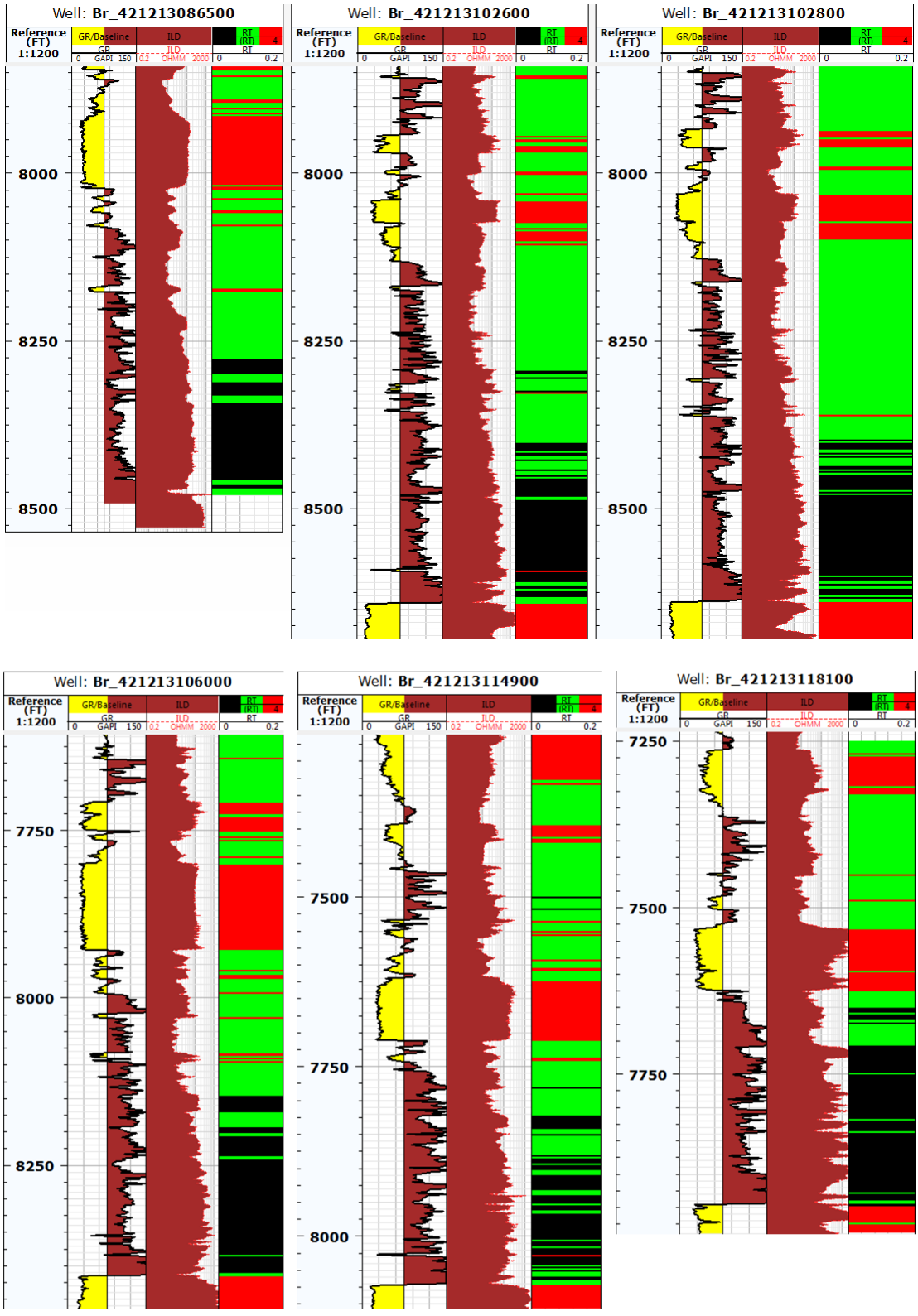

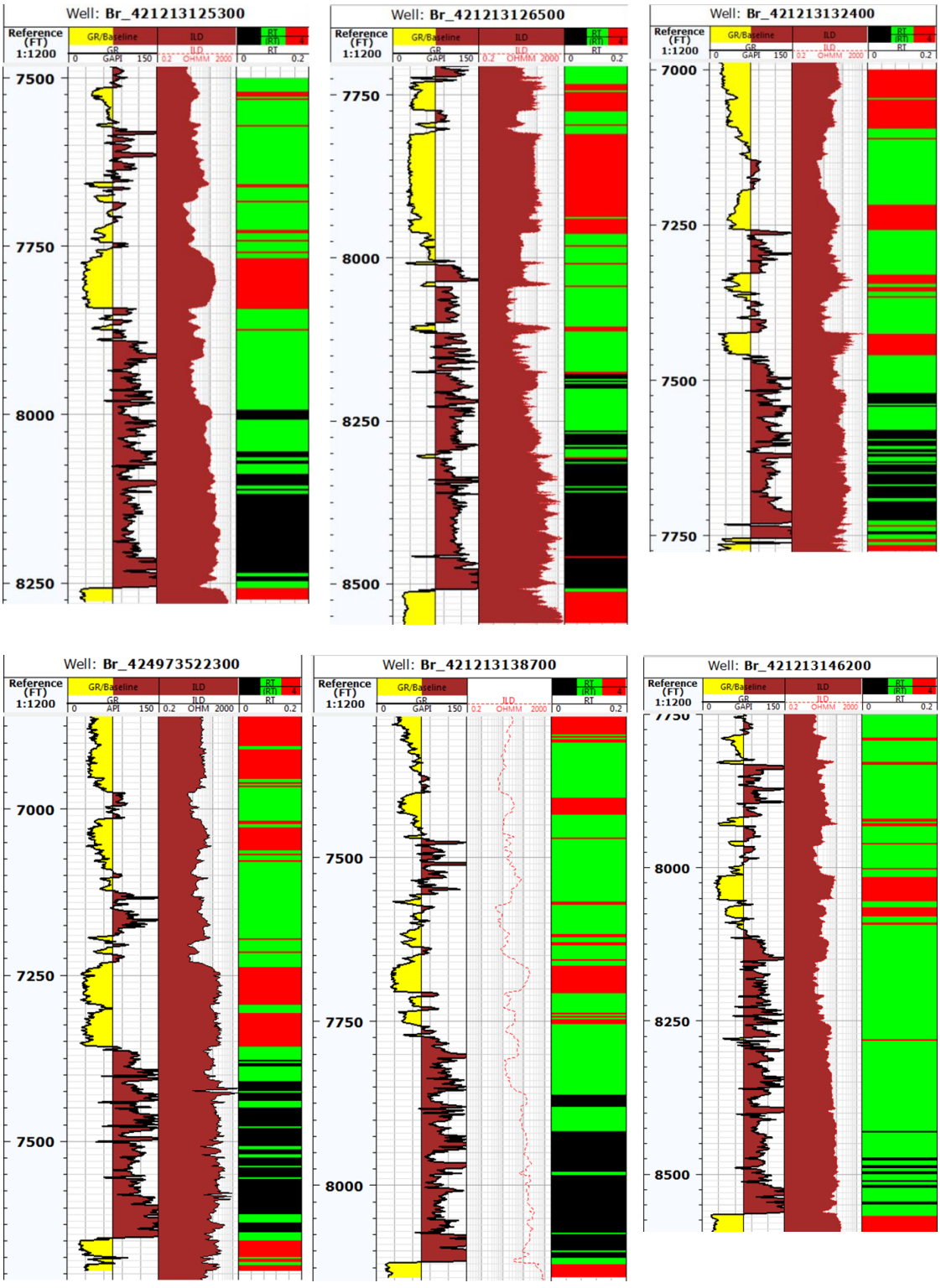
Well: Br_421213125300
Reference (FT) 1:1200
GR/Baseline
ILD
RT (RT)
GR
GAPI
ILD
OHMM
RT
7500
7750
8000
8250
Well: Br_421213126500
7750
8000
8250
8500
Well: Br_421213132400
7000
7250
7500
7750
Well: Br_424973522300
API
OHM
7000
7250
7500
Well: Br_421213138700
7500
7750
8000
Well: Br_421213146200
7750
8000
8250
8500

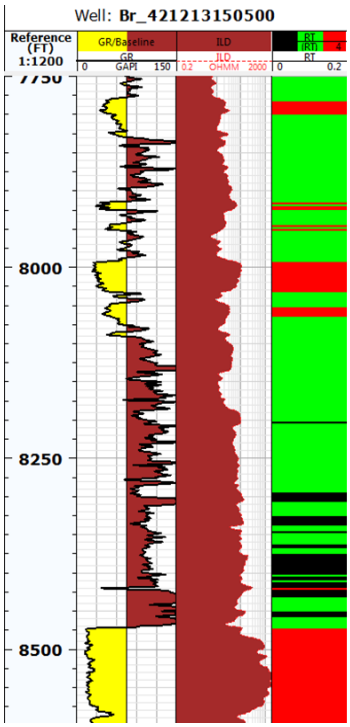
Well: Br_421213150500
Reference (FT) 1:1200
GR/Baseline
ILD
GR
GAPI
ILD
OHMM
RT
8000
8250
8500

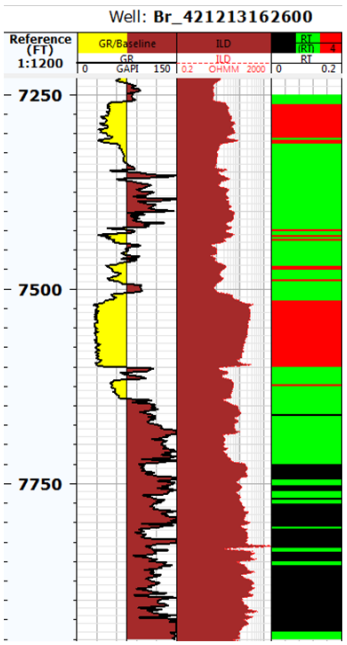
Well: Br_421213162600
Reference (FT) 1:1200
GR/Baseline
ILD
GR
GAPI
ILD
OHMM
RT
7250
7500
7750

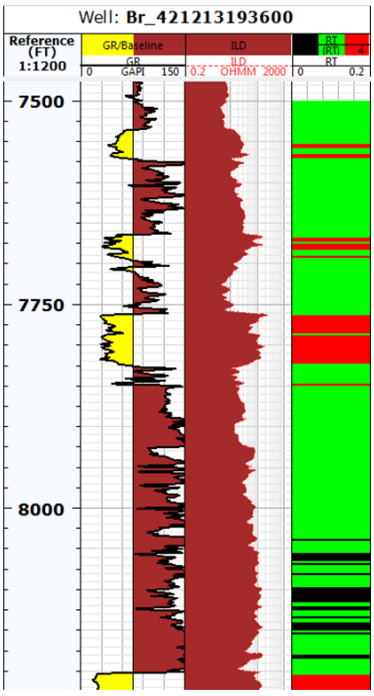
Well: Br_421213193600
Reference (FT) 1:1200
GR/Baseline
ILD
GR
GAPI
ILD
OHMM
RT
7500
7750
8000

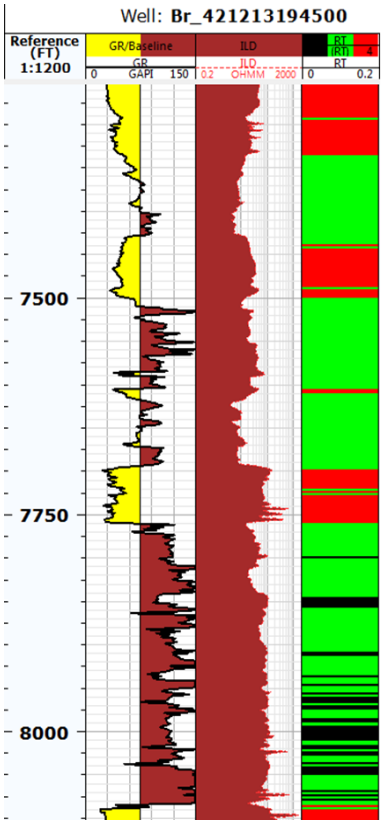
Well: Br_421213194500
Reference (FT) 1:1200
GR/Baseline
ILD
GR
GAPI
ILD
OHMM
RT
7500
7750
8000

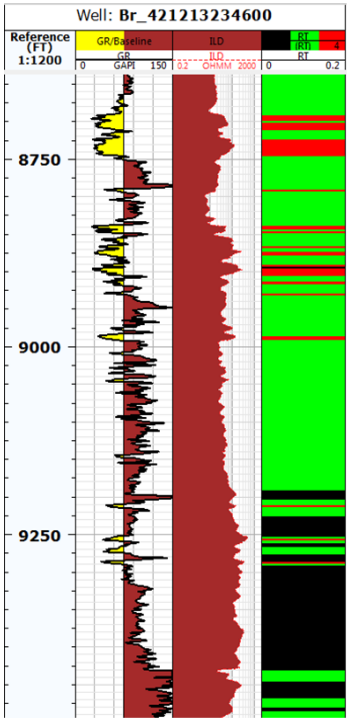
Well: Br_421213234600
Reference (FT) 1:1200
GR/Baseline
ILD
GR
GAPI
ILD
OHMM
RT
8750
9000
9250

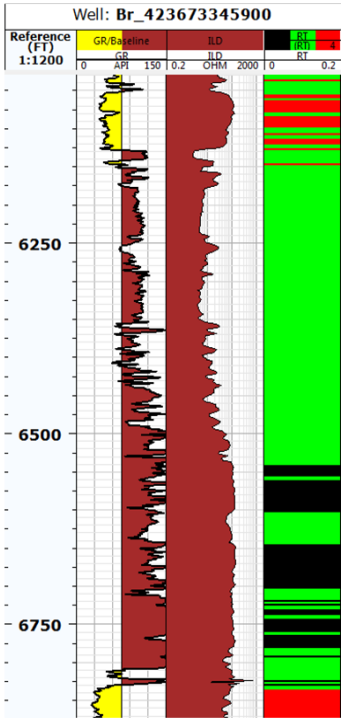
Well: Br_423673345900
Reference (FT) 1:1200
GR/Baseline
ILD
GR
API
ILD
OHM
RT
6250
6500
6750

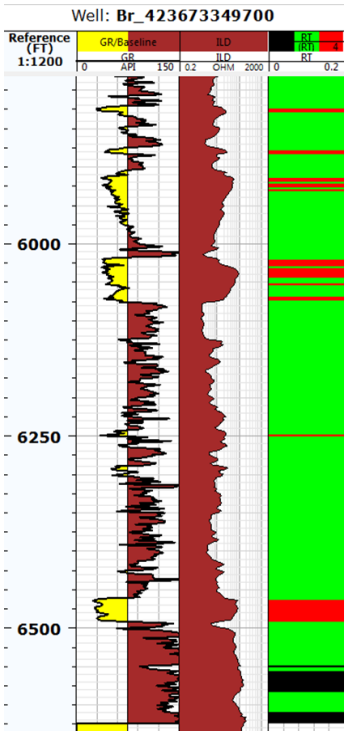
Well: Br_423673349700
Reference (FT) 1:1200
GR/Baseline
ILD
GR
ILD
RT
0 API 150
0.2 OHM 2000
0 0.2
6000
6250
6500

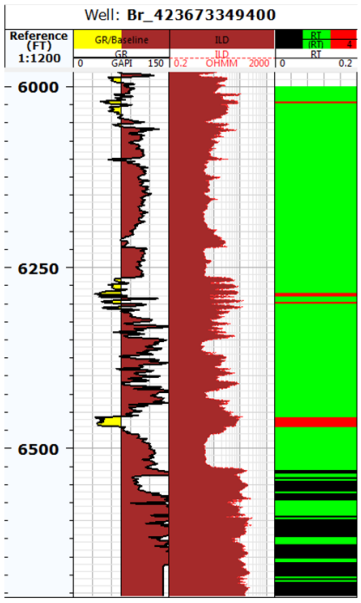
Well: Br_423673349400
Reference (FT) 1:1200
GR/Baseline
ILD
GR
ILD
RT
0 GAPI 150
0.2 OHMM 2000
0 0.2
6000
6250
6500

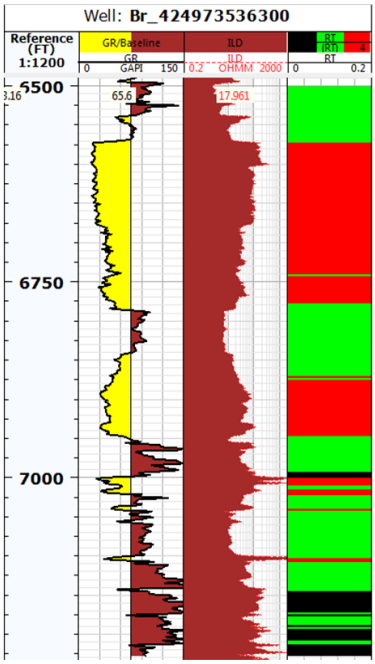
Well: Br_424973536300
Reference (FT) 1:1200
GR/Baseline
ILD
GR
ILD
RT
0 GAPI 150
0.2 OHMM 2000
0 0.2
6500
6750
7000
65.6
17.961

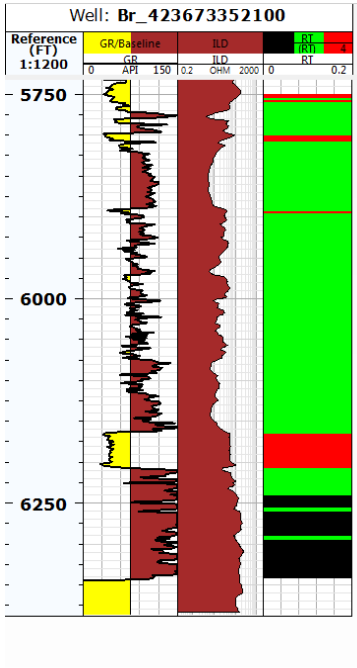
Well: Br_423673352100
Reference (FT) 1:1200
GR/Baseline
ILD
GR
ILD
RT
0 API 150
0.2 OHM 2000
0 0.2
5750
6000
6250

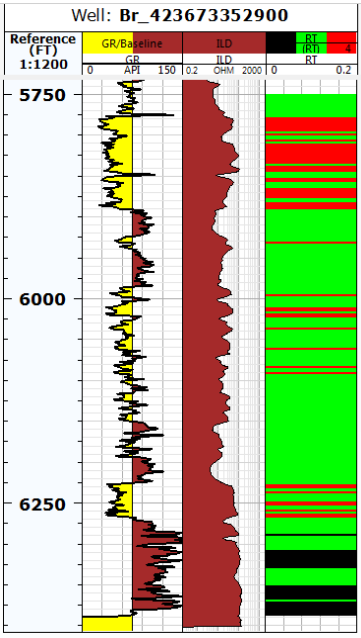
Well: Br_423673352900
Reference (FT) 1:1200
GR/Baseline
ILD
GR
ILD
RT
0 API 150
0.2 OHM 2000
0 0.2
5750
6000
6250

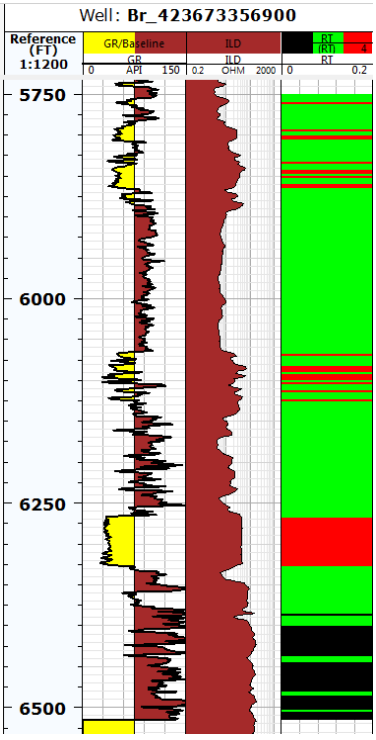
Well: Br_423673356900
Reference (FT) 1:1200
GR/Baseline
ILD
GR
ILD
RT
0 API 150
0.2 OHM 2000
0 0.2
5750
6000
6250
6500

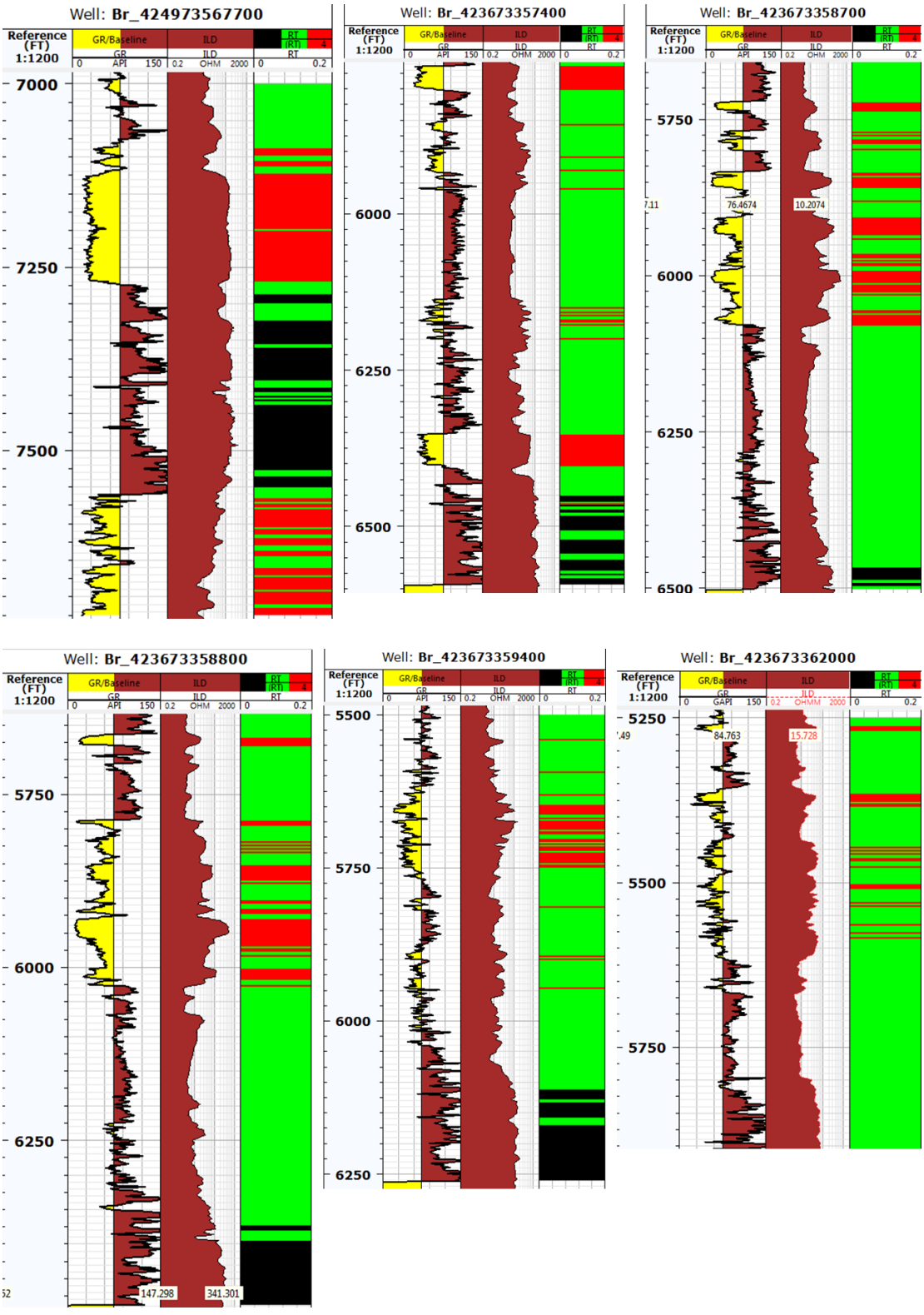
Well: Br_424973567700
Well: Br_423673357400
Well: Br_423673358700
Well: Br_423673358800
Well: Br_423673359400
Well: Br_423673362000
Reference (FT) 1:1200
GR/Baseline
ILD
GR
ILD
RT
API
OHM
GAPI
7000
7250
7500
6000
6250
6500
5750
5500
5250
76.4674
10.2074
147.298
341.301
84.763
15.728

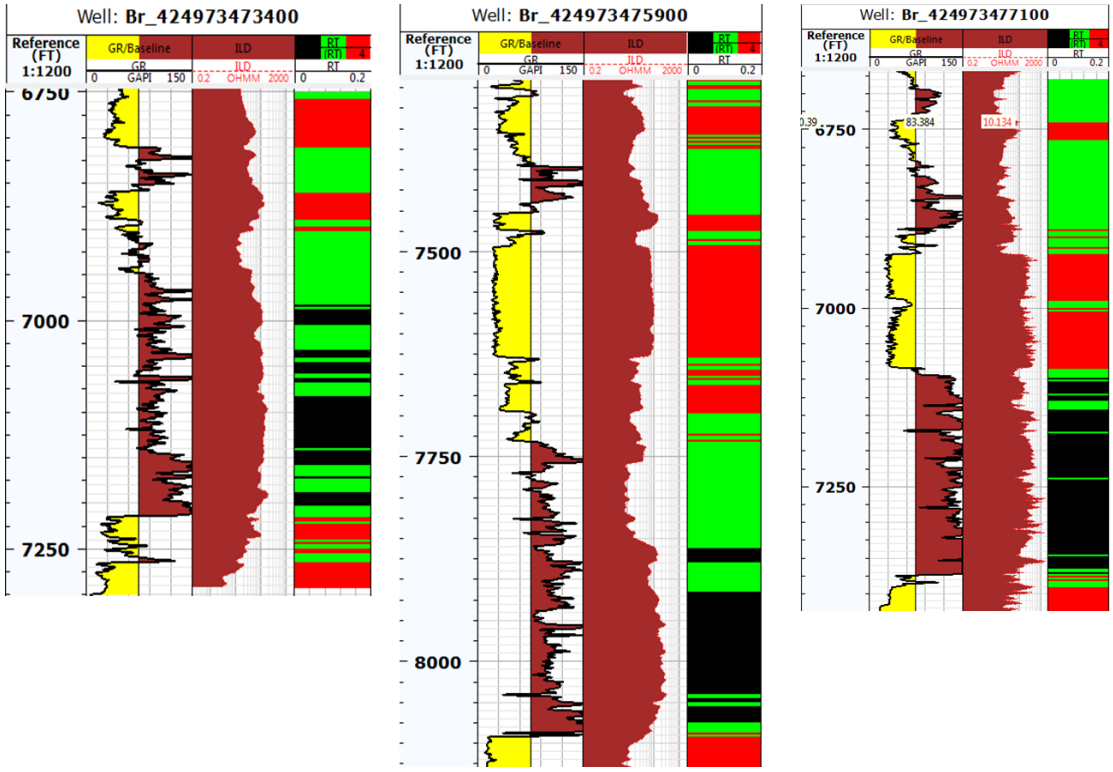
Well: Br_424973473400
Well: Br_424973475900
Well: Br_424973477100
Reference (FT) 1:1200
GR/Baseline
ILD
RT
GR
GAPI
ILD
OHMM
RT
6750
7000
7250
7500
7750
8000
83.384
10.134

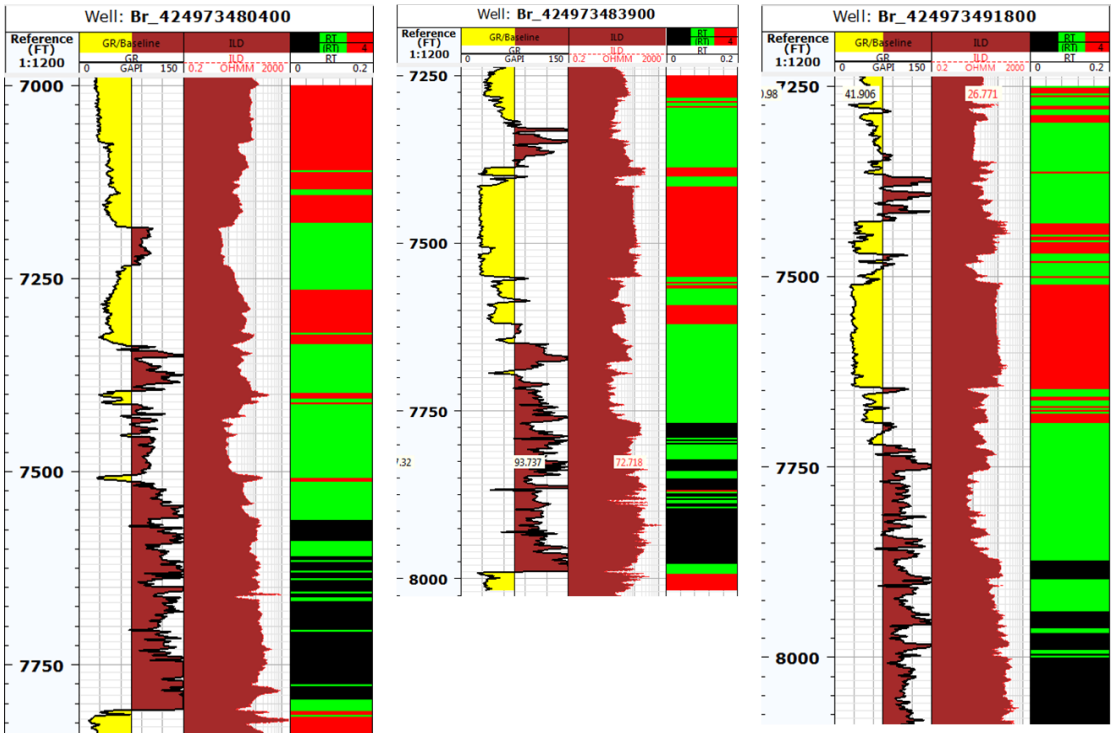
Well: Br_424973480400
Well: Br_424973483900
Well: Br_424973491800
Reference (FT) 1:1200
GR/Baseline
ILD
RT
GR
GAPI
ILD
OHMM
RT
7000
7250
7500
7750
8000
93.737
72.718
41.906
26.771

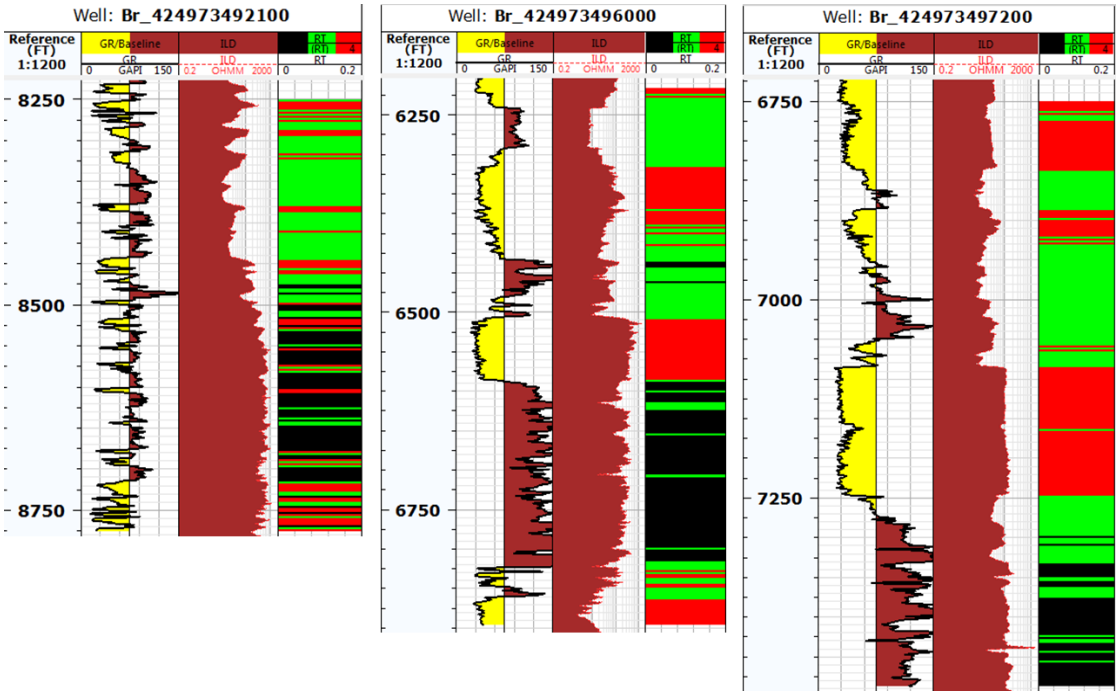
Well: Br_424973492100
Well: Br_424973496000
Well: Br_424973497200
Reference (FT) 1:1200
GR/Baseline
ILD
RT
GR
GAPI
ILD
OHMM
RT
8250
8500
8750
6250
6500
6750
6750
7000
7250

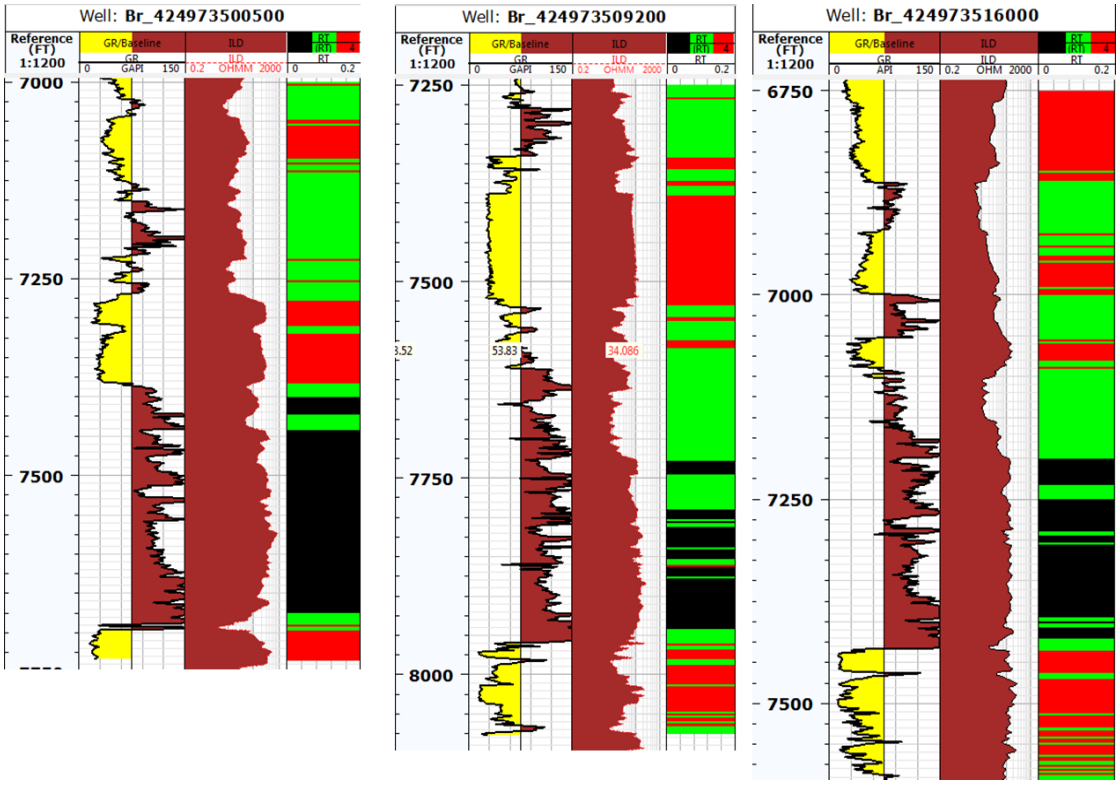
Well: Br_424973500500
Well: Br_424973509200
Well: Br_424973516000
Reference (FT) 1:1200
GR/Baseline
ILD
RT
GR
GAPI
API
ILD
OHMM
RT
7000
7250
7500
7250
7500
7750
8000
6750
7000
7250
7500
53.83
34.086

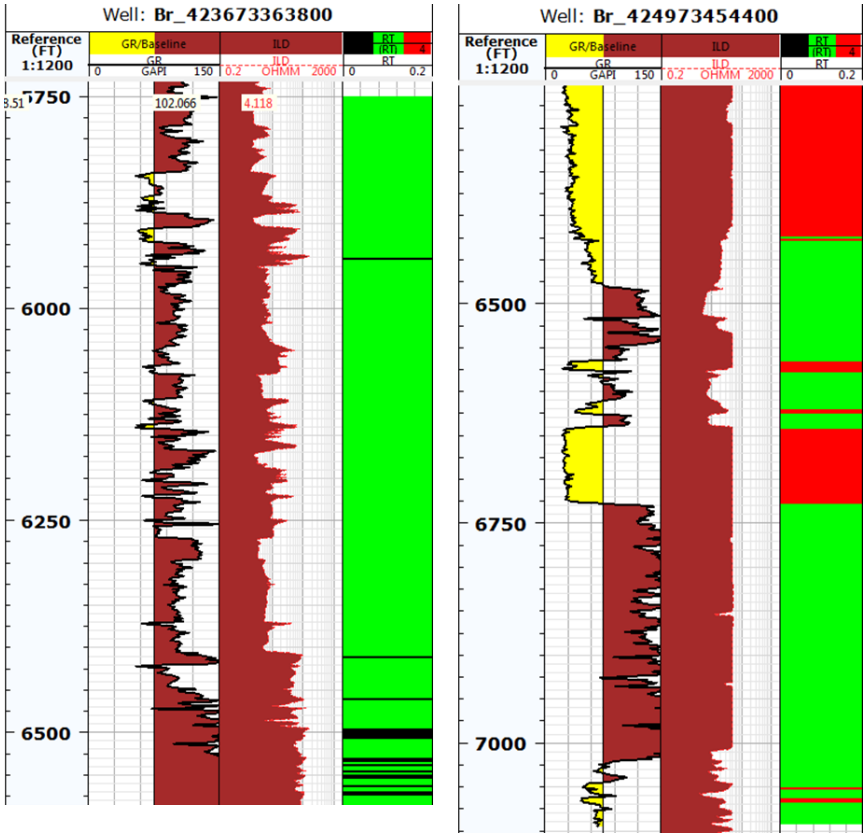
Well: Br_423673363800
Reference (FT) 1:1200
GR/Baseline
GR
GAPI
0
150
ILD
ILD
0.2
OHMM
2000
RT
IRh
4
0
0.2
102.066
4.118
6000
6250
6500
Well: Br_424973454400
Reference (FT) 1:1200
GR/Baseline
GR
GAPI
0
150
ILD
ILD
0.2
OHMM
2000
RT
IRh
4
0
0.2
6500
6750
7000

Appendix C: Rock Type logs for Woodford Wells

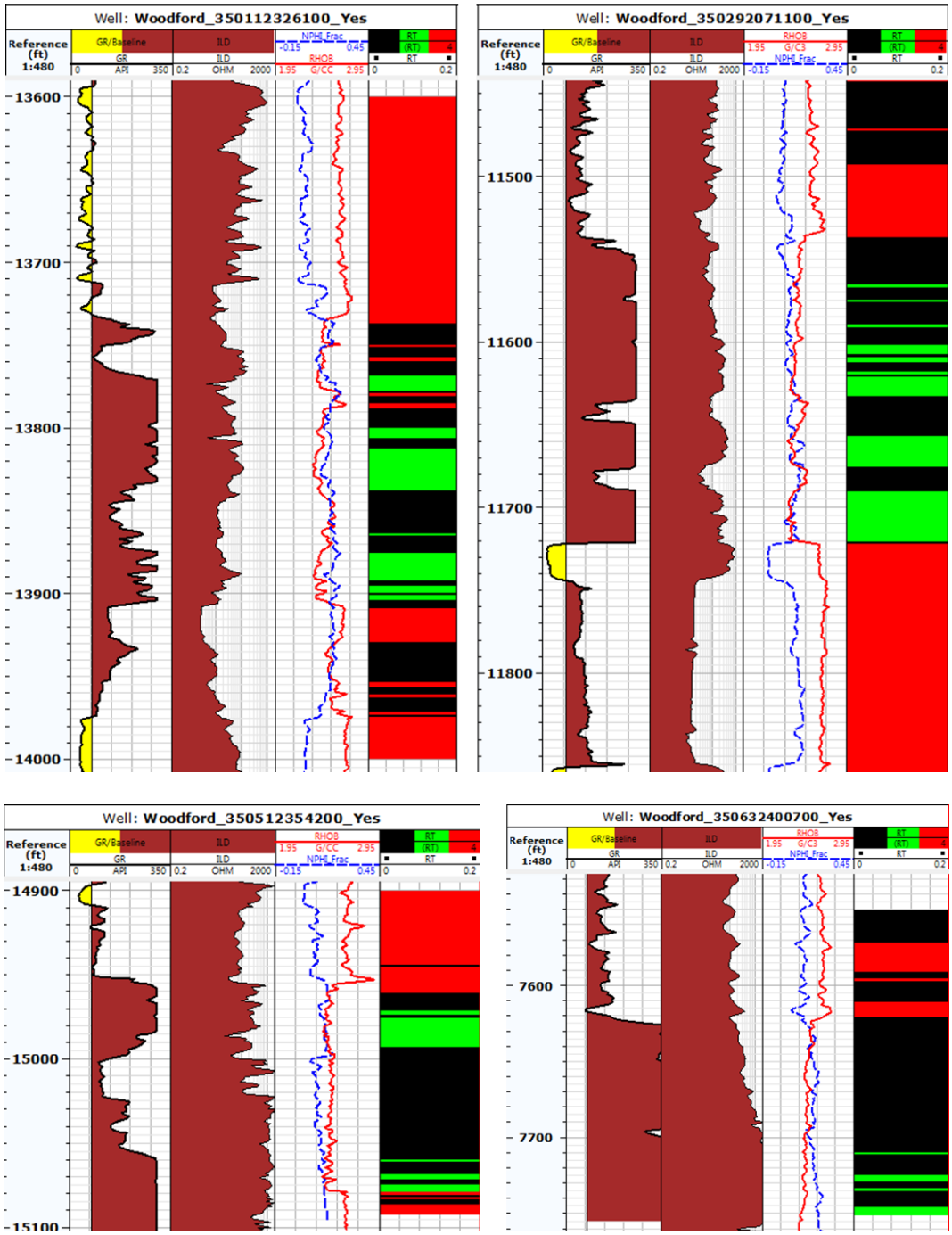

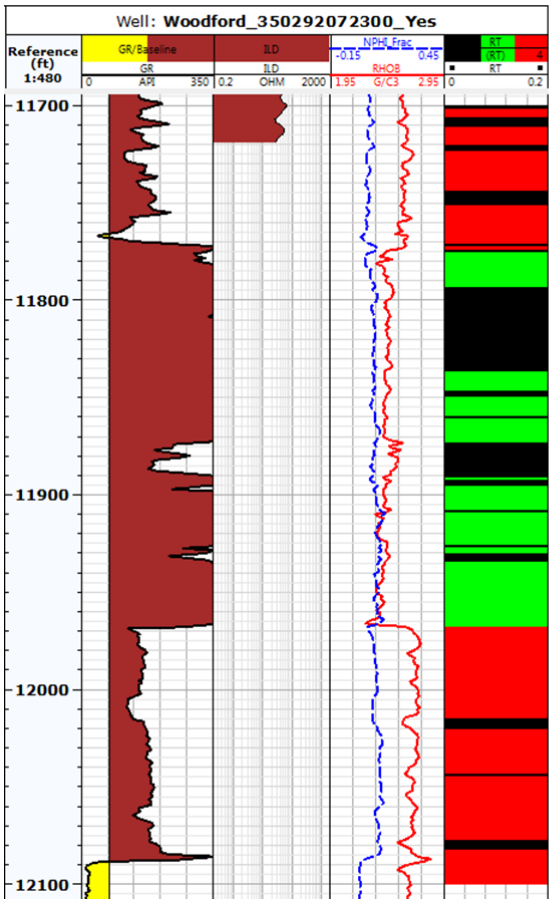
Well: Woodford_350292072300_Yes
Reference (ft) 1:480
GR/Baseline
ILD
NPHI_Frac
RT
GR
ILD
RHOB
(RT)
0 API 350
0.2 OHM 2000
-0.15 0.45
1.95 G/C3 2.95
0 0.2
11700
11800
11900
12000
12100

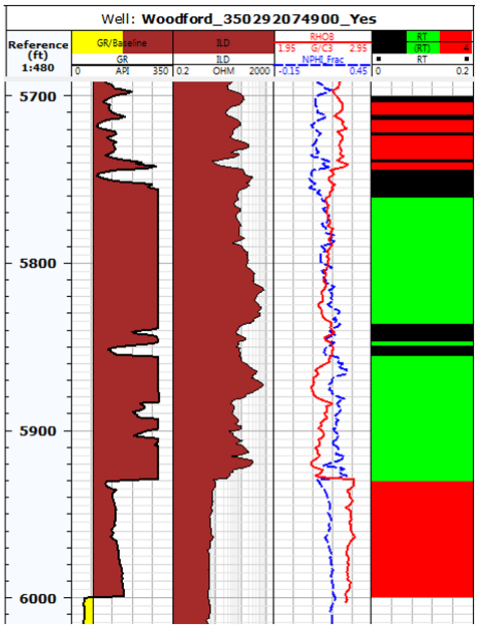
Well: Woodford_350292074900_Yes
Reference (ft) 1:480
GR/Baseline
ILD
RHOB
RT
GR
NPHI_Frac
(RT)
0 API 350
0.2 OHM 2000
1.95 G/C3 2.95
-0.15 0.45
0 0.2
5700
5800
5900
6000

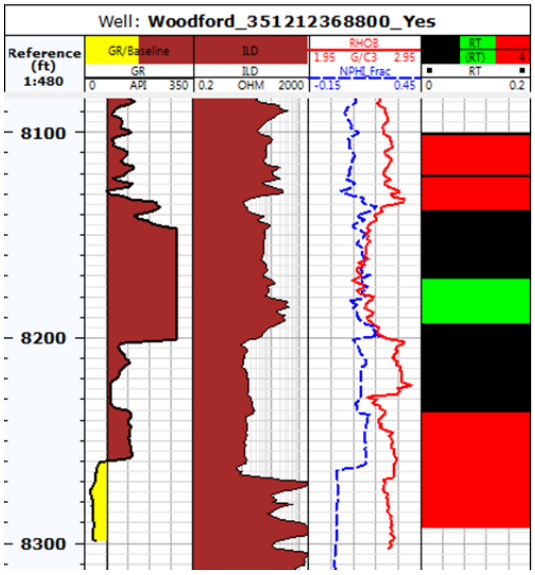
Well: Woodford_351212368800_Yes
Reference (ft) 1:480
GR/Baseline
ILD
RHOB
RT
GR
NPHI_Frac
(RT)
0 API 350
0.2 OHM 2000
1.95 G/C3 2.95
-0.15 0.45
0 0.2
8100
8200
8300

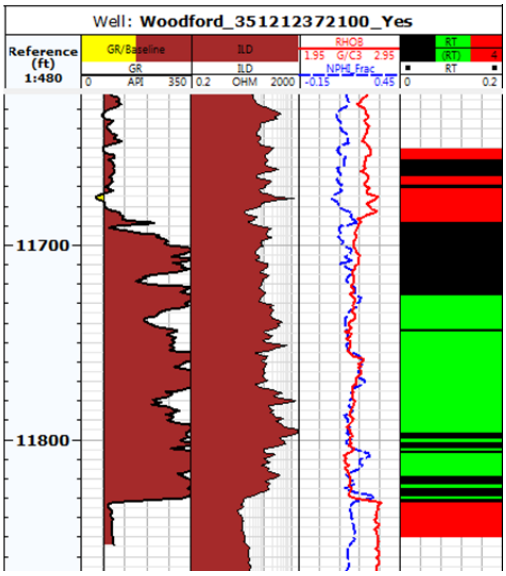
Well: Woodford_351212372100_Yes
Reference (ft) 1:480
GR/Baseline
ILD
RHOB
RT
GR
NPHI_Frac
(RT)
0 API 350
0.2 OHM 2000
1.95 G/C3 2.95
-0.15 0.45
0 0.2
11700
11800

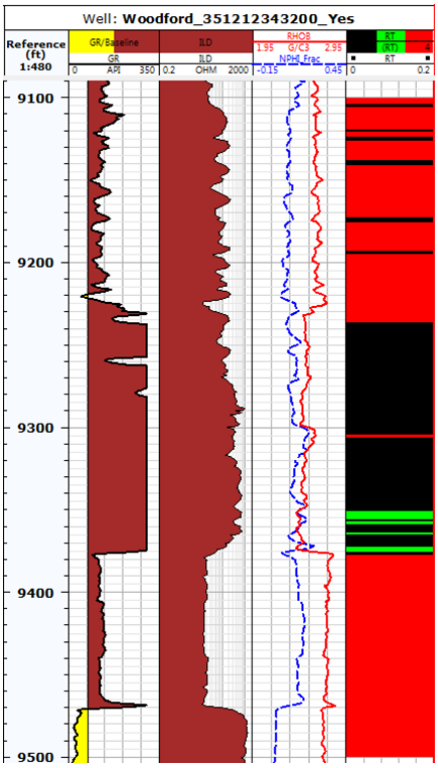

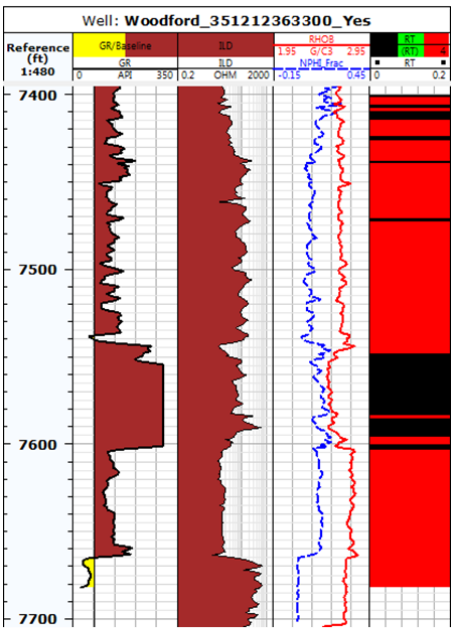

Well : 21

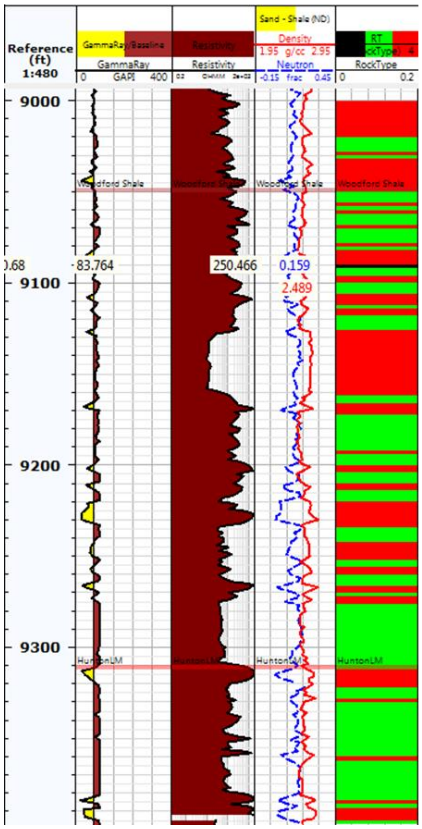

Well : WF_350632417000

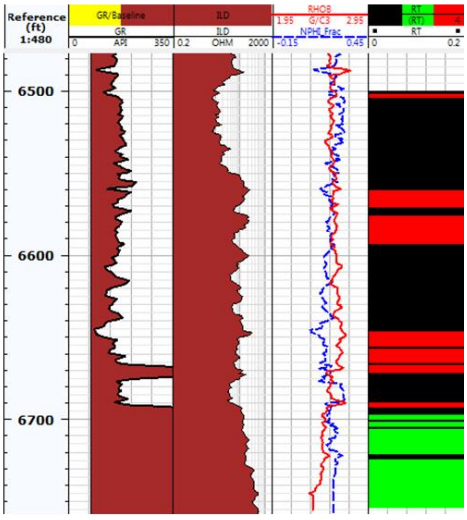

Well : 22

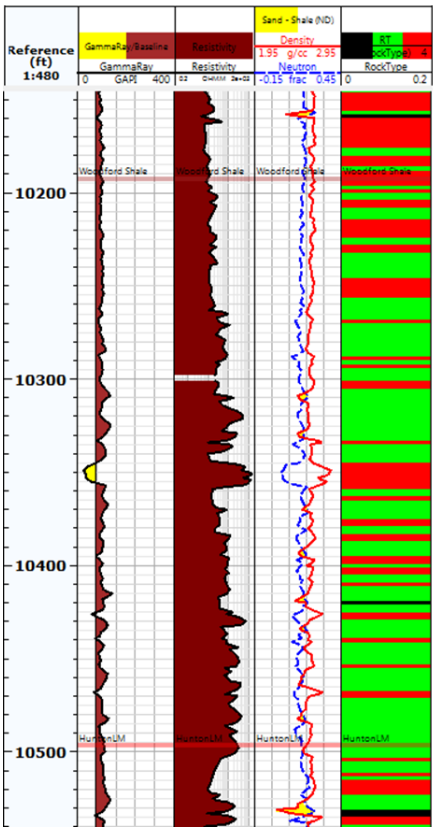

Well : 17

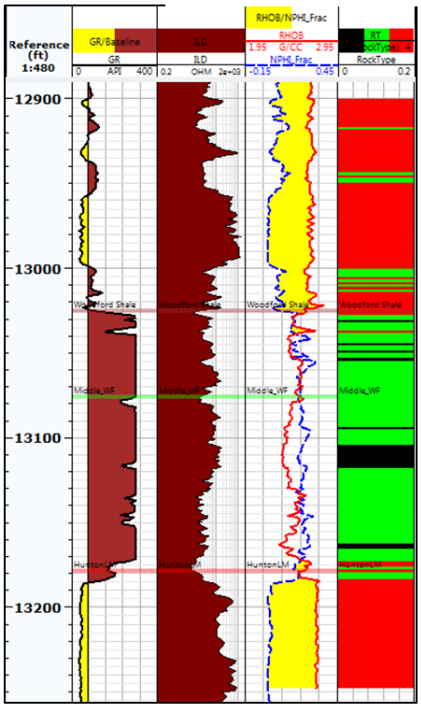

Well : 19

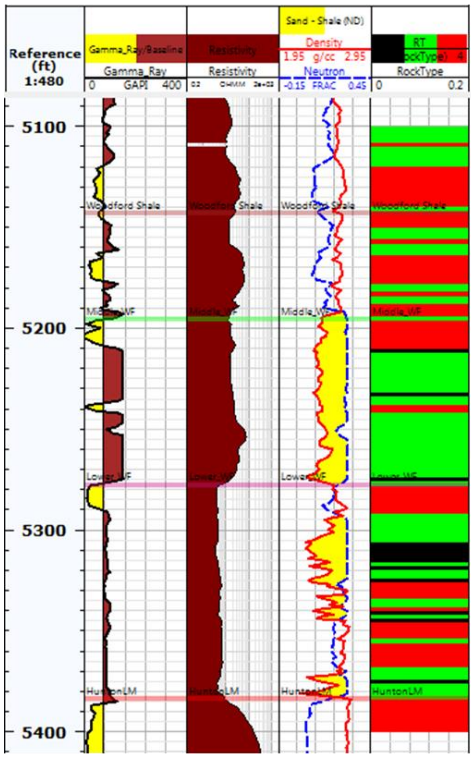

Well : 20

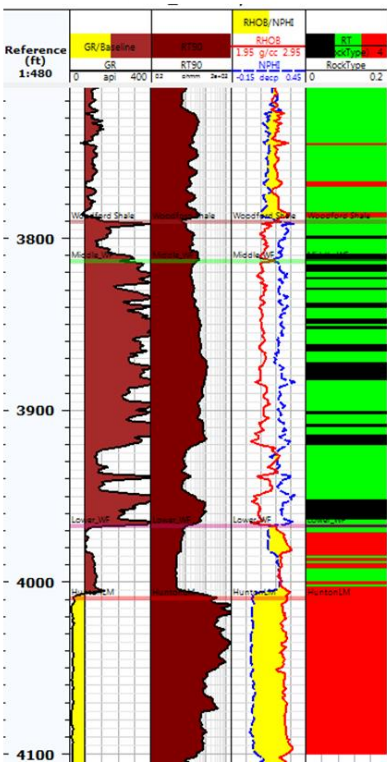

Appendix D: Rock Type logs for Wolfcamp Wells

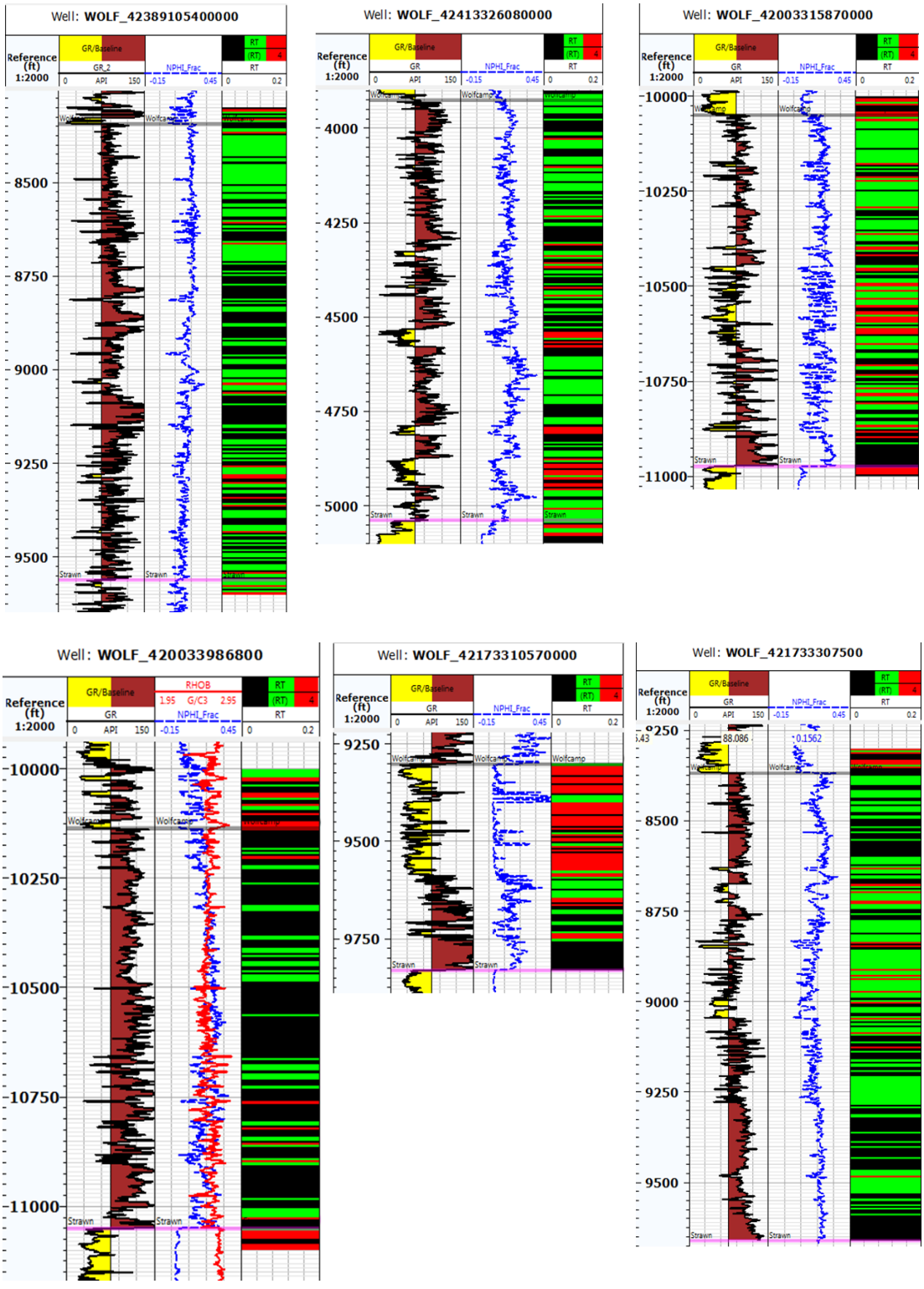

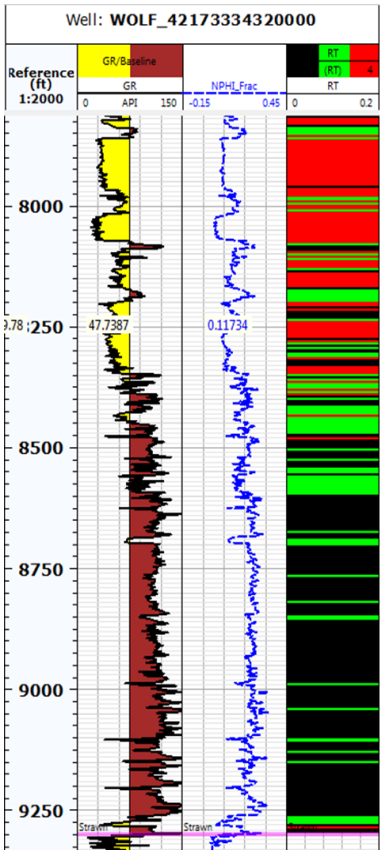
Well: WOLF_42173334320000
Reference (ft) 1:2000
GR/Baseline
GR
NPHI_Frac
RT
0 API 150
-0.15 0.45
0 0.2
8000
8250
8500
8750
9000
9250
47.7387
0.11734
Strawn

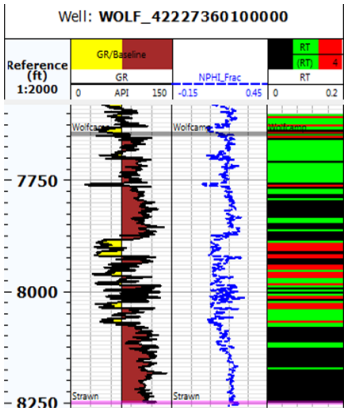
Well: WOLF_42227360100000
Reference (ft) 1:2000
GR/Baseline
GR
NPHI_Frac
RT
7750
8000
8250
Wolfcamp
Strawn

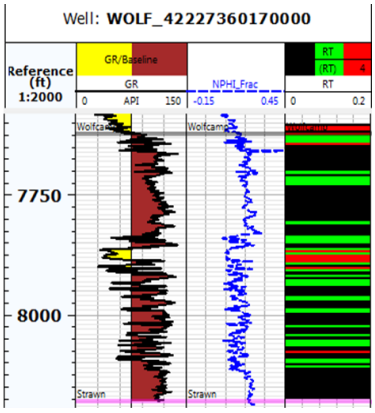
Well: WOLF_42227360170000
Reference (ft) 1:2000
GR/Baseline
GR
NPHI_Frac
RT
7750
8000
Wolfcamp
Strawn

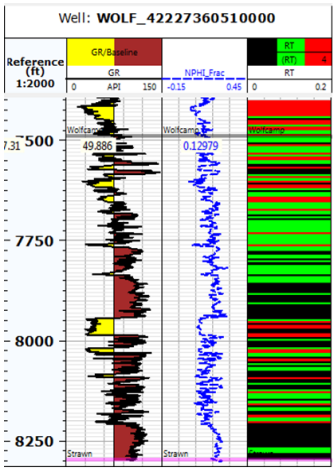
Well: WOLF_42227360510000
Reference (ft) 1:2000
GR/Baseline
GR
NPHI_Frac
RT
7500
7750
8000
8250
49.886
0.12979
Wolfcamp
Strawn

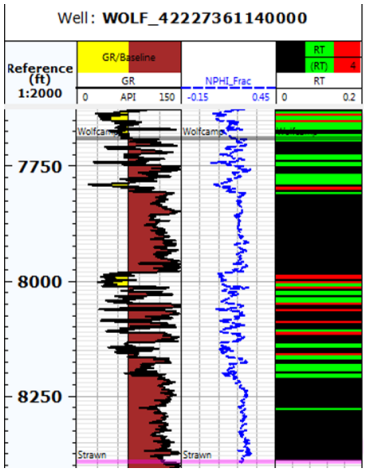
Well: WOLF_42227361140000
Reference (ft) 1:2000
GR/Baseline
GR
NPHI_Frac
RT
7750
8000
8250
Wolfcamp
Strawn

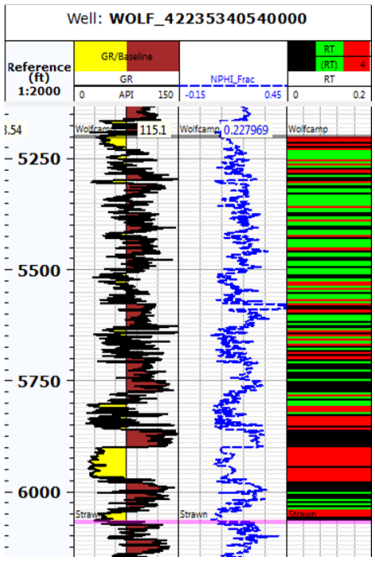
Well: WOLF_42235340540000
Reference (ft) 1:2000
GR/Baseline
GR
NPHI_Frac
RT
5250
5500
5750
6000
115.1
0.227969
Wolfcamp
Strawn

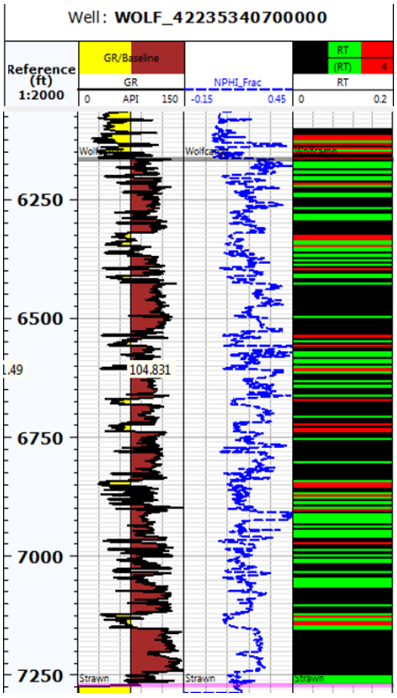
Well: WOLF_42235340700000
Reference (ft) 1:2000
GR/Baseline
GR
NPHI_Frac
RT
0 API 150
-0.15 0.45
0 0.2
6250
6500
6750
7000
7250
104.831
Wolfcamp
Strawn

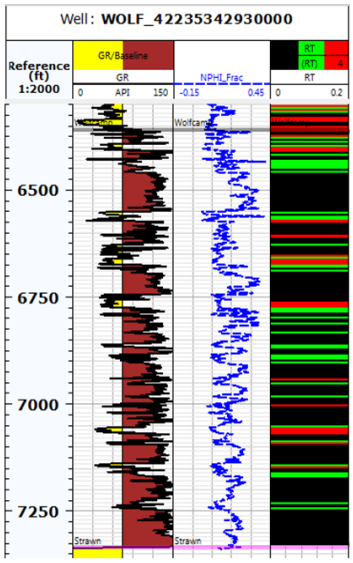
Well: WOLF_42235342930000
Reference (ft) 1:2000
GR/Baseline
GR
NPHI_Frac
RT
0 API 150
-0.15 0.45
0 0.2
6500
6750
7000
7250
Wolfcamp
Strawn

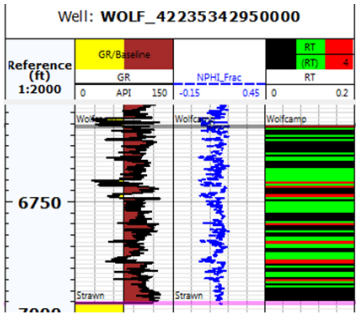
Well: WOLF_42235342950000
Reference (ft) 1:2000
GR/Baseline
GR
NPHI_Frac
RT
0 API 150
-0.15 0.45
0 0.2
6750
Wolfcamp
Strawn

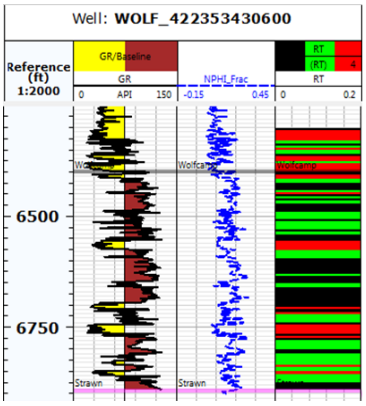
Well: WOLF_422353430600
Reference (ft) 1:2000
GR/Baseline
GR
NPHI_Frac
RT
0 API 150
-0.15 0.45
0 0.2
6500
6750
Wolfcamp
Strawn

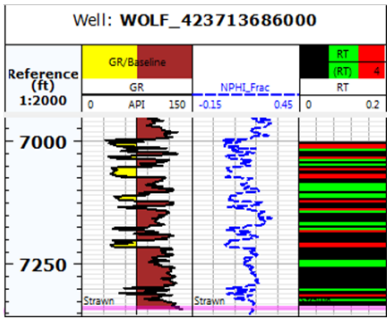
Well: WOLF_423713686000
Reference (ft) 1:2000
GR/Baseline
GR
NPHI_Frac
RT
0 API 150
-0.15 0.45
0 0.2
7000
7250
Wolfcamp
Strawn

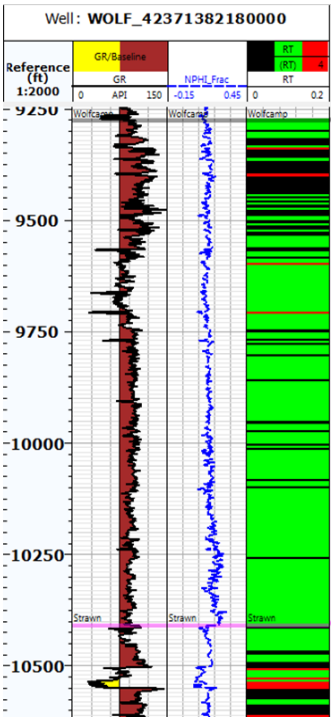
Well: WOLF_42371382180000
Reference (ft) 1:2000
GR/Baseline
GR
NPHI_Frac
RT
0 API 150
-0.15 0.45
0 0.2
9500
9750
10000
10250
10500
Wolfcamp
Strawn

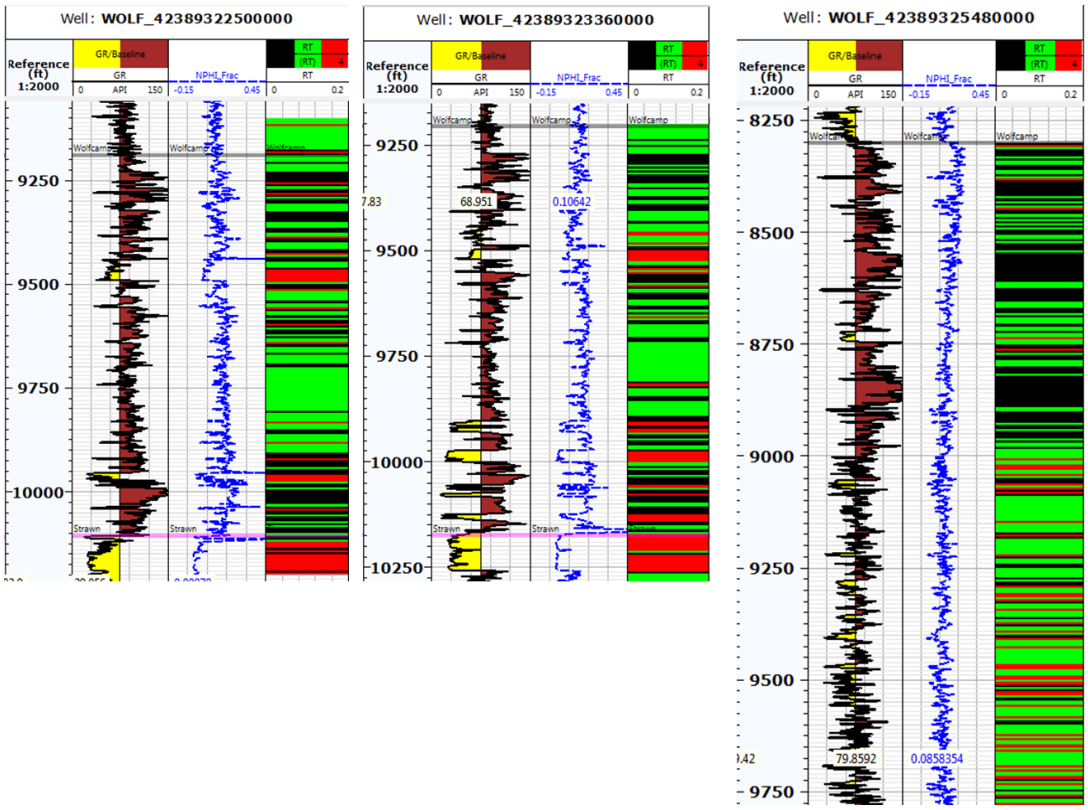
Well: WOLF_42389322500000
Well: WOLF_42389323360000
Well: WOLF_42389325480000
Reference (ft) 1:2000
GR/Baseline
GR
NPHI_Frac
RT
Wolfcamp
Strawn
68.951
0.10642
79.8592
0.0858354

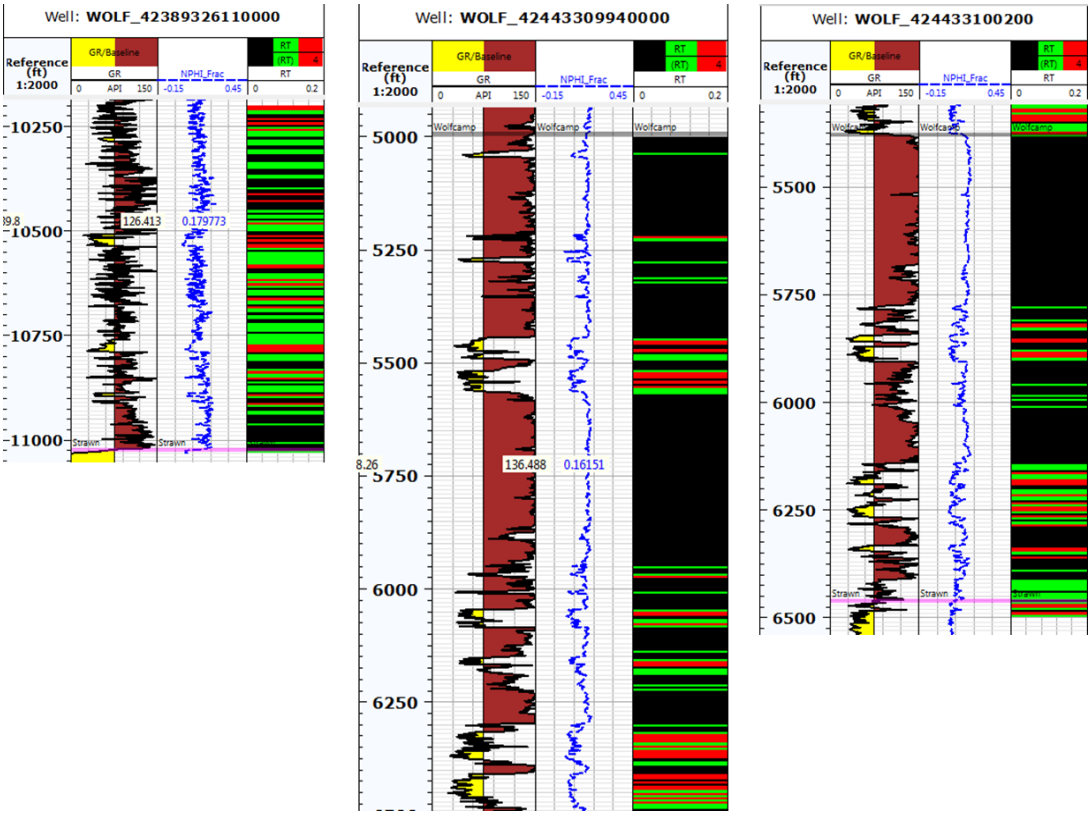
Well: WOLF_42389326110000
Well: WOLF_42443309940000
Well: WOLF_424433100200
Reference (ft) 1:2000
GR/Baseline
GR
NPHI_Frac
RT
Wolfcamp
Strawn
126.413
0.179773
136.488
0.16151

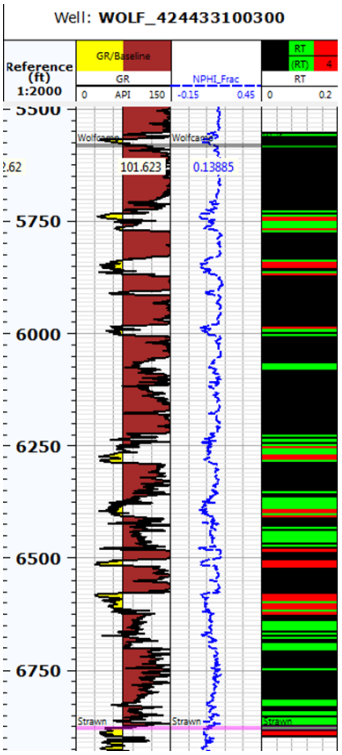
Well: WOLF_424433100300
Reference (ft) 1:2000
GR/Baseline
GR
NPHI_Frac
RT
0 API 150
-0.15 0.45
0 0.2
101.623
0.13885
Wolfcamp
Strawn
5500
5750
6000
6250
6500
6750

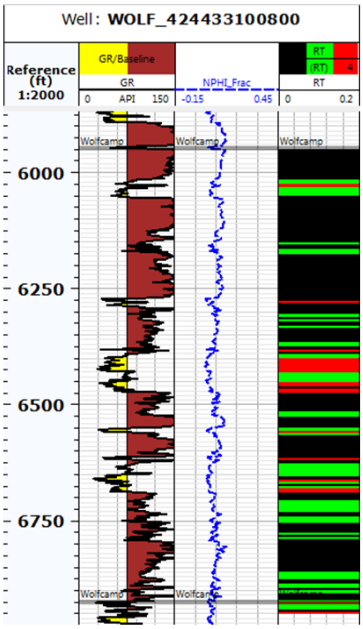
Well: WOLF_424433100800
Reference (ft) 1:2000
GR/Baseline
GR
NPHI_Frac
RT
0 API 150
-0.15 0.45
0 0.2
Wolfcamp
6000
6250
6500
6750

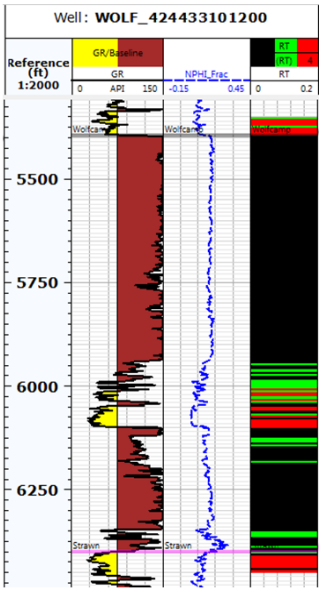
Well: WOLF_424433101200
Reference (ft) 1:2000
GR/Baseline
GR
NPHI_Frac
RT
0 API 150
-0.15 0.45
0 0.2
Wolfcamp
Strawn
5500
5750
6000
6250

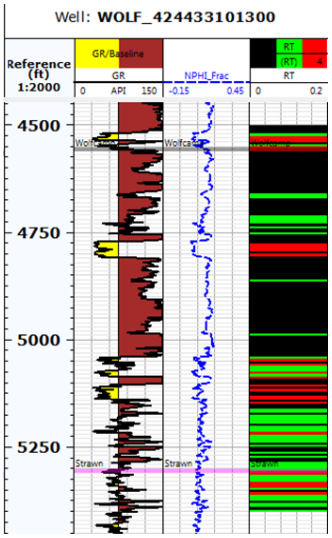
Well: WOLF_424433101300
Reference (ft) 1:2000
GR/Baseline
GR
NPHI_Frac
RT
0 API 150
-0.15 0.45
0 0.2
Wolfcamp
Strawn
4500
4750
5000
5250

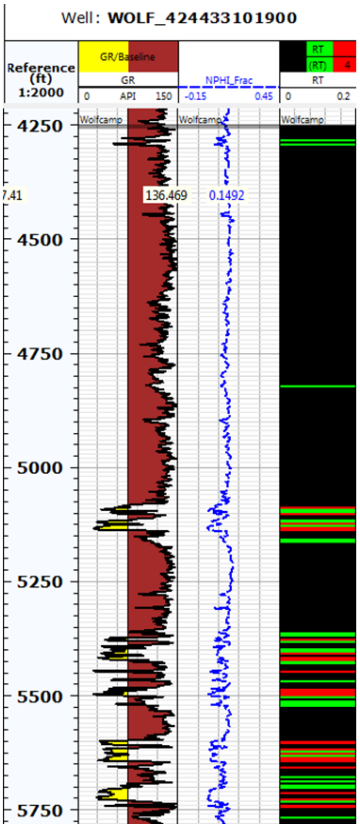
Well: WOLF_424433101900
Reference (ft) 1:2000
GR/Baseline
GR
NPHI_Frac
RT
0 API 150
-0.15 0.45
0 0.2
136.469
0.1492
Wolfcamp
4250
4500
4750
5000
5250
5500
5750

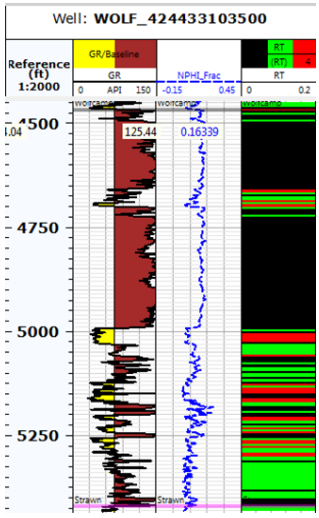
Well: WOLF_424433103500
Reference (ft) 1:2000
GR/Baseline
GR
NPHI_Frac
RT
0 API 150
-0.15 0.45
0 0.2
125.44
0.16339
Wolfcamp
Strawn
4750
5000
5250

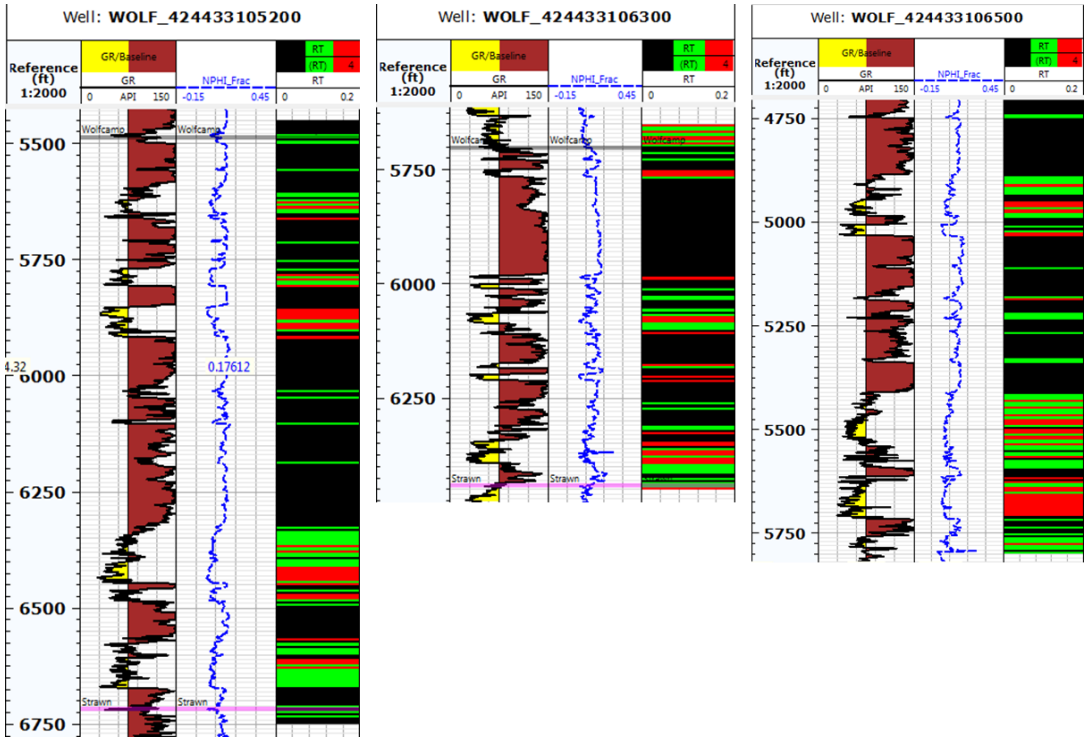
Well: WOLF_424433105200
Well: WOLF_424433106300
Well: WOLF_424433106500
Reference (ft) 1:2000
GR/Baseline
GR
NPHI_Frac
RT
Wolfcamp
Strawn
0.17612

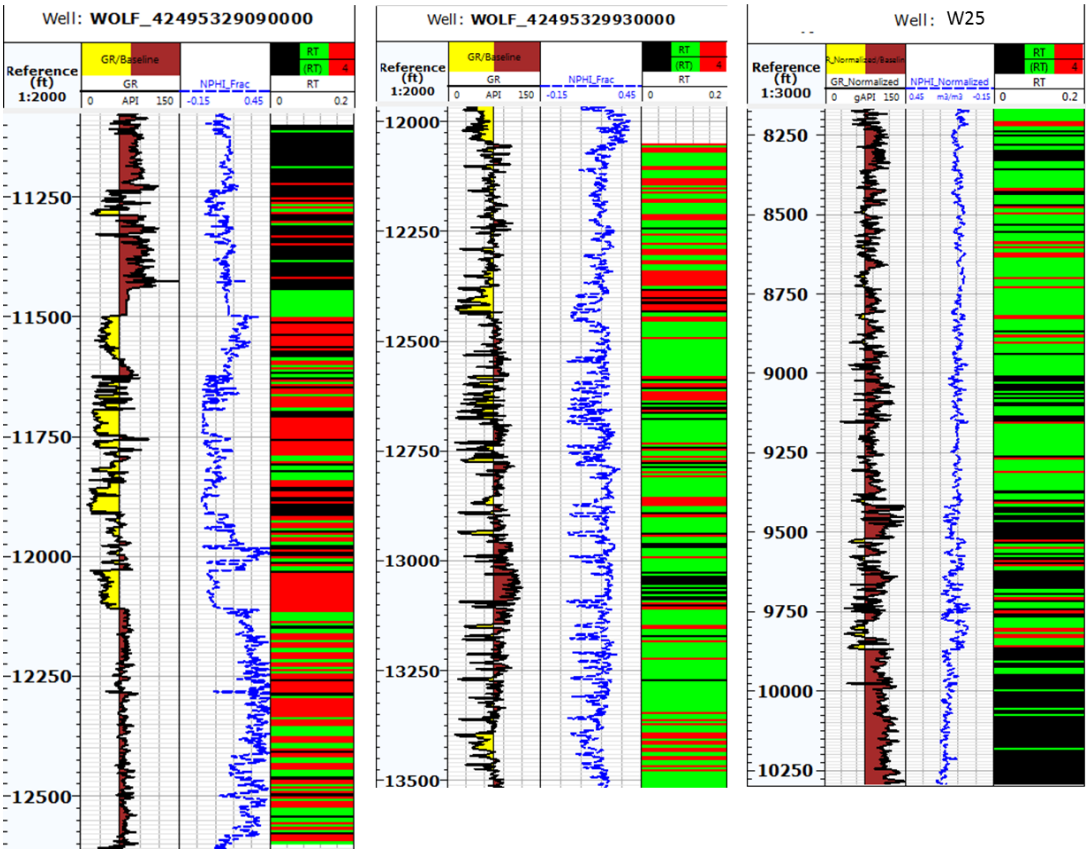
Well: WOLF_42495329090000
Well: WOLF_42495329930000
Well: W25
Reference (ft) 1:2000
Reference (ft) 1:3000
GR/Baseline
GR
NPHI_Frac
RT

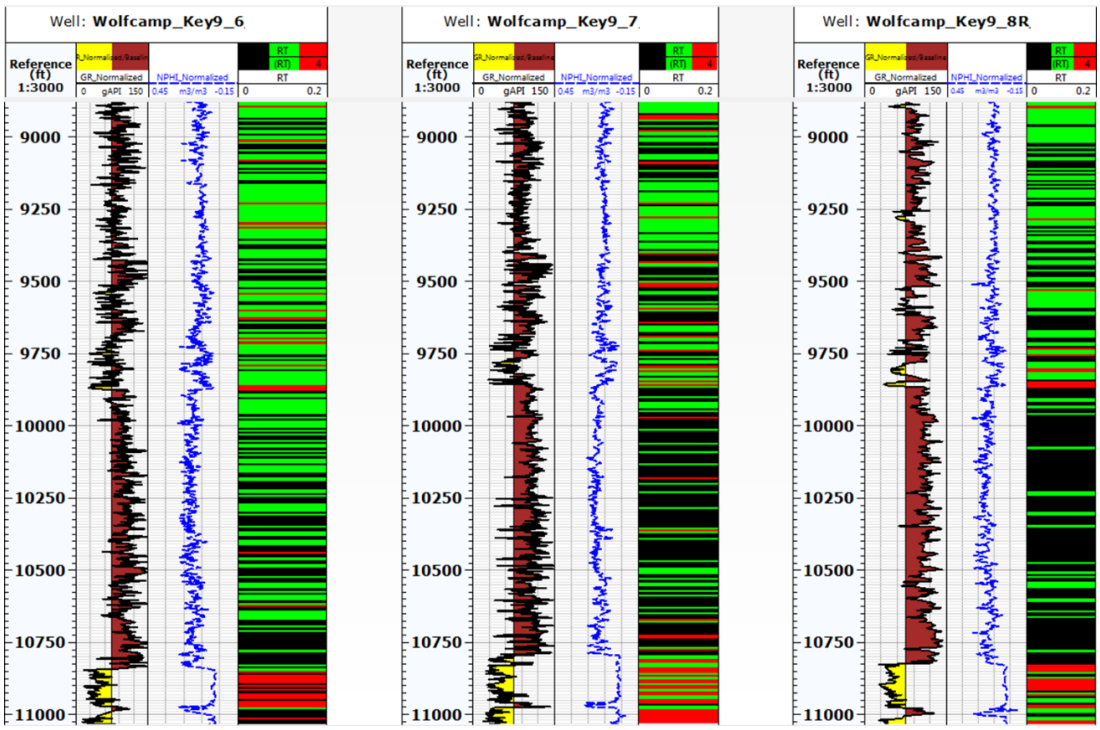
Well: Wolfcamp_Key9_6
Well: Wolfcamp_Key9_7
Well: Wolfcamp_Key9_8R
Reference (ft) 1:3000
GR_Normalized
NPHI_Normalized
RT
0 gAPI 150
0.045 m3/m3 -0.15
0 0.2
9000
9250
9500
9750
10000
10250
10500
10750
11000